

# **Attachment No. 1**

# New Layered Triazine Framework/Exfoliated 2D Polymer with Superior Sodium-Storage Properties

Jingjing Liu, Pengbo Lyu, Yu Zhang, Petr Nachtigall, and Yuxi Xu\*

The efficient synthesis of 2D polymers (2DPs) with tailorable structures and properties is highly desired but remains a considerable challenge. Here, the first solution synthesis of millimeter-size crystalline covalent triazine frameworks (CTFs) with a clear lamellar structure, which can be exfoliated into micrometer-size few-layer 2DP sheets via both micromechanical cleavage and liquid sonication, is reported. The obtained CTFs or 2DPs show a unique staggered AB stacking with a dominant pore size of  $\approx 0.6$  nm, which is different from the common eclipsed AA stacking in various covalent organic frameworks. The preference for AB stacking is due to the specific interaction of triflic acid with CTFs as revealed computationally. When explored as new polymeric anodes for sodium-ion batteries, both crystalline bulk CTF and exfoliated 2DP exhibit very high capacities (225 and 262 mA h g<sup>-1</sup> at 0.1 A g<sup>-1</sup>, respectively), impressive rate capabilities (67 and 119 mA h g<sup>-1</sup> at 5.0 A g<sup>-1</sup>, respectively), and excellent cycling stability (95% capacity retention after 1200 cycles) due to their robust conjugated porous structure, outperforming most organic/polymeric sodium-ion battery anodes ever reported.

Exfoliation of 2D covalent organic frameworks (COFs) with crystalline networks is considered as an important top-down approach to produce crystalline 2D polymers (2DPs) with versatile functionalities.<sup>[1–4]</sup> The synthesis of 2D COFs with highly extended and robust in-plane periodicity and graphite-like layered structure is essential for this strategy. The majority of current 2D COFs are synthesized utilizing the typical reversible reactions such as boronic acid condensations and Schiff base reactions, which may degrade the chemical or thermal stability of the 2D COFs,<sup>[5–8]</sup> while linking molecular building blocks by strong covalent bonds usually yields less defined materials.<sup>[9]</sup> In addition, most 2D COFs exist in a form of small microparticles and the layered structure has rarely been observed in them


clearly, resulting in the difficulty for further exfoliation. Although a few 2D COFs based on boronate ester, hydrazone, and imine bonding have been exfoliated via sonication and mechanical grinding,<sup>[10–15]</sup> the exfoliation of 2D COFs into micrometer-size smooth ultrathin 2DP sheets has still met with very limited success, thus restricting their practical applications such as electronics and energy-related fields. Recently, crystal engineering in which solid-phase polymerization performed between deliberately designed 2D-confined monomers in single crystals has been developed to prepare bulk lamellar crystals, which can be exfoliated to 2DPs.<sup>[16–19]</sup> Despite the current progress, efficient synthesis and exfoliation of large-size crystalline 2D COFs with robust linkage and layered structure remains a considerable challenge and largely unexplored for basic and applied research.

Herein, we demonstrate the first solution synthesis of millimeter-size crystalline covalent triazine frameworks (CTFs) with a distinct lamellar structure, from which micrometer-size few-layer 2DP sheets can be exfoliated via both micromechanical cleavage and liquid sonication. The obtained CTFs or 2DPs show a unique staggered AB stacking configuration, which is different from the eclipsed AA stacking in most 2D COFs<sup>[5,20]</sup> and is attributed to the site-specific adsorption of triflic acid during the CTF synthesis by the detailed theoretical simulations. Due to the robust conjugated porosity with aligned 1D open channels of the crystalline CTF and 2DP, which could afford fast and smooth diffusion pathways for charge transport and storage, we further explore the crystalline CTF and exfoliated 2DP as new polymeric anodes for sodium-ion batteries (SIBs), which can deliver a very high reversible capacity of 225/262 and 67/119 mA h g<sup>-1</sup> at a current density of 0.1 and 5.0 A g<sup>-1</sup>, respectively, and retain 95% of its initial capacity after 1200 cycles at 1.0 A g<sup>-1</sup>, surpassing most organic/polymeric SIB anodes ever reported.

Crystalline CTFs were synthesized by one-pot superacid catalytic trimerization reaction of 1,4-dicyanobenzene in the CH<sub>2</sub>Cl<sub>2</sub>/CF<sub>3</sub>SO<sub>3</sub>H solvent system (for experimental details see the Experimental Section). After overnight reaction, yellow CTF crystals with shining appearance were obtained (Figure 1a). The conversion ratio of monomer to CTF was  $\approx 86\%$  and the synthesis is scalable, allowing gram-scale production of CTFs. Optical microscopy (Figure S1, Supporting Information) and

J. J. Liu, Y. Zhang, Prof. Y. X. Xu  
Department of Macromolecular Science  
State Key Laboratory of Molecular Engineering of Polymers  
Fudan University  
Shanghai 200433, China  
E-mail: xuyuxi@fudan.edu.cn

P. B. Lyu, Prof. P. Nachtigall  
Department of Physical and Macromolecular Chemistry  
Faculty of Science  
Charles University  
Hlavova 2030, Prague 2, Prague 12843, Czech Republic

 The ORCID identification number(s) for the author(s) of this article can be found under <https://doi.org/10.1002/adma.201705401>.

DOI: 10.1002/adma.201705401

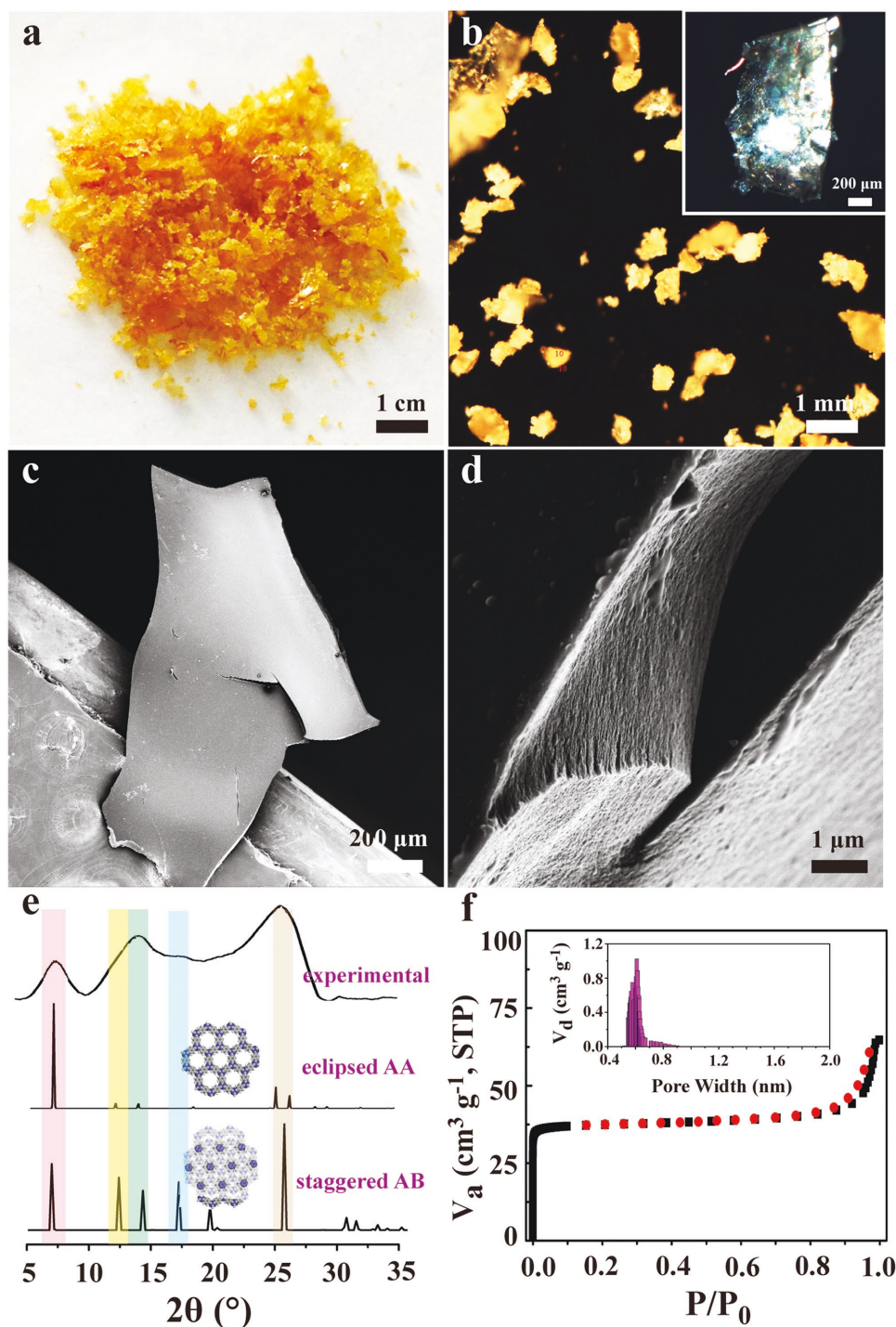


**Figure 1.** a) Photograph of the synthesized CTFs with shining appearance. b) POM image shows the flake morphology and good crystallinity of CTFs. The inset shows a single CTF crystal. c,d) SEM images of the CTF flake in different magnitude. The lamellar structure can be clearly seen from the cross-section. e) XRD pattern of CTFs and simulated XRD patterns using an eclipsed AA and staggered AB stacking mode. f)  $N_2$  adsorption and desorption isotherm profile of CTF at 77 K and its pore size distribution (inset).

polarizing microscopy (POM) (Figure 1b) showed that the as-synthesized CTF crystals have a unique flake morphology and a millimeter-level lateral size, much larger than most 2D COFs with a typical size of several micrometers. The bright birefringence from POM also suggests an internal order within

the CTF crystals (Figure 1b and its inset). Fourier-transform infrared spectroscopy (FT-IR) (Figure S2, Supporting Information) revealed that the carbonitrile group of the monomer was almost fully transformed to the triazine group in the CTF, indicating the high efficiency of trific acid catalytic 2D

polymerization. Scanning electron microscopy (SEM) revealed that the large CTF flake has clear lamellar features (Figure 1c,d; Figure S3, Supporting Information), suggesting an efficient layer-by-layer stacking of 2DP sheets within the CTF similar to graphite. The crystallinity and stacking mode of our layered CTF was further studied by powder X-ray diffraction (XRD) analysis and theoretical investigation. As shown in Figure 1e, the experimental XRD profile matches well with the simulated staggered AB one, reflecting the interlayer distance of 0.35 nm and a decent structural order of CTF. Figure 1f shows a typical type I isotherm for the CTF by N<sub>2</sub> adsorption/desorption isotherm measurement. The Brunauer–Emmett–Teller (BET) surface area was evaluated to be 142 m<sup>2</sup> g<sup>-1</sup>, which is lower than reported amorphous CTFs because of the high crystallinity and AB stacking of our CTF.<sup>[21,22]</sup> The very narrow peak in the pore-volume plot indicates that the pore width is quite homogenous and was estimated to be ≈0.6 nm (the inset in Figure 1f), in accordance with staggered AB stacking channels in the crystalline CTF.

Inspired from graphene,<sup>[23]</sup> our large-size layered CTF crystal not only can be exfoliated by liquid sonication, but also can be readily exfoliated by micromechanical cleavage using Scotch tape (Figure 2a; Figure S4, Supporting Information), which has never been realized in previous 2D COFs due to their small size and unclear lamellar structure.<sup>[2]</sup> Dispersions of micrometer-sized smooth 2DP nanosheets can be obtained by sonication of CTF crystals in *N,N*-dimethylformamide (DMF), and atomic force microscopy (AFM) shows that the thickness of the 2DP sheets was 2–3 nm (Figure 2b). Exfoliated 2DP sheets have a good dispersity in DMF solvent with no precipitates in one month (the inset in Figure 2b), which is desired for many applications. Micromechanical cleavage of CTF crystals can produce even larger 2DP sheets. A triangular micromechanically exfoliated 2DP sheet with sides more than 10 μm in length and neat edges was observed by transmission electron microscopy (TEM) (Figure 2c) and the high-resolution TEM (HRTEM) image of its margin demonstrated a distinct layered structure and the thickness of the micromechanically exfoliated 2DP sheet is ≈4 nm, consisting of ≈12 monolayers (Figure 2d). The measured interlayer distance was 0.35 nm, matching well with the XRD results (Figure 1e). The higher-magnification HRTEM image (Figure 2e) and the sharp selected-area electron diffraction (SAED) pattern (the inset in Figure 2e,) strongly confirmed high structural ordering and the hexagonal lattice within the exfoliated 2DP sheet, in accordance with the structure derived from density functional theory (DFT) calculations (Figure 2f). Raman spectroscopy of the 2DP sheets showed graphene-like sharp peaks (Figure S5, Supporting Information), indicating a 2D honeycomb structure within the 2DP.<sup>[24]</sup> Due to the robust triazine linkage and high crystallinity, the CTF crystal and the exfoliated 2DP sheets demonstrated superior thermal stability (Figure S6, Supporting Information; and Figure 2g). The 2DP sheet on SiO<sub>2</sub> substrate remained intact even after annealing at 500 °C in ambient air for 1 h (Figure 2g).

The above clear TEM images of the lattice structure of the multilayer 2DP sheets allow us to further understand the stacking arrangement of the monolayer 2DP in our crystalline CTF by the computational investigation. Two conceivable stacking possibilities were considered: (1) the eclipsed AA

arrangement, in which consecutive sheets are superimposed over each other (Figure 3a); and (2) the staggered graphite-like AB arrangement, in which a set of triazine (C<sub>3</sub>N<sub>3</sub>) units from the second layer always translate to the voids of the first layer (Figure 3b).<sup>[25]</sup> The lattice parameters of AA and AB unit cells are shown in Table S1 in the Supporting Information. Flat layers are found for AA structure while some deviations from planarity are apparent in AB structure (Figure 3a,b, respectively). Simulated HRTEM images reported in Figure 3c,d for AA and AB structures, respectively, are shown at high and low resolutions. The dotted line area (green) could be compared with the corresponding schematic descriptions (Figure S7, Supporting Information). Under our imaging conditions, the positions of bright areas of HRTEM images might be the electronegative center of triazine and benzene units.<sup>[25]</sup> The experimental HRTEM data (Figure 3e) gave the best fit for AB arrangement, and the distance between two diagonal atomic groups was measured as ≈1.4 nm, in agreement with the theoretical value.<sup>[26]</sup> In addition, comprehensive SAED simulation revealed that the observed diffraction pattern matches exclusively with AB stacking (Figure S8, Supporting Information).<sup>[27]</sup>

Because most 2D COFs including the ionothermal synthesized CTF show an eclipsed AA stacking mode,<sup>[20]</sup> we further investigated layer arrangement in CTF at the DFT-D level (see the Supporting Information for computational details). Based on the calculated interaction energies shown in Table S1 in the Supporting Information, AA stacking is more stable than AB one in a solvent-free environment. However, our CTF was experimentally synthesized in a triflic acid/dichloromethane mixture, and it resulted in the AB stacking. Results of computational investigation of the solvent effects are reported in Table S2 in the Supporting Information. The presence of dichloromethane influences the relative energies of AA and AB stacking only slightly and it does not lead to a qualitative change in interlayer interactions. On the contrary, the interaction of triflic acid with CTF is rather complex; both, associative and dissociative adsorption must be considered and even the triflic acid dimer formation turned out to be important (Figure S9, Supporting Information). Triflic acid interacts more favorably with the AB arrangement than with the AA one and this preference increases with increasing number of triflic acid molecules in the unit cell. There is a qualitative change in the relative stability of AA and AB stackings already for two triflic acid molecules in the unit cell (–428 kJ mol<sup>-1</sup> vs –443 kJ mol<sup>-1</sup>, respectively). Strong triflic acid forms dimers in between two layers, and it results in a qualitative shift from eclipsed AA to staggered AB layer arrangement (Figure 3f; Figure S10, Supporting Information). The adsorption of triflic acid in the CTF was confirmed by the energy-dispersion-spectroscopy in SEM, which showed sulfur element throughout the whole as-synthesized CTF. The triflic acid can be removed by further vacuum heating (Figure S11, Supporting Information), similar to the trap and removal of mesitylene guests in COF-1.<sup>[5]</sup>

SIBs have been considered to be promising candidates for large-scale and low-cost energy storage devices. A key challenge for SIBs is to overcome the sluggish kinetics and structural damage in the electrode material resulting from the electrochemical insertion/extraction of Na ions with larger radius than Li ions, which makes most superb lithium-ion battery

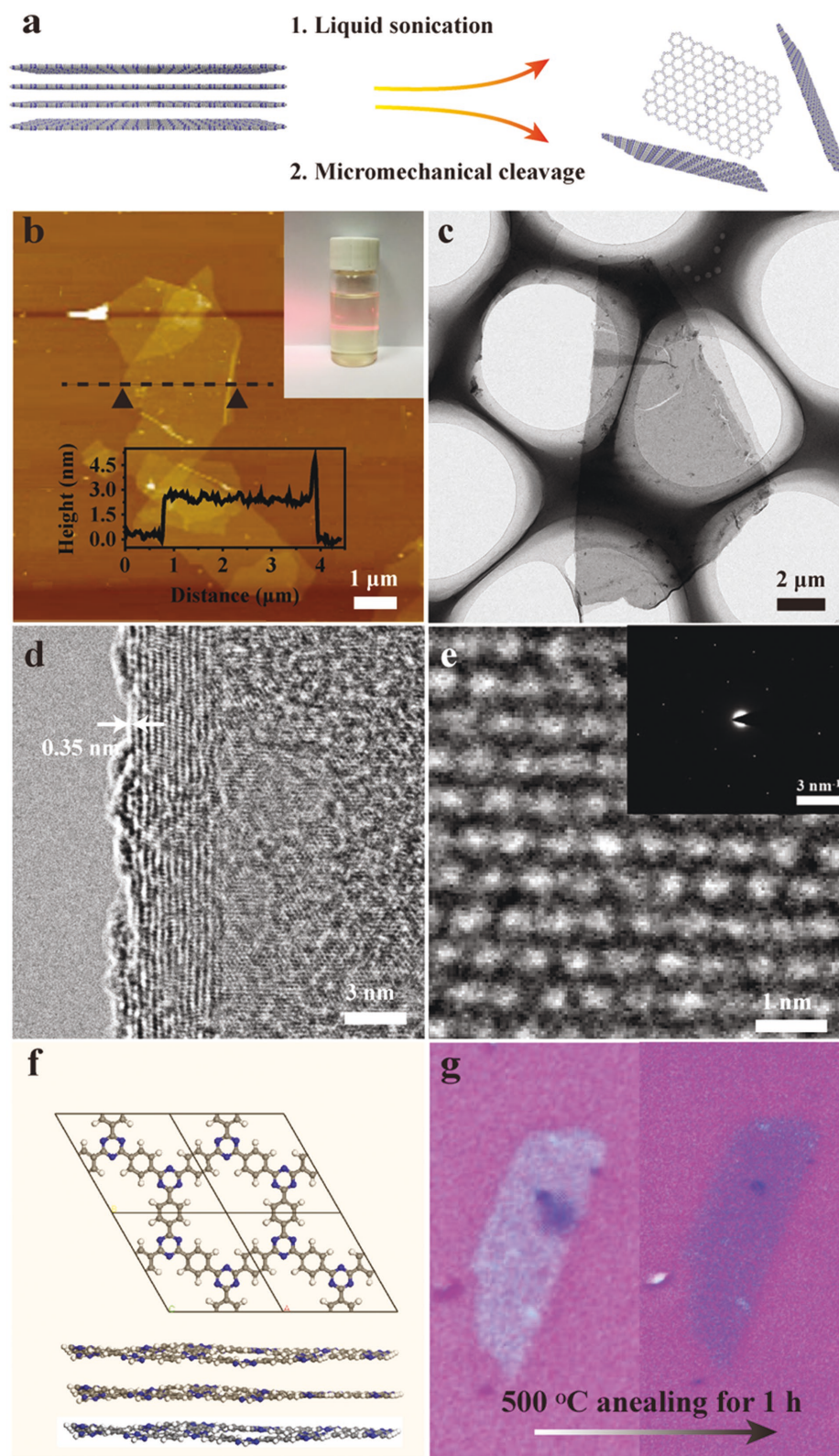


**Figure 2.** a) Schematic illustration for the exfoliation of bulk CTF into few-layer 2DP by liquid sonication or micromechanical cleavage method. b) AFM image of liquid-exfoliated 2DP nanosheets with 2–3 nm thickness. The inset is the photograph of 2DP dispersion in DMF ( $\approx 0.1 \text{ mg mL}^{-1}$ ). c) TEM image of a scotch tape-exfoliated 2DP sheet. d) HRTEM image shows that the sheet is nearly 12-layer thick and the interlayer distance is 0.35 nm. e) Higher-magnification HRTEM image of the same 2DP sheet and its corresponding SAED pattern (inset). f) The atomic structure of a three-layer 2DP from top view and side view calculated at the DFT level. g) Exfoliated 2DP sheet undergoes 500 °C annealing in ambient air for 1 h on  $\text{SiO}_2$  substrate.

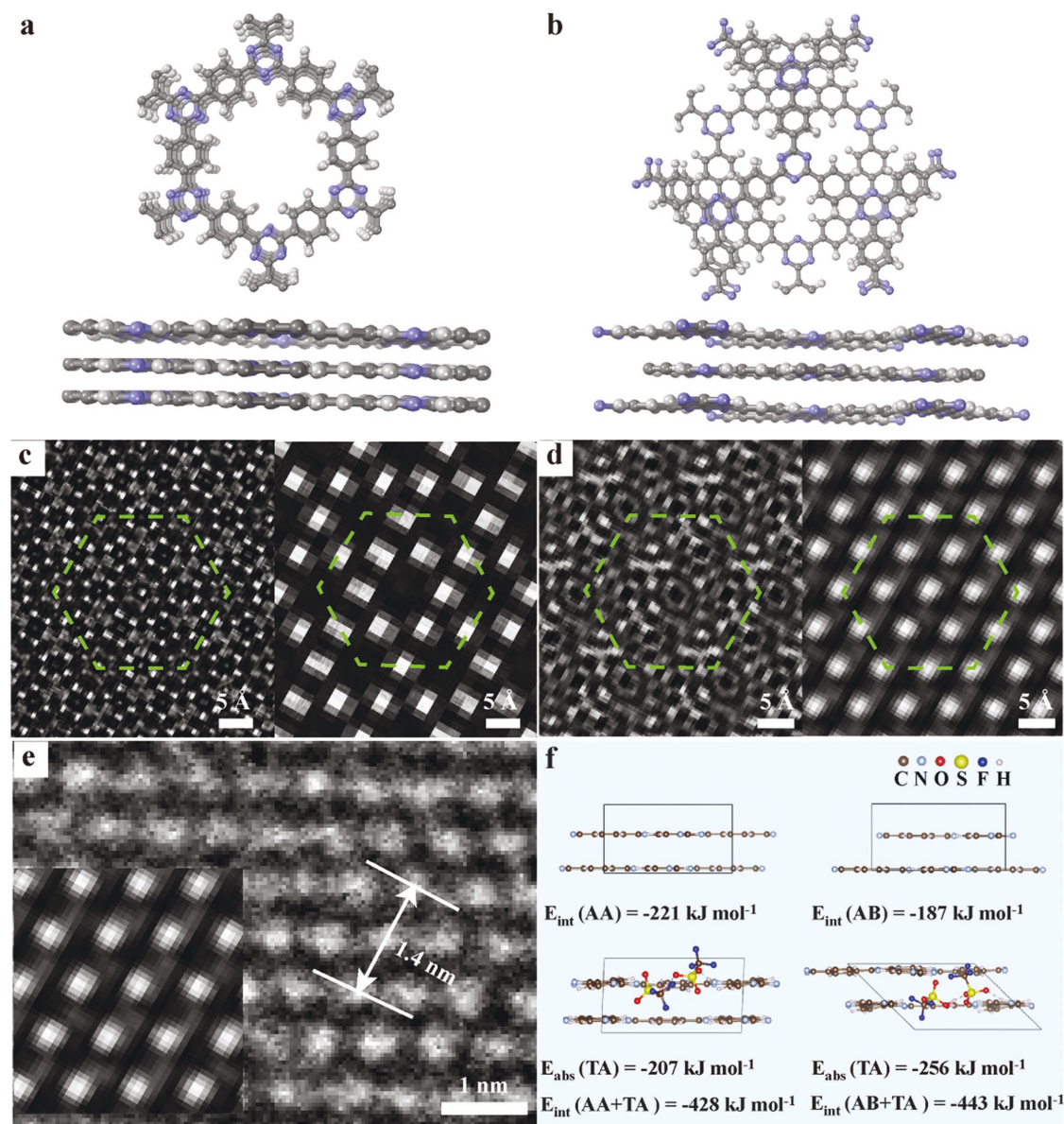


**Figure 3.** Two possible stacking arrangements with their respective calculated HRTEM images of 2DP: a,c) eclipsed AA and b,d) staggered AB. e) Experimental HRTEM image of 2DP matching with staggered AB model. f) The adsorption ( $E_{ads}$ ) and interaction ( $E_{int}$ ) energies of triflic acid molecules inside AA and AB bulks.

anode materials unsuitable for SIBs.<sup>[16]</sup> Our conjugated crystalline CTF shows aligned 1D open channels of  $\approx 0.6$  nm pore size, indicating its potential to afford fast and smooth diffusion pathways for Na ions. Combined with the excellent electronic conductivity from its  $\pi$ -conjugation (Figure S12, Supporting Information),<sup>[28]</sup> the CTF can be expected to demonstrate high sodium-storage ability. We thus studied the CTF as a new polymeric anode for SIBs in combination with metallic Na counter electrodes to fabricate a half-cell and to evaluate its electrochemical performance. The electrochemical performance of CTF was first evaluated by cyclic voltammetry. Due to the decomposition of electrolyte and the formation of a solid electrolyte interface on the surface of active materials, the first negative scan showed some irreversible reactions; however, it could be stable in the

subsequent few cycles (Figure S13, Supporting Information). Figure 4a shows the typical galvanostatic discharge/charge profiles of CTF at different current densities. The CTF showed a high reversible capacity of 225, 186, 160, 121, and 67  $\text{mA h g}^{-1}$  at 0.1, 0.5, 1.0, 2.0, and 5.0  $\text{A g}^{-1}$ , respectively (Figure 4a), surpassing most organic/polymeric SIB anodes. Based on the above-demonstrated efficient exfoliation of CTF, we also investigated the liquid-exfoliated 2DP nanosheets as another new polymeric SIB anode. Figure 4c shows the typical galvanostatic discharge/charge profiles of 2DP sheets at different current densities. Interestingly, the exfoliated 2DP sheets displayed notably increased capacity of 262, 223, 196, 172, and 119  $\text{mA h g}^{-1}$  at 0.1, 0.5, 1.0, 2.0, and 5.0  $\text{A g}^{-1}$ , respectively (Figure 4c). Meanwhile, the rate capability indicated by capacity retention at high

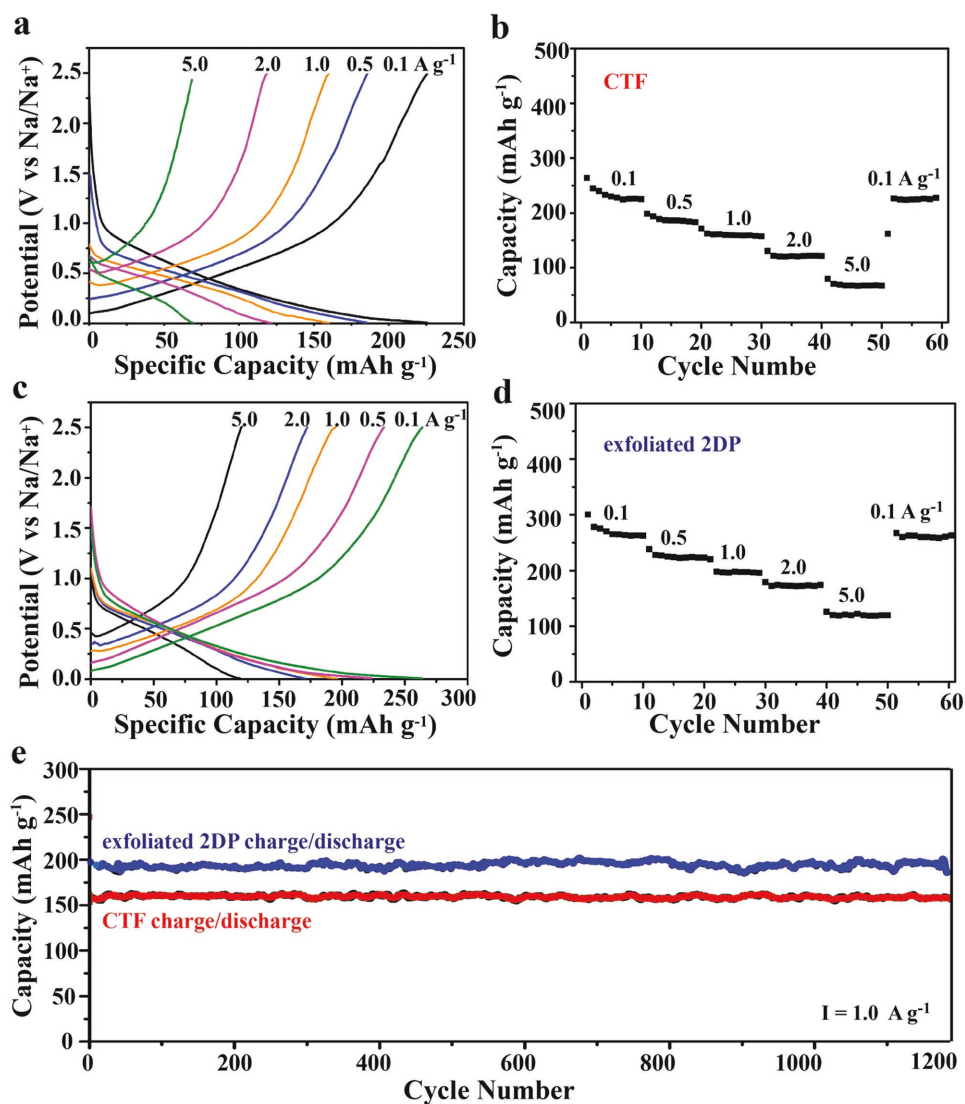


**Figure 4.** a,c) Galvanostatic charge/discharge profiles of CTF and exfoliated 2DP at different current densities, respectively. b,d) Charge capacities of the CTF and exfoliated 2DP electrode at 0.1, 0.5, 1.0, 2.0, and 5.0  $\text{A g}^{-1}$ , respectively. e) Cycle performance of CTF and exfoliated 2DP up to 1200 cycles at 1.0  $\text{A g}^{-1}$ .

current density from 0.1 to 5  $\text{A g}^{-1}$  was enhanced from 30% for bulk CTF to 45% for exfoliated 2DP sheets (Figure 4b,d). The improved electrochemical performance could be ascribed to the exfoliation of bulk CTF into few-layer 2DP nanosheets that promotes electron and Na ion transport in the electrode to realize higher utilization efficiency of active sites and faster kinetics for sodium storage, which was confirmed by the electrochemical impedance spectroscopy (Figure S14, Supporting Information). Remarkably, both the CTF and 2DP anodes achieved excellent cycle performance over 1200 cycles and retained 95% of its initial capacity of 163 and 198  $\text{mA h g}^{-1}$  at a high current density of 1.0  $\text{A g}^{-1}$  (Figure 4e), which is benefited from their robust covalent frameworks with open channels in the  $\pi$ -conjugated porous structure for reversible and smooth electrochemical insertion/extraction of Na ions. It is noteworthy that the electrochemical performance of bulk CTF and 2DP is superior to most organic/polymeric and many inorganic SIB anodes including

hard carbon,<sup>[29]</sup> and particularly the 2DP is among the best organic/polymeric SIB anodes reported so far (Table S3, Supporting Information).

In summary, we have demonstrated the first solution approach to synthesize millimeter-sized crystalline COFs with a clear lamellar structure and robust triazine linkage, which can be exfoliated into micrometer-sized few-layer 2DP sheets via both micromechanical cleavage and liquid sonication. The obtained CTFs and 2DP show a unique staggered AB stacking due to the absorption of triflic acid molecule during the synthesis, and thus possess aligned open channels with a dominant pore size of  $\approx 0.6$  nm. Due to the highly conjugated porous structure, the bulk CTF and exfoliated 2DP demonstrated superior sodium-storage ability, including high capacities, excellent rate capabilities, and stable cycling performances, which render them among the best organic/polymeric SIB anodes ever reported. This study provides a versatile route to construct

a new variety of 2D COFs and 2DPs with great potential in energy-related applications and beyond.

## Experimental Section

**Synthesis of CTF:** Typically, 1 mL of  $\text{CF}_3\text{SO}_3\text{H}$  was added into a 250 mL predried flask and 200 mg of 1,4-dicyanobenzene was previously dissolved into 20 mL  $\text{CH}_2\text{Cl}_2$ . The  $\text{CH}_2\text{Cl}_2$  solution was centrifuged at  $12\,000\text{ r min}^{-1}$  for 30 min to remove the undissolved monomer. Afterward, the transparent monomer solution was transferred into a dropping funnel and was added dropwise to the flask under the temperature of  $100\text{ }^\circ\text{C}$  for 2 h with stirring. The reaction system was equipped with a reflux unit and kept  $100\text{ }^\circ\text{C}$  heating and stirring overnight to promote the complete reaction conversion for the formation of CTF. After 4 h reaction, there were found yellow crystals gradually attached around the flask. Until no more crystals increased, the final product could be gathered through filtration of the solution after quenching by ethanol and was washed with ethanol and *N,N*-dimethylformamide (DMF) alternatively several times to thoroughly remove the unreacted monomer and acid residual. Then the obtained product was dried in a vacuum oven at room temperature for 2 h. To further remove the interior-adsorbed triflic acid molecular, the as-synthesized CTF was vacuum heated at  $150\text{ }^\circ\text{C}$  for 12 h.

**Liquid Exfoliation of CTF to 2DP:** Liquid-exfoliated 2DP was prepared by adding 150 mg bulk CTF into 50 mL DMF. The sample was soaked and stirred for 2 h, and then was sonicated for 60 min (200 W). To prepare AFM samples, the as-prepared sample was centrifuged at  $3000\text{ r min}^{-1}$  for 20 min. The supernatant was dropped cast onto mica for AFM analysis.

**Electrochemical Characterization:** To investigate the sodium-storage performance, a uniform slurry was prepared by mixing pregrinded CTF or exfoliated 2DP (70 wt%), Super P carbon black (20 wt%), and polyvinylidene fluoride binder (10 wt%) in 1-methyl-2-pyrrolidinone solution. The slurry was coated on copper foil and dried at  $120\text{ }^\circ\text{C}$  in vacuum oven overnight. The coated copper foil was cut into 12 mm in diameter disks. CR2016 coin cells were assembled in an Ar-filled glove box by using sodium metal as the reference electrode and counter electrode, with a glass microfiber filter (Whatman) as the separator. Here, 1 M  $\text{NaPF}_6$  in 1:1 (v/v) mixture of ethylene carbonate and dimethyl carbonate as electrolyte was used. Electrochemical experiments were performed using battery cycler (LAND-CT2001 A) at the voltage range of 0.01–2.5 V (vs Na/Na<sup>+</sup>). The capacity was calculated based on the mass of active materials.

**Characterizations:** SEM was conducted on Ultra 55 operated at an acceleration voltage of 10 kV. TEM observations were carried out on a JEM-2011 (JEOL Ltd., Japan) with an accelerating voltage of 80, 120, or 200 kV. TEM samples were prepared by transferring exfoliated 2D CTF onto carbon-coated copper grids. AFM was conducted on a scanning probe microscope (Multimode 8). Optical microscopy and POM observations were carried out with a Leica DM4000M optical microscope from Leica Microsystems Wetzlar GmbH, Germany. FT-IR was recorded on a Nicolet 6700 model using KBr platelets. The thermal properties of 2D-CTF materials were evaluated using a thermogravimetric analysis instrument (Pyris 1) over the temperature range of  $25\text{--}800\text{ }^\circ\text{C}$  under nitrogen atmosphere with a heating rate of  $10\text{ }^\circ\text{C min}^{-1}$ . The BET surface area of the 2D-CTF crystals was performed on JWGB-BK with micropore option.  $\text{N}_2$  sorption analyses were performed using a liquid  $\text{N}_2$  bath. Pore size distribution was calculated by nonlocal DFT (NLDFT) modeling based on  $\text{N}_2$  adsorption data. Powder XRD patterns were recorded on X'pert PRO (PANalytical) with high intensity Microfocus rotating anode X-ray generator. All the samples were recorded in the range of  $3\text{--}40^\circ$ , and data were collected with the help of Control Win software. The Raman spectra were excited by a 532 nm laser, and the spot size of the laser beam was about  $0.5\text{ }\mu\text{m}$ . Electronic conductivity was conducted on transferring a mechanical exfoliated few-layer 2D-CTF sheet onto a p-type Si substrate

with 300 nm  $\text{SiO}_2$ . Then Au films with Ti adhesion layers (30 nm/5 nm) were thermally deposited onto the top of the 2DP film as electrodes. The device was annealed at  $150\text{ }^\circ\text{C}$  for 2 h in Ar atmosphere before testing.

## Supporting Information

Supporting Information is available from the Wiley Online Library or from the author.

## Acknowledgements

J.J.L. and P.B.L. contributed equally to this work. The authors acknowledge support by the National Natural Science Foundation of China (51673042), and the Program for Professor of Special Appointment (Eastern Scholar) at Shanghai Institutions of Higher Learning (TP2015002). P.N. and P.L. acknowledge the Charles University Centre of Advanced Materials (CUCAM) (OP VVV Excellent Research Teams, project number CZ.02.1.01/0.0/0.0/15\_003/0000417).

## Conflict of Interest

The authors declare no conflict of interest.

## Keywords

2D polymers, AB stacking, crystalline triazine frameworks, lamellar structures, sodium-ion batteries

Received: September 19, 2017

Revised: December 29, 2017

Published online: January 23, 2018

- [1] Z. Xiang, D. Cao, L. Dai, *Polym. Chem.* **2015**, *6*, 1896.
- [2] D. R. S. Miguel, P. A. Ochoa, F. Zamora, *Chem. Commun.* **2016**, *52*, 4113.
- [3] P. Payamyar, B. T. King, H. C. Oettinger, A. D. Schlueter, *Chem. Commun.* **2016**, *52*, 18.
- [4] P. J. Waller, F. Gandara, O. M. Yaghi, *Acc. Chem. Res.* **2015**, *48*, 3053.
- [5] A. P. Cote, A. I. Benin, N. W. Ockwig, M. O. Keeffe, A. J. Matzger, O. M. Yaghi, *Science* **2005**, *310*, 1166.
- [6] N. Huang, P. Wang, D. Jiang, *Nat. Rev. Mater.* **2016**, *1*, 16068.
- [7] F. J. U. Romo, C. J. Doonan, H. Furukawa, K. Oisaki, O. M. Yaghi, *J. Am. Chem. Soc.* **2011**, *133*, 11478.
- [8] S. Y. Ding, W. Wang, *Chem. Soc. Rev.* **2013**, *42*, 548.
- [9] J. W. Colson, W. R. Dichtel, *Nat. Chem.* **2013**, *5*, 453.
- [10] I. Berlanga, M. L. R. Gonzalez, J. L. G. Fierro, R. M. Balleste, F. Zamora, *Small* **2011**, *7*, 1207.
- [11] S. Mitra, S. Kandambeth, B. P. Biswal, U. K. Kharu, R. Banerjee, *J. Am. Chem. Soc.* **2016**, *138*, 2823.
- [12] S. Chandra, S. Kandambeth, B. P. Biswal, T. Heine, R. Banerjee, *J. Am. Chem. Soc.* **2013**, *135*, 17853.
- [13] D. N. Bunck, W. R. Dichtel, *J. Am. Chem. Soc.* **2013**, *135*, 14952.
- [14] S. Wang, Q. Wang, P. Shao, X. Ma, J. Zhou, X. Feng, B. Wang, *J. Am. Chem. Soc.* **2017**, *139*, 4258.
- [15] M. Shouvik, S. S. Himadri, K. Tanay, B. Rahul, *J. Am. Chem. Soc.* **2017**, *139*, 4513.



- [16] W. Liu, X. Luo, Y. Bao, C. T. Nai, Z. G. Hu, D. Zhao, B. Liu, S. Y. Quek, K. P. Loh, *Nat. Chem.* **2017**, *9*, 563.
- [17] M. J. Kory, M. Woerle, T. Weber, P. Payammyar, N. Trapp, A. D. Schlueter, *Nat. Chem.* **2014**, *6*, 779.
- [18] P. Kissel, D. J. Murray, W. J. Wulfange, V. J. Catalano, B. T. King, *Nat. Chem.* **2014**, *6*, 774.
- [19] P. Kissel, R. Erni, W. B. Schweizer, M. D. Rossell, A. D. Schlueter, J. Sakamoto, *Nat. Chem.* **2012**, *4*, 287.
- [20] P. Kuhn, M. Antonietti, A. Thomas, *Angew. Chem., Int. Ed.* **2008**, *47*, 3450.
- [21] S. Ren, M. J. Bojdys, R. Dawson, A. Laybourn, Y. Z. Khimyak, D. J. Adams, A. I. Cooper, *Adv. Mater.* **2012**, *24*, 2357.
- [22] M. J. Bojdys, J. Jeromenok, A. Thomas, M. Antonietti, *Adv. Mater.* **2010**, *22*, 2202.
- [23] A. K. Geim, K. S. Novoselov, *Nat. Mater.* **2007**, *6*, 183.
- [24] A. C. Ferrari, J. C. Meyer, D. Jiang, K. S. Novoselov, S. Roth, A. K. Geim, *Phys. Rev. Lett.* **2006**, *97*, 187401.
- [25] G. A. Siller, N. Severin, S. Y. Chong, A. I. Cooper, A. Thomas, M. J. Bojdys, *Angew. Chem.* **2014**, *53*, 7450.
- [26] K. Sakaushi, E. Hosono, G. Nickerl, T. Gemming, H. Zhou, S. Kaskel, J. Eckert, *Nat. Commun.* **2013**, *4*, 1485.
- [27] R. Matsuoka, R. Sakamoto, K. Hoshiko, S. Sasaki, K. Nagashio, H. Nishihara, *J. Am. Chem. Soc.* **2017**, *139*, 3145.
- [28] J. J. Liu, W. Zan, K. Li, Y. Yang, F. X. Bu, Y. X. Xu, *J. Am. Chem. Soc.* **2017**, *139*, 11666.
- [29] H. S. Hou, X. Q. Qiu, W. F. Wei, Y. Zhang, X. B. Ji, *Adv. Energy Mater.* **2017**, *7*, 1602898.

# **Attachment No. 2**

## Donor–Acceptor Systems

7  
EuCheMS

## Fluorescent Sulphur- and Nitrogen-Containing Porous Polymers with Tuneable Donor–Acceptor Domains for Light-Driven Hydrogen Evolution

Dana Schwarz,<sup>[a, b]</sup> Amitava Acharja,<sup>[c]</sup> Arun Ichangi,<sup>[a, d]</sup> Pengbo Lyu,<sup>[e]</sup> Maksym V. Opanasenko,<sup>[e]</sup> Fabian R. Goßler,<sup>[b]</sup> Tobias A. F. König,<sup>[b]</sup> Jiří Čejka,<sup>[e]</sup> Petr Nachtigall,<sup>[e]</sup> Arne Thomas,<sup>[c]</sup> and Michael J. Bojdys\*<sup>[d, f]</sup>

**Abstract:** Light-driven water splitting is a potential source of abundant, clean energy, yet efficient charge-separation and size and position of the bandgap in heterogeneous photocatalysts are challenging to predict and design. Synthetic attempts to tune the bandgap of polymer photocatalysts classically rely on variations of the sizes of their  $\pi$ -conjugated domains. However, only donor–acceptor dyads hold the key to prevent undesired electron-hole recombination within the catalyst via efficient charge separation. Building on our previous success in incorporating electron-donating, sulphur-containing linkers and electron-withdrawing, triazine ( $C_3N_3$ ) units into porous polymers, we report the synthesis of six visible-light-active, triazine-based polymers with a high heteroatom-content of S and N that photocatalytically generate  $H_2$  from water: up to  $915 \mu\text{mol h}^{-1} \text{g}^{-1}$  with Pt co-catalyst, and—as one of the highest to-date reported values  $-200 \mu\text{mol h}^{-1} \text{g}^{-1}$  without. The highly modular Sonogashira–Hagihara cross-coupling reaction we employ, enables a systematic study of mixed (S, N, C) and (N, C)-only polymer systems. Our results highlight that photocatalytic water-splitting does not only require an ideal optical bandgap of  $\approx 2.2$  eV, but that the choice of donor–acceptor motifs profoundly impacts charge-transfer and catalytic activity.

mers. This sets them apart from crystalline inorganic semiconductors that rely on very discrete compositions for bonding or catalytic activity to occur.<sup>[1]</sup> For example, conjugated microporous polymers (CMPs) can be prepared from statistical co-polymerisation of polycyclic, aromatic sub-units of varying sizes that enable pore-size tuning,<sup>[2]</sup> a continuous spectrum of bandgaps,<sup>[3]</sup> and as a result also varying degrees of photocatalytic activity.<sup>[4]</sup> The chemical make-up of the overwhelming majority of CMPs is carbon-only. As a consequence, charge-transfer is insufficient to prevent spontaneous recombination of photo-induced electron-hole pairs,<sup>[5]</sup> and efficient photocatalysis using CMPs strictly relies on electron migration to a noble-metal co-catalyst, usually platinum (Pt). In practice, nearly all photocatalytic water splitting studies explore one half-reaction—proton reduction—in a set-up that provides a sacrificial electron donor, such as triethanolamine (TEOA) and Pt as a co-catalyst. Cooper et al. pointed out that to make use of the full benefit of polymeric photocatalysts, the addition of Pt as a co-catalyst should not be essential.<sup>[4b]</sup> Conversely, polymeric carbon nitride has a very high stoichiometric ratio of carbon-to-nitrogen of 6-to-9. Although this polymer shows some, low activity in noble metal free photocatalysis, again only the addition of a Pt co-catalyst makes this process efficient.<sup>[6]</sup> Substantially higher hydrogen evolution rates are achieved predominantly via post-synthetic modifications of polymeric carbon nitrides by templating or by further heteroatom doping.<sup>[7]</sup> In summary, it seems that introduction of distinct domains or point-defects increases the likelihood of electron-hole separation and thus of enhanced photocatalytic activity; a finding that was confirmed for azine covalent organic frameworks.<sup>[8]</sup> It is worth to note, that claims of no addition of a metal co-cata-

Polymeric semiconductor photocatalysts for hydrogen evolution from water are an intriguing material class, since they can be produced from a continuous spectrum of variable mono-

[a] Dr. D. Schwarz, A. Ichangi  
Department of Organic Chemistry, Charles University  
Hlavova 8, 128 43 Prague 2 (Czech Republic)

[b] Dr. D. Schwarz, F. R. Goßler, T. A. F. König  
Leibniz-Institut für Polymerforschung Dresden e.V.  
Institute of Physical Chemistry and Polymer Physics  
Hohe Str. 6, 01069 Dresden (Germany)

[c] A. Acharja, Prof. Dr. A. Thomas  
Institute of Chemistry, Technische Universität Berlin  
Hardenbergstraße 40, 10623 Berlin (Germany)

[d] A. Ichangi, Dr. M. J. Bojdys  
Institute of Organic Chemistry and Biochemistry of the CAS  
Flemingovo nám. 2, 166 10 Prague 6 (Czech Republic)

[e] P. Lyu, Dr. M. V. Opanasenko, Prof. Dr. J. Čejka, Prof. Dr. P. Nachtigall  
Faculty of Science, Department of Physical and Macromolecular Chemistry  
Charles University  
Hlavova 8, 128 43 Prague 2 (Czech Republic)

[f] Dr. M. J. Bojdys  
Humboldt-Universität zu Berlin, Department of Chemistry  
Brook-Taylor-Str. 2, 12489 Berlin (Germany)  
E-mail: m.j.bojdys.02@cantab.net

Supporting information and the ORCID identification number(s) for the author(s) of this article can be found under:  
<https://doi.org/10.1002/chem.201802902>.

Part of the Special Issue for the 7th EuCheMS Chemistry Congress consisting of contributions from selected speakers and conveners. To view the complete issue, visit Issue 46.

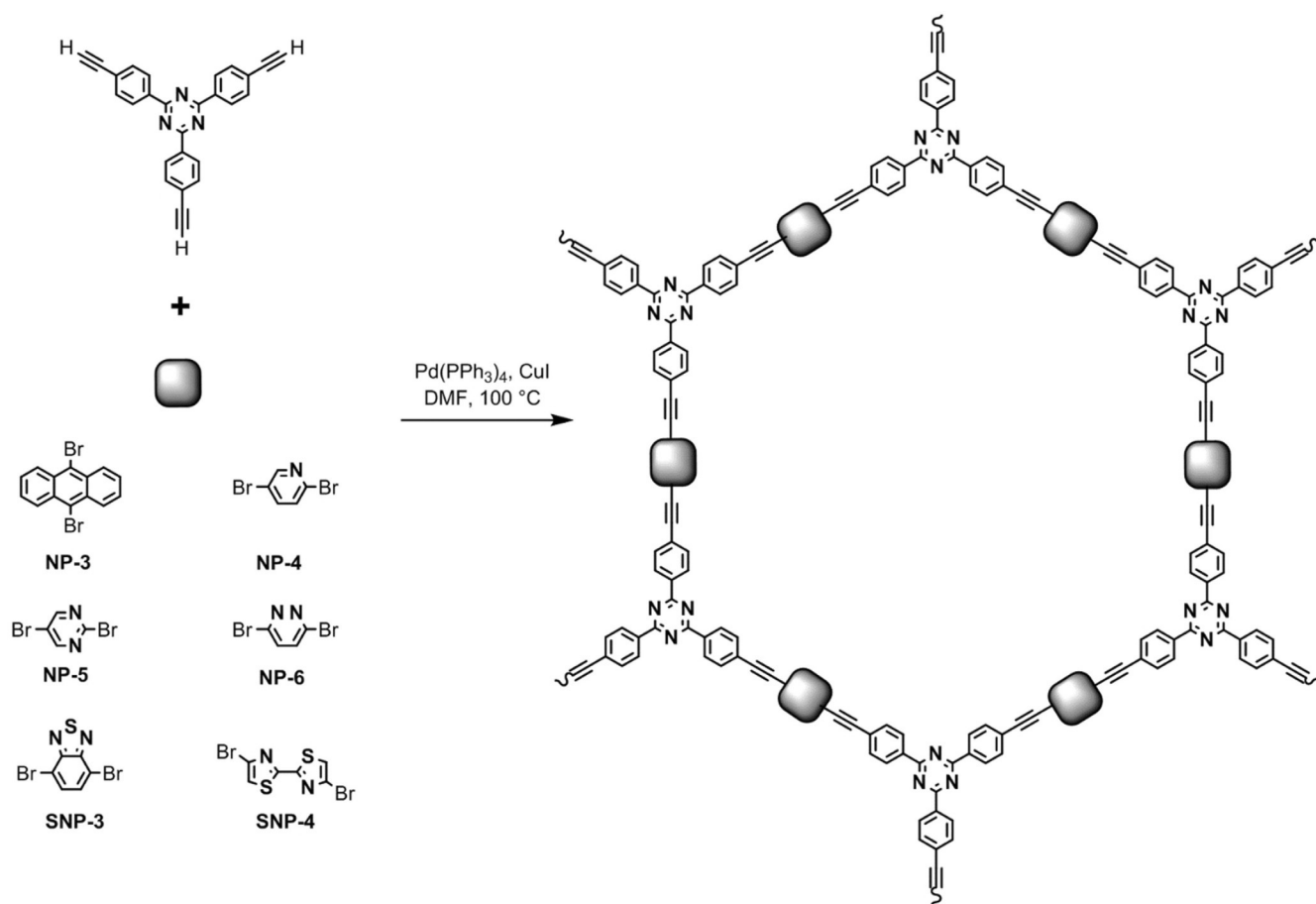
lyst do not necessarily equate to a truly “metal-free” catalysis. Oftentimes, heavy metal ions and other elements (e.g. Pd, Cu, P) remain in the polymer matrix as residue from the linking reaction and have to be taken into account when comparing photocatalytic activity.<sup>[9]</sup>

There are ways of tuning surface polarity, pore structure, and catalytic properties of conjugate polymer frameworks for example by incorporation of the triazine ( $C_3N_3$ ) group—an electron-withdrawing and spatially co-planar,  $C_3$  symmetric building block.<sup>[10]</sup> We explored further modifications in a series of sulphur- and nitrogen-containing porous polymers (SNPs) that exploit donor–acceptor interactions for bandgap-tuning and charge separation for photocatalysis,<sup>[11]</sup> and one of these networks shows the highest reported hydrogen evolution rate under visible light irradiation for an as-received polymer photocatalyst to-date.<sup>[12]</sup> Inspired by the lead that incorporation of donor–acceptor domains holds the key to enhanced photocatalytic activity, here, we explore six covalent triazine-based porous polymer frameworks with subtle variation of their heteroatom content.

Two principle groups of (S, N, C)- and (N, C)-containing porous polymers have been achieved referred to as SNPs and NPs, respectively. The network-forming reaction is the palladium-catalysed Sonogashira–Hagihara cross-coupling protocol.<sup>[13]</sup>

Note, that the polymers contain a very low residual of Pd from the cross-coupling of 0.04 to 0.13 wt% (see below and in the Supporting Information). Hence, it is unlikely that the Pd contributes significantly to the observed hydrogen evolution rates in the presence of co-catalyst. After purification, the products NP-3 (based on anthracene linkers), NP-4, NP-5, NP-6 (based on asymmetric N-heterocycles), SNP-3, and SNP-4 (based on sulphur- and nitrogen-containing tectons) were obtained as yellow (NP-4, NP-5, and NP-6), orange (SNP-4) and brown (NP-3 and SNP-3) powders with yields above  $\approx 90\%$  (see Scheme 1 and Figure S2). Experimental details are given in the Supporting Information.

The polymers were characterised by infrared (IR) spectroscopy, thermogravimetric analysis (TGA),  $^{13}C$  cross-polarisation magnetic-angle spinning (CP/MAS) NMR spectroscopy, X-ray photoelectron spectroscopy (XPS), and combustion elemental analysis (EA) to confirm the structure and possible impurities from the synthesis (see Supporting Information). In  $^{13}C$  CP/MAS NMR spectroscopy all materials show a peak at 172 ppm ascribed to the  $C_3N_3$  ring (Figure 1). Peaks between 142 and 124 ppm are assigned to the  $sp^2$  hybridised carbons (C–C and C–H) and carbons within the sulphur- and nitrogen-containing heterocycles. Quaternary carbons are visible around 124 ppm. Peaks at approx. 99 and 88 ppm are  $sp$ -hybridised  $-C\equiv C-$  sites.



**Scheme 1.** Synthetic route to NPs and SNPs.  $C_3$ -symmetric 2,4,6-tris(4-ethynylphenyl)-1,3,5-triazine is coupled with a  $C_2$ -symmetric bridge such as: 9,10-dibromoanthracene to yield NP-3, 2,5-Dibromopyridine to yield NP-4, 2,5-dibromopyrimidine to yield NP-5, 3,6-dibromopyridazine to yield NP-6, 4,7-dibromobenzo-[c]-1,2,5thiadiazole to yield SNP-3, and 5,5'-dibromo-2,2'-bithiazole to yield SNP-4.

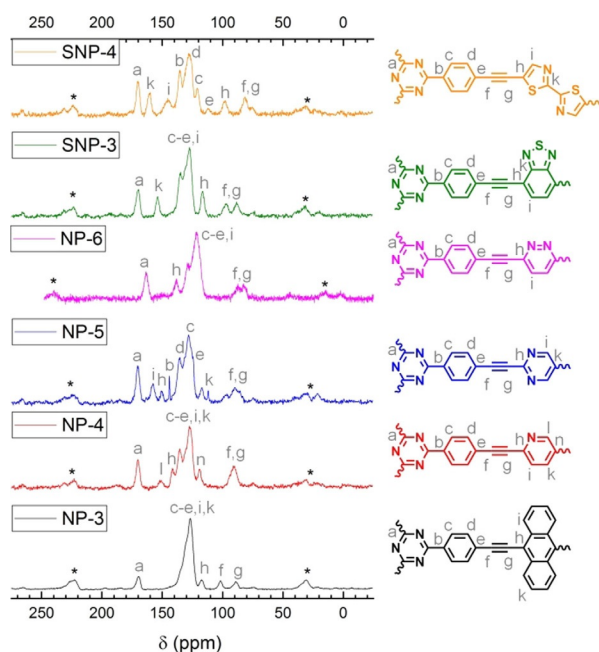


**Figure 1.**  $^{13}\text{C}$  CP-MAS ssNMR spectra of NPs and SNPs from top to bottom SNP-4 (in orange), SNP-3 (in green), NP-6 (in magenta), NP-5 (in blue), NP-4 (in red), and NP-3 (in black). Spectra were recorded at a MAS rate of 12.0 kHz featuring triazine, phenyl and ethylene groups from left to right-hand-side, asterisks denote spinning sidebands.

All networks show two  $sp$ -hybridised  $-\text{C}\equiv\text{C}-$  environments due to asymmetric substitution across this bridge. IR spectra of all six polymers are shown in Figure S10 and reveal miniscule peaks at  $3300\text{ cm}^{-1}$  that correspond to the unreacted  $-\text{C}\equiv\text{C}-\text{H}$  bond vibrations. The  $-\text{C}\equiv\text{C}-$  bond formed during the polymerisation shows as a peak at around  $2200\text{ cm}^{-1}$ .<sup>[14]</sup> EA, EDX, and TGA confirm the yields of around 100% with almost no residual elements from the coupling reaction (e.g. residual Pd content varies between 0.04 to 0.13 wt%) (Table S4, S5, S6 and Figure S5). Similar Sonogashira and also Suzuki coupling reactions often lead to higher concentrations of residual catalyst.<sup>[5,13,15]</sup>

The pore systems of the polymers were investigated by nitrogen sorption measurements at 77 K (Figure 2a). All polymers feature micro- and mesopores with a visible hysteresis. The accessible surface areas calculated by Brunauer–Emmett–Teller (BET) equation are between  $210$  and  $600\text{ m}^2\text{ g}^{-1}$  (Table 1) which is in the range of similar, carbon-only CMPs (e.g. CMP-3 with  $522\text{ m}^2\text{ g}^{-1}$ ).<sup>[13]</sup> In general, surface areas of previously reported S- and N-containing polymers are on average lower with values between  $12$  and  $250\text{ m}^2\text{ g}^{-1}$ .<sup>[14–16]</sup>

$\text{CO}_2$  uptake values are within the range of nitrogen-containing CMPs and show a dependence on overall nitrogen content and surface area.<sup>[2,17]</sup> NP-5 and NP-6 have the highest amount of nitrogen and feature the highest  $\text{CO}_2$  uptake with around  $1.9\text{ mmol g}^{-1}$ . SNP-4 has the lowest  $\text{CO}_2$  uptake with  $1.30\text{ mmol g}^{-1}$  (similar to NP-3) due to the comparably low guest-accessible surface area.  $\text{CO}_2$  sorption isotherms are shown in Figure 2b and show a linear uptake with no discernible hysteresis which is typical for microporous polymers.

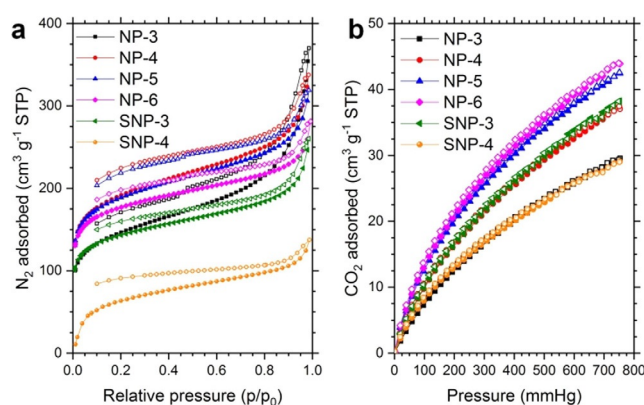


**Figure 2.** a) Nitrogen adsorption/desorption isotherms and b)  $\text{CO}_2$  sorption isotherms measured at 273 K for NP-3 (in black), NP-4 (in red), NP-5 (in blue), NP-6 (in magenta), SNP-3 (in green), SNP-4 (in orange). Data points in the adsorption and desorption branch of the isotherms are indicated by filled and empty circles, respectively.

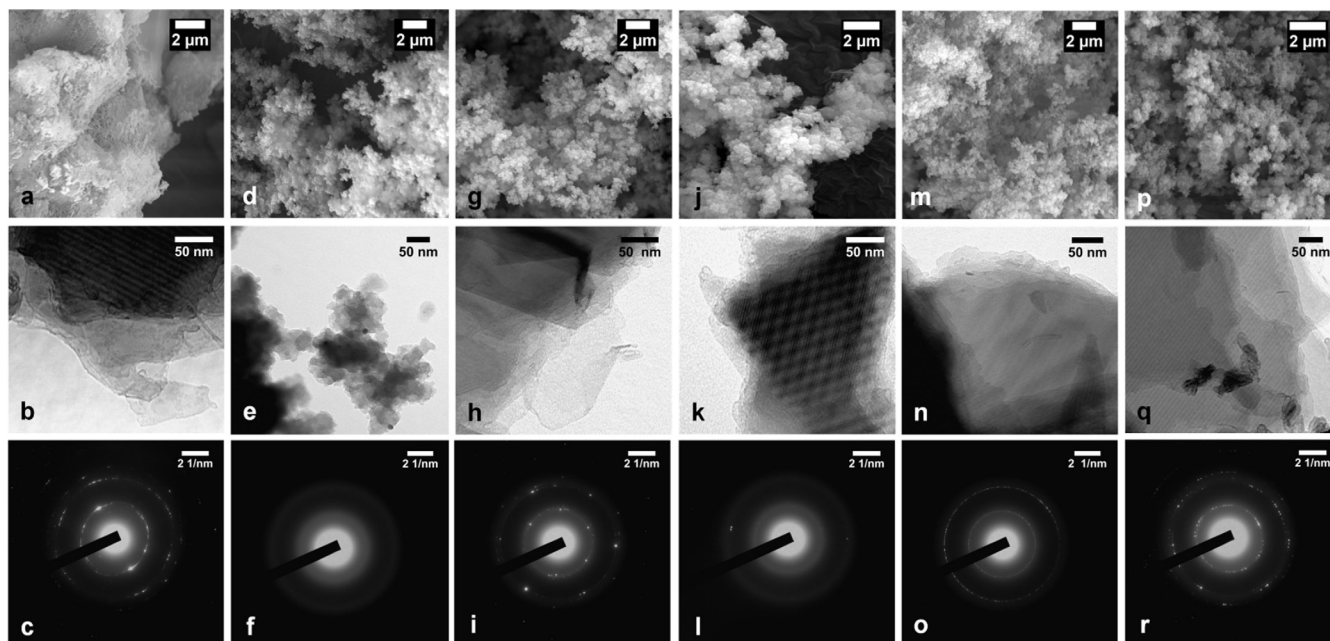
**Table 1.** Gas sorption data of all 6 polymers, including pore sizes and  $\text{CO}_2$  uptake calculated from sorption isotherm.

Sample	$S_{\text{BET}}$ [ $\text{m}^2\text{ g}^{-1}$ ] <sup>[a]</sup>	PV [ $\text{cm}^3\text{ g}^{-1}$ ] <sup>[b]</sup>	$\text{CO}_2$ uptake [ $\text{mmol g}^{-1}$ ]
NP-3	468	0.643	1.32
NP-4	600	0.193	1.65
NP-5	590	0.223	1.89
NP-6	545	0.376	1.96
SNP-3	445	0.382	1.71
SNP-4	210	0.159	1.30

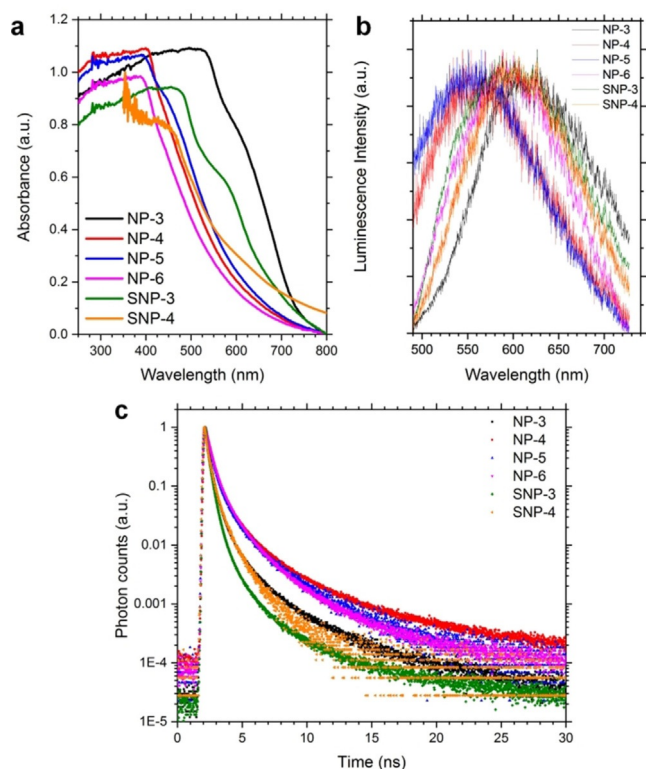
[a] Surface area calculated from  $\text{N}_2$  adsorption isotherm using the BET equation. [b] Pore volume (PV) calculated from  $\text{N}_2$  uptake for pore-sizes between 1.7 and 300 nm. Pore volume calculated via the Barrett–Joyner–Halenda (BJH) method.

Figure 3 shows scanning and transmission electron microscopy (SEM and TEM) images together with the corresponding selected area electron diffraction patterns (SAED). All networks have an intergrown, particle-like morphology. Remarkably, samples NP-3, NP5, NP-6 and SNP-4 feature pronounced Moiré fringes in their TEM images and/or electron diffraction spots indicative of some degree of internal order. Nonetheless, powder X-ray diffraction (PXRD) patterns reveal that the bulk of the samples is predominantly glassy and amorphous (Figure S6). Interlayer stacking peaks around  $25^\circ 2\theta$  are observed and are comparable to other layered, aromatic systems such as CMPs and covalent organic frameworks (COFs).<sup>[18]</sup>

Solid-state UV/Vis spectra of the polymers were recorded at room temperature and are displayed in Figure S9. The direct bandgaps were calculated using the Kubelka–Munk method (Figure S10) and vary between 1.9 and 2.52 eV and are in broad agreement with the calculated band structures (at PBE/DZP/GD2/5×5×16k-points level) of periodic, single layer structures of the corresponding materials (Figure S12). Photoluminescence emission (PLE) measurements show emission maxima in the range of 550 to 610 nm upon excitation at 405 nm (Figure 4b) as a result of the extended conjugation in the polymer network. Furthermore, the red shift implies the



**Figure 3.** Electron microscopic investigation of SNPs. SEM (top), TEM (centre), and SAED (bottom) images for: a–c) NP-3, d–f) NP-4, g–i) NP-5, j–l) NP-6, m–o) SNP-3, and p–r) SNP-4. b, h and n) Networks NP-3, and NP-6 show Moiré fringes in TEM images indicative of overlapping, ordered layers. c, i, o and r) show concentric rings in the electron diffraction that are indicative of polycrystalline domains.



**Figure 4.** a) Absorbance, b) fluorescence spectra, and c) time-correlated fluorescence spectroscopy for SNPs and NPs with SNP-4 (in orange), SNP-3 (in green), NP-6 (in magenta), NP-5 (in blue), NP-4 (in red), and NP-3 (in black).

degree of near-perfect polymerisation which is in agreement with the low residual halogen content in the polymers (see ICP-analysis, Supporting Information).<sup>[19]</sup> NP-3 is the structure

without heteroatoms except for the triazine bridge acceptor and features the highest redshift followed by SNP-3, SNP-4, and NP-6. Time-correlated fluorescence spectra were performed at 400 nm for NPs and SNPs in the solid state to investigate the dynamics of the excited-state (Figure 4c). The average fluorescence lifetimes are 1.49 (NP-3), 1.72 (NP-4), 1.69 (NP-5), 1.48 (NP-6), 1.29 (SNP-3), and 1.17 ns (SNP-4), and they were estimated by a double-exponential fitting. Excitons in NP-4 and NP-5 have the longest lifetime, and they are shortest in SNPs. Electron donation from sulphur heteroatoms may result in faster fluorescence quenching. An increase in N-content from pyridine- (NP-4) or pyrimidine-linkers (NP-5) leads to an increase in exciton lifetimes due to stronger C–H···N hydrogen bonds between adjacent layers. We have seen previously that it is not only the size of the  $\pi$ -conjugated organic tecton that determines the bandgap of the resulting polymer but also the strength of donor–acceptor interactions within the network.<sup>[3,20]</sup> In addition to charge-delocalisation between far-apart sulphur- and nitrogen-containing domains, the triazine-based ethynyl-phenyl linker features intrinsic donor–acceptor properties that can facilitate intramolecular charge transfer and, hence, exciton migration on a more local scale. As a result, all polymers with high nitrogen content (i.e. all NPs) can retain the excited state for a longer time. Indeed calculations suggest that the triazine ring has a larger hyperpolarisability and more electron-withdrawing character than the analogous carbon-only benzene core.<sup>[21]</sup>

All samples were investigated in photocatalytic hydrogen evolution from water using platinum (Pt) co-catalyst and triethanolamine (TEOA) as sacrificial agent under visible light (395 nm cut-off filter). Control reactions in the dark were performed prior to each test run to verify photocatalytic action.

Figure 5 summarises the hydrogen evolution rates (HERs) for all samples with and without platinum as a co-catalyst in dependence of the calculated, direct optical bandgap. NP-5 has the highest HER with Pt at  $915 \pm 10 \mu\text{mol h}^{-1} \text{g}^{-1}$  ( $9.15 \pm$

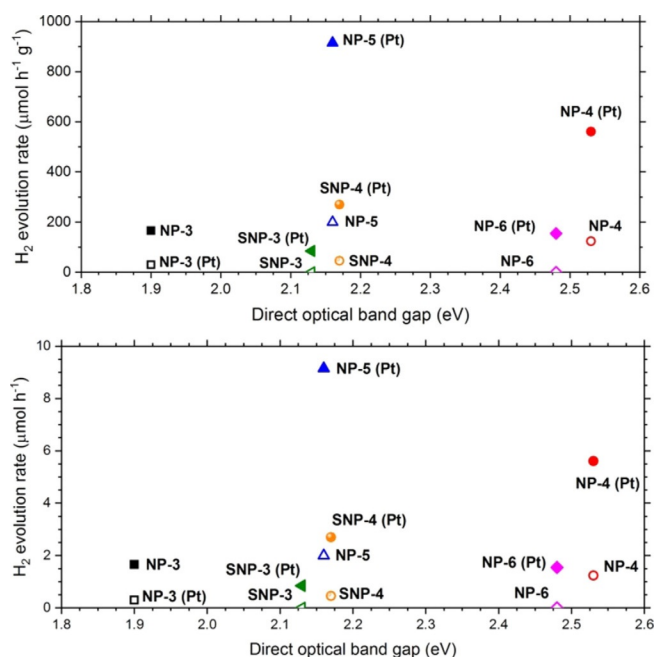


**Figure 5.** Hydrogen evolution rates of NP-3, NNPs, and SNPs (10 mg) under visible light (395 nm cut-off filter) correlated with the direct optical bandgap in  $\mu\text{mol h}^{-1} \text{g}^{-1}$  (above) and  $\mu\text{mol h}^{-1}$  (below). Each measurement was performed in a water:acetonitrile (1:1) mixture using triethanolamine (TEOA) as sacrificial agent with 3 wt % platinum (Pt) (filled symbols) and without Pt co-catalyst (empty symbols). Corresponding solid-state UV/Vis diffuse-reflectance spectra are shown in Figure S9.

$0.1 \mu\text{mol h}^{-1}$ ) and  $200 \pm 10 \mu\text{mol h}^{-1} \text{g}^{-1}$  ( $2.00 \pm 0.1 \mu\text{mol h}^{-1}$ ) without additional co-catalyst; one of the highest HER values for a noble metal free photocatalyst to-date. Common benchmark polymeric photocatalysts based on organic nitrogen rich moieties are heptazine based polymers<sup>[22]</sup> such as pure g-CN,<sup>[23]</sup> CNC<sub>30</sub> (with cytosine),<sup>[23]</sup> B-modified g-CN,<sup>[24]</sup> poly(triazine imide)<sup>[25]</sup> and azine-based COFs.<sup>[26]</sup> At first glance, we see a similar trend to previous publications that an ideal optical bandgap for efficient photocatalysis is situated around 2.2 eV,<sup>[4b,11]</sup> and that bandgaps below 2.0 eV fail to catalyse the reaction presumably because they are too narrow to straddle the potential between proton reduction and oxidation of the sacrificial agent. However, we also observe a (weak) correlation of HER and guest-accessible surface area with more accessible pore structures achieving higher efficiencies (Figure S28). The highest HER values with platinum as co-catalyst were obtained for pyridine (NP-4) and pyrimidine (NP-5) as a tecton. However, within the group of NPs the pyridazine tecton (NP-6) has a low HER. Overall, the absolute heteroatom content did not show any correlation with HER (Figure S29), and hence, we assume that it is the position of heteroatoms in the frameworks (rather than their sheer amount) that has the most impact on donor-acceptor interactions, charge-delocalisation and photocatalytic

activity. In the light of the PLE study, we observe the trend that long exciton life-times in NPs are a good indicator for efficient photocatalysis, most likely, because photoexcited electrons and holes do not spontaneously recombine so readily in these materials.

In conclusion, we have expanded the family of sulphur- and nitrogen-containing porous polymers—a class of photoactive, heterogeneous catalysts—by six further members with mixed (S, N, C) and (N, C)-only heteroatoms in their backbones. Intrinsic donor-acceptor interactions within these networks allow fine-tuning of the optical bandgap between 1.90 and 2.57 eV. Surprisingly, we find that efficient photocatalytic hydrogen evolution from water does not only depend on the optimal size of the bandgap ( $\approx 2.2$  eV)—as suggested in previous reports. We find that materials that effectively extend the lifetime of the photoexcited electron-hole pair—for example via effective charge separation—can achieve high hydrogen evolution rates irrespective at sub-optimal bandgap values. In conventional systems that do not feature intrinsic donor-acceptor dyads, this electron-hole separation needs to be promoted by the addition of Pt or Pd co-catalysts (Figure S30). Thus, we achieve hydrogen evolution rates of up to  $200 \pm 10 \mu\text{mol h}^{-1} \text{g}^{-1}$  without co-catalyst which is one of the highest values reported to date. This is a significant finding and we believe that it highlights the importance of tuneable donor-acceptor domains in the development of a truly noble-metal-free photocatalyst in the future.

## Acknowledgements

We thank Dr. Nikolai Makukhin for discussions, Šárka Pšondrová is acknowledged for IR, Dr. Simona Hybelbauerova and Martin Dracinsky for their support and access in solid-state NMR, Dr. Jiri Rybacek and Dr. Martin Racek for their support in SEM and EDX, Stanislava Matejkova is acknowledged for ICP-OES, Jaroslava Hnilickova is acknowledged for EA and Christina Eichenauer is acknowledged for BET. M.J.B. thanks the European Research Council (ERC) for funding under the Starting Grant Scheme (BEGMAT -678462). M.J.B., J.C. and P.N. further acknowledge the Charles University Centre of Advanced Materials (CUCAM) (OP VVV Excellent Research Teams, project number CZ.02.1.01/0.0/0.0/15\_003/0000417).

## Conflict of interest

The authors declare no conflict of interest.

**Keywords:** conjugated microporous polymers · donor-acceptor systems · dyads · photocatalysis · triazine

- [1] a) L. Yang, H. Zhou, T. Fan, D. Zhang, *Phys. Chem. Chem. Phys.* **2014**, *16*, 6810–6826; b) X. Chen, S. Shen, L. Guo, S. S. Mao, *Chem. Rev.* **2010**, *110*, 6503–6570.
- [2] J.-X. Jiang, F. Su, A. Trewin, C. D. Wood, H. Niu, J. T. A. Jones, Y. Z. Khimyak, A. I. Cooper, *J. Am. Chem. Soc.* **2008**, *130*, 7710–7720.
- [3] J.-X. Jiang, A. Trewin, D. J. Adams, A. I. Cooper, *Chem. Sci.* **2011**, *2*, 1777–1781.

- [4] a) R. S. Sprick, B. Bonillo, R. Clowes, P. Guiglion, N. J. Brownbill, B. J. Slater, F. Blanc, M. A. Zwijnenburg, D. J. Adams, A. I. Cooper, *Angew. Chem.* **2016**, *128*, 1824–1828; b) R. S. Sprick, J.-X. Jiang, B. Bonillo, S. Ren, T. Ratvijitvech, P. Guiglion, M. A. Zwijnenburg, D. J. Adams, A. I. Cooper, *J. Am. Chem. Soc.* **2015**, *137*, 3265–3270.
- [5] P. Guiglion, C. Butchosa, M. A. Zwijnenburg, *Macromol. Chem. Phys.* **2016**, *217*, 344–353.
- [6] X. Wang, K. Maeda, A. Thomas, K. Takanahe, G. Xin, J. M. Carlsson, K. Domen, M. Antonietti, *Nat. Mater.* **2009**, *8*, 76–80.
- [7] F. K. Kessler, Y. Zheng, D. Schwarz, C. Merschjann, W. Schnick, X. Wang, M. J. Bojdys, *Nat. Rev. Mater.* **2017**, *2*, 17030.
- [8] V. S. Vyas, F. Haase, L. Stegbauer, G. Savasci, F. Podjaski, C. Ochsenfeld, B. V. Lotsch, *Nat. Commun.* **2015**, *6*, 8508.
- [9] a) Y. Wang, X. Wang, M. Antonietti, *Angew. Chem. Int. Ed.* **2012**, *51*, 68–89; *Angew. Chem.* **2012**, *124*, 70–92; b) L. Li, W.-Y. Lo, Z. Cai, N. Zhang, L. Yu, *Macromolecules* **2016**, *49*, 6903–6909.
- [10] a) R. Fink, C. Frenz, M. Thelakkat, H.-W. Schmidt, *Macromolecules* **1997**, *30*, 8177–8181; b) H. Meier, E. Karpuk, H. C. Holst, *Eur. J. Org. Chem.* **2006**, 2609–2617; c) I. Nenner, G. J. Schulz, *J. Chem. Phys.* **1975**, *62*, 1747–1758; d) K. M. Omer, S.-Y. Ku, Y.-C. Chen, K.-T. Wong, A. J. Bard, *J. Am. Chem. Soc.* **2010**, *132*, 10944–10952; e) Y. Oumi, Y. Kakinaga, T. Kodaira, T. Teranishi, T. Sano, *J. Mater. Chem.* **2003**, *13*, 181–185; f) S. Ren, Q. Fang, F. Yu, D. Bu, *J. Polym. Sci. Part A* **2005**, *43*, 6554–6561; g) S. Ren, D. Zeng, H. Zhong, Y. Wang, S. Qian, Q. Fang, *J. Phys. Chem. B* **2010**, *114*, 10374–10383; h) T. Yamamoto, S. Watanabe, H. Fukumoto, M. Sato, T. Tanaka, *Macromol. Rapid Commun.* **2006**, *27*, 317–321; i) L. Zou, Y. Fu, X. Yan, X. Chen, J. Qin, *J. Polym. Sci. Part A* **2008**, *46*, 702–712; j) L. Zou, Y. Liu, N. Ma, E. Macoas, J. M. G. Martinho, M. Pettersson, X. Chen, J. Qin, *Phys. Chem. Chem. Phys.* **2011**, *13*, 8838–8846; k) L. Zou, Z. Liu, X. Yan, Y. Liu, Y. Fu, J. Liu, Z. Huang, X. Chen, J. Qin, *Eur. J. Org. Chem.* **2009**, 5587–5593.
- [11] D. Schwarz, Y. S. Kochergin, A. Acharjya, A. Ichangi, M. V. Opanasenko, J. Čejka, U. Lappan, P. Arki, J. He, J. Schmidt, P. Nachtigall, A. Thomas, J. Tarábek, M. J. Bojdys, *Chem. Eur. J.* **2017**, *23*, 13023–13027.
- [12] K. Yaroslav S., S. Dana, A. Amitava, I. Arun, K. Ranjit, E. Pavla, V. Jaroslav, S. Johannes, T. Arne, B. Michael J., *Exploring the “Goldilocks Zone” of Semiconducting Polymer Photocatalysts via Donor–Acceptor Interactions*, **2018**, DOI: <https://doi.org/10.26434/chemrxiv.6210110.v1>.
- [13] J.-X. Jiang, F. Su, A. Trewin, C. D. Wood, N. L. Campbell, H. Niu, C. Dickinson, A. Y. Ganin, M. J. Rosseinsky, Y. Z. Khimiyak, A. I. Cooper, *Angew. Chem. Int. Ed.* **2007**, *46*, 8574–8578; *Angew. Chem.* **2007**, *119*, 8728–8732.
- [14] S. Ren, R. Dawson, D. J. Adams, A. I. Cooper, *Polym. Chem.* **2013**, *4*, 5585–5590.
- [15] H. Bildirir, J. P. Paraknowitsch, A. Thomas, *Chem. Eur. J.* **2014**, *20*, 9543–9548.
- [16] a) K. Kailasam, M. B. Mesch, L. Möhlmann, M. Baar, S. Blechert, M. Schwarze, M. Schröder, R. Schomäcker, J. Senker, A. Thomas, *Energy Technol.* **2016**, *4*, 744–750; b) K. Zhang, D. Kopetzki, P. H. Seeberger, M. Antonietti, F. Vilela, *Angew. Chem. Int. Ed.* **2013**, *52*, 1432–1436; *Angew. Chem.* **2013**, *125*, 1472–1476; c) H. Bohra, S. Y. Tan, J. Shao, C. Yang, A. Efreem, Y. Zhao, M. Wang, *Polym. Chem.* **2016**, *7*, 6413–6421; d) A. Efreem, K. Wang, P. N. Amaniampong, C. Yang, S. Gupta, H. Bohra, S. H. Mushrif, M. Wang, *Polym. Chem.* **2016**, *7*, 4862–4866.
- [17] R. S. Sprick, B. Bonillo, M. Sachs, R. Clowes, J. R. Durrant, D. J. Adams, A. I. Cooper, *Chem. Commun.* **2016**, 10008–10011.
- [18] P. Kuhn, M. Antonietti, A. Thomas, *Angew. Chem. Int. Ed.* **2008**, *47*, 3450–3453; *Angew. Chem.* **2008**, *120*, 3499–3502.
- [19] T. M. Figueira-Duarte, S. C. Simon, M. Wagner, S. I. Druzhinin, K. A. Zachariasse, K. Müllen, *Angew. Chem. Int. Ed.* **2008**, *47*, 10175–10178; *Angew. Chem.* **2008**, *120*, 10329–10332.
- [20] a) Y. Xu, A. Nagai, D. Jiang, *Chem. Commun.* **2013**, 49, 1591–1593; b) P. Dai, L. Yang, M. Liang, H. Dong, P. Wang, C. Zhang, Z. Sun, S. Xue, *ACS Appl. Mater. Interfaces* **2015**, *7*, 22436–22447.
- [21] V. R. Thalladi, S. Brasselet, H.-C. Weiss, D. Bläser, A. K. Katz, H. L. Carrell, R. Boese, J. Zyss, A. Nangia, G. R. Desiraju, *J. Am. Chem. Soc.* **1998**, *120*, 2563–2577.
- [22] Y. Wang, X. Wang, M. Antonietti, *Angew. Chem. Int. Ed.* **2012**, *51*, 68–89; *Angew. Chem.* **2012**, *124*, 70–92.
- [23] C. Yan, B. Wang, L. Zhang, L. Yin, X. Wang, *Angew. Chem. Int. Ed.* **2017**, *56*, 6627–6631; *Angew. Chem.* **2017**, *129*, 6727–6731.
- [24] Z. Lin, X. Wang, *Angew. Chem. Int. Ed.* **2013**, *52*, 1735–1738; *Angew. Chem.* **2013**, *125*, 1779–1782.
- [25] L. Lin, C. Wang, W. Ren, H. Ou, Y. Zhang, X. Wang, *Chem. Sci.* **2017**, *8*, 5506–5511.
- [26] K. Schwinghammer, B. Tuffy, M. B. Mesch, E. Wirnhier, C. Martineau, F. Taulelle, W. Schnick, J. Senker, B. V. Lotsch, *Angew. Chem. Int. Ed.* **2013**, *52*, 2435–2439; *Angew. Chem.* **2013**, *125*, 2495–2499.

Manuscript received: June 6, 2018

Revised manuscript received: July 11, 2018

Version of record online: July 25, 2018



# **Attachment No. 3**

# Tuning the Porosity and Photocatalytic Performance of Triazine-Based Graphdiyne Polymers through Polymorphism

Dana Schwarz,<sup>[a]</sup> Amitava Acharjya,<sup>[b]</sup> Arun Ichangi,<sup>[a, c]</sup> Yaroslav S. Kochergin,<sup>[a]</sup> Pengbo Lyu,<sup>[d]</sup> Maksym V. Opanasenko,<sup>[d, e]</sup> Ján Tarábek,<sup>[c]</sup> Jana Vacek Chocholoušová,<sup>[c]</sup> Jaroslav Vacek,<sup>[c]</sup> Johannes Schmidt,<sup>[b]</sup> Jiří Čejka,<sup>[d, e]</sup> Petr Nachtigall,<sup>[d]</sup> Arne Thomas,<sup>[b]</sup> and Michael J. Bojdys\*<sup>[a, c]</sup>

Crystalline and amorphous organic materials are an emergent class of heterogeneous photocatalysts for the generation of hydrogen from water, but a direct correlation between their structures and the resulting properties has not been achieved so far. To make a meaningful comparison between structurally different, yet chemically similar porous polymers, two porous polymorphs of a triazine-based graphdiyne (TzG) framework are synthesized by a simple, one-pot homocoupling polymerization reaction using as catalysts Cu<sup>I</sup> for TzG<sub>Cu</sub> and Pd<sup>II</sup>/Cu<sup>I</sup> for TzG<sub>Pd/Cu</sub>. The polymers form through irreversible coupling reactions and give rise to a crystalline (TzG<sub>Cu</sub>) and an amorphous (TzG<sub>Pd/Cu</sub>) polymorph. Notably, the crystalline and amorphous polymorphs are narrow-gap semiconductors with permanent surface areas of 660 m<sup>2</sup>g<sup>-1</sup> and 392 m<sup>2</sup>g<sup>-1</sup>, respectively. Hence, both polymers are ideal heterogeneous photocatalysts for water splitting with some of the highest hydrogen evolution rates reported to date (up to 972 μmolh<sup>-1</sup>g<sup>-1</sup> with and 276 μmolh<sup>-1</sup>g<sup>-1</sup> without Pt cocatalyst). Crystalline order is found to improve delocalization, whereas the amorphous polymorph requires a cocatalyst for efficient charge transfer. This will need to be considered in future rational design of polymer catalysts and organic electronics.

Organic porous polymer networks have recently attracted considerable attention as gas storage materials and as heterogeneous catalysts, particularly in photocatalytic hydrogen evolution.<sup>[1]</sup> The introduction of heteroatoms such as nitrogen into organic polymers has led to the discovery of organic semiconductors,<sup>[2]</sup> metal-free catalysts for hydrogen evolution from water,<sup>[3]</sup> and catalysts for CO<sub>2</sub> fixation.<sup>[4]</sup> In addition, (C,N)-containing crystalline frameworks are candidate materials for “postsilicon electronics”.<sup>[5]</sup> Two major classes of organic porous polymers emerged over the last 15 years, based on two distinct design principles. On the one hand, covalent organic frameworks (COFs) feature a predictable, long-range order of building blocks. These COFs are linked by covalent, yet reversible, bond formation.<sup>[6]</sup> On the other hand, conjugated microporous polymers (CMPs) have enhanced stability and optical properties, owing to overall π-conjugation between building blocks, albeit at the expense of structural order.<sup>[7]</sup> These systems are of great interest not only because they have the potential to combine high surface areas with useful (opto)electronic effects, but also because they offer—in principle—a wide scope for the rational design of their structures and properties. However, a direct comparison of the structure–property relationship between ordered COFs and amorphous CMPs has not been possible to date because the underlying chemistry of their respective building blocks and their linking chemistry is fundamentally different.

Herein, we address the importance of the structural order of organic porous polymers for the (opto)electronic properties of the bulk materials. For this purpose, we use a modular, synthetic platform of triazine-based graphdiyne (TzG) that enables the synthesis of ordered and amorphous networks while maintaining desirable π-conjugation (Figure 1). Triazine-based graphdiyne features an intriguing donor–acceptor (D–A) motif consisting of electron-rich buta-1,3-diyne (D) and electron-poor triazines (A). Indeed, the triazine (C<sub>3</sub>N<sub>3</sub>, Tz) core is predicted to offer larger hyperpolarizabilities than the analogous carbon-only benzene core because triazine is more electron withdrawing and nucleophilic.<sup>[8]</sup> Triazine is a particularly interesting structural motif for the design of organic polymer networks because it combines heteroatoms held in π-conjugation and C<sub>3</sub>-symmetric co-planarity.<sup>[9]</sup> We have successfully used this D–A motif of TzG as part of a 2D/3D van der Waals heterostructure for noble metal-free photocatalytic hydrogen evolution.<sup>[10]</sup>

[a] Dr. D. Schwarz, A. Ichangi, Y. S. Kochergin, Dr. M. J. Bojdys  
Faculty of Science, Department of Organic Chemistry  
Charles University, Hlavova 8, 128 43 Prague 2 (Czech Republic)  
E-mail: m.j.bojdys.02@cantab.net

[b] A. Acharjya, Dr. J. Schmidt, Prof. Dr. A. Thomas  
Institute of Chemistry, Technische Universität Berlin  
Hardenbergstraße 40, 10623 Berlin (Germany)

[c] A. Ichangi, Dr. J. Tarábek, Dr. J. Vacek Chocholoušová, Dr. J. Vacek,  
Dr. M. J. Bojdys  
Institute of Organic Chemistry and Biochemistry of the CAS  
Flemingovo nám. 2, 166 10 Prague 6 (Czech Republic)

[d] P. Lyu, Dr. M. V. Opanasenko, Prof. Dr. J. Čejka, Prof. Dr. P. Nachtigall  
Faculty of Science, Department of Physical and Macromolecular Chemistry  
Charles University, Hlavova 8, 128 43 Prague 2 (Czech Republic)

[e] Dr. M. V. Opanasenko, Prof. Dr. J. Čejka  
J. Heyrovský Institute of Physical Chemistry of the CAS, v.v.i.  
Dolejškova 2155/3, 182 23 Prague 8 (Czech Republic)

Supporting information and the ORCID identification number(s) for the author(s) of this article can be found under:  
<https://doi.org/10.1002/cssc.201802034>.

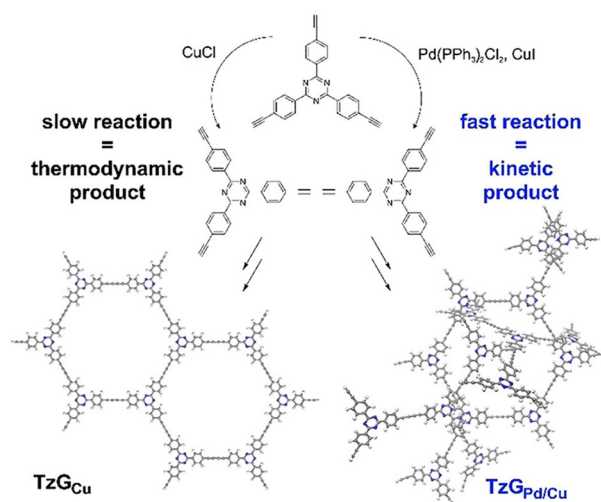


**Figure 1.** Reaction Scheme for the formation of the thermodynamic, ordered TzG<sub>Cu</sub> (left, black) and the kinetic, disordered TzG<sub>Pd/Cu</sub> (right, blue) polymorphs starting with the synthon (2,4,6-tris(4-ethynylphenyl)-1,3,5-triazine). Both reactions yield the buta-1,3-diyne bridged products.

Triazine-based graphdiyne polymers are constructed by using the principle synthon 2,4,6-tris(4-ethynylphenyl)-1,3,5-triazine, which consists of a central 1,3,5-triazine moiety connected to 1,4-phenyl rings and is terminated by ethynes. Details of the synthesis are given in the Supporting Information (Scheme S1). In brief, the triazine ring was formed by treating 4-bromobenzonitrile with trifluoromethanesulfonic acid.<sup>[11]</sup> The trimethylsilyl group-protected acetylene group was attached to the molecule by Negishi coupling. Deprotection proceeded in a good yield on adding K<sub>2</sub>CO<sub>3</sub> in THF/MeOH. The triazine-based graphdiyne polymer (TzG) was obtained by using CuCl (TzG<sub>Cu</sub>) or [Pd(PPh<sub>3</sub>)<sub>2</sub>Cl<sub>2</sub>] with CuI (TzG<sub>Pd/Cu</sub>) as catalysts (Figure 1). The network-forming reaction that couples ethynes into 1,3-diyne bridges is commonly achieved by Glaser coupling catalyzed by a copper(I) salt.<sup>[12]</sup> Alternatively, the diacetylene bridge can be formed under common and efficient Sonogashira-like conditions.<sup>[13]</sup> Numerous studies have shown that combined catalytic systems—for example, Pd<sup>0</sup> or Pd<sup>II</sup> together with Cu<sup>I</sup>—couple terminal acetylenes faster and at higher yields than traditional Glaser protocols that use Cu<sup>I</sup> salts only.<sup>[14]</sup> Although highly efficient coupling is beneficial for small molecule synthesis, we believe that it can lead to the preferred formation of kinetic and disordered rather than thermodynamic and ordered materials. These parameters have an influence on the nanoscopic (Figure 2d and h) and the macroscopic scale (Figure 2a–c and e–g). The product from the Sonogashira-like reaction is a macroporous sponge made up of fibers or rods 20 nm in diameter with no discernible internal structure (Figure 2b–d). The Glaser product has a less defined macroscopic structure but shows a crystalline internal order (Figures 2f–h).

Both reaction pathways yielded buta-1,3-diyne-bridged TzG polymers (Figure 2i,k,l). We confirmed the chemical composition of TzG by inductively coupled plasma optical emission spectroscopy (ICP-OES; see the Supporting Information) and <sup>13</sup>C cross-polarization magic angle spinning (CP-MAS) solid-

state NMR spectroscopy (Figure 2i). Both polymers match the theoretical stoichiometric C/N ratio of 9:1 (Tables S1 and S2) and feature the triazine carbon ( $\delta \approx 170$  ppm) and the diyne ( $\delta \approx 80$  ppm) signals. Fourier-transform infrared (FTIR) spectroscopy (Figure 2k, Figure S1) shows characteristic signals at 3290 cm<sup>-1</sup> corresponding to C≡C, and strong peaks at 1359 and 816 cm<sup>-1</sup> ascribed to the breathing modes of the triazine ring.<sup>[15]</sup> The peaks at 2200 cm<sup>-1</sup> and 1929 cm<sup>-1</sup> correspond to the buta-1,3-diyne bridge (–C≡C–C≡C–).<sup>[16]</sup> The sluggish Glaser reaction gives rise to a few unreacted C≡C–H end groups with signals at 3300 cm<sup>-1</sup>. These end groups, however, are not discernible in <sup>13</sup>C CP-MAS NMR (c.f., Figure 2i), hence, they are most likely only found at the external surfaces of TzG<sub>Cu</sub> particles and do not dominate the bulk. Raman spectra of TzG<sub>Cu</sub> and TzG<sub>Pd/Cu</sub> show C≡C stretching at around 2200 cm<sup>-1</sup> (Figure 2l). X-ray photoelectron spectroscopy (XPS) shows that TzG<sub>Cu</sub> retains some copper catalyst—0.85 wt% by energy-dispersive X-ray spectroscopy (EDX; Table S1) and up to 4.45 wt% by ICP-OES (Table S2) and thermogravimetric analysis (TGA; Figure S2)—either as Cu metal, or as Cu<sup>I</sup> oxides (Figure 2j, Figure S3). The difference in copper content from both methods indicates that copper is embedded within the polymer matrix away from the external surfaces, and that it is unlikely to affect the photocatalytic activity and bulk properties of the polymer at such low quantities, as previously reported.<sup>[10]</sup>

As expected, we see no long range order for the polymer obtained through Sonogashira-like coupling (Figure 2d),<sup>[17]</sup> and it is likely that interdigitation of polymer strands and rings occurs because pore sizes are sufficiently large (Figures 2d and 3c).<sup>[18]</sup> In contrast, TzG<sub>Cu</sub> has a high degree of crystalline order. Small-angle X-ray scattering (SAXS) shows a diagnostic, low-angle peak that is absent for TzG<sub>Pd/Cu</sub> (Figure 3c, Figure S5). This feature corresponds to the (100) reflection of a hexagonal unit cell with 2D lattice parameters  $a = b = 30.7898$  Å (Figure 3d). We use density functional theory (DFT) calculations to predict feasible packing arrangements of TzG<sub>Cu</sub> layers (see the Supporting Information). Turbostratic stacking disorder and low energy gains from different stacking modes are known for analogous,  $\pi$ -stacked systems.<sup>[19]</sup> Here, we compare DFT results against physical data from high-resolution transmission electron microscopy (HR-TEM; Figure 3a, Figure S6) and selected-area electron diffraction (SAED; Figure 3b, Figure S6). The best fit is achieved by using a DFT-optimized, ABC-stacked TzG<sub>Cu</sub> structure with a unit cell of  $a = b = 30.7898$  Å,  $c = 6.1397$  Å, and space group  $R\bar{3}m$  (no. 166; Figure 3d,e, Figure S8).

UV/Vis spectra of TzG<sub>Cu</sub> and TzG<sub>Pd/Cu</sub> polymorphs have a similar absorption edge at around 580 nm, yet the spectrum of TzG<sub>Cu</sub> shows a long tail towards the visible region (Figure 4a). This feature is a direct effect of the improved planarity of crystalline TzG<sub>Cu</sub> and is thought to be caused by exciton-hopping between layers.<sup>[20]</sup> Consequently, TzG<sub>Cu</sub> appears darker (c.f., Figure 2e) and the Kubelka–Munk function predicts a direct optical band gap of 2.04 eV and an indirect optical band gap of 0.88 eV (Figure 4c). TzG<sub>Pd/Cu</sub> has a direct optical band gap of 1.97 eV and an indirect optical band gap of 1.23 eV, according to the same calculation (Figure 4b). The color of a material—and, hence, the derived optical band gap—is a bulk effect of

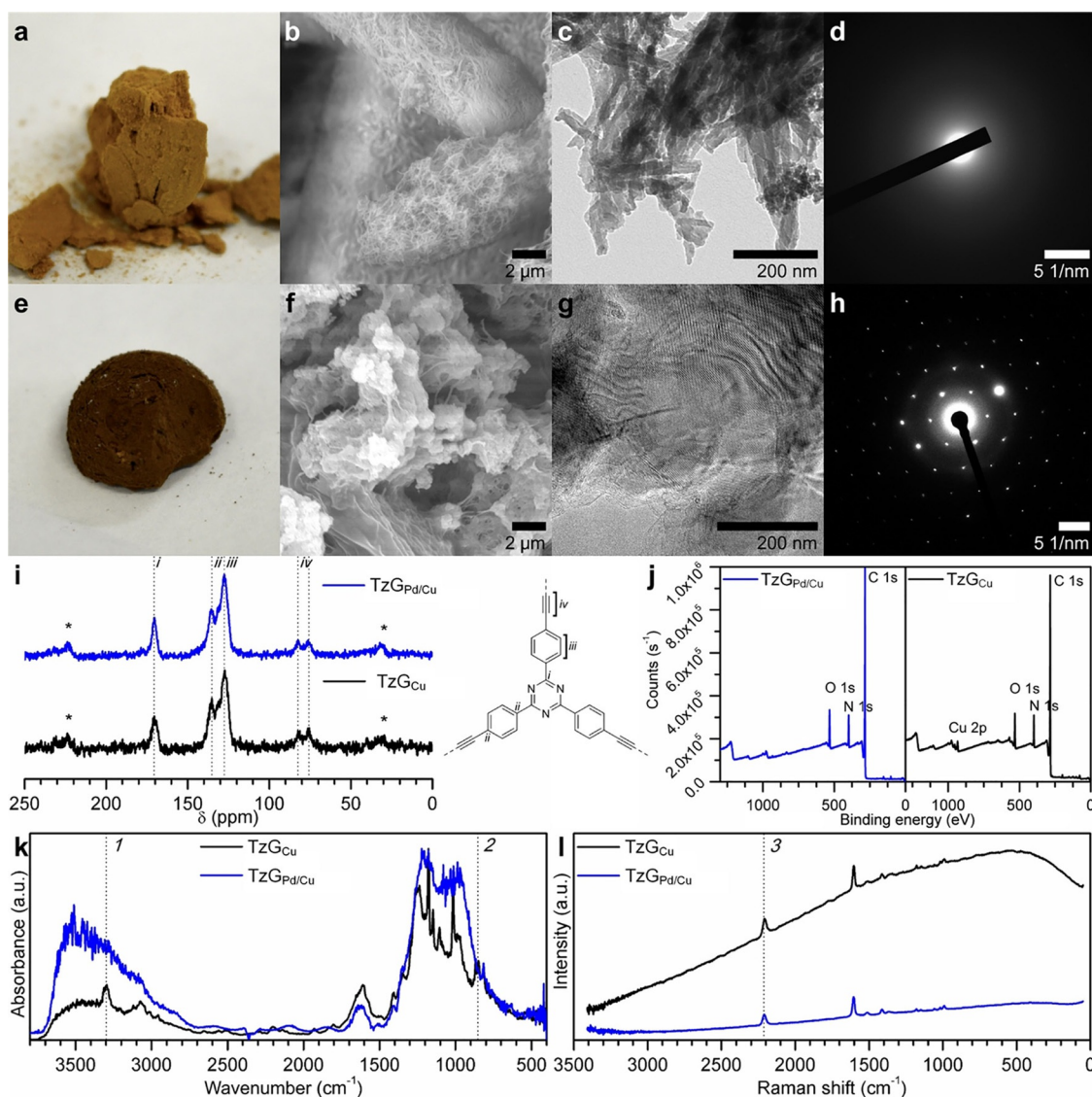


**Figure 2.** Composition and morphology of TzG polymers obtained via a coupling reaction with CuCl or Pd(PPh<sub>3</sub>)<sub>2</sub>Cl<sub>2</sub>/Cu as catalyst. Photographs of a) TzG<sub>pd/Cu</sub> and e) TzG<sub>cu</sub> as-synthesized powders. SEM images show aggregated strands for b) TzG<sub>pd/Cu</sub> and overgrown layers for f) TzG<sub>cu</sub>. TEM images of c) TzG<sub>pd/Cu</sub> show rod-like structures with diameters of 20 nm and no discernible internal structure, whereas g) TzG<sub>cu</sub> features highly crystalline sheets on the order of 500–1000 nm. Corresponding electron diffraction images confirm that d) TzG<sub>pd/Cu</sub> has no internal crystallinity, whereas h) TzG<sub>cu</sub> shows pronounced hexagonal diffraction spots. i) <sup>13</sup>C CP-MAS NMR of TzG<sub>pd/Cu</sub> (blue) and TzG<sub>cu</sub> (black). The triazine carbon signal (marked *i*) appears at 170 ppm, and the quaternary diyne carbons (marked *iv*) at around 80 ppm. Phenyl peaks are marked as *ii* and *iii*. Spinning side bands are denoted with an asterisk (\*). j) XPS data for TzG<sub>pd/Cu</sub> (left, blue) and TzG<sub>cu</sub> (right, black) shows near identical plots and composition, except for some residual copper in TzG<sub>cu</sub>. k) FTIR spectra of TzG<sub>pd/Cu</sub> (blue) and TzG<sub>cu</sub> (black). Terminal unreacted C≡C–H bonds are identified as *1*, whereas the characteristic triazine breathing mode is observed at *2*. The stacked plot of this figure can be found in the Supporting Information (Figure S1). l) Raman spectra of TzG<sub>pd/Cu</sub> (blue) and TzG<sub>cu</sub> (black) at 780 nm. The characteristic diyne stretch can be discerned for both polymers at around 2200 cm<sup>-1</sup> (marked as *3*).

layer stacking (or lack thereof). Therefore, color can be misleading when analyzing the actual electronic band gap, in particular when the volume, mass, and density of the UV/Vis-irradiated material are unknown.<sup>[21]</sup> Hence, we complement the investigation of optical properties of both polymorphs by photoluminescence (PL) spectroscopy. Both materials show near-identical excitation spectra with peak maxima centered at around 480 nm, corresponding to exciton transition energies of 2.5–2.6 eV (Figure 4d). The lack of structural order of the TzG<sub>pd/Cu</sub> polymorph inhibits exciton annihilation, which often occurs in tightly packed,  $\pi$ -aromatic systems.<sup>[11,22]</sup> Consequently, the PL

response of TzG<sub>pd/Cu</sub> in excitation and emission is one to two orders of magnitude higher than that of TzG<sub>cu</sub> (Figure 4d and e). DFT calculations (using the PBE0 hybrid functional with many-body dispersion in the FHI-Aims code) predict that the overall HOMO–LUMO gap of a TzG material is 2.60 eV, which appears to be an indirect band gap. The smallest direct gap is 2.93 eV (Figure 4f–h, Figure S8). Hence, both TzG polymorphs are expected to be indirect band gap semiconductors.

To clarify how polymorphism affects the spin states, we examined both polymorphs by electron paramagnetic resonance (EPR). Both TzG<sub>cu</sub> and TzG<sub>pd/Cu</sub> are EPR active and display an in-

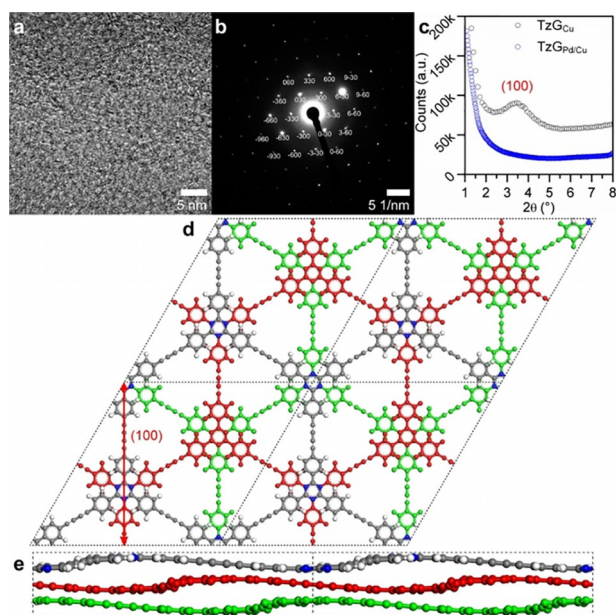


**Figure 3.** Structure analysis of the crystalline  $\text{TzG}_{\text{Cu}}$  polymorph. a) The high-resolution TEM image of  $\text{TzG}_{\text{Cu}}$  reveals a hexagonal bonding motif, and b) the selected-area electron diffraction pattern corresponds to a covalently bonded, ABC-stacked TzG structure. c) The small-angle X-ray diffraction pattern of  $\text{TzG}_{\text{Cu}}$  (black) shows a characteristic (100) peak that is absent in  $\text{TzG}_{\text{Pd/Cu}}$  (blue). The ABC packing motif of  $\text{TzG}_{\text{Cu}}$  (with the lower-lying layer indicated in red and green) is shown along the  $c$ -vector in d) and along the  $ab$ -vector in e). This is a stable structure obtained at DFT level with unit cell parameters of  $a = b = 30.7898 \text{ \AA}$ ,  $c = 6.1397 \text{ \AA}$ , space group  $R\bar{3}m$  (no. 166). The characteristic (100) repeat is marked in red.

tense polaronic-like spectrum at similar  $g$  values of 2.0032 (linewidth 0.63 mT) and 2.0035 (linewidth 0.66 mT), respectively (Figure 4i). This is comparable to other conductive polymers ( $g$  values of 2.0030–2.0035, and linewidths of 0.42–0.80 mT).<sup>[23]</sup> Note though, that the radical component of  $\text{TzG}_{\text{Cu}}$  has a two-fold higher intensity (Figure 4i). This indicates a higher concentration of induced polaron-like centers in  $\text{TzG}_{\text{Cu}}$  than in  $\text{TzG}_{\text{Pd/Cu}}$ —presumably caused by denser, crystalline packing. There is no qualitative difference between the spin delocalization along the  $\pi$ -aromatic backbone of both polymorphs, as observed previously for compounds with  $\pi$ -aromatic domains of varying sizes.<sup>[24]</sup> Hence, the observed optical differences between the two polymorphs are purely a morphological effect.

The pore structure of both polymorphs was investigated by argon sorption (Figure 4j, Table S4). The  $\text{TzG}_{\text{Cu}}$  polymorph has a higher specific surface area ( $660 \text{ m}^2 \text{ g}^{-1}$ ) than  $\text{TzG}_{\text{Pd/Cu}}$  ( $392 \text{ m}^2 \text{ g}^{-1}$ ), according to the Brunauer–Emmett–Teller (BET) model. The dominant micropore size diameter for both polymorphs is approximately 0.6 nm, which was calculated using the Barrett–Joyner–Halenda (BJH) model (Figure S10). The adsorption and desorption branches for both polymorphs show no discernible hysteresis over the mesoporous and microporous range. Hence, we can assume that the two polymorphs have similar rigidity with little or no swelling. Consequently, the comparatively smaller accessible surface area of  $\text{TzG}_{\text{Pd/Cu}}$  is presumably not a consequence of pore collapse but more likely, a result of pore blockage by interdigitation (or inter-

growth) during its kinetically controlled formation. The relatively small micropores in both materials are ideal for  $\text{CO}_2$  uptake with high values of  $2.23 \text{ mmol g}^{-1}$  for  $\text{TzG}_{\text{Pd/Cu}}$  and  $2.02 \text{ mmol g}^{-1}$  for  $\text{TzG}_{\text{Cu}}$  at 273 K (Figure S11).

Evidently, both TzG polymorphs combine a useful band gap and permanent pore structure. Hence, they are interesting candidates as heterogeneous photocatalysts in light-promoted hydrogen evolution from water. We performed hydrogen evolution experiments by irradiating a suspension of TzG powders in a water/acetonitrile mixture (1:1 v/v) at room temperature with visible light (395 nm cut-off filter). Triethanolamine (TEOA) was the sacrificial electron donor and the reaction was performed with and without a platinum cocatalyst (see the Supporting Information).<sup>[2]</sup> The disordered  $\text{TzG}_{\text{Pd/Cu}}$  polymorph showed one of the highest hydrogen evolution rates reported for this class of polymeric materials ( $972 \mu\text{mol h}^{-1} \text{ g}^{-1}$  and  $101 \mu\text{mol h}^{-1} \text{ g}^{-1}$  without Pt), which is comparable to that of the covalent triazine framework CTF-1 ( $1072 \mu\text{mol h}^{-1} \text{ g}^{-1}$ ).<sup>[25]</sup>  $\text{TzG}_{\text{Cu}}$  performed at  $490 \mu\text{mol h}^{-1} \text{ g}^{-1}$  ( $276 \mu\text{mol h}^{-1} \text{ g}^{-1}$  without Pt). Interestingly, the cocatalyst had the stronger effect on the photocatalytic performance of  $\text{TzG}_{\text{Pd/Cu}}$ —the disordered material with no interplanar annihilation pathways for generated excitons as shown by UV/Vis spectroscopy. Indeed, Pt usually mediates the transfer of electrons from the photoactive framework to the sites of water reduction,<sup>[26]</sup> which is not efficiently achieved by  $\text{TzG}_{\text{Pd/Cu}}$  alone. The addition of Pt has a markedly lower effect on  $\text{TzG}_{\text{Cu}}$ . Here, improved interlayer packing leads to a relatively efficient electron transfer, with or without a cocatalyst, as shown previously for crystalline, conductive triazine films.<sup>[10]</sup>

In summary, we have demonstrated a direct correlation between structure and properties, such as crystallinity vs. disorder and its impact on charge carrier mobility and catalytic activity. We studied the photocatalytic hydrogen evolution rates of amorphous  $\text{TzG}_{\text{Pd/Cu}}$  and crystalline  $\text{TzG}_{\text{Cu}}$  by using sacrificial hole-scavengers and compared the performance and (opto)-electronic properties of the materials with predictions from DFT calculations and evidence from spectroscopic and crystallographic measurements. The ordered  $\text{TzG}_{\text{Cu}}$  polymorph has the highest accessible surface area and a coplanar  $\pi$ -conjugated backbone that yields itself to interplanar hopping of charge carriers and more efficient electron transfer. In contrast, the disordered  $\text{TzG}_{\text{Pd/Cu}}$  polymorph shows inter-growth, pore blockage, and isolated  $\pi$ -aromatic segments. This lack of pathways for exciton annihilation give rise to a highly fluorescent material that—in terms of photocatalytic performance—benefits most from a noble metal cocatalyst that mediates electron transfer. More importantly, for the first time, we combined the worlds of ordered, covalent organic frameworks and disordered, conjugated microporous polymers in a comprehensive polymorph study based on the highly modular and malleable synthetic platform of triazine-based graphdiyne polymers. This lays the foundations for truly rational design of functional nanomaterials—be it as tailored upconverting phosphors, as heterogeneous catalysts, or in (opto)electronic applications.

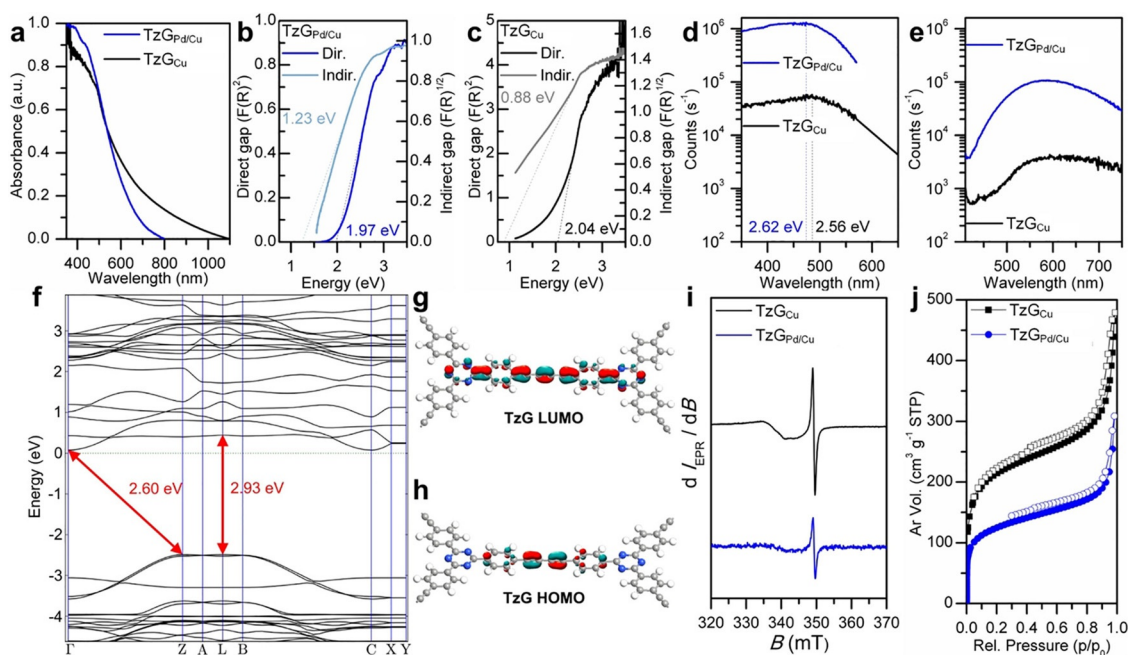


**Figure 4.** Optical, electronic and sorption properties of TzG<sub>pd/Cu</sub> and TzG<sub>cu</sub> polymorphs. a) Solid-state UV/Vis diffuse-reflectance spectra of TzG<sub>pd/Cu</sub> (blue) and TzG<sub>cu</sub> (black), and the corresponding Kubelka–Munk plots for b) TzG<sub>pd/Cu</sub> with a direct (1.97 eV) and indirect (1.23 eV) optical band gap, and for c) TzG<sub>cu</sub> with a direct (2.04 eV) and indirect (0.88 eV) optical band gap. d) Photoluminescence emission and e) excitation spectra for TzG<sub>pd/Cu</sub> (blue) and TzG<sub>cu</sub> (black). The two maxima at 2.62 eV and 2.56 eV are attributed to excitation transitions within TzG<sub>pd/Cu</sub> and TzG<sub>cu</sub>, respectively. f) The band-gap diagram for TzG indicates an indirect band gap of 2.60 eV and a direct band gap of 2.93 eV. g, h) Plots of orbital coefficients for the frontier orbitals of TzG as derived from DFT calculations. i) Experimental EPR spectrum of TzG<sub>pd/Cu</sub> (blue) and TzG<sub>cu</sub> (black). The radical component of TzG<sub>cu</sub> (*g* factor 2.0032, linewidth 0.63 mT) is two times more intense than that of TzG<sub>pd/Cu</sub> (*g* factor 2.0035, linewidth 0.66 mT), indicating a higher concentration of induced polaron-like centers in TzG<sub>cu</sub> than in TzG<sub>pd/Cu</sub>. The spectrum of TzG<sub>cu</sub> shows in addition a feature between 340 mT and 345 mT that corresponds to paramagnetic Cu<sup>2+</sup> species.<sup>[10]</sup> j) Argon sorption isotherms for TzG<sub>pd/Cu</sub> (blue) and TzG<sub>cu</sub> (black) measured at 87 K.

## Acknowledgements

We thank Dr. Carlos Henrique Vieira Melo for proof reading this manuscript, Dr. Ivana Sloufová for Raman measurements, Dr. Martin Dračinský for solid-state NMR measurements, Šárka Pšondrová for IR measurements, and Stanislava Matějková for ICP-OES. Jaroslava Hnilickova is acknowledged for elemental analysis and Christina Eichenauer is acknowledged for CO<sub>2</sub> measurements. Furthermore, we thank Dr. Simona Hybelbauerova for her help with solid-state NMR measurements, Dr. Miroslav Stepanek for his help with solid-state fluorescence measurements, Dr. Jiri Rybacek and Dr. Martin Racek for their support with SEM and EDX, and Prof. Ivo Marek for access to HR-TEM. M.J.B. thanks the European Research Council (ERC) for funding under the Starting Grant Scheme (BEGMAT-678462). M.J.B., J.C., and P.N. further acknowledge the Charles University Centre of Advanced Materials (CUCAM; OP VVV Excellent Research Teams, project number CZ.02.1.01/0.0/0.0/15\_003/0000417).

## Conflict of interest

The authors declare no conflict of interest.

**Keywords:** carbon • covalent organic frameworks • photocatalysis • porous polymers • semiconductors

- [1] a) J. X. Jiang, Y. Y. Li, X. F. Wu, J. L. Xiao, D. J. Adams, A. I. Cooper, *Macromolecules* **2013**, *46*, 8779–8783; b) J. X. Jiang, A. Trewin, D. J. Adams, A. I. Cooper, *Chem. Sci.* **2011**, *2*, 1777–1781; c) G. G. Zhang, Z. A. Lan, X. C. Wang, *Angew. Chem. Int. Ed.* **2016**, *55*, 15712–15727; *Angew. Chem.* **2016**, *128*, 15940–15956; d) R. S. Sprick, B. Bonillo, R. Clowes, P. Guiglian, N. J. Brownbill, B. J. Slater, F. Blanc, M. A. Zwijnenburg, D. J. Adams, A. I. Cooper, *Angew. Chem. Int. Ed.* **2016**, *55*, 1792–1796; *Angew. Chem.* **2016**, *128*, 1824–1828; e) J. S. Zhang, Y. Chen, X. C. Wang, *Energy Environ. Sci.* **2015**, *8*, 3092–3108.
- [2] X. Wang, K. Maeda, A. Thomas, K. Takanabe, G. Xin, J. M. Carlsson, K. Domen, M. Antonietti, *Nat. Mater.* **2009**, *8*, 76–80.
- [3] a) A. Thomas, A. Fischer, F. Goettmann, M. Antonietti, J.-O. Muller, R. Schlögl, J. M. Carlsson, *J. Mater. Chem.* **2008**, *18*, 4893–4908; b) J. Wang, Y. Chen, Y. Shen, S. Liu, Y. Zhang, *Chem. Commun.* **2017**, *53*, 2978–2981.
- [4] F. Goettmann, A. Thomas, M. Antonietti, *Angew. Chem. Int. Ed.* **2007**, *46*, 2717–2720; *Angew. Chem.* **2007**, *119*, 2773–2776.
- [5] M. J. Bojdyš, *Macromol. Chem. Phys.* **2016**, *217*, 232–241.
- [6] a) A. P. Cote, A. I. Benin, N. W. Ockwig, M. O’Keeffe, A. J. Matzger, O. M. Yaghi, *Science* **2005**, *310*, 1166–1170; b) H. M. El-Kaderi, J. R. Hunt, J. L. Mendoza-Cortes, A. P. Cote, R. E. Taylor, M. O’Keeffe, O. M. Yaghi, *Science* **2007**, *316*, 268–272.
- [7] a) A. I. Cooper, *Adv. Mater.* **2009**, *21*, 1291–1295; b) J. X. Jiang, F. Su, A. Trewin, C. D. Wood, H. Niu, J. T. A. Jones, Y. Z. Khimyak, A. I. Cooper, *J. Am. Chem. Soc.* **2008**, *130*, 7710–7720; c) Y. H. Xu, S. B. Jin, H. Xu, A. Nagai, D. L. Jiang, *Chem. Soc. Rev.* **2013**, *42*, 8012–8031.
- [8] V. R. Thalladi, S. Brasselet, H.-C. Weiss, D. Bläser, A. K. Katz, H. L. Carrell, R. Boese, J. Zyss, A. Nangia, G. R. Desiraju, *J. Am. Chem. Soc.* **1998**, *120*, 2563–2577.
- [9] a) I. Nenner, G. J. Schulz, *J. Chem. Phys.* **1975**, *62*, 1747–1758; b) R. Fink, C. Frenz, M. Thelakkat, H.-W. Schmidt, *Macromolecules* **1997**, *30*, 8177–8181; c) H. Meier, E. Karpuk, H. C. Holst, *Eur. J. Org. Chem.* **2006**, 2609–2617; d) S. Ren, Q. Fang, F. Yu, D. Bu, *J. Polym. Sci. Part A* **2005**, *43*, 6554–6561; e) T. Yamamoto, S. Watanabe, H. Fukumoto, M. Sato, T.

- Tanaka, *Macromol. Rapid Commun.* **2006**, *27*, 317–321; f) S. Ren, D. Zeng, H. Zhong, Y. Wang, S. Qian, Q. Fang, *J. Phys. Chem. B* **2010**, *114*, 10374–10383; g) L. Zou, Y. Fu, X. Yan, X. Chen, J. Qin, *J. Polym. Sci. Part A* **2008**, *46*, 702–712; h) K. M. Omer, S.-Y. Ku, Y.-C. Chen, K.-T. Wong, A. J. Bard, *J. Am. Chem. Soc.* **2010**, *132*, 10944–10952; i) R. Kannan, G. S. He, T.-C. Lin, P. N. Prasad, R. A. Vaia, L.-S. Tan, *Chem. Mater.* **2004**, *16*, 185–194; j) L. Zou, Y. Liu, N. Ma, E. Macoas, J. M. G. Martinho, M. Pettersson, X. Chen, J. Qin, *Phys. Chem. Chem. Phys.* **2011**, *13*, 8838–8846; k) L. Zou, Z. Liu, X. Yan, Y. Liu, Y. Fu, J. Liu, Z. Huang, X. Chen, J. Qin, *Eur. J. Org. Chem.* **2009**, 5587–5593.
- [10] D. Schwarz, Y. Noda, J. Klouda, K. Schwarzová-Pecková, J. Tarábek, J. Rybáček, J. Janoušek, F. Simon, M. V. Opanasenko, J. Čejka, A. Acharjya, J. Schmidt, S. Selve, V. Reiter-Scherer, N. Severin, J. P. Rabe, P. Ecorchard, J. He, M. Polozij, P. Nachtigall, M. J. Bojdys, *Adv. Mater.* **2017**, *29*, 1703399.
- [11] S. Ren, M. J. Bojdys, R. Dawson, A. Laybourn, Y. Z. Khimyak, D. J. Adams, A. I. Cooper, *Adv. Mater.* **2012**, *24*, 2357–2361.
- [12] L. Wang, J. Yan, P. H. Li, M. Wang, C. N. Su, *J. Chem. Res.* **2005**, *2005*, 112–115.
- [13] a) I. J. S. Fairlamb, P. S. Bauerlein, L. R. Marrison, J. M. Dickinson, *Chem. Commun.* **2003**, 632–633; b) A. S. Batsanov, J. C. Collings, I. J. S. Fairlamb, J. P. Holland, J. A. K. Howard, Z. Lin, T. B. Marder, A. C. Parsons, R. M. Ward, J. Zhu, *J. Org. Chem.* **2005**, *70*, 703–706; c) J.-X. Jiang, F. Su, H. Niu, C. D. Wood, N. L. Campbell, Y. Z. Khimyak, A. I. Cooper, *Chem. Commun.* **2008**, 486–488.
- [14] a) Q. Chen, X.-H. Fan, L.-P. Zhang, L.-M. Yang, *Synth. Commun.* **2015**, *45*, 824–830; b) S. Wang, D. Hu, W. Hua, J. Gu, Q. Zhang, X. Jia, K. Xi, *RSC Adv.* **2015**, *5*, 53935–53939.
- [15] V. G. Manecke, D. Wöhrle, *Makromol. Chem.* **1968**, *120*, 176–191.
- [16] D. Tan, W. Xiong, H. Sun, Z. Zhang, W. Ma, C. Meng, W. Fan, A. Li, *Microporous Mesoporous Mater.* **2013**, *176*, 25–30.
- [17] a) J.-X. Jiang, F. Su, A. Trewin, C. D. Wood, N. L. Campbell, H. Niu, C. Dickinson, A. Y. Ganin, M. J. Rosseinsky, Y. Z. Khimyak, A. I. Cooper, *Angew. Chem. Int. Ed.* **2007**, *46*, 8574–8578; *Angew. Chem.* **2007**, *119*, 8728–8732; b) M. Trunk, A. Herrmann, H. Bildirir, A. Yassin, J. Schmidt, A. Thomas, *Chem. Eur. J.* **2016**, *22*, 7179–7183.
- [18] Y. Liao, J. Weber, C. F. J. Faul, *Chem. Commun.* **2014**, *50*, 8002–8005.
- [19] G. Algara-Siller, N. Severin, S. Y. Chong, T. Björkman, R. G. Palgrave, A. Laybourn, M. Antonietti, Y. Z. Khimyak, A. V. Krashennikov, J. P. Rabe, U. Kaiser, A. I. Cooper, A. Thomas, M. J. Bojdys, *Angew. Chem. Int. Ed.* **2014**, *53*, 7450–7455; *Angew. Chem.* **2014**, *126*, 7580–7585.
- [20] C. Merschjann, T. Tyborski, S. Orthmann, F. Yang, K. Schwarzburg, M. Lublow, M. C. Lux-Steiner, T. Schedel-Niedrig, *Phys. Rev. B* **2013**, *87*, 205204.
- [21] F. K. Kessler, Y. Zheng, D. Schwarz, C. Merschjann, W. Schnick, X. Wang, M. J. Bojdys, *Nat. Rev. Mater.* **2017**, *2*, 17030.
- [22] a) Y. Yuan, J. Shu, P. Liu, Y. Zhang, Y. Duan, J. Zhang, *J. Phys. Chem. B* **2015**, *119*, 8446–8456; b) C. B. Meier, R. S. Sprick, A. Monti, P. Guiglion, J.-S. M. Lee, M. A. Zwijnenburg, A. I. Cooper, *Polymer* **2017**, *126*, 283–290.
- [23] K. D. Gourley, C. P. Lillya, J. R. Reynolds, J. C. W. Chien, *Macromolecules* **1984**, *17*, 1025–1033.
- [24] D. L. Meyer, R. Matsidik, M. Sommer, T. Biskup, *Adv. Electronic Mater.* **2018**, *4*, 1700385.
- [25] S. Kuecken, A. Acharjya, L. Zhi, M. Schwarze, R. Schomacker, A. Thomas, *Chem. Commun.* **2017**, *53*, 5854–5857.
- [26] J. Kiwi, M. Grätzel, *Nature* **1979**, *281*, 657.

---

 Manuscript received: September 4, 2018

Revised manuscript received: October 17, 2018

Accepted manuscript online: October 18, 2018

Version of record online: November 21, 2018

# **Attachment No. 4**



# Semiconducting Crystalline Two-Dimensional Polyimide Nanosheets with Superior Sodium Storage Properties

Haiyan Duan,<sup>†</sup> Pengbo Lyu,<sup>‡</sup> Jingjing Liu,<sup>†</sup> Yanli Zhao,<sup>†</sup> and Yuxi Xu<sup>\*,†</sup>

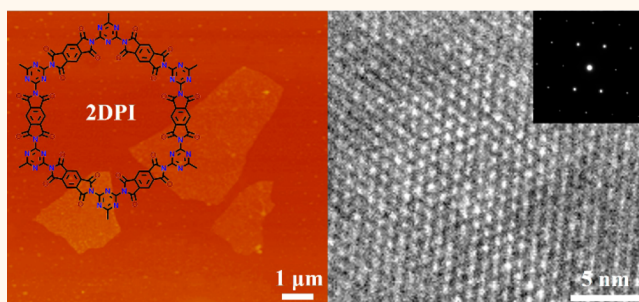
<sup>†</sup>State Key Laboratory of Molecular Engineering of Polymers, Department of Macromolecular Science, Fudan University, Shanghai 200433, China

<sup>‡</sup>Department of Physical and Macromolecular Chemistry, Faculty of Science, Charles University, Hlavova 2030, Prague 2 12800, Czech Republic

## Supporting Information

**ABSTRACT:** The efficient synthesis of crystalline two-dimensional polymers (2DPs) with designed structures and properties is highly desired but remains a considerable challenge. Herein, we report the synthesis of two-dimensional polyimide (2DPI) nanosheets *via* hydrogen-bond-induced preorganization and subsequent imidization reaction. The formed intermolecular hydrogen bonds can significantly improve the internal order and in-plane periodicity of 2DPI. The crystalline few-layer 2DPI nanosheets are micrometer-size, solvent dispersible, and thermally stable. Interestingly, the 2DPI with  $\pi$ -conjugation shows a favorable bandgap of 2.2 eV and can function as a p-type semiconducting layer in field-effect transistor devices with an appreciable mobility of  $4.3 \times 10^{-3} \text{ cm}^2 \text{ V}^{-1} \text{ s}^{-1}$ . Furthermore, when explored as a polymeric anode for sodium-ion batteries, the 2DPI exhibits ultrahigh capacity ( $312 \text{ mAh g}^{-1}$  at  $0.1 \text{ A g}^{-1}$ ), impressive rate capability ( $137 \text{ mAh g}^{-1}$  at  $10.0 \text{ A g}^{-1}$ ), and excellent cycling stability (95% capacity retention after 1100 cycles) due to its robust 2D conjugated porous structure, outperforming most organic/polymeric anodes ever reported. This work provides a versatile strategy for synthesizing 2DP nanosheets with promising electronics and energy-related applications.

**KEYWORDS:** semiconducting, crystalline, two-dimensional polyimide, sodium-ion batteries, field-effect transistor



Two-dimensional polymers (2DPs) that are atomic or molecular thin and covalently linked planar macromolecules with long-range structural ordering have received great interest recently.<sup>1–4</sup> As a natural and archetypical 2DP, graphene has demonstrated extraordinary physicochemical properties and stimulated rational design and organic synthesis of 2DPs with desired structures, properties, and functions at the atomic or molecular level.<sup>5–11</sup> For example, 2D monolayers of molecular networks can be fabricated on single-crystal metal surfaces under ultrahigh vacuum conditions.<sup>12,13</sup> However, the obtained 2D monolayers exhibited limited lateral dimensions on a nanometer scale, and the separation from the substrate is very difficult. As an alternative approach, 2DPs have been recently achieved by exfoliation of presynthesized 2D covalent organic frameworks or crystalline layered polymers.<sup>14–20</sup> Another major method is to perform 2D polymerization reactions such as Schiff-base condensation at two-phase interfaces typically at the air–liquid or liquid–liquid interface to synthesize 2DP films.<sup>21–23</sup> These two methods usually suffer from relatively low yield. Thus,

despite the progress achieved so far, the types and efficient synthetic routes of 2DPs are still very limited, which severely impedes their fundamental and applied research. Moreover, the functionalities and applications of 2DPs in electronics and energy-related fields remain largely unexplored. Therefore, developing scalable synthetic methodology to efficiently construct free-standing functional 2DPs is highly desired but remains a tremendous challenge.

Herein, we report the synthesis of crystalline few-layer 2D polyimide (2DPI) nanosheets through the hydrogen-bond-induced preorganization of pyromellitic acid (PMA) and melamine (MA) followed by imidization reaction of the obtained planar hydrogen-bonded networks (HBN) under solvothermal process. The achieved ultrathin 2DPI nanosheets not only have lateral dimensions of micrometers but also show excellent thermal stability and superior solvent dispersibility.

**Received:** December 12, 2018

**Accepted:** February 12, 2019

**Published:** February 12, 2019

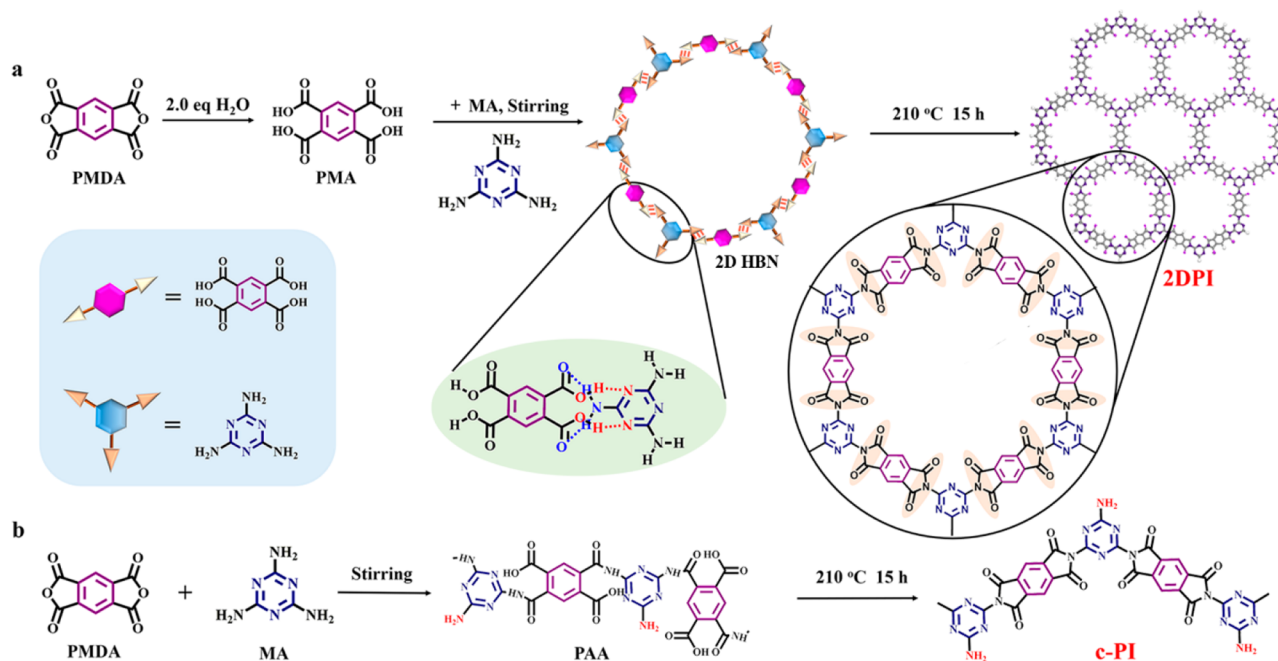


**Figure 1.** (a) Schematic illustration of the hydrogen bond-directed 2D polymerization reaction to produce crystalline 2DPI. (b) Schematic illustration of the direct reaction between PMDA and MA to produce c-PI.

Interestingly, the crystalline 2DPI with  $\pi$ -conjugation shows a favorable bandgap of 2.2 eV and can function as a p-type semiconducting layer in field-effect transistor (FET) devices with an appreciable mobility of  $4.3 \times 10^{-3} \text{ cm}^2 \text{ V}^{-1} \text{ s}^{-1}$ , in contrast to the well-known insulator property of linear PI. Furthermore, because of its robust 2D conjugated porous structure enabling convenient charge transport and storage, 2DPI can achieve ultrahigh capacity ( $312 \text{ mAh g}^{-1}$  at  $0.1 \text{ A g}^{-1}$ ), impressive rate capability ( $137 \text{ mAh g}^{-1}$  at  $10.0 \text{ A g}^{-1}$ ), and excellent cycling stability (95% capacity retention after 1100 cycles) as a polymeric anode for sodium-ion batteries (SIBs), outperforming most organic/polymeric SIB anodes ever reported.

## RESULTS AND DISCUSSION

In a typical synthesis process (Figure 1a), the pyromellitic dianhydride (PMDA) dissolved in *N*-methylpyrrolidone (NMP) was first hydrolyzed into PMA by adding 2.0 equiv of  $\text{H}_2\text{O}$  (Figure S1). Then the MA was added and the hydrogen bond interaction could generate between the carboxylic acid of PMA and amido or triazine of MA to form HBN, which can preorganize the monomers into a 2D network and significantly benefit 2D topological polymerization. Upon further solvothermal treatment and purification, crystalline few-layer 2DPI nanosheets were obtained. The control experiments which performed direct polymerization reaction of PDMA and MA under the same experimental conditions (without adding 2.0 equiv of  $\text{H}_2\text{O}$ ) failed to obtain 2D sheets but instead obtained irregular conventional-PI (c-PI) (Figure 1b). In this process, the monomers PMDA and MA were not preorganized and thus randomly reacted into poly(amic acids) (PAA) with residual unreacted functional groups, which lead to dislocation polymerization without 2D topological order due to the irreversibility of imidization reaction.

We first studied the above-proposed reaction mechanism experimentally. As can be seen in Figure 2a, when the turbid

MA dispersion due to the insolubility of MA was added into the PMA solution, a transparent colorless solution can be quickly obtained. Once  $\text{H}_2\text{O}$ , which is a hydrogen bond competitor, was introduced into the above complex solution, a turbid dispersion containing precipitated MA was obtained again (Figure S2), which indicated the existence of an intermolecular hydrogen bond between PMA and MA. Fourier transform infrared (FTIR) spectra (Figure 2b) clearly showed an obvious red shift in the peaks associated with the free groups of individual monomers and the ones of the complex, further verifying the existence of an H-bond between PMA and MA.<sup>24</sup> Meanwhile, no peaks corresponding to the amic acid (around  $1650 \text{ cm}^{-1}$ ) appeared, suggesting that the complex intermediates are fully H-bonded. Transmission electron microscopy (TEM) (Figure 2c) was further employed to image the complex and unambiguously revealed the ultrathin sheetlike morphology, which confirmed the proposed 2D HBN intermediates (Figure 1a). Such HBN is beneficial for the 2D topological polymerization and internal structural order for the target 2DPI. In contrast, the direct reaction between PMDA and MA produced the colored PAA intermediates (Figure 2d). FTIR spectra (Figure 2e) showed characteristic peaks of amino and amide (around  $3480$ ,  $3420$ , and  $1650 \text{ cm}^{-1}$  respectively), and TEM (Figure 2f) revealed irregular nanoparticles for PAA, verifying the disordered polymerization process and the presence of unreacted  $-\text{NH}_2$  in the generated PAA intermediate. Furthermore, solid-state  $^1\text{H}$  NMR were conducted and also confirmed this mechanism (Figure S3). Because of the significant difference between HBN and PAA intermediates, upon the same solvothermal reaction, brown 2DPI nanosheets and light yellow spherulike c-PI micro-particles were obtained, respectively (Figure S4). Therefore, the hydrogen bond preorganization is the key to successful synthesis of 2DPI, which provides important insight into the 2D polymerization reaction.

The structure of 2DPI was then characterized in detail. Scanning electron microscopy (SEM) and TEM images

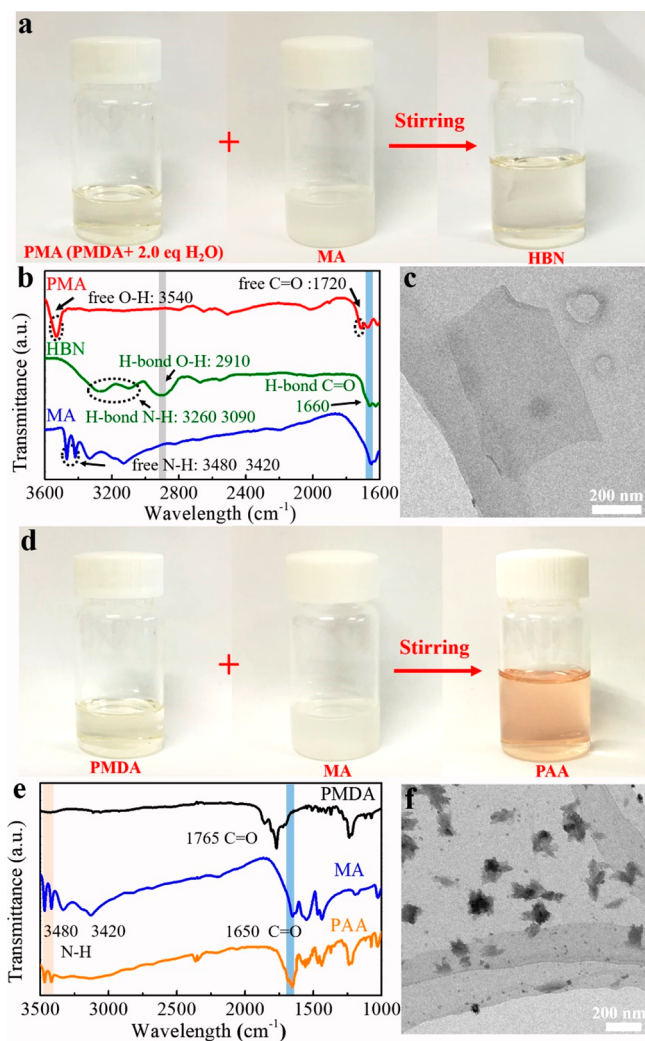


**Figure 2.** (a) Photographs of the HBN formed after adding MA in PMA. (b) FTIR spectra of HBN, PMA, and MA. (c) TEM image of 2D HBN. (d) Photographs of the PAA formed after adding MA in PMDA. (e) FTIR spectra of PAA, PMDA, and MA. (f) TEM image of PAA.

simultaneously revealed an ultrathin sheetlike morphology with a lateral dimension of several micrometers for 2DPI (Figure 3a, b), similar to that of graphene. According to the SEM images and the histogram of size distribution, we can find that the 2DPI nanosheets showed an average size of  $\sim 4 \mu\text{m}$  (Figure S5). Besides, the 2DPI has excellent dispersibility in ethanol (the inset of Figure 3b), and stable dispersions can be still accessible after 2 months (Figure S6), which provides the desired processability for various applications. The atomic force microscopy (AFM) image (Figure 3c) demonstrated that the thickness of a micrometer-size 2DPI nanosheet was 1.5–2.6 nm, confirming the ultrathin few-layer feature of 2DPI. High-resolution TEM (HRTEM) (Figure 3d) and the sharp selected area electron diffraction (SAED) pattern (Figure 3e) clearly certify the high crystallinity and hexagonal 2D crystal structures with long-range order within the 2DPI sheets, which is in good agreement with the structure derived from density functional based tight binding (DFTB) calculations (Figure S7). In terms of the scalability and material quality, our synthetic method is overall better than previous limited approaches (Table S1). Based on the theoretical simulation

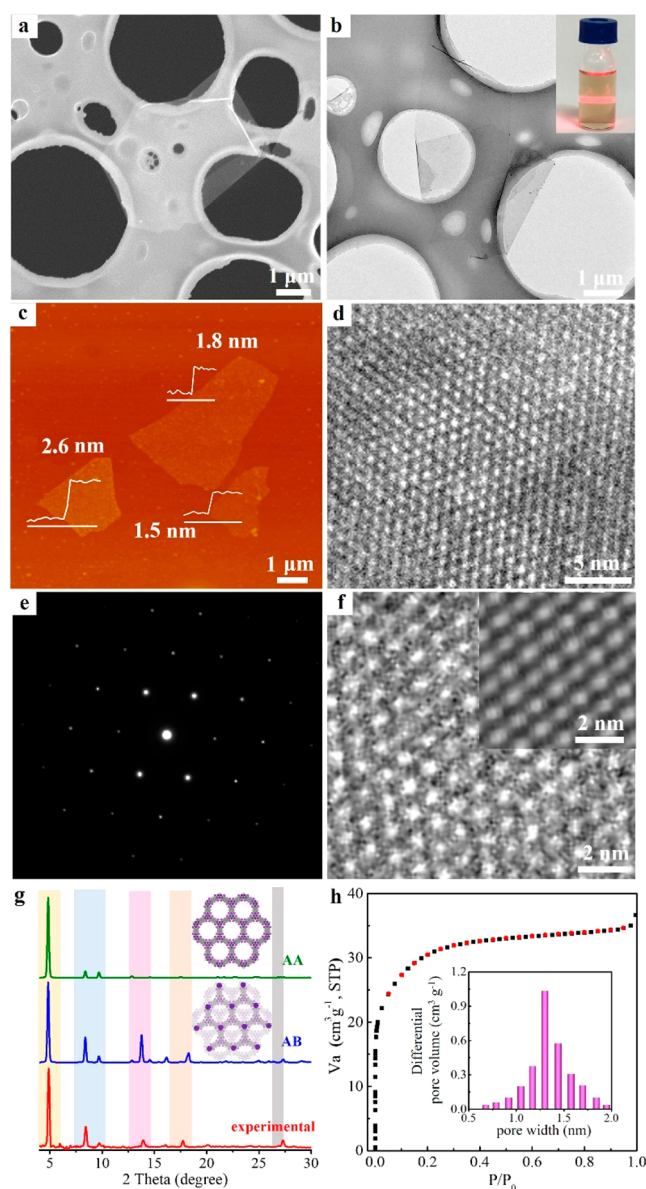


**Figure 3.** (a) SEM, (b) TEM, and (c) AFM images of 2DPI. The inset of Figure 3b shows a photograph of 2DPI dispersion in ethanol ( $\sim 0.1 \text{ mg mL}^{-1}$ ). (d) HRTEM image and (e) SAED pattern of 2DPI. (f) Experimental HRTEM image matching with the simulated one of staggered AB stacking mode. (g) XRD pattern of 2DPI and simulated XRD patterns using an eclipsed AA and staggered AB mode. (h)  $\text{N}_2$  adsorption/desorption isotherm and pore size distribution profile of 2DPI and its pore size distribution (inset).

of possible stacking modes and the comparison of their interlayer interaction energies (Figure S8 and Table S2), we proposed that the few-layer 2DPI has a staggered AB stacking mode in which one set of polyimide units from the first layer always fill in the voids of the second layer. We further compared the experimental HRTEM images of 2DPI with the simulated ones of different stacking modes and confirmed the AB stacking in the few-layer 2DPI (Figure 3f and Figure S9). X-ray diffraction (XRD) analysis and theoretical investigation (Figure 3g) further verified the excellent crystallinity with the AB-stacking mode for the 2DPI, which is significantly different from that of c-PI (Figure S10). We further studied the porosity of 2DPI by a gas adsorption/desorption test.  $\text{N}_2$  adsorption/

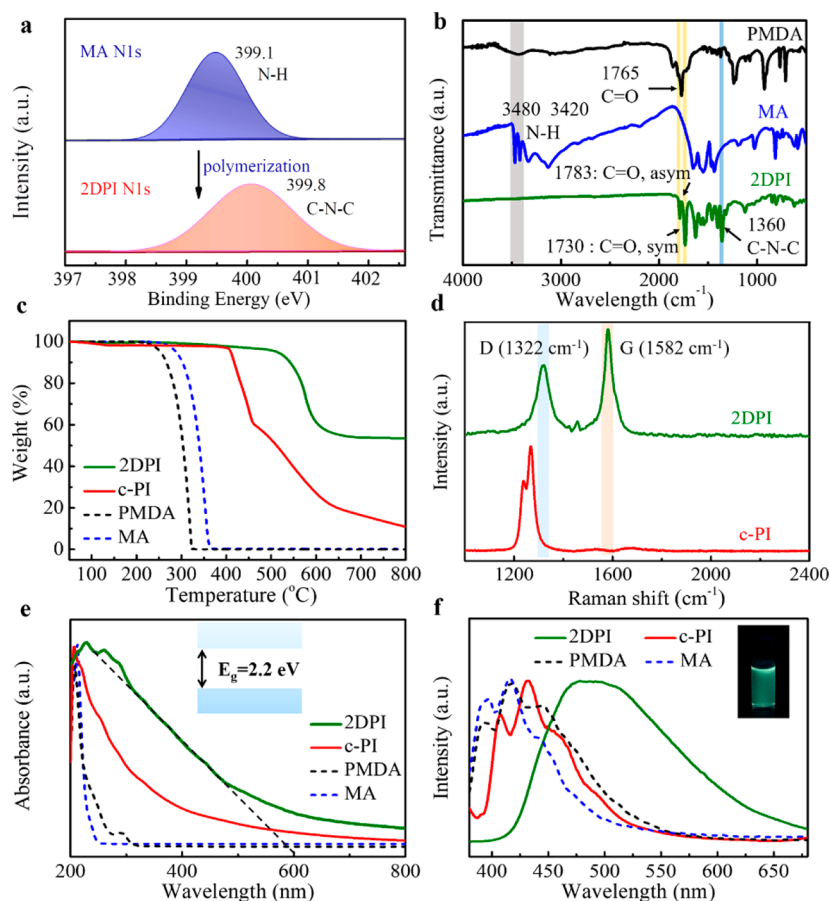


**Figure 4.** (a) XPS N 1s spectra and (b) FTIR spectra of monomer and 2DPI. (c) TGA curves, (d) Raman spectra, (e) UV–vis spectra, and (f) steady-state photoluminescence spectra of 2DPI, c-PI, and monomers. The inset of (f) shows a photograph of 2DPI dispersion after excitation under UV light.

desorption isotherm measurements revealed a type-I isotherm for the 2DPI, indicating a microporous structure of 2DPI (Figure 3h). The predominant microporous characteristic of 2DPI could be mainly attributed to its in-plane porosity within the AB-stacked 2DPI nanosheets. The Brunauer–Emmett–Teller (BET) specific surface area of 2DPI was evaluated to be  $108 \text{ m}^2 \text{ g}^{-1}$ , which is lower than conventional bulk covalent–organic frameworks (COFs) due to the AB stacking and the absence of long-range aligned pores in 2DPI compared to those bulk COFs with AA stacking.<sup>14</sup> The pore size distribution (the inset of Figure 3h) was mainly located at around 1.3 nm, suggesting the homogeneous porosity and consistent with staggered AB stacking structures.

The X-ray photoelectron spectroscopy (XPS) (Figure 4a and Figure S11) and FTIR (Figure 4b and Figure S12) revealed that the  $-\text{NH}_2$  of the MA monomer was almost fully transformed to C–N–C of the 2DPI, suggesting the high efficiency of the 2D polymerization and fully imidize networks. In contrast, the FTIR of c-PI showed the obvious presence of unreacted  $-\text{NH}_2$  (Figure S12), indicating a malposed polymerization and thus resulting in an irregular structure. The  $^{13}\text{C}$  cross-polarization magic-angle-spinning (CP-MAS) solid-state NMR spectroscopy of 2DPI also confirmed the complete and regular 2D polymerization. In contrast, the NMR spectra of c-PI presented a carbon signal in the triazine units of unreacted  $-\text{NH}_2$  (Figure S13), which is consistent with the FTIR results. Relative to the monomers and c-PI, the crystalline 2DPI showed significantly improved thermal

stability due to its robust and ordered polymer framework (Figure 4c). Raman spectra (Figure 4d) further demonstrated a graphene-like sharp G peak for 2DPI compared with c-PI, verifying a 2D honeycomb structure and a high crystallinity in 2DPI.<sup>20,25,26</sup> The 2DPI displayed a much broader absorbance range (Figure 4e) and red-shifted fluorescence emission (Figure 4f) compared to the monomers and c-PI, suggesting an extended in-plane delocalization of  $\pi$ -conjugated skeleton after 2D polymerization. Notably, the optical bandgap of the 2DPI was determined to be 2.2 eV by UV–vis spectrum, implying a favorable bandgap for 2DPI. Meanwhile, the 2DPI showed blue-green fluorescence (inset of Figure 4f) upon UV light irradiation, implying its potential opportunities for electronic/optoelectronic applications.

Based on the above results, we further investigated the electronic properties of 2DPI theoretically based on the structure model in Figure S14. The first-principles density-functional theory (DFT) calculation revealed that the electronic structure of the 2DPI has a direct band gap of 2.24 eV (Figure 5a), in accordance with the experimental value of 2.2 eV and again confirming high crystalline and low defect within the 2DPI. Inspired by this, we fabricated FET devices based on the 2DPI as the active semiconducting layer (inset of Figure 5b). The atomic flat surface of the 2DPI nanosheet can create a high-quality interface between the 2DPI semiconductor,  $\text{SiO}_2$  dielectric, and source/drain electrodes. Figure 5b shows the typical transfer curve ( $I_{\text{DS}}$  vs  $V_{\text{G}}$  with  $V_{\text{DS}} = 1 \text{ V}$ ) of the 2DPI-based FET device. Interestingly, the device

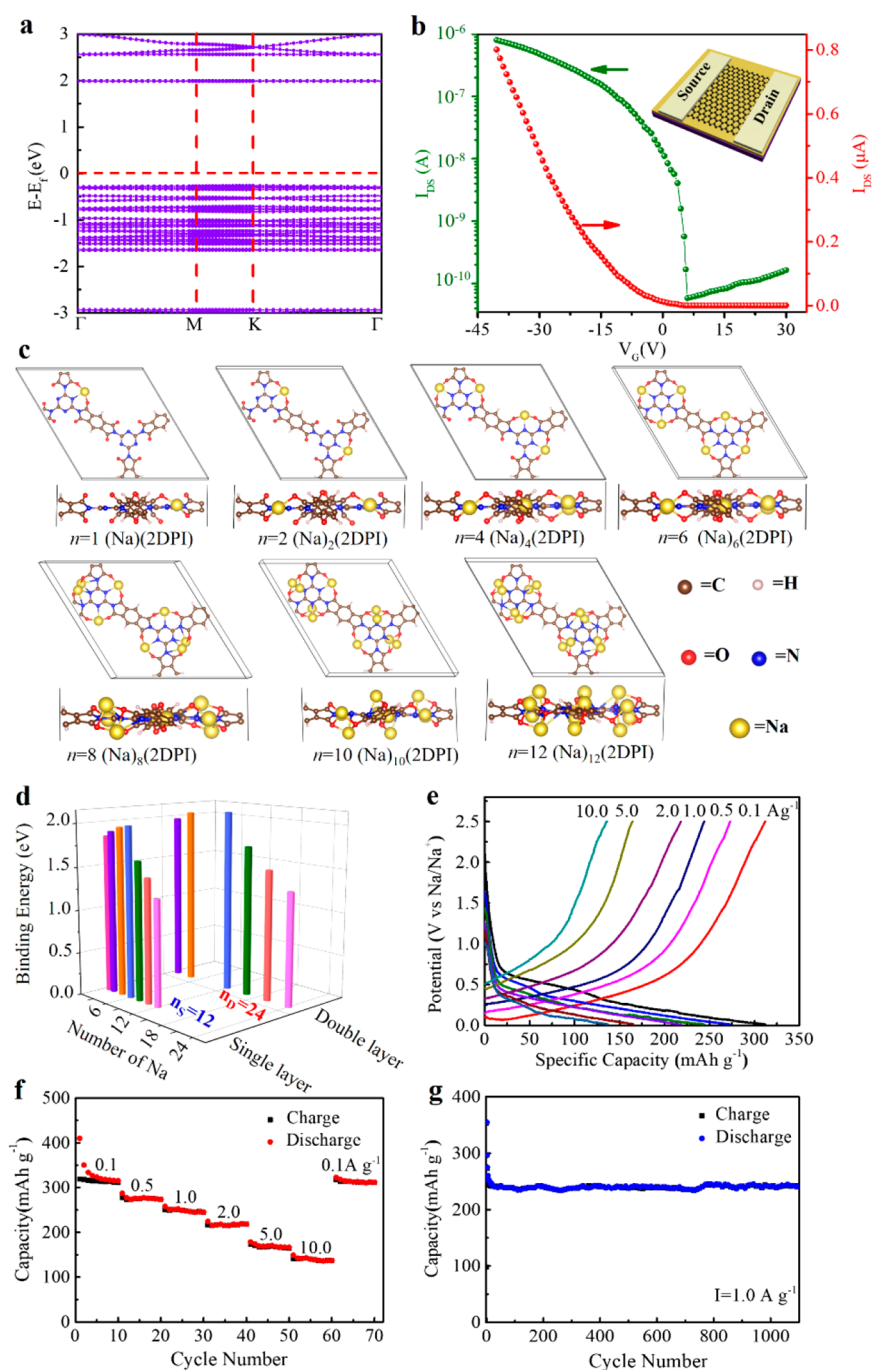


**Figure 5.** (a) DFT band structure of the 2DPI triangular lattice. (b) Transfer curve of the 2DPI-based FET device. The inset shows the schematic of FET device employing 2DPI as the semiconducting layer,  $V_G$  is the gate-source voltage, and  $I_{DS}$  is the drain current. (c) Top and side view of sodiated single-layer 2DPI,  $(Na)_n(2DPI)$  of varying Na number,  $n$ . (d) Binding energy  $E_b$  as a function of Na atom number, for single-layer and double-layer 2DPI. The blue and red numbers represent the saturated Na number for fully occupied single-layer and double-layer 2DPI. (e) Charge–discharge profiles of 2DPI anode at different current densities. (f) Rate performance of 2DPI anode at 0.1, 0.5, 1.0, 2.0, 5.0, and 10.0  $A g^{-1}$ . (g) Cycling performance of 2DPI anode up to 1100 cycles at 1.0  $A g^{-1}$ .

showed a p-type behavior with an on/off ratio of  $1.4 \times 10^4$ , and the mobility was calculated to be  $4.3 \times 10^{-3} cm^2 V^{-1} s^{-1}$ , confirming the semiconductor characteristic of 2DPI in contrast to the well-known insulator property for linear PI polymers and demonstrating the important role and advantage of 2D planar structure. It is also worth noting that our 2DPI demonstrated comparable mobility with recently reported 2DPs,<sup>21,27–29</sup> suggesting its prospects in organic electronics.

SIBs hold great potential for large-scale and low-cost energy storage but suffer from the sluggish kinetics and structural destructions in the electrode material resulting from the electrochemical insertion/extraction of Na ions with larger radius than Li ions, which render most superior lithium-ion battery electrode materials unsuitable for SIBs.<sup>26,30</sup> Our 2DPI combines an ultrathin few-layer structure with an in-plane  $\pi$ -conjugated periodic porous structure with a uniform pore size of  $\sim 1.3$  nm, which can enable fast transport of electron and Na

ion for charge storage. Thus, the 2DPI can be expected to achieve high sodium storage ability. We first studied the interaction between single-layer/double-layer 2DPI and Na theoretically. The results demonstrated that imide functional groups and triazine rings in a single-layer (Figure 5c) and double-layer 2DPI molecular plane (Figure S15) could function as redox-active sites and coordinate with Na ions for charge storage. In the case of the reduction process, imide functional groups and triazine rings are accompanied by sodium ion association, which formed complexes with the formula  $(\text{Na})_n(2\text{DPI})$  or  $(\text{Na})_n(2\text{DPI})_2$ , while in the case of the oxidation process, imide functional groups and triazine rings are rebuilt and accompanied by sodium ion disassociation. In the entire redox process, the 2DPI can keep the robust 2D  $\pi$ -conjugated porous structure with open channels and promote the electrochemical insertion/extraction of Na ions. The stabilities of the complexes with the formula  $(\text{Na})_n(2\text{DPI})$  and  $(\text{Na})_n(2\text{DPI})_2$  were examined by their binding energies. When 12 Na atoms adsorb on single-layer 2DPI, the adsorption sites are fully occupied and the binding energy (1.23 eV) is still favorable for Na adsorption (Figure 5c,d), which is similar in double-layer 2DPI (Figure S15 and Figure 5c). Consequently, the fully sodiated single-layer and double-layer 2DPI can be represented by  $(\text{Na})_{12}(2\text{DPI})$  and  $(\text{Na})_{24}(2\text{DPI})_2$ , respectively. Thus, the theoretical capacities for both single-layer and double-layer 2DPI were calculated to be as high as 403 mAh  $\text{g}^{-1}$ . On the basis of the above calculation results, we further studied the sodium storage performance of 2DPI experimentally. Figure 5e shows the typical galvanostatic discharge/charge profiles of 2DPI at different current densities. The 2DPI showed very high reversible capacities of 312, 273, 244, 218, and 165 mAh  $\text{g}^{-1}$  at 0.1, 0.5, 1.0, 2.0, and 5.0 A  $\text{g}^{-1}$ , respectively (Figure 5f). Even at an ultrahigh current density of 10.0 A  $\text{g}^{-1}$ , an impressive capacity of 137 mAh  $\text{g}^{-1}$  can still be achieved for 2DPI. Furthermore, the 2DPI anode demonstrated superior cycling stability with a capacity retention of 95% over 1100 cycles at 1.0 A  $\text{g}^{-1}$  (Figure 5g). The electrical conductivity of the 2DPI nanosheets was measured to be  $\sim 1.0 \times 10^{-4}$  S/m (Figure S16), which is typical for nondoped semiconducting conjugated polymers.<sup>26,31,32</sup> In addition, the electrochemical impedance spectroscopy study of 2DPI electrode showed a smaller semicircle in the high- to medium-frequency region and a straighter line in the low-frequency region compared with some recently reported 2DP anodes for SIBs (Figure S17), indicating a lower charge-transfer resistance and a faster ion diffusion and thus a better rate performance for 2DPI.<sup>17,20</sup> Such excellent performance of 2DPI outperformed most reported organic/polymeric SIB anodes and many inorganic SIB anodes (Table S3) and can be ascribed to its ultrathin and robust 2D  $\pi$ -conjugated porous structure with open channels for reversible and smooth electrochemical insertion/extraction of Na ions.

## CONCLUSIONS

In summary, we have presented the synthesis of crystalline few-layer 2DPI via a synthetic strategy of hydrogen bond induced preorganization and subsequent imidization reaction. Detailed studies demonstrate that the hydrogen bond preorganization is the key to successful synthesis of 2DPI, which provides important insights into the 2D polymerization reaction. The crystalline 2DPI sheets show an ultrathin AB-stacking few-layer structure with a lateral size of several micrometers and

excellent thermal stability as well as desired solvent dispersibility. Excitingly, the crystalline 2DPI with  $\pi$  conjugation demonstrates a favorable bandgap of 2.2 eV and can function as a p-type semiconducting layer in FET with an appreciable mobility of  $4.3 \times 10^{-3}$   $\text{cm}^2 \text{V}^{-1} \text{s}^{-1}$ . Furthermore, by virtue of the robust 2D conjugated porous structure, 2DPI enables prominent sodium storage ability with ultrahigh capacity (312 mAh  $\text{g}^{-1}$  at 0.1 A  $\text{g}^{-1}$ ) and excellent rate capability (137 mAh  $\text{g}^{-1}$  at 10.0 A  $\text{g}^{-1}$ ) as well as superior cycling stability (95% capacity retention after 1100 cycles). This study provides a versatile and scalable route to synthesize a variety of 2DPs with tailorable structures and promising electronics and energy-related applications.

## EXPERIMENTAL SECTION

**Synthesis of 2DPI.** 2DPI was synthesized in an autoclave with Teflon lining. Typically, PMDA (130.8 mg, 0.6 mmol) dissolved in 30 mL of NMP solution was first hydrolyzed into PMA by addition of 2.0 equiv of  $\text{H}_2\text{O}$  (21.6  $\mu\text{L}$ ), then MA (50.4 mg, 0.4 mmol) dispersed in 30 mL of NMP solution was added, and a transparent colorless solution was quickly obtained. After being stirred for about 30 min, the mixture was upon further solvothermal treatment at 210  $^\circ\text{C}$  for 15 h in preheated oven. The resultant samples were collected by filtration followed by washing with NMP, ethanol, and hot water. After further purification by sonication and centrifuge, the yield of 2DPI was about 36%, which was calculated based on the initial monomers. The obtained 2DPI has a good dispersity in ethanol by simple sonication. Typically, 1 mg of 2DPI powder was added into 10 mL of ethanol followed by sonication with a power of 200 W for 20 min.

**Synthesis of c-PI.** The direct polymerization reaction of PDMA and MA was performed under the same experimental conditions (without addition of 2.0 equiv of  $\text{H}_2\text{O}$ ) to obtain c-PI.

**Instrumental Characterizations.** SEM was performed on Zeiss Ultra 55, and TEM images were obtained on a Tecnai G2 F20 S-Twin (acceleration voltage: 200 kV). AFM images were obtained on a Bruker Multimode 8 operated in tapping mode. XRD patterns were obtained on a PANalytical X'pert PRO.  $\text{N}_2$  adsorption–desorption measurements were carried out on JWGB-BK with a micropore option, and the samples were treated in vacuum states by degasification at 473 K before tests. Pore size distribution was calculated by nonlocal DFT modeling based on  $\text{N}_2$  adsorption data. XPS measurements were performed on a PerkinElmer PHI 5000C ESCA system equipped with a dual X-ray source using a 45 Mg Ka (1253.6 eV) anode and a hemispherical energy analyzer. FTIR was recorded on a Nicolet 6700 model. The  $^{13}\text{C}$  cross-polarization magic-angle-spinning (CP-MAS) solid state NMR spectroscopies were obtained on a Bruker 400WB AVANCE III. The thermal properties were evaluated using a thermogravimetric analysis instrument (Mettler Toledo A39) over the temperature range of 50–800  $^\circ\text{C}$  under  $\text{N}_2$  atmosphere with a heating rate of 10  $^\circ\text{C}/\text{min}$ . Raman spectra were obtained on XploRA A35. UV–vis spectra were conducted on PerkinElmer Lambda 35. Steady-state photoluminescence spectra measurements were performed on PTI QM-40 at room temperature.

**Field-Effect Transistor (FET) Devices.** After careful washing of heavily doped p-type Si substrates with 300 nm  $\text{SiO}_2$  by ultrasonication in acetone, ethanol, and deionized water for 10 min each, 2DPI sheets were deposited on the above substrates by dropping coating. Then the source and drain electrodes involving Au films with Ti adhesion layers (30 nm/5 nm) were thermally deposited onto the top of 2DPI. Before measurements, the devices were heat treated at 150  $^\circ\text{C}$  under reduced pressure ( $5 \times 10^{-6}$  Torr) to remove impurities. The transfer curves of the 2DPI-based FET device were characterized by a SUMMIT 11000B-M probe.

**Sodium-Ion Batteries (SIBs).** The anode of SIB was fabricated by homogeneously mixing 70 wt % of 2DPI, 20 wt % of Super P carbon black, and 10 wt % of polyvinylidene fluoride (PVDF) binder

in NMP solution. The obtained slurry was then loaded onto copper foil and dried at 120 °C in vacuum oven overnight. The coated copper foil was cut into 12 mm in diameter disks. The areal mass loading of active materials was  $\sim 1 \text{ mg cm}^{-2}$ . CR2016 coin cells were assembled in an Ar-filled glovebox via utilization of sodium metal as the reference electrode and counter electrode, using a glass microfiber filter (Whatman) as the separator. We used 1 M NaPF<sub>6</sub> in a 1:1 (v/v) mixture of ethylene carbonate and dimethyl carbonate as electrolyte. Electrochemical experiments were performed using a battery cycler (LAND-CT2001 A) at a voltage range of 0.01–2.5 V (versus Na/Na<sup>+</sup>). The capacity was calculated based on the mass of active materials. A CHI 760D electrochemical workstation was used to perform electrochemical impedance spectroscopy in the frequency range of 100 kHz to 0.01 Hz.

**DFT Calculations.** Details of the DFT calculations are given in the Supporting Information.

## ASSOCIATED CONTENT

### Supporting Information

The Supporting Information is available free of charge on the ACS Publications website at DOI: 10.1021/acsnano.8b09416.

Experimental details for synthesis and characterization studies, additional DFT calculations and simulation, additional photograph of products, FTIR, solid-state NMR, SEM, XRD, and XPS, conductivity measurements, Nyquist plot of 2DPI electrode, comparison of scalability and material quality of various synthetic methods, and comparison of sodium-storage performance among various materials (PDF)

## AUTHOR INFORMATION

### Corresponding Author

\*E-mail: xuyuxi@fudan.edu.cn.

### ORCID

Pengbo Lyu: 0000-0002-1785-9861

Yuxi Xu: 0000-0003-0318-8515

### Notes

The authors declare no competing financial interest.

## ACKNOWLEDGMENTS

We acknowledge support by the National Natural Science Foundation of China (51673042, 51873039) and the Young Elite Scientist Sponsorship Program by CAST (2017QNRC001).

## REFERENCES

- (1) Stupp, S. I.; Son, S.; Lin, H. C.; Li, L. S. Synthesis of Two-Dimensional Polymers. *Science* **1993**, *259*, 59–63.
- (2) Zhuang, X. D.; Mai, Y. Y.; Wu, D. Q.; Zhang, F.; Feng, X. L. Two-Dimensional Soft Nanomaterials: A Fascinating World of Materials. *Adv. Mater.* **2015**, *27*, 403–427.
- (3) Sakamoto, J.; van Heijst, H. J.; Lukin, O.; Schlüter, A. D. Two-Dimensional Polymers: Just A Dream of Synthetic Chemists? *Angew. Chem., Int. Ed.* **2009**, *48*, 1030–1069.
- (4) Cai, S. L.; Zhang, W. G.; Zuckermann, R. N.; Li, Z. T.; Zhao, X.; Liu, Y. The Organic Flatland—Recent Advances in Synthetic 2D Organic Layers. *Adv. Mater.* **2015**, *27*, S762–S770.
- (5) Geim, A. K.; Novoselov, K. S. The Rise of Graphene. *Nat. Mater.* **2007**, *6*, 183–191.
- (6) Novoselov, K. S.; Geim, A. K.; Morozov, S. V.; Jiang, D.; Zhang, Y.; Dubonos, S. V.; Grigorieva, I. V.; Firsov, A. A. Electric Field Effect in Atomically Thin Carbon Films. *Science* **2004**, *306*, 666–669.
- (7) Liu, J. J.; Zan, W.; Li, K.; Yang, Y.; Bu, F. X.; Xu, Y. X. Solution Synthesis of Semiconducting Two-Dimensional Polymer via Trimerization of Carbonitrile. *J. Am. Chem. Soc.* **2017**, *139*, 11666–11669.
- (8) Colson, J. W.; Dichtel, W. R. Rationally Synthesized Two-Dimensional Polymers. *Nat. Chem.* **2013**, *5*, 453–465.
- (9) Rodriguez-San-Miguel, D.; Amo-Ochoa, P.; Zamora, F. Cooking 2D-Polymers. *Chem. Commun.* **2016**, *52*, 4113–4127.
- (10) Yang, Y.; Bu, F. X.; Liu, J. J.; Shakir, I.; Xu, Y. X. Mechanochemical Synthesis of Two-Dimensional Aromatic Polyamides. *Chem. Commun.* **2017**, *53*, 7481–7484.
- (11) Liu, J. J.; Yang, Y.; Lyu, P. B.; Nachtigall, P.; Xu, Y. X. Few-Layer Silicene Nanosheets with Superior Lithium-Storage Properties. *Adv. Mater.* **2018**, *30*, 1800838–1800844.
- (12) Kissel, P.; Murray, D. J.; Wulfstange, W. J.; Catalano, V. J.; King, B. T. Nanoporous Two-Dimensional Polymer by Single-Crystal-to-Single-Crystal Photopolymerization. *Nat. Chem.* **2014**, *6*, 774–778.
- (13) Lafferentz, L.; Eberhardt, V.; Dri, C.; Africh, C.; Comelli, G.; Esch, F.; Hecht, S.; Grill, L. Controlling on-Surface Polymerization by Hierarchical and Substrate-Directed Growth. *Nat. Chem.* **2012**, *4*, 215–220.
- (14) Chandra, S.; Kandambeth, S.; Biswal, B. P.; Lukose, B.; Kunjir, S. M.; Chaudhary, M.; Babarao, R.; Heine, T.; Banerjee, R. Chemically Stable Multilayered Covalent Organic Nanosheets from Covalent Organic Frameworks via Mechanical Delamination. *J. Am. Chem. Soc.* **2013**, *135*, 17853–17861.
- (15) Berlanga, I.; Ruiz-González, M. L.; González-Calbet, J. M.; Fierro, J. L.; Mas-Ballesté, R.; Zamora, F. Delamination of Layered Covalent Organic Frameworks. *Small* **2011**, *7*, 1207–1211.
- (16) Bunck, D. N.; Dichtel, W. R. Bulk Synthesis of Exfoliated Two-Dimensional Polymers Using Hydrazone-Linked Covalent Organic Frameworks. *J. Am. Chem. Soc.* **2013**, *135*, 14952–14955.
- (17) Liu, W.; Luo, X.; Bao, Y.; Liu, Y. P.; Ning, G. H.; Abdelwahab, I.; Li, L.; Nai, C. T.; Hu, Z. G.; Zhao, D.; Liu, B.; Quek, S. Y.; Loh, K. P. A Two-Dimensional Conjugated Aromatic Polymer via C-C Coupling Reaction. *Nat. Chem.* **2017**, *9*, 563–570.
- (18) Kissel, P.; Erni, R.; Schweizer, W. B.; Rossell, M. D.; King, B. T.; Bauer, T.; Götzinger, S.; Schlüter, A. D.; Sakamoto, J. A Two-Dimensional Polymer Prepared by Organic Synthesis. *Nat. Chem.* **2012**, *4*, 287–291.
- (19) Bhola, R.; Payamyar, P.; Murray, D. J.; Kumar, B.; Teator, A. J.; Schmidt, M. U.; Hammer, S. M.; Saha, A.; Sakamoto, J.; Schlüter, A. D. A Two-Dimensional Polymer from the Anthracene Dimer and Triptycene Motifs. *J. Am. Chem. Soc.* **2013**, *135*, 14134–14141.
- (20) Liu, J. J.; Lyu, P. B.; Zhang, Y.; Nachtigall, P.; Xu, Y. X. New Layered Triazine Framework/Exfoliated 2D Polymer with Superior Sodium-Storage Properties. *Adv. Mater.* **2018**, *30*, 1705401–1705408.
- (21) Sahabudeen, H.; Qi, H.; Glatz, B. A.; Tranca, D.; Dong, R.; Hou, Y.; Zhang, T.; Kuttner, C.; Lehnert, T.; Seifert, G.; Kaiser, U.; Fery, A.; Zheng, Z.; Feng, X. L. Wafer-Sized Multifunctional Polyimine-Based Two-Dimensional Conjugated Polymers with High Mechanical Stiffness. *Nat. Commun.* **2016**, *7*, 13461–13468.
- (22) Matsuoka, R.; Sakamoto, R.; Hoshiko, K.; Sasaki, S.; Masunaga, H.; Nagashio, K.; Nishihara, H. Crystalline Graphdiyne Nanosheets Produced at a Gas/Liquid or Liquid/Liquid Interface. *J. Am. Chem. Soc.* **2017**, *139*, 3145–3152.
- (23) Murray, D. J.; Patterson, D. D.; Payamyar, P.; Bhola, R.; Song, W.; Lackering, M.; Schlüter, A. D.; King, B. T. Large Area Synthesis of a Nanoporous Two-Dimensional Polymer at the Air/Water Interface. *J. Am. Chem. Soc.* **2015**, *137*, 3450–3453.
- (24) Yan, X.; Liu, Z.; Zhang, Q.; Lopez, J.; Wang, H.; Wu, H. C.; Niu, S.; Yan, H.; Wang, S.; Lei, T.; Li, J.; Qi, D.; Huang, P.; Huang, J.; Zhang, Y.; Wang, Y.; Li, G.; Tok, J. B.; Chen, X.; Bao, Z. Quadruple H-Bonding Cross-Linked Supramolecular Polymeric Materials As Substrates for Stretchable, Antitearing, and Self-Healable Thin Film Electrodes. *J. Am. Chem. Soc.* **2018**, *140*, S280–S289.
- (25) Ferrari, A. C.; Meyer, J. C.; Scardaci, V.; Casiraghi, C.; Lazzeri, M.; Mauri, F.; Piscanec, S.; Jiang, D.; Novoselov, K. S.; Roth, S.; Geim, A. K. Raman Spectrum of Graphene and Graphene Layers. *Phys. Rev. Lett.* **2006**, *97*, 187401–187405.
- (26) Sakaushi, K.; Hosono, E.; Nickerl, G.; Gemming, T.; Zhou, H.; Kaskel, S.; Eckert, J. Aromatic Porous-Honeycomb Electrodes for a

Sodium-Organic Energy Storage Device. *Nat. Commun.* **2013**, *4*, 1485–1491.

(27) Feldblyum, J. I.; McCreery, C. H.; Andrews, S. C.; Kurosawa, T.; Santos, E. J.; Duong, V.; Fang, L.; Ayzner, A. L.; Bao, Z. Few-layer, Large-area, 2D Covalent Organic Framework Semiconductor Thin Films. *Chem. Commun.* **2015**, *51*, 13894–13897.

(28) Mahmood, J.; Lee, E. K.; Jung, M.; Shin, D.; Jeon, I. Y.; Jung, S. M.; Choi, H. J.; Seo, J. M.; Bae, S. Y.; Sohn, S. D.; Park, N.; Oh, J. H.; Shin, H. J.; Baek, J. B. Nitrogenated Holey Two-Dimensional Structures. *Nat. Commun.* **2015**, *6*, 6486–6492.

(29) Zhou, D.; Tan, X. Y.; Wu, H. M.; Tian, L. H.; Li, M. Synthesis of C-C Bonded Two-Dimensional Conjugated Covalent Organic Framework Films via Suzuki Polymerization on Liquid-Liquid Interface. *Angew. Chem., Int. Ed.* **2019**, *58*, 1376–1381.

(30) Wang, N.; Li, X.; Tu, Z.; Zhao, F.; He, J.; Guan, Z.; Huang, C.; Yi, Y.; Li, Y. Synthesis and Electronic Structure of Boron-Graphdiyne with an Sp-Hybridized Carbon Skeleton and Its Application in Sodium Storage. *Angew. Chem., Int. Ed.* **2018**, *57*, 3968–3973.

(31) MacDiarmid, A. G. Synthetic Metals: A Novel Role for Organic Polymers (Nobel Lecture). *Angew. Chem., Int. Ed.* **2001**, *40*, 2581–2590.

(32) Liu, W.; Ulaganathan, M.; Abdelwahab, I.; Luo, X.; Chen, Z. X.; Rong Tan, S. J.; Wang, X. W.; Liu, Y. P.; Geng, D. C.; Bao, Y.; Chen, J. Y.; Loh, K. P. Two-Dimensional Polymer Synthesized via Solid-State Polymerization for High-Performance Supercapacitors. *ACS Nano* **2018**, *12*, 852–860.



# **Attachment No. 5**

# Few-Layer Silicene Nanosheets with Superior Lithium-Storage Properties

Jingjing Liu, Yang Yang, Pengbo Lyu, Petr Nachtigall, and Yuxi Xu\*

Silicene, a 2D silicon allotrope with unique low-buckled structure, has attracted increasing attention in recent years due to its many superior properties. So far, epitaxial growth is one of the very limited ways to obtain high-quality silicene, which severely impedes the research and application of silicene. Therefore, large-scale synthesis of silicene is a great challenge, yet urgently desired. Herein, the first scalable preparation of free-standing high-quality silicene nanosheets via liquid oxidation and exfoliation of  $\text{CaSi}_2$  is reported. This new synthesis strategy successfully induces mild oxidation of the  $(\text{Si}^{2n})^{2n-}$  layers in  $\text{CaSi}_2$  into neutral  $\text{Si}^{2n}$  layers without damage of pristine silicene structure and promotes the exfoliation of stacked silicene layers. The obtained silicene sheets are dispersible and ultrathin ones with monolayer or few-layer thickness and exhibit excellent crystallinity. As a unique 2D layered silicon allotrope, the silicene nanosheets are further explored as new anodes for lithium-ion batteries and exhibit a nearly theoretical capacity of  $721 \text{ mAh g}^{-1}$  at  $0.1 \text{ A g}^{-1}$  and an extraordinary cycling stability with no capacity decay after 1800 cycles in contrast to previous most silicon anodes showing rapid capacity decay, thus holding great promise for energy storage and beyond.

The discovery of graphene marked the dawn of a new era of 2D materials.<sup>[1]</sup> As graphene exhibits outstanding properties and broad applications compared with bulk graphite, exploring other 2D materials has become a popular and significant research frontier.<sup>[2–5]</sup> Among various 2D materials, silicene is a dazzling one with increasing attention due to its outstanding electronic properties. Unlike graphene, Si atoms in a silicene sheet are not exactly in the same plane, but exhibit low buckled structure with  $\text{sp}^3$ -like hybridization.<sup>[6,7]</sup> Thus, it can be predicted that the spin–orbit coupling effect in silicene is stronger and more remarkable quantum spin Hall effect in silicene can be forecasted than that in graphene.<sup>[8]</sup> As its


superior properties, silicene will have wide applications in electronic device, chemical sensor, hydrogen storage, and electrode material for lithium-ion battery.<sup>[6]</sup> Therefore, the experimental synthesis of silicene is essential for the fundamental research and practical application of silicene.

To date, silicene sheets have been successfully synthesized by the molecular-beam-epitaxy deposition method on various substrates. Monolayer silicene sheets were first prepared on Ag (111) substrate.<sup>[9–13]</sup> Besides, Ir (111),  $\text{ZrB}_2$  (001), ZrC (111), and  $\text{MoS}_2$  surfaces were also demonstrated as the silicene growth substrate.<sup>[14–17]</sup> However, the synthesized silicene are limited to nanometers in size and it is difficult to release them from the substrate, which severely impedes the research and application of silicene. As an alternative approach,  $\text{CaSi}_2$  was synthesized by heating a mixture of high-purity Ca and Si via a solid-state reaction method to form a layered Zintl phase ionic compound (i.e.,  $\text{Ca}^{2+}(\text{Si}_2)^{2-}$ ),<sup>[18]</sup> which consists of alternately stacked Ca layers and silicene layers. Using  $\text{CaSi}_2$  as the precursor, a few silicon-derivative nanosheets have been fabricated. For example, ultrathin silicon sheets capped by abundant oxygen atoms were prepared via chemical exfoliation of Mg-doped  $\text{CaSi}_2$ .<sup>[19]</sup> By treating  $\text{CaSi}_2$  with ice-cold concentrated aqueous HCl, layered siloxene  $(\text{Si}_6\text{H}_3(\text{OH})_3)$  was obtained and could be further exfoliated into nanosheets.<sup>[20,21]</sup> Although there have been such advances about silicon-derivative sheets derived from  $\text{CaSi}_2$ , the pristine silicene structure was destroyed in all these studies. So far, large-scale synthesis of high-quality free-standing silicene is still a considerable challenge yet urgently desired to promote the fundamental research and practical application of silicene.

Herein, we report the first scalable synthesis of free-standing few-layer silicene nanosheets via liquid oxidation and exfoliation of  $\text{CaSi}_2$ . As  $\text{CaSi}_2$  is ionic with alternately stacked  $(\text{Ca}^{2+})_n$  and  $(\text{Si}_2)_n^{2n-}$  layers, the electrostatic interaction between these two types of layers is strong. Therefore, mild oxidation of the  $(\text{Si}_2)_n^{2n-}$  layers into neutral  $\text{Si}_{2n}$  layers without damage of pristine silicene structure is the key to successfully synthesize silicene sheets. Based on this idea, we tried to prepare silicene sheets through oxidation and exfoliation of  $\text{CaSi}_2$  at room temperature in the presence of  $\text{I}_2$  in acetonitrile ( $\text{CH}_3\text{CN}$ ) (Figure 1a). We utilized  $\text{I}_2$  as the oxidant due to its weak oxidizability at room temperature and we chose  $\text{CH}_3\text{CN}$  as the solvent

J. J. Liu, Dr. Y. Yang, Prof. Y. X. Xu  
Key Laboratory of Molecular Engineering of Polymers  
Department of Macromolecular Science  
Fudan University  
Shanghai 200433, China  
E-mail: xuyuxi@fudan.edu.cn

P. B. Lyu, Prof. P. Nachtigall  
Department of Physical and Macromolecular Chemistry  
Faculty of Science  
Charles University  
Hlavova 2030, 12843 Prague 2, Czech Republic

 The ORCID identification number(s) for the author(s) of this article can be found under <https://doi.org/10.1002/adma.201800838>.

DOI: 10.1002/adma.201800838

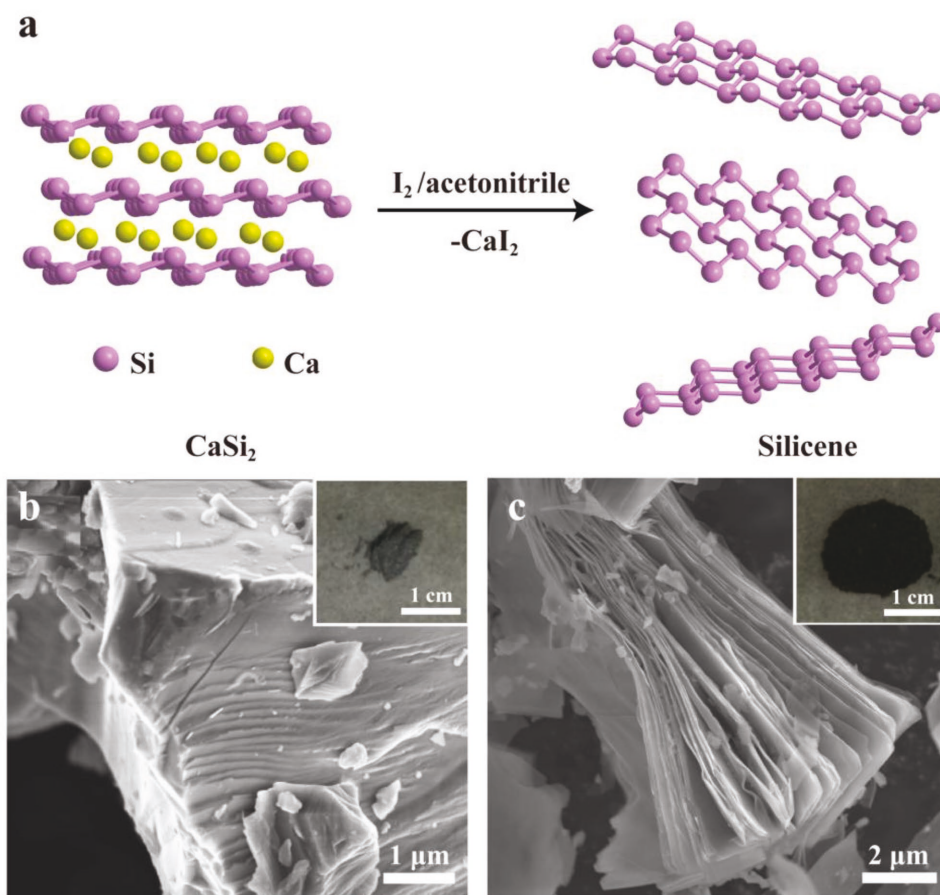


**Figure 1.** a) Schematic illustration for the synthesis of silicene from  $\text{CaSi}_2$  via liquid oxidation and exfoliation. b,c) SEM images of pristine bulk  $\text{CaSi}_2$  (b) and the as-reacted product (c) with the insets showing their photographs.

because both  $\text{I}_2$  and by-product  $\text{CaI}_2$  have good solubility in it. The reaction can be carried out on a large scale. Finally, after 3 weeks of reaction time, we successfully obtained dispersible crystalline silicene nanosheets with a monolayer thickness of 0.6 nm.

The as-reacted product looks very different from the starting material,  $\text{CaSi}_2$  (Figure 1b,c). The  $\text{CaSi}_2$  is a deep gray polycrystalline powder (Figure 1b, inset), while the silicene is a dark brown soil-like powder (Figure 1c, inset). Furthermore, the as-reacted product has a much larger specific volume than that of the pristine  $\text{CaSi}_2$ , which indicates that the product was adequately exfoliated. Scanning electron microscopy (SEM) observations show the slow and gradual delamination process of pristine bulk  $\text{CaSi}_2$  with compact layered stacking structure (Figure 1b and Figure S1a,b, Supporting Information) transformed to insufficiently exfoliated  $\text{CaSi}_2$  with the intermediately loose stacking structure after 3 d reaction (Figure S1c,d, Supporting Information), and then to the final adequately exfoliated silicene sheets derived from  $\text{CaSi}_2$  (Figure 1c and Figure S1e,f, Supporting Information), verifying the 3 weeks' reaction time is necessary for complete oxidation and exfoliation of  $\text{CaSi}_2$ . Through further ultrasonic exfoliation and centrifugation treatment, dispersible graphene-like silicene sheets were obtained. The transparent and smooth morphology in SEM and transmission electron microscopy (TEM) observations (Figure 2a,b

and Figure S2, Supporting Information) indicated the ultrathin silicene sheets have lateral size of several micrometers. Moreover, the silicene nanosheets showed good dispersability in *N*-methylpyrrolidone (NMP) (Figure 2b, inset), promising the potential processible applications of silicene.

High-resolution TEM (HRTEM) was further performed to investigate the interior structure of the silicene sheets (Figure 2c). The HRTEM image of the sample clearly depicts honeycomb hexagonal lattice of Si atoms and the  $d_{(100)}$  was measured as 0.34 nm. We predict three conceivable stacking possibilities to further understand the stacking arrangement of silicene layers by computational investigation: 1) eclipsed AA; 2) staggered AAB; and 3) staggered ABC arrangement,<sup>[22]</sup> in which all other stacking sequences can be constructed by the combination of the AA and ABC stacking (Figure S3, Supporting Information). The experimental HRTEM image (Figure 2c) gave the best fit for AA arrangement (inset in Figure 2c and Figure S3a, Supporting Information) and the model honeycomb hexagonal lattice was also measured as 0.34 nm. The selected area electron diffraction (SAED) pattern (Figure 2d) showed the hexagonal and single-crystal structure of the silicene sheets. The SAED data further prove that the crystallinity of the original Si framework in the pristine  $\text{CaSi}_2$  was well preserved upon  $\text{I}_2$  treatment. By indexing the SAED pattern, the interplanar spacing  $d_{(100)}$  is 3.39 Å, in consistent

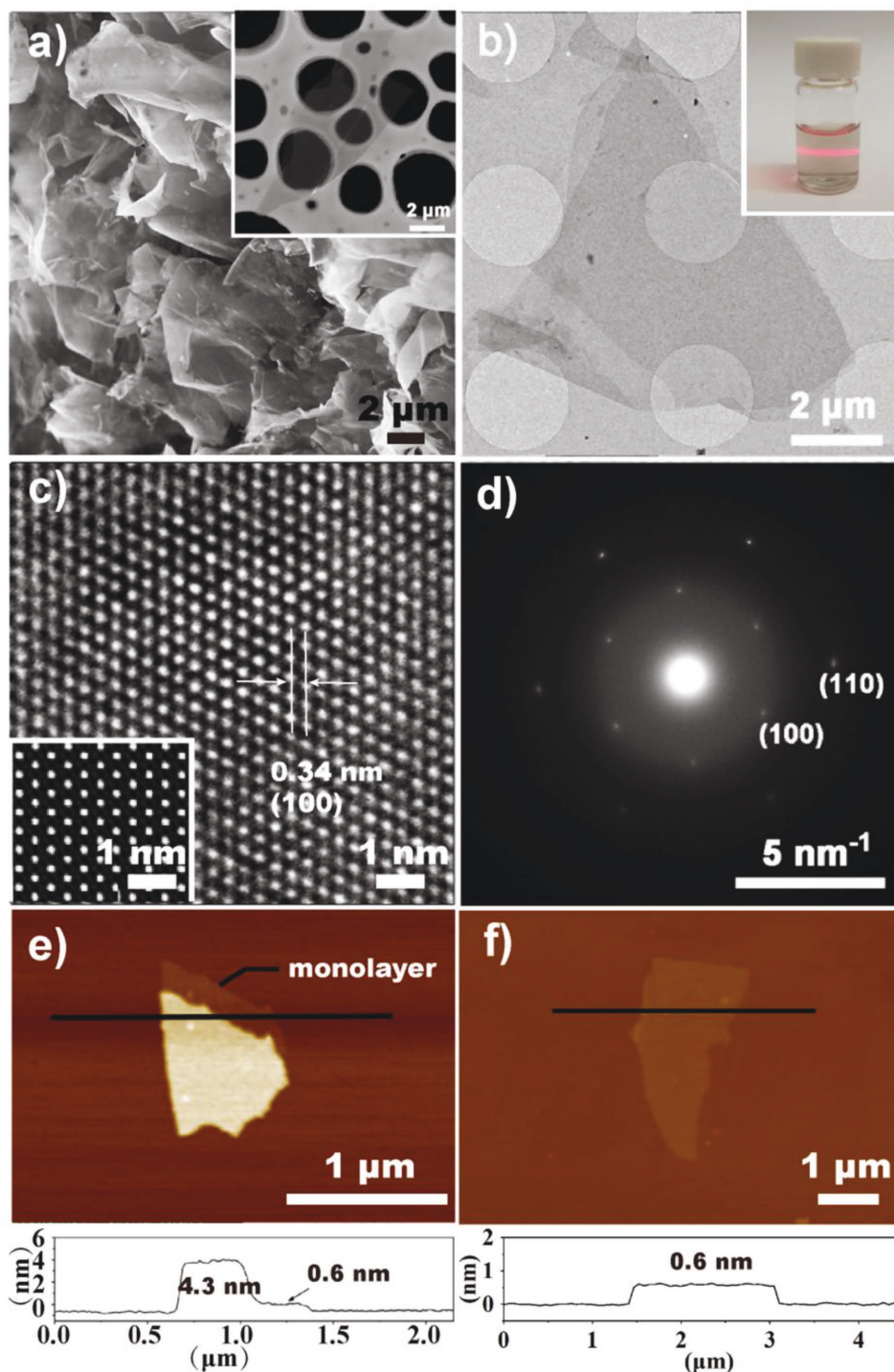


**Figure 2.** a) SEM images of silicene nanosheets and a single silicene sheet (inset), respectively. b) TEM image of silicene sheets with the inset showing the photograph of a stable dispersion of silicene in NMP ( $5 \mu\text{g ml}^{-1}$ ). c) HRTEM image of silicene matching with AA stacking model. d) SAED pattern of a silicene sheet. e, f) AFM images of silicene sheets with a monolayer thickness of 0.6 nm.

with HRTEM result and simulated AA stacking SAED pattern (Figure 2c and Figure S4, Supporting Information). The parameters of the simple hexagonal unit cell are calculated as  $a = b = 3.91 \text{ \AA}$ , which is very similar to the lattice constant ( $3.88 \text{ \AA}$ ) of silicene  $1 \times 1$  reported before.<sup>[6,23]</sup> Due to the excellent dispersion

of silicene in NMP, we can understand the exact thickness of the silicene sheets via atomic force microscopy (AFM) measurements by drop coating method. Interestingly, Figure 2e clearly showed a layered structure for silicene sheets with a monolayer thickness of 0.6 nm similar to graphene. We can also obtain

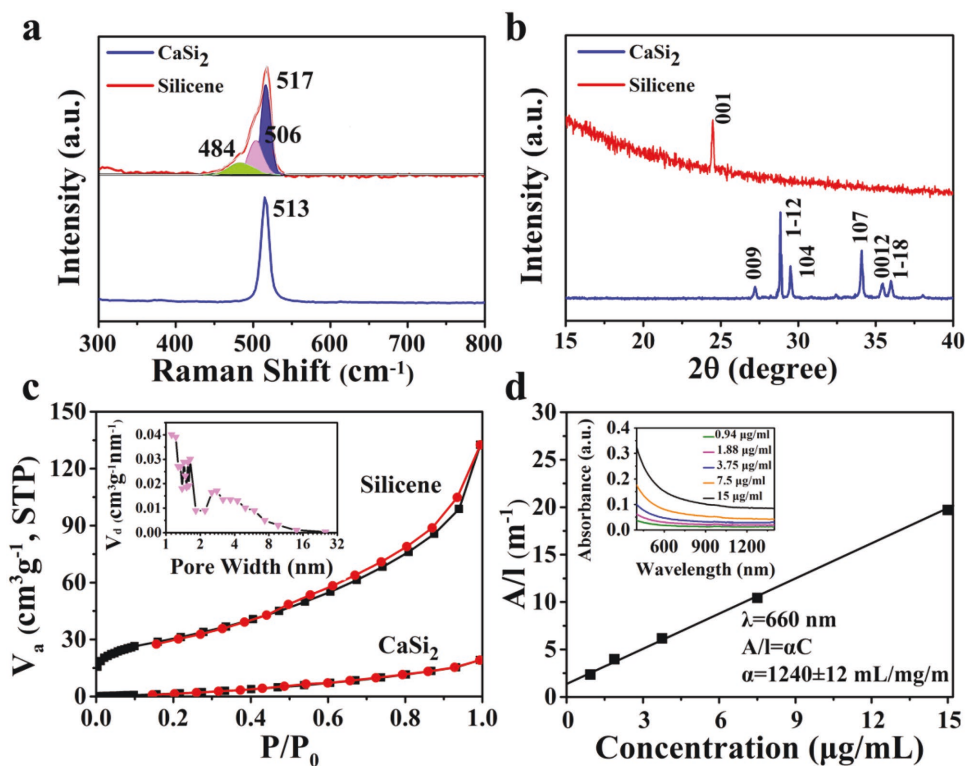


**Figure 3.** a) Raman spectra and b) PXRD patterns of the pristine  $\text{CaSi}_2$  and silicene nanosheets, respectively. c) Nitrogen sorption isotherms of silicene nanosheets and bulk  $\text{CaSi}_2$  with the inset showing the pore size distribution of silicene. d) Absorbance per unit path length ( $\lambda = 660$  nm) as a function of concentration of silicene in NMP with the inset showing the absorption spectra for silicene dispersed in NMP at different concentrations.

entire monolayer silicene sheets (Figure 2f), although most of silicene sheets in our product is few-layer with the typical thickness of 3–4 nm (Figure S5, Supporting Information). To the best of our knowledge, this is the first time for observation of layered structure of multilayer silicene and obtaining monolayer silicene by liquid-phase method.

As Raman spectroscopy is often used for the study of silicon materials, our silicene nanosheets was characterized by Raman spectroscopy (Figure 3a). The measured Raman spectrum is typical for silicene with buckled structure and can be decomposed (Figure 3a).<sup>[24]</sup> The peak at  $517\text{ cm}^{-1}$  is induced by the symmetric stretching ( $E_{2g}$ ) of Si–Si bonds in planar hexagonal  $\text{Si}_6$  rings and verifies the integrity of the silicene.<sup>[25]</sup> Moreover, the vertical buckling is responsible for the  $A_{1g}$  breathing mode, which generates the asymmetric shoulder in the range of  $450\text{--}500\text{ cm}^{-1}$  otherwise absent in  $\text{CaSi}_2$  and bulk silicon (Figure S6, Supporting Information).<sup>[24]</sup> In order to further investigate the crystal structure of the silicene, powder X-ray diffraction (PXRD) was performed on both the silicene and pristine  $\text{CaSi}_2$  (Figure 3b). The characteristic diffraction peaks of (009), (104), (107), (0012), and (1–18) in the pristine  $\text{CaSi}_2$  indicate 6R polycrystalline.<sup>[26]</sup> In the PXRD pattern of the silicene nanosheets, all characteristic diffraction peaks of the pristine  $\text{CaSi}_2$  disappeared and a new diffraction peak is found at  $2\theta = 24.5^\circ$  and attributed to the (001) stacking layer diffraction with a layer distance of  $3.62\text{ \AA}$  via Bragg's formula, which was significantly different from bulk silicon and amorphous silicon oxide (Figure S7, Supporting Information). X-ray photoelectron spectroscopy (XPS) characterization could give a detailed

message of Si 2p core level. As shown in Figure S8 (Supporting Information), there are two groups of binding components, labeled as Si1 and Si2, respectively. The Si1 and Si2 peaks at a binding energy around 98.5 and 99.4 eV were related to  $\text{Si}^0 2p_{3/2}$  and  $\text{Si}^0 2p_{1/2}$  in silicene, consistent with the previous report.<sup>[27]</sup> The Brunauer–Emmett–Teller (BET) surface area of the silicene nanosheets was evaluated to be  $102\text{ m}^2\text{ g}^{-1}$ , much higher than that of the pristine  $\text{CaSi}_2$  ( $4\text{ m}^2\text{ g}^{-1}$ ), indicating the efficient exfoliation and the ultrathin thickness of the silicene sheets. Moreover, the pore size distribution of the porous-like stacked silicene (Figure 2a) shows the pore width was concentrated on micro- and mesopore scale (inset in Figure 3c). The dispersion of our silicene nanosheets creates an opportunity to characterize the absorption spectra and the absorption coefficient of silicene in NMP via UV–vis–IR absorption spectroscopy. As shown in the inset of Figure 3d, the absorption spectra is featureless with a very broad absorption range from 400 to 1400 nm, which is similar to graphene and is very different from silicon wafer (Figure S9, Supporting Information). This is due to that silicene has a zero bandgap theoretically like graphene while the silicon has a bandgap of  $\approx 1.2\text{ eV}$ . The accurate relationship between silicene concentration,  $C$ , and absorbance per unit path length,  $A/l$ , was obtained. A straight line fit gave an absorption coefficient  $\alpha = 1240\text{ mL mg}^{-1}\text{ m}^{-1}$  at 660 nm, which is close to that of graphene.<sup>[28]</sup>

As a unique 2D layered material and potentially promising anode material for the next generation lithium ion batteries,<sup>[29]</sup> we first use density-functional theory (DFT) computational method to evaluate the lithium ion storage capability of

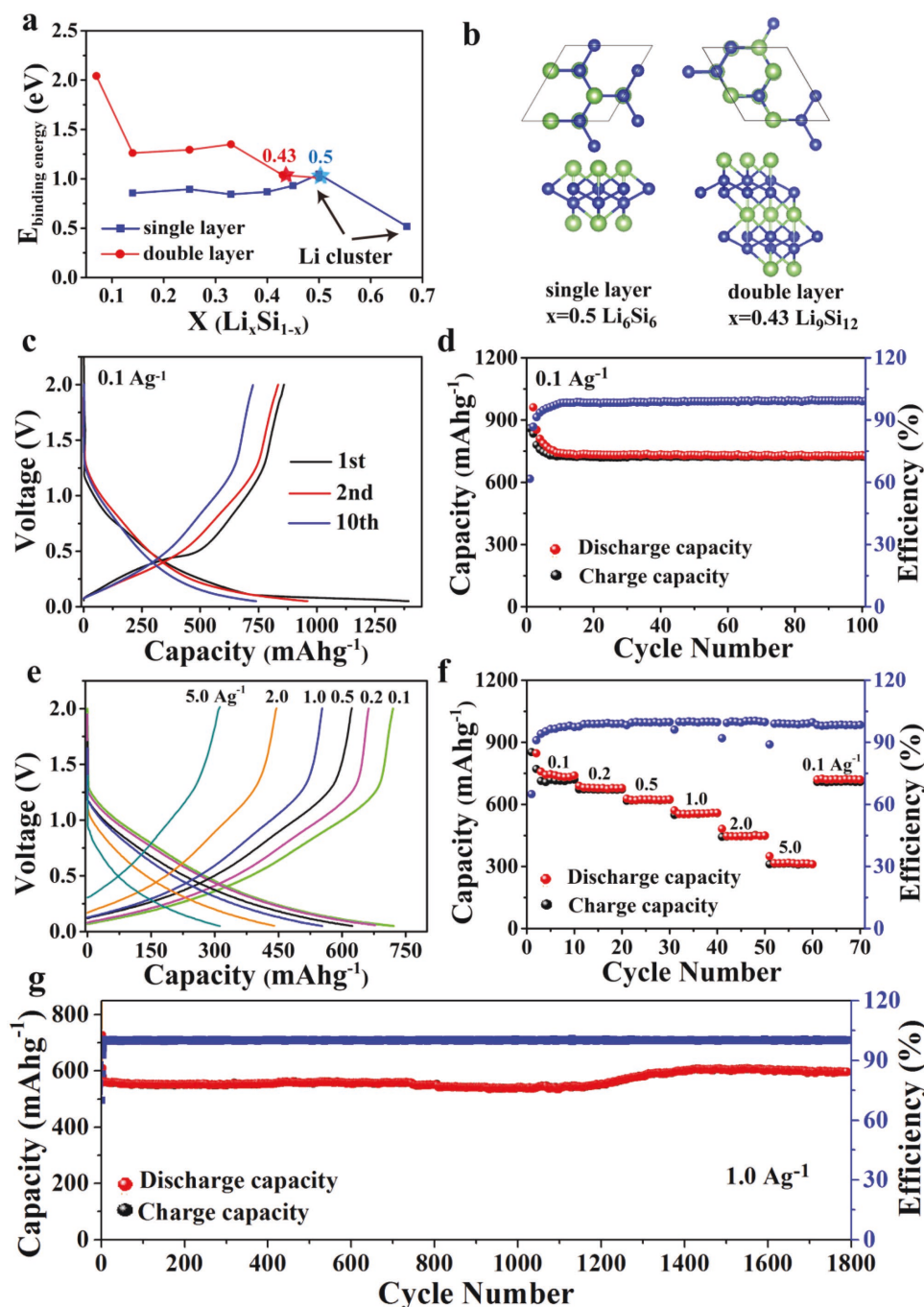


**Figure 4.** a) Binding energy  $E_b$  of Li as a function of Li content  $x$ , for single- and double-layer silicene with the red and blue stars indicating the content  $x$  where Li atoms has already clustered with each other. b) Atomic structures corresponding to the maximum lithiated single-layer and double-layer silicene. c) The 1st, 2nd, and 10th charge–discharge curves of silicene nanosheets anode at a current density of  $0.1 \text{ A g}^{-1}$  within a voltage range from 0.05 to 2.0 V versus  $\text{Li}^+/\text{Li}$ . d) Cycling performance at  $0.1 \text{ A g}^{-1}$ . e) Galvanostatic charge–discharge profiles and f) rate capacities of silicene nanosheets at different current densities. g) Cycling performance of silicene up to 1800 cycles at  $1.0 \text{ A g}^{-1}$ .

single-layer and few-layer (double-layer) silicene (Figure S10, Supporting Information). The binding energy as a function of Li content  $x$  ( $\text{Li}_x\text{Si}_{1-x}$ ) for single- and double-layer is shown in Figure 4a and the corresponding structure evolutions of lithiated single- and double-layer are shown in Figures S11 and S12 (Supporting Information). Through the detailed study of different

Li atoms adsorption on the silicene sites without formation of Li cluster (see the Supporting Information), the maximum Li adsorption for single-layer and double-layer silicene were at the coverage of  $x = 0.5$  and  $x = 0.43$ , respectively (Figure 4b), which correspond to the capacity of  $954$  and  $715 \text{ mAh g}^{-1}$  for single-layer and double-layer silicene, respectively, in accordance

with the previous calculation result.<sup>[23]</sup> We thus experimentally studied the silicene nanosheets as new anode material for Li ion batteries by combination with metallic Li counter electrodes to fabricate a half-cell to evaluate its electrochemical performance. The electrochemical performance of silicene was first evaluated by cyclic voltammetry. Due to the decomposition of electrolyte and the formation of a solid electrolyte interface on the surface of active materials, the first negative scan showed some irreversible reactions (Figure S13, Supporting Information). The 1st, 2nd, and 10th charge–discharge curves of silicene anode at a current density of 0.1 A g<sup>-1</sup> are shown in Figure 4c. The irreversible capacity in the first cycle resulted in an initial coulombic efficiency of 61.6%. The capacity of the silicene anode quickly became stable after several charge/discharge cycles and showed no obvious decay over 100 cycles at 0.1 A g<sup>-1</sup>, demonstrating superior cycling stability of the silicene nanosheets (Figure 4d and Figure S14, Supporting Information). Interestingly, the silicene anode achieved a high reversible capacity of 721 mAh g<sup>-1</sup> after 100 cycles (Figure 4d), which is nearly the theoretical capacity value of double-layer silicene, suggesting a highly efficient utilization of active sites in the silicene nanosheets. The rate performance of silicene nanosheets was further investigated by performing galvanostatic charge–discharge tests at various current densities (Figure 4e). Even at a very high current density of 5.0 A g<sup>-1</sup>, the silicene nanosheets can still deliver a high reversible capacity of 312 mAh g<sup>-1</sup> (Figure 4f) with a 43% capacity retention from 0.1 to 5.0 A g<sup>-1</sup>, demonstrating an superior rate capability. Moreover, the reversible capacity of silicene anode can recover to 710 mAh g<sup>-1</sup> when current density returned to 0.1 A g<sup>-1</sup>, indicating excellent structural stability of silicene nanosheets. The long-term cycling performance, which is an intractable problem for silicon-based anodes, was also studied. As shown in Figure 4g, the silicene nanosheets demonstrated a remarkable stability with the capacity retention surprisingly increased to 107% (553 vs 596 mAh g<sup>-1</sup>) after 1800 charge/discharge cycles at 1.0 A g<sup>-1</sup> (Figure 4g). This unexpected phenomenon could be ascribed to the further exfoliation of few-layer silicene to single-layer silicene as the continual insertion/desorption of lithium ions, leading to more exposure of silicene adsorption sites to lithium ions. The extraordinary cycling stability of silicene nanosheets is probably attributed to its unique 2D layered structure similar to graphite/few-layer graphene, which is in contrast to previous most silicon anodes showing significant capacity decay during cycling due to the huge volume expansion and subsequent pulverization.<sup>[30,31]</sup> We have further performed XRD characterization of (001) peak of silicene after discharging the electrode to 0.05 V and recharging it to 2.0 V to monitor the structure changes during cycling (Figure S15, Supporting Information). We found at the maximum Li adsorption stage (after discharging to 0.05 V), the peak at  $2\theta = 24.5^\circ$  totally transferred to the peak at  $2\theta = 22.7^\circ$ , which indicates that the interlayer distance of 3.62 Å in original silicene increased to 3.91 Å in lithium-ion adsorbed silicene and it could recover to 3.62 Å after desorbing the lithium ions, showing a different adsorption/desorption mechanism of silicene anode from the alloy mechanism of silicon in Li-ion batteries.<sup>[32]</sup> To better understand the morphological changes of silicene nanosheets after cycling, the silicene electrodes were disassembled and

characterized by TEM. As shown in Figure S16 (Supporting Information), the silicene samples almost preserved their original sheet structures after 1800 cycles, further confirming its superior cycling stability.

In summary, we have demonstrated large-scale solution synthesis of ultrathin silicene nanosheets for the first time via liquid oxidation and exfoliation of CaSi<sub>2</sub>. The pristine CaSi<sub>2</sub> could be slightly oxidized without damage of original Si framework and exfoliated efficiently into silicene sheets in the presence of I<sub>2</sub> in CH<sub>3</sub>CN. The obtained silicene sheets are ultrathin ones with monolayer or few-layer thickness and exhibit excellent crystallinity. When explored as new anodes for lithium-ion batteries, the silicene nanosheets exhibit almost the theoretical capacities of double-layer silicene and an ultrastable cycling performance as well as a unique Li adsorption/desorption mechanism, thus holding great promise in electrochemical energy storage. As silicene is a distinctive 2D material with many intriguing properties and wide applications, our large-scale preparation strategy will be a valuable solution to meet the needs of both fundamental research and practical application of silicene in the future.

## Experimental Section

**Synthesis of the Silicene Nanosheets:** In an Ar-filled glovebox, CaSi<sub>2</sub> (480 mg, 5 mmol), and I<sub>2</sub> (1.27 g, 5 mmol) were added into a 200 mL flask. 150 mL of CH<sub>3</sub>CN was then added into the flask. The flask was sealed with a PTFE screw plug. The resulting mixture was stirred at room temperature for 3 weeks. After this long time, the reaction mixture was filtered through a 0.22 μm membrane. The filter cake was redispersed in 100 mL of CH<sub>3</sub>CN and filtered again. This step was repeated for 5 times to remove the by-product CaI<sub>2</sub> and additional I<sub>2</sub> completely. The finally obtained filter cake was seen as the as-reacted product and used for SEM and optical characterization. Next, the filter cake was redispersed in 100 mL NMP for 2 h ultrasonic treatment (200 W) followed with 1000 r min<sup>-1</sup> centrifugation for 30 min to further exfoliate the Mxene-like stacked silicene. SEM, TEM, and AFM images of single silicene nanosheets were characterized by the collected supernatant. All experimental steps were carried out under Ar atmosphere.

**Electrochemical Characterization:** The silicene nanosheets-based lithium-ion batteries were fabricated in Ar-filled glovebox. First, a uniform slurry of silicene nanosheets, Super P carbon black and polyvinylidene fluoride were mixed in NMP at the ratio of 7:2:1. The slurry was coated on copper foil and dried at 60 °C in vacuum oven overnight. The coated copper foil was cut into 12 mm in diameter discs. The areal mass loading of silicene in the electrode was ≈1.1 mg cm<sup>-2</sup>, which is typical in the most reported studies. CR2016 coin cells were assembled in glove box by using lithium metal as the reference electrode and counter electrode. LiPF<sub>6</sub> (1 mol L<sup>-1</sup>) in 1:1 (v/v) mixture of ethylene carbonate and dimethyl carbonate with 10 wt% fluoroethylene carbonate was used as electrolyte. Electrochemical experiments were performed using battery cyler (LAND-CT2001 A) at the voltage range of 0.05–2.0 V. The capacity was calculated based on the mass of active materials.

**Instrumentation and Characterization:** As silicene is easy to degrade in air, the silicene sample was preserved in Ar atmosphere before all characterizations. TEM images were obtained on a Tecnai G2 F20 S-Twin (acceleration voltage: 200 kV). The silicene sample was dispersed in NMP via sonication and then dropped onto carbon mesh grids and dried under Ar protection condition. The carbon grids were stored in an Ar-filled sealed vial before loading into the TEM to minimize exposure to air. SEM images were obtained on a Zeiss Ultra 55. For SEM observations, the carbon mesh grids with the silicene were obtained and stored the same as those for TEM. CaSi<sub>2</sub> was also dispersed in NMP and then dropped onto carbon mesh grids and dried without special treatment. The

carbon grids were attached to an aluminum sample holder without gold coating and then directly placed into the instrument as soon as possible to minimize exposure to air. AFM images were obtained on a Bruker Multimode 8. For AFM measurements, the dispersion of the sample was dropped onto freshly cleaved mica and dried for measurement. Raman spectrum was obtained on a HORIBA JobinYvon XploRA. The sample was measured as soon as possible to minimize exposure to air. XPS measurements were performed with S4EXPLORER with Al K $\alpha$  radiation as X-ray source. PXRD patterns were obtained on a PANalytical X'pert PRO. Samples were also measured as soon as possible to minimize exposure to air. The BET surface area of the silicene nanosheets and pristine CaSi $_2$  was performed on JWGB-BK with micropore option. N $_2$  sorption analyses were performed using a liquid N $_2$  bath. Pore size distribution was calculated by nonlocal DFT modeling based on N $_2$  adsorption data. UV-vis absorption spectroscopy was conducted on Lambda 35 and the silicene sheets were dispersed in NMP.

## Supporting Information

Supporting Information is available from the Wiley Online Library or from the author.

## Acknowledgements

J.J.L. and Y.Y. contributed equally to this work. The authors acknowledge the support by the National Natural Science Foundation of China (51673042), the Young Elite Scientist Sponsorship Program by CAST (2017QNRC001), and the Program for Professor of Special Appointment (Eastern Scholar) at Shanghai Institutions of Higher Learning (TP2015002).

## Conflict of Interest

The authors declare no conflict of interest.

## Keywords

few-layer structure, lithium storage, silicene nanosheets, solution synthesis, ultrastable anodes

Received: February 6, 2018

Revised: March 17, 2018

Published online: May 7, 2018

- [1] K. S. Novoselov, A. K. Geim, S. V. Morozov, D. Jiang, Y. Zhang, S. V. Dubonos, I. V. Grigorieva, A. A. Firsov, *Science* **2004**, 306, 666.
- [2] P. Miro, M. Audiffred, T. Heine, *Chem. Soc. Rev.* **2014**, 43, 6537.
- [3] M. Xu, T. Liang, M. Shi, H. Chen, *Chem. Rev.* **2013**, 113, 3766.
- [4] S. Balendhran, S. Walia, H. Nili, S. Sriram, M. Bhaskaran, *Small* **2015**, 11, 640.
- [5] M. Pumera, Z. Sofer, *Adv. Mater.* **2017**, 1605299.
- [6] J. Zhao, H. Liu, Z. Yu, R. Q. He, S. Zhou, Y. Wang, C. C. Liu, H. Zhong, N. Han, J. Lu, Y. Yao, K. Wu, *Prog. Mater. Sci.* **2016**, 83, 24.
- [7] C. C. Liu, W. Feng, Y. Yao, *Phys. Rev. Lett.* **2011**, 107, 076802.
- [8] J. C. Zhuang, X. Xu, Y. Du, K. H. Wu, L. Chen, W. C. Hao, J. O. Wang, W. K. Yeoh, X. L. Wang, S. X. Dou, *Phys. Rev. B* **2015**, 91, 161409.
- [9] Y. Du, J. C. Zhuang, J. O. Wang, Z. Li, H. S. Liu, J. J. Zhao, X. Xu, *Sci. Adv.* **2015**, 2, e1600067.
- [10] P. Vogt, P. D. Padova, C. Quaresima, J. Avila, E. Frantzeskakis, M. C. Asensio, A. Resta, B. Ealet, G. L. Lay, *Phys. Rev. Lett.* **2012**, 108, 105551.
- [11] B. Feng, Z. Ding, S. Meng, Y. Yao, X. He, P. Cheng, L. Chen, K. Wu, *Nano Lett.* **2012**, 12, 3507.
- [12] D. Chiappe, C. Grazianetti, G. Tallarida, M. Fanciulli, A. Molle, *Adv. Mater.* **2012**, 24, 5088.
- [13] H. Jamgotchian, Y. Colignon, N. Hamzaoui, B. Ealet, J. Y. Hoarau, B. Aufray, J. P. Biberian, *J. Phys.: Condens. Matter* **2012**, 24, 172001.
- [14] L. Meng, Y. Wang, L. Zhang, S. Du, R. Wu, L. Li, Y. Zhang, G. Li, H. Zhou, W. Hofer, H. J. Gao, *Nano Lett.* **2013**, 13, 685.
- [15] A. Fleurence, R. Friedlein, T. Ozaki, H. Kawai, Y. Wang, Y. Yamada-Takamura, *Phys. Rev. Lett.* **2012**, 108, 245501.
- [16] T. Aizawa, S. Suehara, S. Otani, *J. Phys. Chem. C* **2014**, 118, 23049.
- [17] D. Chiappe, E. Scalise, E. Cinquanta, M. Houssa, A. Molle, *Adv. Mater.* **2014**, 26, 2096.
- [18] E. Noguchi, K. Sugawara, R. Yaokawa, T. Hitosugi, H. Nakano, T. Takahashi, *Adv. Mater.* **2015**, 27, 856.
- [19] H. Nakano, T. Mitsuoka, M. Harada, K. Horibuchi, H. Nozaki, N. Takahashi, T. Nonaka, Y. Seno, H. Nakamura, *Angew. Chem., Int. Ed.* **2006**, 45, 6303.
- [20] H. Nakano, M. Ishii, H. Nakamura, *Chem. Commun.* **2005**, 2945.
- [21] S. Yamanaka, H. Matsu-ura, M. Ishikawa, *Mater. Res. Bull.* **1996**, 31, 307.
- [22] Y. Liu, H. B. Shu, P. Liang, D. Cao, X. S. Chen, W. Lu, *J. Appl. Phys.* **2013**, 114, 094308.
- [23] G. A. Tritsarlis, E. Kaxiras, S. Meng, E. Wang, *Nano Lett.* **2013**, 13, 2258.
- [24] L. Tao, E. Cinquanta, D. Chiappe, C. Grazianetti, M. Fanciulli, M. Dubey, A. Molle, D. Akinwande, *Nat. Nanotechnol.* **2015**, 10, 227.
- [25] E. Cinquanta, E. Scalise, D. Chiappe, C. Grazianetti, M. Fanciulli, A. Molle, *J. Phys. Chem. C* **2013**, 117, 16719.
- [26] S. M. Castillo, Z. Tang, A. P. Litvinchuk, A. M. Guloy, *Inorg. Chem.* **2016**, 55, 10203.
- [27] X. Xu, J. C. Zhuang, Y. Du, H. F. Feng, N. A. Zhang, C. Liu, T. Lei, J. Wang, S. Dou, *Sci. Rep.* **2014**, 4, 7543.
- [28] Y. Hernandez, V. Nicolosi, M. Lotya, F. M. Blighe, Z. Sun, S. De, I. T. McGovern, B. Holland, A. C. Ferrari, J. N. Coleman, *Nat. Nanotechnol.* **2008**, 3, 563.
- [29] J. C. Zhuang, X. Xu, G. Peleckis, W. C. Hao, S. X. Dou, Y. Du, *Adv. Mater.* **2017**, 29, 1606716.
- [30] K. Q. Xu, L. B. Ben, H. Li, X. J. Huang, *Nano Res.* **2015**, 8, 2654.
- [31] C. K. Chan, H. Peng, G. Liu, K. McClwrath, X. F. Zhang, R. Huggins, Y. Cui, *Nat. Nanotechnol.* **2008**, 3, 31.
- [32] J. Li, J. R. Dahn, *J. Electrochem. Soc.* **2007**, 154, A156.



# **Attachment No. 6**

# A Pseudolayered MoS<sub>2</sub> as Li-Ion Intercalation Host with Enhanced Rate Capability and Durability

Shan Gong, Guangyu Zhao,\* Pengbo Lyu, and Kening Sun\*

As a popular strategy, interlayer expansion significantly improves the Li-ion diffusion kinetics in the MoS<sub>2</sub> host, while the large interlayer spacing weakens the van der Waals force between MoS<sub>2</sub> monolayers, thus harming its structural stability. Here, an oxygen-incorporated MoS<sub>2</sub> (O-MoS<sub>2</sub>)/graphene composite as a self-supported intercalation host of Li-ion is prepared. The composite delivers a specific capacity of 80 mAh g<sup>-1</sup> in only 36 s at a mass loading of 1 mg cm<sup>-2</sup>, and it can be cycled 3000 times (over 91% capacity retention) with a 5 mg cm<sup>-2</sup> loading at 2 A g<sup>-1</sup>. The O-MoS<sub>2</sub> exhibits a dominant 1T phase with an expanded layer spacing of 10.15 Å, leading to better Li-ion intercalation kinetics compared with pristine MoS<sub>2</sub>. Furthermore, ex situ X-ray diffraction tests indicate that O-MoS<sub>2</sub> sustains a stable structure in cycling compared with the gradual collapse of pristine MoS<sub>2</sub>, which suffers from excessive lattice breathing. Density functional theory calculations suggest that the MoO<sub>x</sub>(OH)<sub>y</sub> pillars in O-MoS<sub>2</sub> interlayers not only expand the layer spacing, but also tense the MoS<sub>2</sub> layers to avoid exfoliation in cycling. Therefore, the O-MoS<sub>2</sub> shows a pseudolayered structure, leading to remarkable durability besides the outstanding rate capability as a Li-ion intercalation host.

## 1. Introduction

As one member of the 2D layered transition-metal dichalcogenides (TMDs), MoS<sub>2</sub> has a semiconductor phase crystal structure (2H-MoS<sub>2</sub>) with an interlayer spacing of ≈6.15 Å.<sup>[1,2]</sup> The large van der Waals gaps can offer typical tunnels for fast 2D Li-ion diffusion, and thus enabling MoS<sub>2</sub> to be a promising alternative host material for Li-ion batteries (LIBs).<sup>[3–6]</sup> Furthermore, owing to the weak van der Waals interactions between adjacent MoS<sub>2</sub> monolayers, interlayer expansion can be realized

by incorporating foreign species into the interlayer gaps,<sup>[7,8]</sup> such as alkali metal ions,<sup>[9–13]</sup> oxygen,<sup>[14–19]</sup> NH<sub>3</sub>/NH<sub>4</sub><sup>+</sup>,<sup>[20–22]</sup> carbon materials,<sup>[23–26]</sup> and organic molecules.<sup>[27–29]</sup> Several studies have revealed that the MoS<sub>2</sub> with expanded interlayer spacing exhibits enhanced electrochemical performances as the anode material of LIBs<sup>[30–35]</sup> and other alkali metal-ion batteries.<sup>[26,36–41]</sup> In addition, the foreign species may influence the electronic structure of the MoS<sub>2</sub>,<sup>[42–44]</sup> thus, the MoS<sub>2</sub> incorporated with foreign species always exhibits the properties of a metallic phase.<sup>[9,20,26,29]</sup> another typical crystal structure of MoS<sub>2</sub> (1T-MoS<sub>2</sub>), which exhibits better performance than its semiconducting counterpart in LIBs.<sup>[45–47]</sup> However, most of the abovementioned studies in LIBs focus on the high capacity of MoS<sub>2</sub> by utilizing the conversion reaction (0–3 V vs Li/Li<sup>+</sup>), in which Li<sub>2</sub>S/sulfur becomes the sole redox couple after the first cycle and the main contributor to


the reversible capacity.<sup>[48–50]</sup> Thus, the parent crystalline atomic structure is completely destroyed and cannot be restored.<sup>[48–50]</sup> The irreversible process also makes the tuning of MoS<sub>2</sub> interlayer spacing meaningless to enhance its electrochemical performance.

Very recently, research on the extremely fast and highly reversible intercalation reaction of alkali metal ions in MoS<sub>2</sub> was reported.<sup>[29,51–57]</sup> Dunn and co-workers investigated the electrochemical performance of 1T-MoS<sub>2</sub> as an intercalation host for LIBs in the potential range of 1–3 V versus Li/Li<sup>+</sup> and highlighted its excellent rate capability based on the feature of Li-ion intercalation pseudocapacitance.<sup>[51,52]</sup> However, the current research on the intercalation reaction in expanded 1T-MoS<sub>2</sub> is insufficient. First, the common methods for expanding 1T-MoS<sub>2</sub> using chemical exfoliation are complicated and dangerous.<sup>[43,58–60]</sup> In addition, it should be noted that the roles of the foreign species incorporated into the interlayer gaps of MoS<sub>2</sub> need to be understood when the MoS<sub>2</sub> is applied to LIBs.<sup>[55,61,62]</sup> To date, in-depth and comprehensive investigations on the foreign species and their roles in the interlayer expansion and structure stability of MoS<sub>2</sub> are rare. Moreover, the structural stability of MoS<sub>2</sub> with expanded interlayer spacing during Li-ion intercalation/deintercalation has been barely studied.<sup>[63]</sup>

In the present study, a 3D porous graphene aerogel decorated with oxygen-incorporated MoS<sub>2</sub> (O-MoS<sub>2</sub>) clusters was

Dr. S. Gong  
School of Chemistry and Chemical Engineering  
Harbin Institute of Technology  
Harbin 150001, P. R. China  
Prof. G. Zhao, Prof. K. Sun  
Academy of Fundamental and Interdisciplinary Sciences  
Harbin Institute of Technology  
Harbin 150001, P. R. China  
E-mail: zhaogy810525@gmail.com, zhaogy@hit.edu.cn;  
keningsunhit@126.com

Dr. P. Lyu  
Department of Physical and Macromolecular Chemistry  
Charles University  
Hlavova 2030, Prague 2, Prague 12843, Czech Republic

 The ORCID identification number(s) for the author(s) of this article can be found under <https://doi.org/10.1002/smll.201803344>.

DOI: 10.1002/smll.201803344

prepared. The O-MoS<sub>2</sub> shows an inherent dominant 1T phase with an expanded layer spacing of around 10.15 Å. The composite was used directly as self-supported electrode for Li-ion intercalation host and showed outstanding rate capability and durability. Furthermore, comprehensive investigation on the Li-ion intercalation performance and its relationship with the structure of O-MoS<sub>2</sub> was undertaken. During the battery cycling, the structural evolution of O-MoS<sub>2</sub> and pristine MoS<sub>2</sub> were studied in detail by ex situ X-ray diffraction (XRD). The results indicate that O-MoS<sub>2</sub> possesses a more stable structure than pristine MoS<sub>2</sub>. Electrochemical impedance spectroscopy (EIS) analysis shows that the larger interlayer spacing leads to higher Li-ion diffusion coefficients of O-MoS<sub>2</sub> than pristine MoS<sub>2</sub>. In addition, density functional theory (DFT) calculations reveal that intercalating MoO<sub>x</sub>(OH)<sub>y</sub> species into MoS<sub>2</sub> interlayers is reasonable to explain the oxygen incorporation. The MoO<sub>x</sub>(OH)<sub>y</sub> pillars in MoS<sub>2</sub> interlayers lead to the expansion and steadiness of the layer structure, resulting in a pseudolayered structure of O-MoS<sub>2</sub>. The most evident distinction of pseudolayered structural O-MoS<sub>2</sub> from pristine MoS<sub>2</sub> is the incorporated MoO<sub>x</sub>(OH)<sub>y</sub> pillars in the interlayers; moreover, the pillars play a bifunctional role of expansion and tension. This interesting structure offers us an opportunity to realize an ideal 2D host material for metal ion intercalation that possesses both enlarged and firm ion transport tunnels.

## 2. Results and Discussion

The 3D porous graphene aerogels decorated with O-MoS<sub>2</sub> clusters were prepared by a hydrothermal process at 180 °C (O-MoS<sub>2</sub>/GAs-180). This facile and accessible method for preparing ultrathin MoS<sub>2</sub> with expanded interlayer spacing was reported in the literatures,<sup>[14–16]</sup> in which residual Mo–O bonds inherited from the molybdate precursors and lower hydrothermal temperatures (<200 °C) are crucial to the spacing expansion. For comparison, 3D porous graphene aerogels decorated with pristine MoS<sub>2</sub> clusters were prepared at 200 °C (MoS<sub>2</sub>/GAs-200). The schematic diagrams of the synthesis process are illustrated in Figure 1. The self-supported electrodes for LIB tests were prepared by cutting the aerogels and mechanically compressing into thin slices. In addition, O-MoS<sub>2</sub> without graphene oxides (O-MoS<sub>2</sub>-180) and blank graphene

aerogels (GAs-180) were synthesized at 180 °C. Pristine MoS<sub>2</sub> without graphene oxides (MoS<sub>2</sub>-200) was also synthesized at 200 °C (experimental details in the Supporting Information).

The XRD patterns of O-MoS<sub>2</sub>/GAs-180 and MoS<sub>2</sub>/GAs-200 are shown in Figure 2a. The pattern of MoS<sub>2</sub>/GAs-200 can be assigned to 2H-MoS<sub>2</sub> (JCPDS card No. 037–1492) except the (002) peak slightly shifting left to 14.1°. This implies that the interlayer spacing is expanded to 6.27 Å from 6.15 Å of pristine MoS<sub>2</sub>, which is in agreement with the previous reports on nanosized MoS<sub>2</sub>.<sup>[31,64,65]</sup> In the pattern of O-MoS<sub>2</sub>/GAs-180, two new peaks center at 8.7° (d = 10.15 Å) and 17.5° (d = 5.06 Å) with a diploid relation are observed, indicating the formation of a new lamellar structure with enlarged interlayer spacing. This phenomenon is consistent with the reported results of O-MoS<sub>2</sub>,<sup>[14–19]</sup> in which Mo–O bonds are preserved in the inadequate sulphur reaction at 180 °C. While pristine MoS<sub>2</sub> is synthesized at the proper temperature (200 °C). The appearance of MoO<sub>2</sub> of 500 °C sintered O-MoS<sub>2</sub>-180 in Ar further verifies the oxygen incorporation (Figure S1, Supporting Information) because the incorporated O element should be the only source of MoO<sub>2</sub>. Thermogravimetric analysis shows that the mass fraction of MoS<sub>2</sub> in O-MoS<sub>2</sub>/GAs-180 and MoS<sub>2</sub>/GAs-200 are 74.9% and 79.2%, respectively (Figure S2, Supporting Information). In addition, the (002) peaks of GAs at 26° in the two samples rise sharply after compressing the aerogels into slices due to the stack of the graphene layers (Figure S3, Supporting Information).

The morphology of O-MoS<sub>2</sub>/GAs-180 was investigated by scanning electron microscopy (SEM). As shown in Figure 2b, flower-like O-MoS<sub>2</sub> clusters of around 300 nm (O-MoS<sub>2</sub>-180 presents micrometer-sized particles, Figure S4, Supporting Information) assembled with nanosheets anchor homogeneously both on the surface and inside the aerogels. In addition, the MoS<sub>2</sub>/GAs-200 exhibits a similar morphology (Figure S5, Supporting Information) as O-MoS<sub>2</sub>/GAs-180 (Figure 2c,d). The GAs creates highly conductive network architecture, guaranteeing a facilitated ion and electron transport in LIBs.<sup>[66]</sup> The large surface area of O-MoS<sub>2</sub>/GAs-180 (81.0 m<sup>2</sup> g<sup>-1</sup>) and MoS<sub>2</sub>/GAs-200 (77.9 m<sup>2</sup> g<sup>-1</sup>) (Figure S6, Supporting Information) leads to a high density of redox active sites for ion storage. The pores ranging from dozens to more than 100 nm (Figure S6 inset, Supporting Information), would form sufficient mass transport channels, facilitating ion transport and mitigating

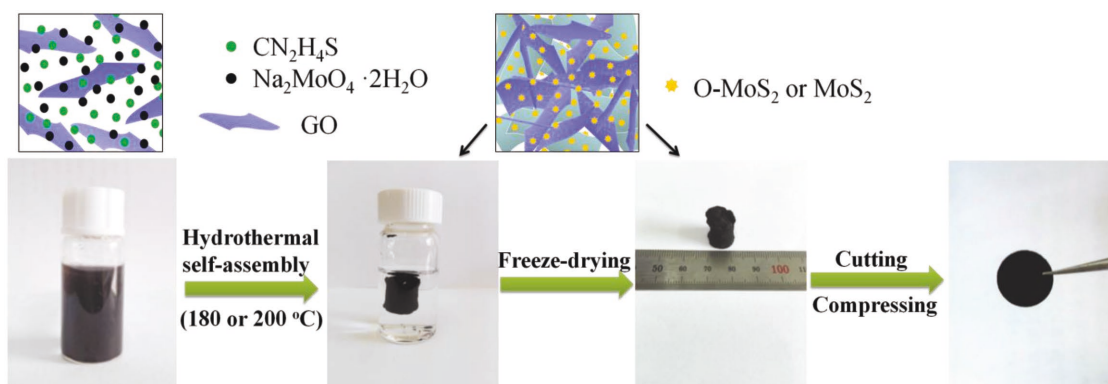
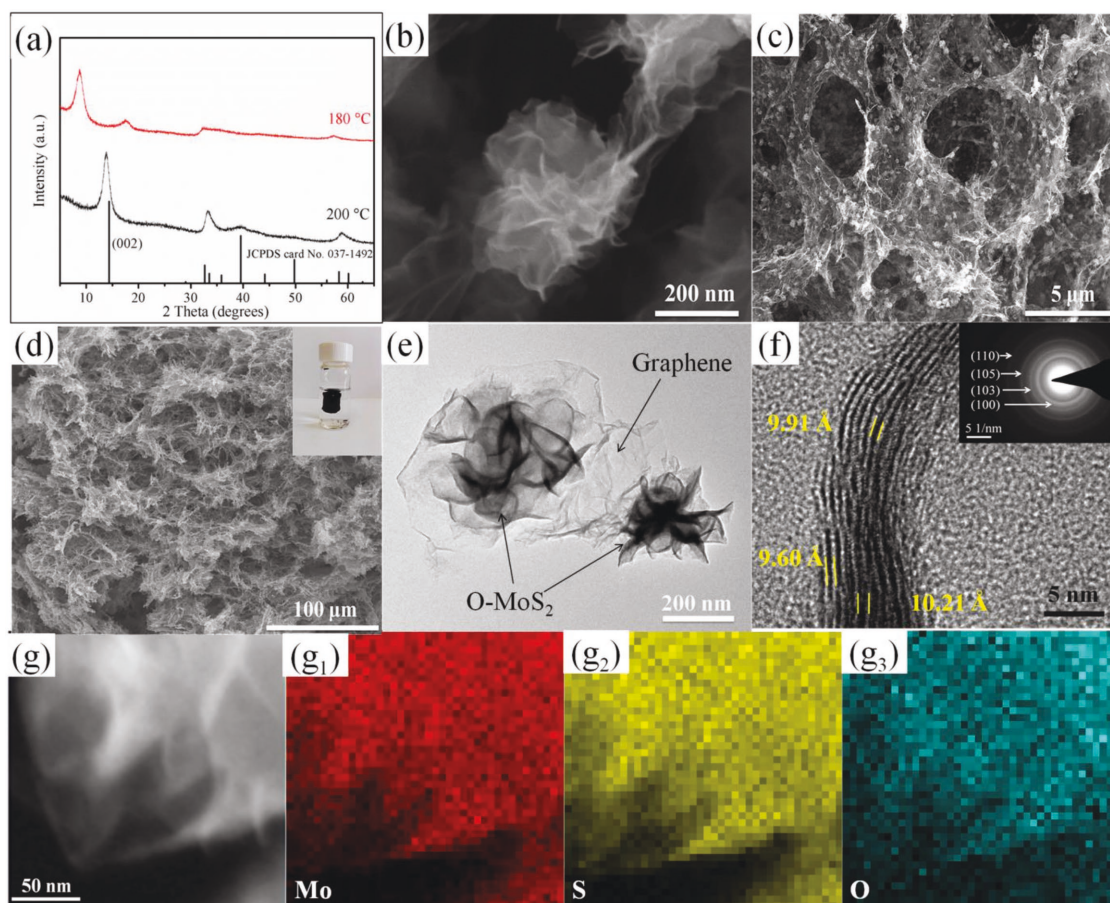


Figure 1. Schematic diagrams of synthesizing 3D O-MoS<sub>2</sub>/GAs.



**Figure 2.** a) XRD patterns of O-MoS<sub>2</sub>/GAs-180 and MoS<sub>2</sub>/GAs-200. b–d) SEM images of O-MoS<sub>2</sub>/GAs-180, the inset in (d) is the photograph of O-MoS<sub>2</sub>/GAs-180. e, f) TEM and HRTEM images of O-MoS<sub>2</sub>/GAs-180, the inset in (f) is the corresponding SAED pattern. g<sub>1</sub>, g<sub>2</sub>, g<sub>3</sub>) Element mapping images of O-MoS<sub>2</sub> nanosheets in (g): Mo (g<sub>1</sub>), S (g<sub>2</sub>), and O (g<sub>3</sub>) elements are in homogenous distribution.

diffusion limitations throughout the entire electrode.<sup>[32,51]</sup> GAs-180 also shows a porous structure, similar to the composite (Figure S7, Supporting Information).

Further structural insights into O-MoS<sub>2</sub>/GAs-180 were obtained from a transmission electron microscopy (TEM) study. Figure 2e shows that the flower-like O-MoS<sub>2</sub> clusters are assembled with pieces of nanosheets. The thickness of the O-MoS<sub>2</sub> nanosheets is only several nanometers. High-resolution TEM (HRTEM) image (Figure 2f) reveals the expanded interlayer spacing of O-MoS<sub>2</sub> ranging from 9.60 to 10.21 Å, which is in good agreement with the value calculated from the XRD analysis. By contrast, MoS<sub>2</sub>/GAs-200 exhibits an interlayer distance near the pristine value of around 6.27 Å (Figure S8, Supporting Information), which is also consistent with the XRD results. The selected-area electron diffraction (SAED) result displaying a pattern of concentric rings (Figure 2f inset) reveals the polycrystallinity of O-MoS<sub>2</sub>. Furthermore, the element mapping images of the energy dispersive spectroscopy analysis in Figure 2g demonstrate the homogeneous distribution of Mo, S, and O in the O-MoS<sub>2</sub> nanosheets, implying the successful oxygen incorporation.

X-ray photoelectron spectroscopy (XPS) spectra were conducted to characterize the chemical state of O-MoS<sub>2</sub>/GAs-180 and MoS<sub>2</sub>/GAs-200. More O contents were detected in

O-MoS<sub>2</sub>/GAs-180 than MoS<sub>2</sub>/GAs-200 (Figure S9, table inset, Supporting Information). **Figure 3a** shows the Mo 3d spectrum of MoS<sub>2</sub>/GAs-200. Two principal peaks located at around 229.4 and 232.5 eV are assigned to the Mo 3d<sub>5/2</sub> and Mo 3d<sub>3/2</sub> components of 2H-MoS<sub>2</sub>, respectively. The peaks at 235.3 and 233.0 eV are attributed to Mo(VI),<sup>[22,53,67]</sup> and the peak located at 226.1 eV is from S 2s. As for the S 2p spectra in Figure 3b, two doublets around 161.9 and 163.1 eV corresponding to the binding energies of S 2p<sub>3/2</sub> and S 2p<sub>1/2</sub> of 2H-MoS<sub>2</sub> can be detected. Compared with MoS<sub>2</sub>/GAs-200, the Mo 3d<sub>3/2</sub> and Mo 3d<sub>5/2</sub> peaks of O-MoS<sub>2</sub>/GAs-180 shift toward lower binding energies (228.6 and 231.7 eV, Figure 3c), demonstrating a much higher content of 1T-MoS<sub>2</sub>.<sup>[68–70]</sup> Meanwhile, similar downshifts of binding energies are also observed in the S 2p peaks of O-MoS<sub>2</sub>/GAs-180 (161.0 and 162.2 eV), as shown in Figure 3d. The deconvolution of the Mo 3d and S 2p spectra reveals that the O-MoS<sub>2</sub> exhibits a dominant 1T phase. The existence of Mo(IV)–O and Mo(V)–O bonds are revealed by the deconvolution of O 1s XPS spectra (Figure S10, Supporting Information), further verifying the successful oxygen incorporation. Raman spectroscopy was performed to verify the formation of the 1T-MoS<sub>2</sub> and oxygen incorporation in O-MoS<sub>2</sub>/GAs-180 (Figure S11, Supporting Information). The results show the development of four additional peaks from 120 to 355 cm<sup>-1</sup>,

which can be assigned to the 1T phase of MoS<sub>2</sub>.<sup>[68–70]</sup> In addition, two new peaks at 285 and 338 cm<sup>-1</sup> can be identified as the vibrational modes for Mo–O bonds, thus proving the successful oxygen incorporation in the product.

To understand the effect of larger interlayer spacing on electrochemical behavior, coin cells (2025-type) were assembled to evaluate the electrochemical performances of O-MoS<sub>2</sub>/GAs-180 and MoS<sub>2</sub>/GAs-200 in LIBs. First of all, cyclic voltammetry (CV) was performed to examine the Li storage mechanisms. As illustrated in Figure S12a of the Supporting Information, MoS<sub>2</sub>/GAs-200 undergoes an obvious phase transition from 2H to 1T during 1.0–1.5 V in the cathodic sweeps. This phase transition was further verified by the XPS test (Figure S13, Supporting Information). The deconvolution of the Mo 3d spectra (228.63 and 231.58 eV) reveals that the binding energies of Mo 3d<sub>3/2</sub> and Mo 3d<sub>5/2</sub> peaks have downshifts after cycling than before. Similar downshifts are also observed in S 2p peaks (161.08 and 162.38 eV). These results indicate that MoS<sub>2</sub>/GAs-200 exhibits a dominant 1T phase after cycling. While O-MoS<sub>2</sub>/GAs-180 shows an inherent characteristic of the 1T phase with broad current response between 1.5 and 2.5 V (Figure S12b, Supporting Information).<sup>[51,52,71]</sup> The capacitive contributions in O-MoS<sub>2</sub>/GAs-180 and MoS<sub>2</sub>/GAs-200 (after phase transition) at different scan rates are calculated based on the CV curves (Figure S14, Supporting Information). This kinetic analysis indicates that the main charge storages in both samples are capacitive in the tested voltage window.<sup>[52,72,73]</sup> The higher capacitive contribu-

tion in O-MoS<sub>2</sub>/GAs-180 at all tested scan rates implies that the expanded interlayer spacings can definitely facilitate Li ion intercalation/deintercalation.<sup>[53,64,65]</sup>

The rate performances of O-MoS<sub>2</sub>/GAs-180 and MoS<sub>2</sub>/GAs-200 electrodes with a mass loading of 1.0 mg cm<sup>-2</sup> are shown in Figure 4a. The O-MoS<sub>2</sub>/GAs-180 electrode exhibits outstanding rate performances; it retains 53% of the original capacity (151 mAh g<sup>-1</sup> at 0.2 A g<sup>-1</sup>) when the current densities rise 40 times to 8 A g<sup>-1</sup> (80 mAh g<sup>-1</sup>, charge/discharge in only 36 s). Moreover, a capacity of 25 mAh g<sup>-1</sup> is retained at a very high rate of 32 A g<sup>-1</sup>. When the current density returns to 0.2 A g<sup>-1</sup>, a high capacity of 150 mAh g<sup>-1</sup> resumes immediately, suggesting the good reversibility of Li-ion intercalation/deintercalation in the electrodes. In contrast, less capacity is retained at high rates in the MoS<sub>2</sub>/GAs-200 electrode compared with those of O-MoS<sub>2</sub>/GAs-180. Considering the similar surface areas and close MoS<sub>2</sub> contents in O-MoS<sub>2</sub>/GAs-180 and MoS<sub>2</sub>/GAs-200, the better rate capability should be attributed to the inherent features of O-MoS<sub>2</sub>. In addition, the poor capacities of GAs-180 electrode in the tested voltage window (Figure S15, Supporting Information) indicate the rare capacity contribution of graphene in the materials. The charge/discharge curves of both samples at the 10th cycle at various rate currents corresponding to Figure 4a are depicted in Figure 4b,c. No traditional charge/discharge plateau is found in both samples; the galvanostatic traces both display pseudolinear voltage responses with respect to Li-ion concentrations at various current densities,

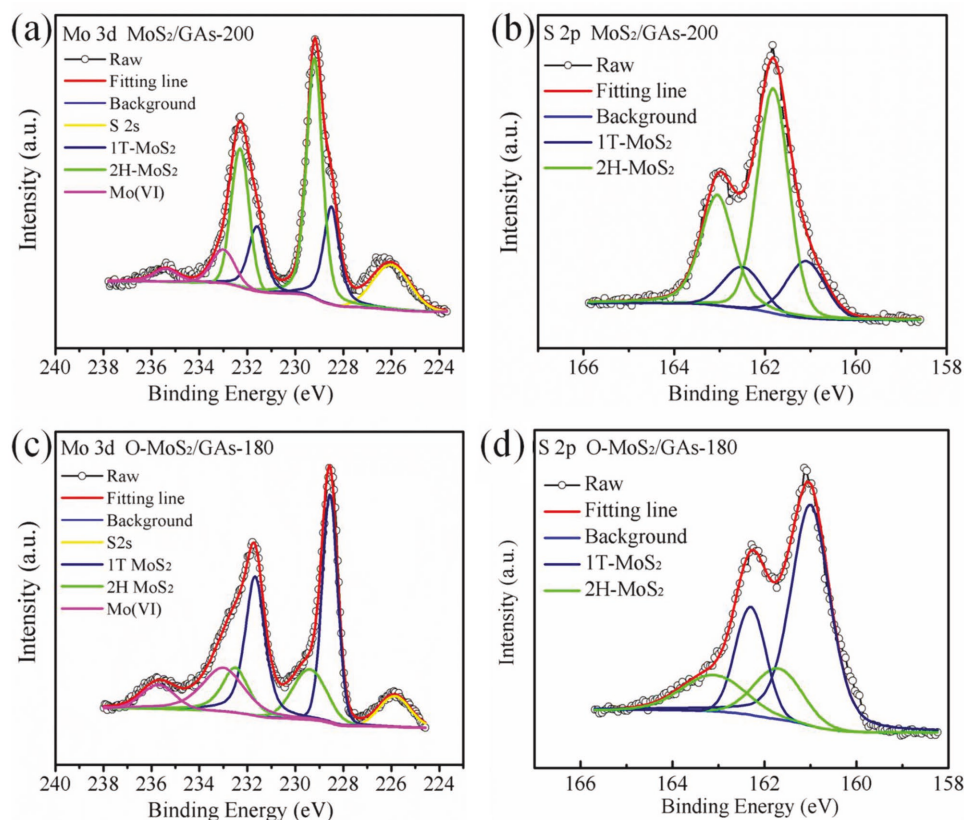


**Figure 3.** XPS spectra of MoS<sub>2</sub>/GAs-200 and O-MoS<sub>2</sub>/GAs-180: a) Mo 3d and b) S 2p spectra of MoS<sub>2</sub>/GAs-200. c) Mo 3d and d) S 2p spectra of O-MoS<sub>2</sub>/GAs-180.

suggesting a pseudocapacitive behavior, which is in good agreement with the CV results. In addition, the comparison of the charge/discharge curves at the first and 10th cycle for both samples (Figure S16, Supporting Information) further reveals the phase transition process in MoS<sub>2</sub>/GAs-200 and the inherent dominant 1T phase feature of O-MoS<sub>2</sub>/GAs-180.<sup>[74]</sup>

Ex situ XRD was carried out to explore further the structural features of O-MoS<sub>2</sub>/GAs-180 and MoS<sub>2</sub>/GAs-200 during the lithiation/delithiation processes. During the first full cycle of the MoS<sub>2</sub>/GAs-200 electrode at a low current density of 0.05 A g<sup>-1</sup> (Figure 5a), the pattern shows no change before lithiation to 2 V. Further discharging the battery to 1 V (full lithiation), a new peak is observed at 9.8°, and the (002) peak of MoS<sub>2</sub> disappears. This means the interlayer spacing is expanded from 6.27 to 9.0 Å after the Li-ion intercalation. During the charge stage, a weak peak reappears at 14.1°, although there is a weak peak at 9.8° with delithiation to 2 V. After delithiation to 3 V, the peak at 9.8° returns to the original position (14.1°) completely, implying the interlayer spacing returns to 6.27 Å. Obviously, a lattice breathing phenomenon occurs during Li-ion intercalating/deintercalating into/from the MoS<sub>2</sub>/GAs-200, and this observation is consistent with previous reports about MoS<sub>2</sub> during the lithiation/delithiation processes.<sup>[69,75]</sup> By contrast, as for the O-MoS<sub>2</sub>/GAs-180 electrode, the (002) peak of O-MoS<sub>2</sub> at 8.7° stays at the original location whether in the processes of lithiation or delithiation at the current density of 0.05 A g<sup>-1</sup> (Figure 5b), indicating that the O-MoS<sub>2</sub> does not undergo an interlayer spacing variation during the Li-ion intercalation/deintercalation.

The subsequent cycles at the same current density of 0.05 A g<sup>-1</sup> were also investigated by ex situ XRD. As cycling proceeds, the XRD patterns of the full delithiated MoS<sub>2</sub>/GAs-200 electrode undergo continuous variation (Figure 5c). After 30 cycles, a weak peak appears at 9.8°; meanwhile, the (002) diffraction peak of pristine MoS<sub>2</sub> (14.1°) is retained. Furthermore, only the peak at 9.8° was observed after 100 cycles, suggesting an irreversible increase of (002) interlayer spacing after excessive lattice breathing. When the cycle number rises to 300, the (002) peak almost disappears, revealing the collapse of 2D structure (Figure 5e). The fluctuating capacity of the corresponding 300 cycles also reflects the structural variation (Figure S17a, Supporting Information). The weakened van der Waals force between the individual monolayers of MoS<sub>2</sub> after interlayer expansion becomes unable to maintain the regular configuration of MoS<sub>2</sub> layers, even causes exfoliation after a long cycle charge/discharge process.<sup>[7,8,74]</sup> However, the XRD patterns of the O-MoS<sub>2</sub>/GAs-180 electrode show no obvious difference after 30, 100, and even 300 cycles (Figure 5d), indicating the 2D structure is maintained well during the long cycle test (Figure 5f). The corresponding capacity can keep nearly steady based on the stable structure (Figure S17b, Supporting Information). Moreover, the structural stability of both O-MoS<sub>2</sub>/GAs-180 and MoS<sub>2</sub>/GAs-200 after cycling was verified by TEM and HRTEM (Figure S18, Supporting Information). The flower-like morphology of MoS<sub>2</sub> is still observed in both MoS<sub>2</sub>/GAs-200 and O-MoS<sub>2</sub>/GAs-180 after cycling, in spite of some exfoliated pieces are observed in MoS<sub>2</sub>/GAs-200. However, the *d*-spacing of (002) crystal plane of MoS<sub>2</sub> in MoS<sub>2</sub>/GAs-200 is observed

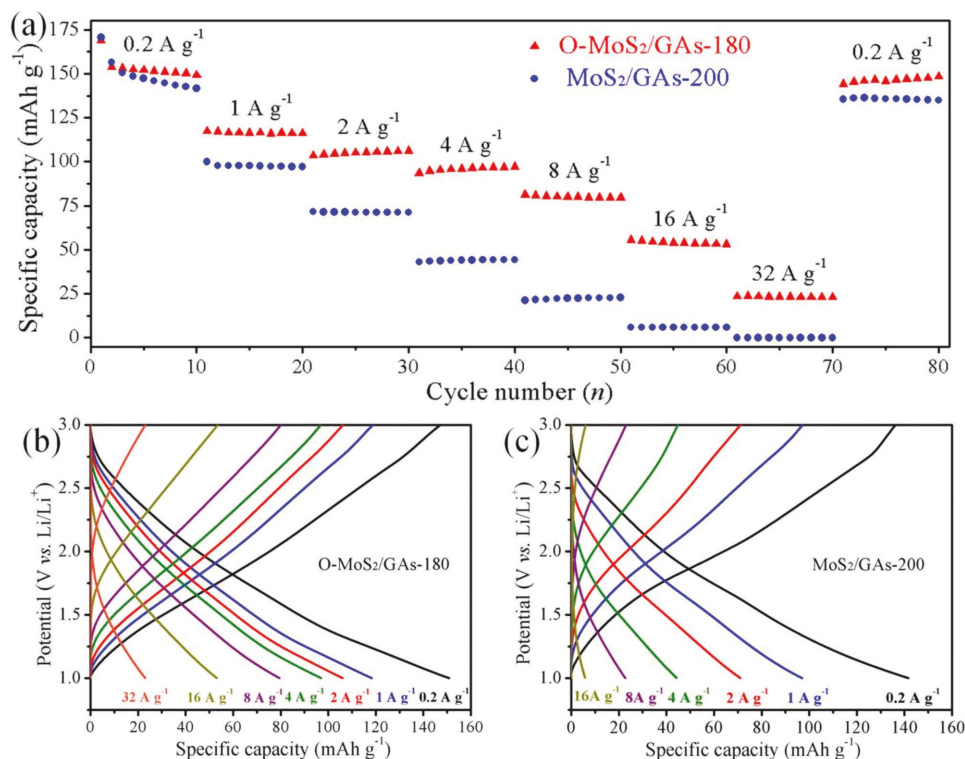


**Figure 4.** a) Comparison of the rate performances of O-MoS<sub>2</sub>/GAs-180 and MoS<sub>2</sub>/GAs-200 at various rate currents. The galvanostatic charge/discharge curves of b) O-MoS<sub>2</sub>/GAs-180 and c) MoS<sub>2</sub>/GAs-200. The curves are based on the 10th cycles of various rate currents in (a).

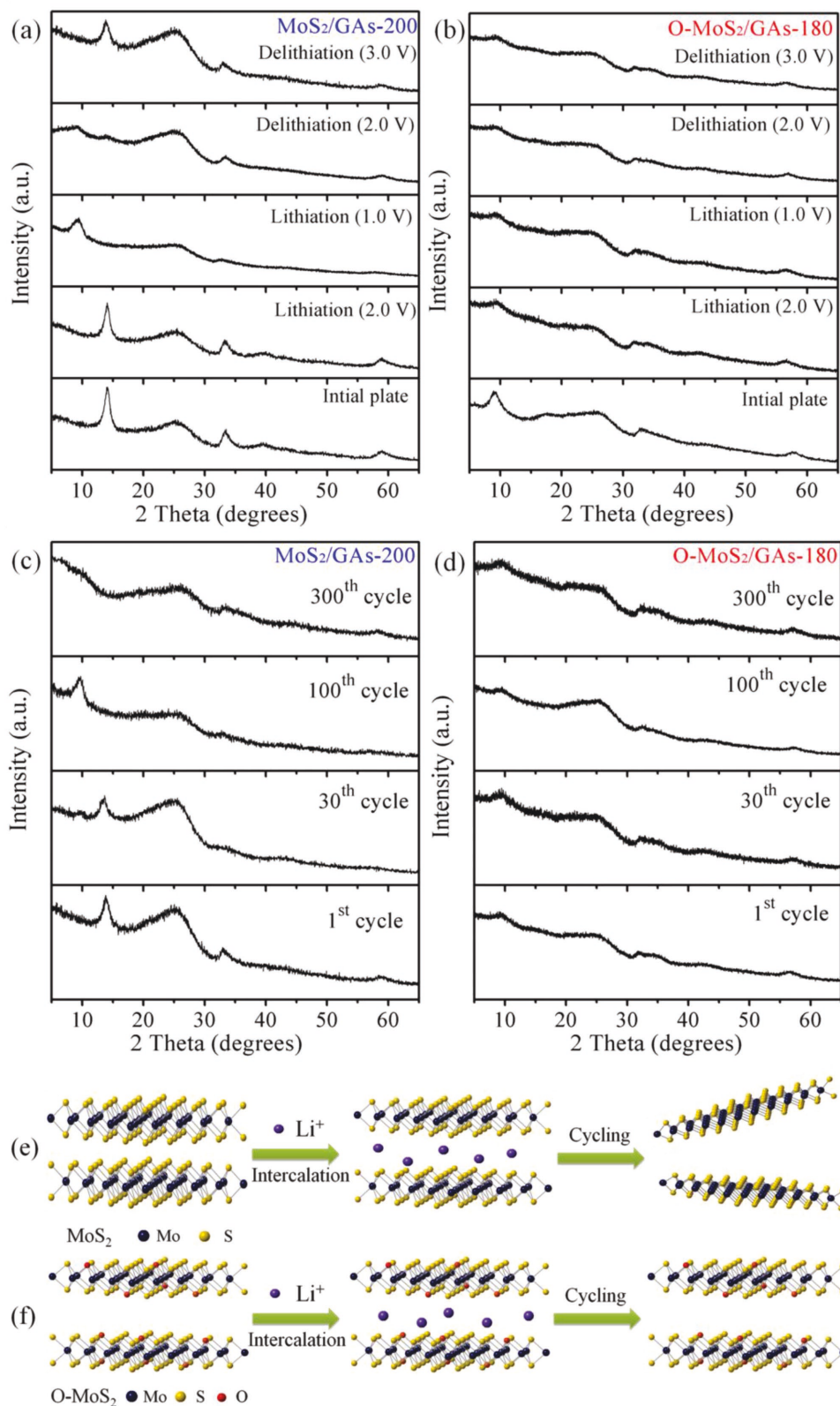


**Figure 5.** Ex situ XRD patterns at various lithiated and delithiated states in a) MoS<sub>2</sub>/GAs-200 and b) O-MoS<sub>2</sub>/GAs-180. Ex situ XRD patterns of c) MoS<sub>2</sub>/GAs-200 and d) O-MoS<sub>2</sub>/GAs-180 at various fully cycled states. Schematic illustration of the 2D structural evolution of e) pristine MoS<sub>2</sub> and f) O-MoS<sub>2</sub> during the Li-ion intercalation/deintercalation processes.

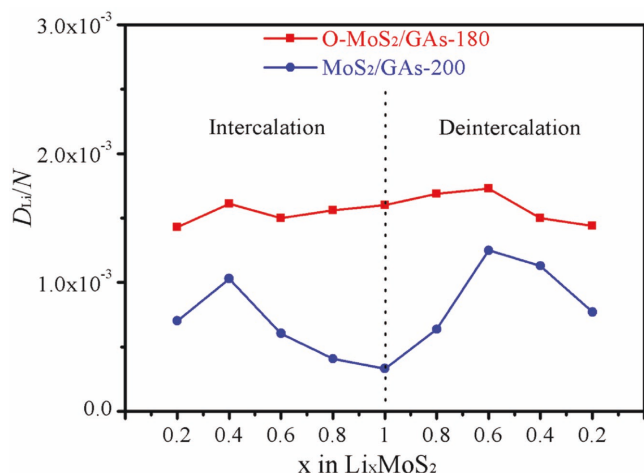


**Figure 6.** The relationships of the Li-ion diffusion coefficients ( $D_{Li}$ ) with lithium concentrations ( $x$  in  $Li_xMoS_2$ ).

to be expanded to 9.1 Å, larger than the pristine value. This result is consistent with the XRD result. Moreover, the layer numbers decrease obviously, verifying the exfoliation of  $MoS_2$  after long cycles. As for O- $MoS_2$ /GAs-180, the HRTEM image shows that the (002) crystal planes are well preserved, verifying its stable structure. According to the XRD and HRTEM results above, it can be concluded that the Li-ion intercalation drives the structural change of pristine  $MoS_2$ , which is in sharp contrast to the structural stability of O- $MoS_2$ . It may be attributed to that, the suitable lattice spacing and firm frame of O- $MoS_2$  cater to the requirement of the Li-ion comfortably transporting in the lattice and remaining stable in charge/discharge. In this work, we suggest that the incorporation species with Mo–O bonds are crucial to the unique characteristics.

To examine further the relationship of Li-ion intercalation/deintercalation with the material structures, EIS was used to study the Li-ion transport during the full cycle of O- $MoS_2$ /GAs-180 and  $MoS_2$ /GAs-200 electrodes (both electrodes were precycled 10 times to complete the 2H–1T phase transition). The relationships of Li-ion diffusion coefficients ( $D_{Li}$ ) depending on lithium concentrations ( $x$  in  $Li_xMoS_2$ ) in the two samples were analyzed from their Nyquist plots (details in Figures S19 and S20, Tables S1 and S2, Supporting Information). As shown in **Figure 6**, the  $D_{Li}$  values of the  $MoS_2$ /GAs-200 electrode display fluctuations at different lithium concentrations, but the  $D_{Li}$  values of O- $MoS_2$ /GAs-180 remain nearly stable whether in Li-ion intercalation or deintercalation. Otherwise, the  $D_{Li}$  values of the O- $MoS_2$ /GAs-180 electrode are larger than that for  $MoS_2$ /GAs-200 in the whole cycle (4.8 times when full lithiation ( $x = 1$ )), confirming the better Li-ion diffusion kinetics in the O- $MoS_2$ /GAs-180 electrode. The results are in good agreement with the conclusion from the ex situ XRD results in the first cycles. The large interlayer spacing in O- $MoS_2$  is beneficial to Li-ion transport, and the Li-ion concentration causes no harm to the stability of the 2D structure in O- $MoS_2$ . With respect to  $MoS_2$ /GAs-200, the lattice breathing during Li-ion intercalation/deintercalation harms the Li-ion diffusion coefficients at different Li-ion concentrations.

The intrinsic reason for O- $MoS_2$  possessing a larger interlayer spacing as well as more stable structure was investigated. As assumed in the literature, the oxygen atoms substitute sulfur atoms which expands the interlayer spacing of  $MoS_2$ .<sup>[14–19]</sup> However, it is not very reasonable according to our DFT calculations (Figure S21, Supporting Information). There is a huge difference in structural stability between O- $MoS_2$  and pristine  $MoS_2$  during the lithiation/delithiation processes according to above results. Considering the previous reports about  $MoS_2$  with large interlayer spacing,<sup>[7,8]</sup> we suppose that some molybdenum oxide species are incorporated into  $MoS_2$  which cause the expansion of interlayer spacing. The incorporation should also be responsible for the stability. Because O- $MoS_2$  is prepared at a relatively low temperature, the insufficient reaction results in the residual molybdenum species with Mo–O bonds inherited from the molybdate precursor.<sup>[14]</sup> However, the existence of molybdenum species is still not well understood. Therefore, DFT calculations were carried out to gain some insight into the explanation. Considering water serving as the solvent for the reaction, molybdenum hydroxide ( $MoO_x(OH)_y$ ) may be the target species, which are evolved from  $Na_2MoO_4$  in a hydrothermal environment. The presence of hydroxyl groups in O- $MoS_2$  were confirmed by Fourier transformed infrared tests in paraffin oil (Figure S22, Supporting Information). Therefore, three typical molybdenum hydroxides,  $MoO(OH)_3$ ,  $Mo(OH)_4$ , and  $MoO(OH)_2$  were chosen as model compounds in this study.

As shown in **Figure 7**, for 1T- $MoS_2$  without oxygen substitution, the interlayer spacings are 10.01, 9.96, and 8.25 Å corresponding to the incorporation of  $Mo(OH)_4$ ,  $MoO(OH)_3$ , and  $MoO(OH)_2$ , respectively. When a sulfur atom is substituted by an oxygen atom in one  $3 \times 3$  supercell of  $MoS_2$ , the corresponding interlayer spacings are 9.99, 10.42, and 8.06 Å, respectively. It is clear that, no matter if there is oxygen substitution in 1T- $MoS_2$  or not, the incorporation of above-mentioned  $MoO_x(OH)_y$  enlarges the interlayer spacing. The interlayer spacings of O- $MoS_2$  incorporated with  $Mo(OH)_4$  and  $MoO(OH)_3$  are consistent with the values measured from the XRD and TEM tests, whereas the  $MoO(OH)_2$  incorporation results in a relatively smaller interlayer spacing. The situation of two sulfur atoms substituted by oxygen atoms in  $Mo(OH)_4$  and  $MoO(OH)_3$  was also investigated with DFT calculations. The results in Figure S23 of the Supporting Information are also consistent with the experimental results.

According to the results of the simulation,  $Mo(OH)_4$  and  $MoO(OH)_3$  are among molybdenum species possible to be incorporated into the  $MoS_2$  interlayers. The expanded interlayer spacing of O- $MoS_2$  and the stable layer structure of O- $MoS_2$ /GAs-180 during cycling reveal that the incorporation of  $MoO_x(OH)_y$  species not only plays a role in expanding the  $MoS_2$  interlayer spacing but also acts as a “tensioner” to increase the stability of the pseudolayered structure for Li-ion intercalation/deintercalation. We suggest that the robust hydrogen-bonding between hydroxyl groups in  $MoO_x(OH)_y$  and the unsaturated oxygen/sulfur atoms in  $MoS_2$  tenses the adjacent  $MoS_2$  monolayers, ensuring the structural stability. In addition, the content of  $MoO_x(OH)_y$  pillars should be limited and few, given the limited oxygen content in Figure S9 of the Supporting Information and the remarkable rate capability of O- $MoS_2$ /GAs-180.



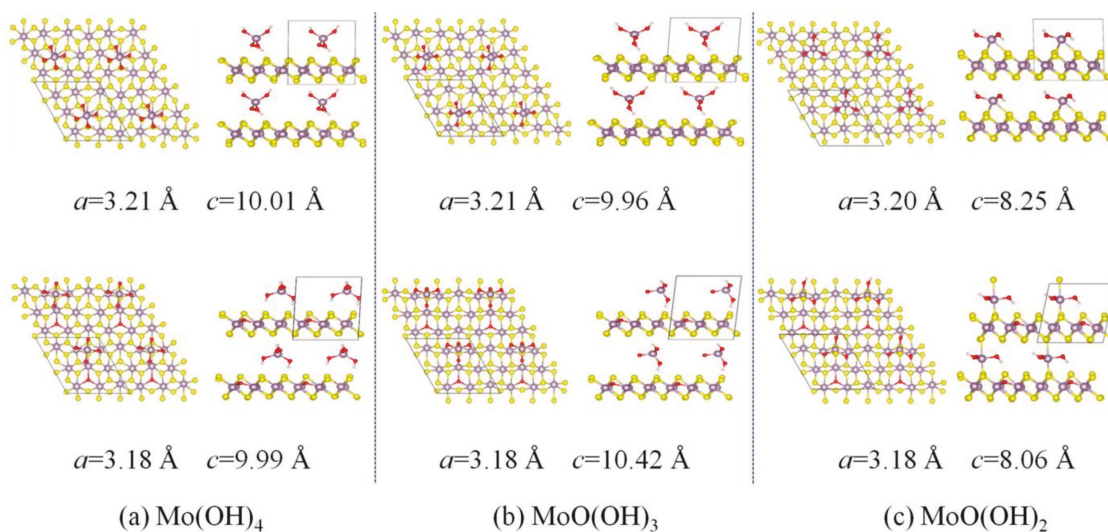


**Figure 7.** The atomic structures of molybdenum species (including a)  $\text{Mo}(\text{OH})_4$ , b)  $\text{MoO}(\text{OH})_3$ , and c)  $\text{MoO}(\text{OH})_2$  incorporated into  $\text{MoS}_2$  and  $\text{O-MoS}_2$  with corresponding lattice constants.

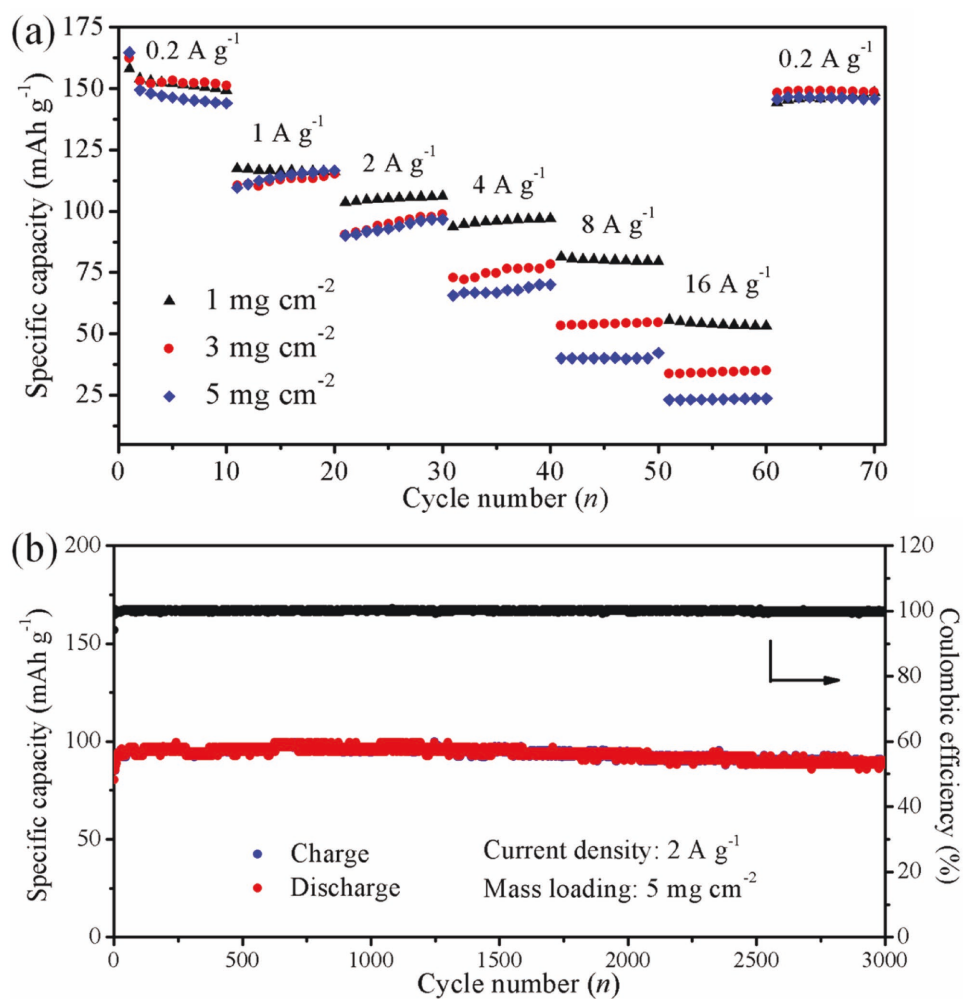


**Figure 8.** a) Comparison of the rate performances of  $\text{O-MoS}_2/\text{GAS-180}$  electrode at various rate currents under different mass loadings ( $1$ ,  $3$ , and  $5 \text{ mg cm}^{-2}$ ). b) Specific capacity and coulombic efficiency versus cycle number at a current density of  $2 \text{ A g}^{-1}$  with the mass loading of  $5 \text{ mg cm}^{-2}$ .

The rate performances of the O-MoS<sub>2</sub>/GAs-180 electrode with higher mass loading (3 and 5 mg cm<sup>-2</sup>) were further examined (Figure 8a). Only small capacity degradation was induced with increased mass loading at 0.2 and 1 A g<sup>-1</sup>, and a capacity of 70 mAh g<sup>-1</sup> remained with 5 mg cm<sup>-2</sup> loading at a high rate of 4 A g<sup>-1</sup> (71% of the 1 mg cm<sup>-2</sup> loading). Even at the high rate of 8 A g<sup>-1</sup>, the electrode with a mass loading of 5 mg cm<sup>-2</sup> retains a capacity of 40 mAh g<sup>-1</sup>, showing a capacity retention of 50% compared with that at 1 mg cm<sup>-2</sup>. This indicates that the O-MoS<sub>2</sub>/GAs-180 electrode exhibits remarkable gravimetric energy storage performance in thick electrodes. In addition, the electrode with the mass loading of 5 mg cm<sup>-2</sup> exhibits an outstanding durability. It retains a discharge capacity of 88 mAh g<sup>-1</sup> with capacity retention over 91% at a current density of 2.0 A g<sup>-1</sup> after 3000 cycles (Figure 8b). Furthermore, the comparison between the exciting performance results in this work and the other reported MoS<sub>2</sub>-based pseudocapacitors is shown in Table S3 of the Supporting Information. This self-supported pseudolayered O-MoS<sub>2</sub> electrode exhibits an excellent performance close to the best materials reported to date. What makes the material significant is the ability to preserve high rate capability and good cycling performance in thicker electrodes with high mass loading.

### 3. Conclusion

A composite of pseudolayered O-MoS<sub>2</sub> loading on GAs was prepared. More comprehensive analyses on O-MoS<sub>2</sub> than previous reports were achieved, and this is the first report of its electrochemical performance as the host material for LIBs. The O-MoS<sub>2</sub> shows an inherent dominant 1T phase with an expanded layer spacing of around 10.15 Å. When this self-supported composite is directly used as Li-ion intercalation host, the electrode possesses a high rate capability (80 mAh g<sup>-1</sup> at 8 A g<sup>-1</sup>, charge/discharge in only 36 s, mass loading of 1 mg cm<sup>-2</sup>) and exhibits long-term cyclic stability (with a capacity retention over 91% for 3000 cycles at 2 A g<sup>-1</sup>) at a high mass loading of 5 mg cm<sup>-2</sup>. Kinetic analysis reveals that the lithium storage capacity of O-MoS<sub>2</sub> is mainly contributed from pseudocapacitive processes. During the battery cycling, ex situ XRD revealed that O-MoS<sub>2</sub> possesses an excellent stable structure, in contrast to the gradually collapsed structure of pristine MoS<sub>2</sub> suffering from lattice breathing. EIS analysis indicates that the larger layer spacing leads to better Li-ion intercalation kinetics of O-MoS<sub>2</sub> than pristine MoS<sub>2</sub>. DFT calculations show that intercalating MoO<sub>x</sub>(OH)<sub>y</sub> species into MoS<sub>2</sub> interlayers is reasonable to explain the oxygen incorporation and interlayer expansion, resulting in a pseudolayered structure of O-MoS<sub>2</sub>. The combination of the stable structure and DFT calculations provides the basis that the MoO<sub>x</sub>(OH)<sub>y</sub> pillars play a bifunctional role of expansion and tension, maintaining the stability of the pseudolayered structure. This work demonstrates that the pseudolayered structural materials with large interlayer spacing and stable frame are promising hosts for metal-ion batteries, and thus proposing an avenue for exploring new candidate materials for power batteries.

### Supporting Information

Supporting Information is available from the Wiley Online Library or from the author.

### Acknowledgements

This work was supported by the National Natural Science Foundation of China (No. 21776052), the Natural Science Foundation of Heilongjiang Province (No. QC2016010), and the Fundamental Research Funds for the Central Universities (No. HIT. IBRSEM. A. 201407).

### Conflict of Interest

The authors declare no conflict of interest.

### Keywords

high mass loading, interlayer spacing, Li-ion intercalation, MoS<sub>2</sub>, oxygen-incorporation

Received: August 20, 2018  
Revised: September 28, 2018  
Published online: October 21, 2018

- [1] Q. H. Wang, K. Kalantar-Zadeh, A. Kis, J. N. Coleman, M. S. Strano, *Nat. Nanotechnol.* **2012**, *7*, 699.
- [2] K. F. Mak, C. Lee, J. Hone, J. Shan, T. F. Heinz, *Phys. Rev. Lett.* **2010**, *105*, 136805.
- [3] T. Stephenson, Z. Li, B. Olsen, D. Mitlin, *Energy Environ. Sci.* **2014**, *7*, 209.
- [4] W. Choi, N. Choudhary, G. H. Han, J. Park, D. Akinwande, Y. H. Lee, *Mater. Today* **2017**, *20*, 116.
- [5] X. Wang, Q. Weng, Y. Yang, Y. Bando, D. Golberg, *Chem. Soc. Rev.* **2016**, *45*, 4042.
- [6] Q. Xue, J. Sun, Y. Huang, M. Zhu, Z. Pei, H. Li, Y. Wang, N. Li, H. Zhang, C. Zhi, *Small* **2017**, *13*, 1701827.
- [7] J. Xu, J. Zhang, W. Zhang, C. Lee, *Adv. Energy Mater.* **2017**, *7*, 1700571.
- [8] K. D. Rasamani, F. Alimohammadi, Y. Sun, *Mater. Today* **2017**, *20*, 83.
- [9] M. Acerce, D. Voiry, M. Chhowalla, *Nat. Nanotechnol.* **2015**, *10*, 313.
- [10] P. Gao, L. Wang, Y. Zhang, Y. Huang, K. Liu, *ACS Nano* **2015**, *9*, 11296.
- [11] X. Fan, P. Xu, D. Zhou, Y. Sun, Y. C. Li, M. A. T. Nguyen, M. Terrones, T. E. Mallouk, *Nano Lett.* **2015**, *15*, 5956.
- [12] A. Ambrosi, Z. Sofer, M. Pumera, *Small* **2015**, *11*, 605.
- [13] Z. Zeng, Z. Yin, X. Huang, H. Li, Q. He, G. Lu, F. Boey, H. Zhang, *Angew. Chem., Int. Ed.* **2011**, *50*, 11093.
- [14] J. Xie, J. Zhang, S. Li, F. Grote, X. Zhang, H. Zhang, R. Wang, Y. Lei, B. Pan, Y. Xie, *J. Am. Chem. Soc.* **2013**, *135*, 17881.
- [15] J. Guo, F. Li, Y. Sun, X. Zhang, L. Tang, *J. Power Sources* **2015**, *291*, 195.
- [16] D. Wu, Y. Wang, F. Wang, H. Wang, Y. An, Z. Gao, F. Xu, K. Jjiang, *Carbon* **2017**, *123*, 756.
- [17] A. Liu, L. Zhao, J. Zhang, L. Lin, H. Wu, *ACS Appl. Mater. Interfaces* **2016**, *8*, 25210.
- [18] J. Zhou, G. Fang, A. Pan, S. Liang, *ACS Appl. Mater. Interfaces* **2016**, *8*, 33681.
- [19] W. Zhou, K. Zhou, D. Hou, X. Liu, G. Li, Y. Sang, H. Liu, L. Li, S. Chen, *ACS Appl. Mater. Interfaces* **2014**, *6*, 21534.

- [20] Q. Liu, X. Li, Q. He, A. Khalil, D. Liu, T. Xiang, X. Wu, L. Song, *Small* **2015**, *11*, 5556.
- [21] Q. Liu, Q. Fang, W. Chu, Y. Wan, X. Li, W. Xu, M. Habib, S. Tao, Y. Zhou, D. Liu, T. Xiang, A. Khalil, X. Wu, M. Chowalla, P. M. Ajayan, L. Song, *Chem. Mater.* **2017**, *29*, 4738.
- [22] Y. Tang, Y. Wang, X. Wang, S. Li, W. Huang, L. Dong, C. Liu, Y. Li, Y. Lan, *Adv. Energy Mater.* **2016**, *6*, 1600116.
- [23] K. Chang, W. Chen, L. Ma, H. Li, H. Li, F. Huang, Z. Xu, Q. Zhang, J. Lee, *J. Mater. Chem.* **2011**, *21*, 6251.
- [24] H. Jiang, D. Ren, H. Wang, Y. Hu, S. Guo, H. Yuan, P. Hu, L. Zhang, C. Li, *Adv. Mater.* **2015**, *27*, 3687.
- [25] H. Zhu, F. Zhang, J. Li, Y. Tang, *Small* **2018**, *14*, 1703951.
- [26] Z. Shi, W. Kang, J. Xu, Y. Sun, M. Jiang, T. Ng, H. Xue, D. Y. W. Yu, W. Zhang, C. Lee, *Nano Energy* **2016**, *22*, 27.
- [27] M. Gao, M. K. Y. Chan, Y. Sun, *Nat. Commun.* **2015**, *6*, 7493.
- [28] J. Ding, Y. Zhou, Y. Li, S. Guo, X. Huang, *Chem. Mater.* **2016**, *28*, 2074.
- [29] Y. Li, Y. Liang, F. C. Robles Hernandez, H. Deog Yoo, Q. An, Y. Yao, *Nano Energy* **2015**, *15*, 453.
- [30] Z. Wan, J. Shao, J. Yun, H. Zheng, T. Gao, M. Shen, Q. Qu, H. Zheng, *Small* **2014**, *10*, 4975.
- [31] Y. Wang, L. Yu, X. W. Lou, *Angew. Chem., Int. Ed.* **2016**, *55*, 7423.
- [32] Y. Chao, R. Jalili, Y. Ge, C. Wang, T. Zheng, K. Shu, G. G. Wallace, *Adv. Funct. Mater.* **2017**, *27*, 1700234.
- [33] Y. Jiao, A. Mukhopadhyay, Y. Ma, L. Yang, A. M. Hafez, H. Zhu, *Adv. Energy Mater.* **2018**, *8*, 1702779.
- [34] R. Wang, S. Wang, D. Jin, Y. Zhang, Y. Cai, J. Ma, L. Zhang, *Energy Storage Mater.* **2017**, *9*, 195.
- [35] X. Yu, H. Hu, Y. Wang, H. Chen, X. W. Lou, *Angew. Chem., Int. Ed.* **2015**, *54*, 7395.
- [36] X. Geng, Y. Jiao, Y. Han, A. Mukhopadhyay, L. Yang, H. Zhu, *Adv. Funct. Mater.* **2017**, *27*, 1702998.
- [37] X. Hu, Y. Li, G. Zeng, J. Jia, H. Zhan, Z. Wen, *ACS Nano* **2018**, *12*, 1592.
- [38] K. Xie, K. Yuan, X. Li, W. Lu, C. Shen, C. Liang, R. Vajtai, P. Ajayan, B. Wei, *Small* **2017**, *13*, 1701471.
- [39] Y. Liang, R. Feng, S. Yang, H. Ma, J. Liang, J. Chen, *Adv. Mater.* **2011**, *23*, 640.
- [40] C. Zhao, C. Yu, M. Zhang, Q. Sun, S. Li, M. Norouzi Banis, X. Han, Q. Dong, J. Yang, G. Wang, X. Sun, J. Qiu, *Nano Energy* **2017**, *41*, 66.
- [41] D. Su, S. Dou, G. Wang, *Adv. Energy Mater.* **2015**, *5*, 1401205.
- [42] M. A. Py, R. R. Haering, *Can. J. Phys.* **1983**, *61*, 76.
- [43] M. A. Lukowski, A. S. Daniel, F. Meng, A. Forticaux, L. Li, S. Jin, *J. Am. Chem. Soc.* **2013**, *135*, 10274.
- [44] Y. Yang, X. Liu, Z. Zhu, Y. Zhong, Y. Bando, D. Golberg, J. Yao, X. Wang, *Joule* **2018**, *2*, 1075.
- [45] G. Eda, H. Yamaguchi, D. Voiry, T. Fujita, M. Chen, M. Chowalla, *Nano Lett.* **2011**, *11*, 5111.
- [46] M. Wu, J. Zhan, K. Wu, Z. Li, L. Wang, B. Geng, L. Wang, D. Pan, *J. Mater. Chem. A* **2017**, *5*, 14061.
- [47] Y. Yang, X. Liu, Z. Dai, F. Yuan, Y. Bando, D. Golberg, X. Wang, *Adv. Mater.* **2017**, *29*, 1606922.
- [48] L. Zhang, D. Sun, J. Kang, J. Feng, H. A. Bechtel, L. Wang, E. J. Cairns, J. Guo, *Nano Lett.* **2018**, *18*, 1466.
- [49] L. Wang, Z. Xu, W. Wang, X. Bai, *J. Am. Chem. Soc.* **2014**, *136*, 6693.
- [50] X. Hu, W. Zhang, X. Liu, Y. Mei, Y. Huang, *Chem. Soc. Rev.* **2015**, *44*, 2376.
- [51] J. B. Cook, H. Kim, T. C. Lin, C. Lai, B. Dunn, S. H. Tolbert, *Adv. Energy Mater.* **2017**, *7*, 1601283.
- [52] J. B. Cook, H. Kim, Y. Yan, J. S. Ko, S. Robbennolt, B. Dunn, S. H. Tolbert, *Adv. Energy Mater.* **2016**, *6*, 1501937.
- [53] L. Huang, Q. Wei, X. Xu, C. Shi, X. Liu, L. Zhou, L. Mai, *Phys. Chem. Chem. Phys.* **2017**, *19*, 13696.
- [54] Y. Liang, H. D. Yoo, Y. Li, J. Shuai, H. A. Calderon, F. C. Robles Hernandez, L. C. Grabow, Y. Yao, *Nano Lett.* **2015**, *15*, 2194.
- [55] G. Jia, D. Chao, N. H. Tiep, Z. Zhang, H. J. Fan, *Energy Storage Mater.* **2018**, *14*, 136.
- [56] X. Xu, R. Zhao, W. Ai, B. Chen, H. Du, L. Wu, H. Zhang, W. Huang, T. Yu, *Adv. Mater.* **2018**, *30*, 1800658.
- [57] Z. Hu, L. Wang, K. Zhang, J. Wang, F. Cheng, Z. Tao, J. Chen, *Angew. Chem.* **2014**, *126*, 13008.
- [58] M. Calandra, *Phys. Rev. B* **2013**, *88*, 245428.
- [59] J. Zheng, H. Zhang, S. Dong, Y. Liu, C. Tai Nai, H. Suk Shin, H. Young Jeong, B. Liu, K. Ping Loh, *Nat. Commun.* **2014**, *5*, 2995.
- [60] Q. Ding, F. Meng, C. R. English, M. Cabán-Acevedo, M. J. Shearer, D. Liang, A. S. Daniel, R. J. Hamers, S. Jin, *J. Am. Chem. Soc.* **2014**, *136*, 8504.
- [61] P. He, G. Zhang, X. Liao, M. Yan, X. Xu, Q. An, J. Liu, L. Mai, *Adv. Energy Mater.* **2018**, *8*, 1702463.
- [62] X. Wang, Z. Guan, Y. Li, Z. Wang, L. Chen, *Nanoscale* **2015**, *7*, 637.
- [63] Y. Xue, Q. Zhang, W. Wang, H. Cao, Q. Yang, L. Fu, *Adv. Energy Mater.* **2017**, *7*, 1602684.
- [64] H. Liu, D. Su, R. Zhou, B. Sun, G. Wang, S. Z. Qiao, *Adv. Energy Mater.* **2012**, *2*, 970.
- [65] H. Hwang, H. Kim, J. Cho, *Nano Lett.* **2011**, *11*, 4826.
- [66] Y. Yang, D. Tang, C. Zhang, Y. Zhang, Q. Liang, S. Chen, Q. Weng, M. Zhou, Y. Xue, J. Liu, J. Wu, Q. H. Cui, C. Lian, G. Hou, F. Yuan, Y. Bando, D. Golberg, X. Wang, *Energy Environ. Sci.* **2017**, *10*, 979.
- [67] H. Tang, J. Wang, H. Yin, H. Zhao, D. Wang, Z. Tang, *Adv. Mater.* **2015**, *27*, 1117.
- [68] Y. Yin, J. Han, Y. Zhang, X. Zhang, P. Xu, Q. Yuan, L. Samad, X. Wang, Y. Wang, Z. Zhang, P. Zhang, X. Cao, B. Song, S. Jin, *J. Am. Chem. Soc.* **2016**, *138*, 7965.
- [69] H. Wang, Z. Lu, S. Xu, D. Kong, J. J. Cha, G. Zheng, P. C. Hsu, K. Yan, D. Bradshaw, F. B. Prinz, Y. Cui, *Proc. Natl. Acad. Sci. USA* **2013**, *110*, 19701.
- [70] L. Cai, J. He, Q. Liu, T. Yao, L. Chen, W. Yan, F. Hu, Y. Jiang, Y. Zhao, T. Hu, Z. Sun, S. Wei, *J. Am. Chem. Soc.* **2015**, *137*, 2622.
- [71] H. D. Yoo, Y. Li, Y. Liang, Y. Lan, F. Wang, Y. Yao, *ChemNanoMat* **2016**, *2*, 688.
- [72] H. Kim, J. B. Cook, H. Lin, J. S. Ko, S. H. Tolbert, V. Ozolins, B. Dunn, *Nat. Mater.* **2017**, *16*, 454.
- [73] M. Zhu, Y. Huang, Y. Huang, H. Li, Z. Wang, Z. Pei, Q. Xue, H. Geng, C. Zhi, *Adv. Mater.* **2017**, *29*, 1605137.
- [74] Y. Huang, M. Zhu, Y. Huang, Z. Pei, H. Li, Z. Wang, Q. Xue, C. Zhi, *Adv. Mater.* **2016**, *28*, 8344.
- [75] F. Xiong, H. Wang, X. Liu, J. Sun, M. Brongersma, E. Pop, Y. Cui, *Nano Lett.* **2015**, *15*, 6777.

# **Attachment No. 7**

Cite this: *J. Mater. Chem. A*, 2019, 7, 1187Insights into the intrinsic capacity of interlayer-expanded MoS<sub>2</sub> as a Li-ion intercalation host†Shan Gong,<sup>a</sup> Guangyu Zhao,<sup>b</sup> Pengbo Lyu<sup>c</sup> and Kening Sun<sup>\*b</sup>

Hierarchical MoS<sub>2</sub> hollow nanospheres with expanded interlayer spacing are synthesized and used as intercalation hosts to clarify the role of interlayer engineering in enhancing the Li-ion storage capacity. The interlayer-expanded MoS<sub>2</sub> possesses a high capacity of 220 mA h g<sup>-1</sup> at 1C rate, nearly 32% higher than the theoretical capacity of pristine MoS<sub>2</sub> (167 mA h g<sup>-1</sup>). Electrochemical characterization clarifies unambiguously that this increased capacity mainly originates from the increased Li-ion intercalation amount due to the enlarged interlayer spacing. The related mechanism is illustrated by density functional theory calculations and the universality is inspected on micro-sized MoS<sub>2</sub>. This study gives a clear insight into the intrinsic capacity of interlayer-expanded MoS<sub>2</sub> as a Li-ion intercalation host, which can facilitate the further development of high performance MoS<sub>2</sub>-based electrodes.

Received 21st August 2018  
Accepted 6th December 2018

DOI: 10.1039/c8ta08120d

rsc.li/materials-a

## Introduction

In recent years, intercalation host materials have attracted great attention due to their great promise of high-rate and safe anodes for Li-ion batteries (LIBs).<sup>1,2</sup> Unfortunately, the intercalation reactions of these materials, such as Li<sub>4</sub>Ti<sub>5</sub>O<sub>12</sub> (175 mA h g<sup>-1</sup>),<sup>3</sup> Nb<sub>2</sub>O<sub>5</sub> (200 mA h g<sup>-1</sup>),<sup>4</sup> and MoS<sub>2</sub> (167 mA h g<sup>-1</sup>),<sup>5</sup> have intrinsic limitations in terms of theoretical specific capacity. This common defect of intercalation host materials results in a limited energy density of the batteries, restricting their practical application, although they benefit from a unique layer structure with good safety and rate capability, and long cycle life.<sup>6</sup> For example, Dunn and co-workers emphasized the excellent rate capability and cycle life of MoS<sub>2</sub> as a host material for LIBs between 1 and 3 V vs. Li/Li<sup>+</sup> thanks to the Li-ion intercalation pseudocapacitance behaviour that is free from semi-infinite diffusion control. However, the Li-ion intercalation concentration in MoS<sub>2</sub> is limited to only 1 mole, corresponding to a low theoretical capacity of 167 mA h g<sup>-1</sup>.<sup>7,8</sup> Recently, several reports have indicated that interlayer engineering (expanding interlayer spacing) is an effective way to increase the intrinsic capacity of layered materials by the accommodation of more ions.<sup>9–15</sup> Although this strategy has been carried out on MoS<sub>2</sub>,<sup>16–18</sup> studies on the intrinsic source of

the capacity increase in MoS<sub>2</sub> are insufficient. It is still unclear whether the original source of the increased capacity is its geometric morphology, electric double-layer capacitance (*C<sub>dl</sub>*) or expanded interlayer spacing. Moreover, very few studies have paid attention to the bulk MoS<sub>2</sub> to eliminate the influence of nanostructures on the capacity increase; thus the universality of the higher capacity caused by interlayer engineering on non-nanometer materials is unknown. Hence, an in-depth and comprehensive investigation is needed to provide insight into the mechanism of intrinsic metal ion storage in the interlayer-distance enlarged MoS<sub>2</sub>.

Interlayer-expanded MoS<sub>2</sub> can be realized by incorporating foreign species into the interlayer gaps,<sup>19,20</sup> such as alkali metal ions,<sup>21</sup> oxygen,<sup>22–25</sup> NH<sub>3</sub>/NH<sub>4</sub><sup>+</sup>,<sup>26,27</sup> carbon materials,<sup>28</sup> and organic molecules.<sup>29</sup> Among these species, incorporation with oxygen is recognized as a simple and effective approach to expand the interlayer spacing of MoS<sub>2</sub>.<sup>22</sup> MoS<sub>2</sub> incorporated oxygen (O-MoS<sub>2</sub>) can be easily synthesized at a low reaction temperature (≤200 °C) in a hydrothermal environment, by which Mo–O bonds are inherited from the molybdate precursor in an insufficient sulfidation reaction. However, in contrast to conventional assumptions, our recent research has revealed that simply substituting the oxygen atoms for the sulfur atoms cannot achieve the detected interlayer distance of about 10 Å in O-MoS<sub>2</sub>.<sup>30</sup> A more reasonable explanation is that some molybdenum oxide species (MoO<sub>*x*</sub>(OH)<sub>*y*</sub>) are incorporated into the MoS<sub>2</sub> interlayers, and this has been verified by various measurements and density functional theory (DFT) calculations. The MoO<sub>*x*</sub>(OH)<sub>*y*</sub> pillars play a bifunctional role of expansion and stabilization, and this helps in maintaining the stability of the pseudolayered structure of MoS<sub>2</sub> when it is used as a Li-ion host material.

Based on the understanding of the structural characteristics of O-MoS<sub>2</sub>, herein, hollow nanospheres (HNSs) assembled using

<sup>a</sup>School of Chemistry and Chemical Engineering, Harbin Institute of Technology, Harbin 150001, P. R. China

<sup>b</sup>Academy of Fundamental and Interdisciplinary Sciences, Harbin Institute of Technology, Harbin 150001, P. R. China. E-mail: kening\_sunhit@126.com; zhaogy810525@gmail.com

<sup>c</sup>Department of Physical and Macromolecular Chemistry, Charles University, Hlavova 2030, Prague 2, Prague 12843, Czech Republic

† Electronic supplementary information (ESI) available: Fig. S1–S21. See DOI: 10.1039/c8ta08120d

O-MoS<sub>2</sub> nanosheet subunits (named O-MoS<sub>2</sub> HNSs) are first synthesized as a model to clarify the role of interlayer engineering in enhancing the Li-ion storage capacity of MoS<sub>2</sub>. Their hollow and porous structure can guarantee sufficient contact of electrolyte with active sites, thus facilitating a complete release of the material capacity in LIBs. The interlayer spacing of O-MoS<sub>2</sub> ranges from 9.5 to 10.0 Å, and is much larger than that of pristine MoS<sub>2</sub> (6.2 Å). We find that the enlargement of the interlayer spacing leads to a high capacity of 220 mA h g<sup>-1</sup>, nearly 32% higher than the theoretical capacity of pristine MoS<sub>2</sub>. In addition, C<sub>d1</sub> is measured and its value has a negligible contribution to the total capacity. DFT calculations are performed to illustrate the mechanism of larger interlayer spacing affording a higher Li-ion intercalation amount. Moreover, O-MoS<sub>2</sub> HNSs show extremely fast charge/discharge kinetics (111 mA h g<sup>-1</sup> at 50C, charge/discharge in less than 50 s) and a long cycling lifespan (with a capacity retention over 83% after 5000 cycles at 20C). Furthermore, O-MoS<sub>2</sub> microsized particles (O-MoS<sub>2</sub> MPS) also show an enhanced capacity of nearly 200 mA h g<sup>-1</sup>, revealing the universality of interlayer engineering on intrinsically improving the capacity of MoS<sub>2</sub>.

## Experimental

### Synthesis

**Synthesis of Mo-glycerate (MoG) spheres.** MoG spheres were synthesized *via* a solvothermal process. 60 mg MoCl<sub>5</sub> and 15 mL glycerol were dispersed in 40 mL isopropanol. The mixture was stirred for 30 min to obtain a uniform dispersion, and then transferred to a 100 mL Teflon-lined stainless steel autoclave and kept at 200 °C for 3 h. After cooling down, the dark brownish products were centrifuged and washed with water and ethanol.

**Synthesis of O-MoS<sub>2</sub> HNSs and MoS<sub>2</sub> HNSs.** MoG spheres were further sulfidated to obtain hollow MoS<sub>2</sub> nanospheres. Typically, 80 mg MoG sphere precursors were added into a 30 mL ethanol solution containing 100 mg Na<sub>2</sub>S·9H<sub>2</sub>O. The mixture was then stirred for 30 min and transferred to a 50 mL Teflon-lined stainless steel autoclave and kept at 180 °C for 6 h. The black precipitate was centrifuged, washed several times with an ethanol/H<sub>2</sub>O solution and dried at 80 °C under vacuum. MoS<sub>2</sub> HNSs were prepared by annealing the O-MoS<sub>2</sub> HNSs at 500 °C for 2 h under a H<sub>2</sub>/Ar atmosphere with a temperature ramp of 2 °C min<sup>-1</sup>.

**Synthesis of O-MoS<sub>2</sub> MPS and MoS<sub>2</sub> MPS.** 2 mmol Na<sub>2</sub>MoO<sub>4</sub>·2H<sub>2</sub>O and 4 mmol thiourea (C<sub>2</sub>H<sub>5</sub>NS) were added into 30 mL H<sub>2</sub>O, and sonicated for 30 min to get a homogeneous solution. Then the solution was transferred into a 50 mL Teflon-lined stainless steel autoclave and maintained at 180 °C for 24 h. The autoclave was naturally cooled to room temperature and the obtained sample was collected by centrifugation, washed with pure water and ethanol, and dried at 80 °C under vacuum. MoS<sub>2</sub> MPS were prepared by annealing the O-MoS<sub>2</sub> MPS at 500 °C for 2 h under a H<sub>2</sub>/Ar atmosphere with a temperature ramp of 2 °C min<sup>-1</sup>.

### Materials characterization

The samples were characterized by powder X-ray diffraction (XRD, PANalytical X'Pert PRO, with monochromated Cu K $\alpha$  radiation at 40 mA and 40 kV), X-ray photoelectron spectroscopy (XPS, Fisher Scientific Ltd, Nepean, ON), Raman spectroscopy (Renishaw inVia), scanning electron microscopy (SEM, Hitachi SU8010, 15 kV), transmission electron microscopy (TEM), high-resolution TEM (HRTEM) and selected-area electron diffraction (SAED) (Tecnai G2 F30, 200 kV); the BET surface area and BJH pore size distribution were determined using a Micromeritics ASAP 2020. Thermogravimetric analysis (TA, Q600 SDT) was conducted in air atmosphere from room temperature to 1000 °C at a heating rate of 5 °C min<sup>-1</sup>. Fourier transform infrared spectra (FT-IR) were obtained on an SP100 analyzer (Perkin Elmer).

### Electrochemical measurements

Electrochemical tests were conducted by cycling two-electrode 2025 coin cells with lithium foil as the counter/reference electrode and a Celgard 2400 membrane as the separator. A mixed slurry consisting of the O-MoS<sub>2</sub> HNSs, carbon black, and polyvinylidene difluoride in a weight ratio of 80 : 10 : 10 on copper foil was used as the working electrode. The O-MoS<sub>2</sub> HNS electrode was pressed before assembling the coin cells. The loading density of the prepared electrodes was ~1 mg cm<sup>-2</sup>. The cells were assembled in an argon-filled glove box with moisture and oxygen partial pressure under 0.1 ppm. 1 M LiPF<sub>6</sub> in a diethyl carbonate, ethylene carbonate and ethyl methyl carbonate (DC/EC/EMC, 1 : 1 : 1 by vol.) solvent (Sigma-Aldrich) was used as the electrolyte. An Arbin Battery Testing System was employed for galvanostatic charge/discharge tests in the potential range of 1.0–3.0 V (*vs.* Li/Li<sup>+</sup>). A PARSTAT 2273 electrochemical workstation was used for cyclic voltammetry (CV) and electrochemical impedance spectroscopy (EIS) measurements. The EIS measurements were performed in a frequency range from 100 kHz to 10 mHz at an amplitude of 10 mV.

### Computational methods

DFT calculations were performed using the projector augmented wave (PAW)<sup>31</sup> formalism within the generalized gradient approximation (GGA) method with the Perdew–Burke–Ernzerhof (PBE) exchange–correlation functional as implemented in the Vienna Ab Initio Simulation Package (VASP).<sup>32–34</sup> The cutoff energy of 500 eV for the plane-wave basis set has been consistently used in all calculations. A convergence criterion of 0.01 was used for the forces in geometry optimizations and 10<sup>-5</sup> eV was used for the energy convergence. Slab models which contain double layers were used with 3 × 3 supercells and 3 × 3 × 1 Monkhorst–Pack grids.<sup>35</sup>

The formation energy per Li ( $E_f$ ) of MoS<sub>2</sub> and O-MoS<sub>2</sub> is defined in eqn (1) and (2)

$$E_f = (E_{\text{tot}}(\text{MoS}_2 + n\text{Li}) - E_{\text{tot}}(\text{MoS}_2) - n\mu_{\text{Li}})/n \quad (1)$$

$$E_f = (E_{\text{tot}}(\text{O-MoS}_2 + n\text{Li}) - E_{\text{tot}}(\text{O-MoS}_2) - n\mu_{\text{Li}})/n \quad (2)$$

respectively, where  $E_{\text{tot}}(\text{MoS}_2)$  and  $E_{\text{tot}}(\text{O-MoS}_2)$  are the total energies of  $\text{MoS}_2$  and  $\text{O-MoS}_2$ ,  $\mu_{\text{Li}}$  is the chemical potential of Li and is taken as the cohesive energy per atom of bulk Li, and  $E_{\text{tot}}(\text{MoS}_2 + n\text{Li})$  and  $E_{\text{tot}}(\text{O-MoS}_2 + n\text{Li})$  are the total energies of lithiated structures, respectively.  $n$  is the number of Li atoms.

Considering the energy difference between neighboring  $\text{Li}_x\text{MoS}_2$  phases and neglecting the volume and entropy effects, the open-circuit voltage (OCV) could be given by eqn (3):

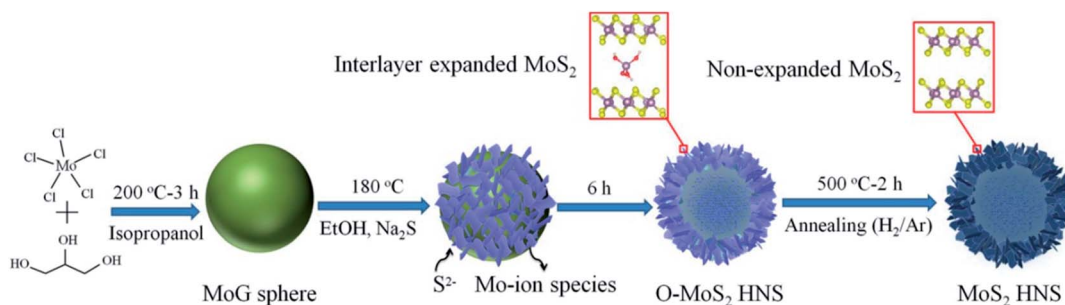
$$\text{OCV} = -[E(\text{Li}_{x_2}\text{MoS}_2) - E(\text{Li}_{x_1}\text{MoS}_2) - (x_2 - x_1)n\mu_{\text{Li}}]/(x_2 - x_1) \quad (3)$$

where  $E(\text{Li}_{x_2}\text{MoS}_2)$  and  $E(\text{Li}_{x_1}\text{MoS}_2)$  are the total energies of  $\text{MoS}_2$  after lithiation at  $x = x_1$  and  $x = x_2$ , respectively.  $\mu_{\text{Li}}$  is the chemical potential of Li and is taken as the cohesive energy per atom of bulk Li.

## Results and discussion

The synthesis process of both  $\text{O-MoS}_2$  HNSs and  $\text{MoS}_2$  HNSs is shown in Scheme 1. First of all, highly uniform Mo-glycerate ( $\text{MoG}$ ) solid spheres were synthesized *via* a solvothermal method using  $\text{MoCl}_5$  as the molybdenum source, and glycerol and isopropanol together as the mixed solvent. Subsequent sulfidation with  $\text{Na}_2\text{S}$  at  $180^\circ\text{C}$  converted the  $\text{MoG}$  solid spheres to  $\text{O-MoS}_2$  HNSs. The relatively low reaction temperature ( $\leq 200^\circ\text{C}$ ) caused insufficient sulfidation, resulting in the incorporation of residual Mo–O bonds ( $\text{MoO}_x(\text{OH})_y$ ) into the adjacent  $\text{MoS}_2$  layers and the enlargement of the interlayer spacing.<sup>22,30</sup> As for the unique hollow structure, the inner cavity should result from the anion exchange reaction, including the slow inward diffusion of  $\text{S}^{2-}$  and fast outward diffusion of Mo-ion species.<sup>36,37</sup> Finally, non-expanded  $\text{MoS}_2$  HNSs were obtained by annealing  $\text{O-MoS}_2$  HNSs at  $500^\circ\text{C}$  in  $\text{H}_2/\text{Ar}$ . The variation in layer spacing implies a change in the interlaminar structure, and this will be discussed in the following.

The XRD pattern of  $\text{O-MoS}_2$  HNSs (Fig. 1a) shows that the (002) peak shifts to a low-angle region ( $2\theta = 9.0^\circ$ ) compared with the standard pattern of  $\text{MoS}_2$  (2H phase  $\text{MoS}_2$ , JCPDS card no. 37-1492). This indicates that the corresponding  $d$  spacing is enlarged from  $6.2 \text{ \AA}$  to around  $9.8 \text{ \AA}$ . However, the two broad peaks in the high-angle region ( $32^\circ$  and  $57^\circ$ ) are still well indexed to the (100) and (110) planes of pristine 2H phase  $\text{MoS}_2$ , indicating a normal atomic arrangement in the basal planes.



Scheme 1 Schematic illustration of the synthesis process of both  $\text{O-MoS}_2$  HNSs and  $\text{MoS}_2$  HNSs.

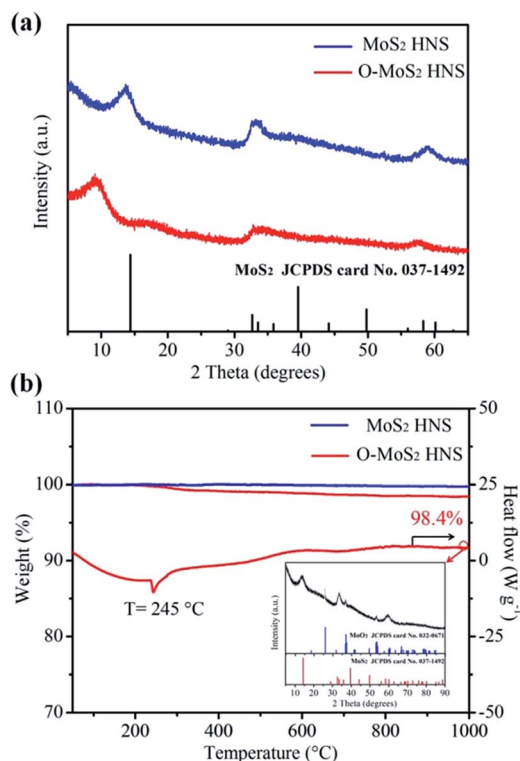


Fig. 1 (a) XRD patterns of  $\text{O-MoS}_2$  HNSs and  $\text{MoS}_2$  HNSs; (b) TGA curves of  $\text{O-MoS}_2$  HNSs and  $\text{MoS}_2$  HNSs, and DSC curve of  $\text{O-MoS}_2$  HNSs. The inset shows the XRD pattern of  $\text{O-MoS}_2$  HNSs after thermal treatment.

According to our previous report, some molybdenum oxide species are considered to be incorporated into the  $\text{MoS}_2$  interlayers and cause the expansion of the interlayer spacing.<sup>30</sup> Among the three typical  $\text{MoO}_x(\text{OH})_y$  species ( $\text{Mo}(\text{OH})_4$ ,  $\text{MoO}(\text{OH})_3$ , and  $\text{MoO}(\text{OH})_2$ ), the interlayer distance of  $\text{O-MoS}_2$  HNSs matches well with that of  $\text{MoS}_2$  incorporated with  $\text{Mo}(\text{OH})_4$ , as shown in the calculated results in Fig. S1.† As for  $\text{MoS}_2$  HNSs, their XRD pattern can be assigned to the 2H phase. The variation in the XRD patterns reveals that  $\text{O-MoS}_2$  HNSs convert to a thermodynamically stable phase after annealing. To better understand the structural characteristics of  $\text{O-MoS}_2$  HNSs and to study the structural conversion in the heating process, TGA and DSC measurements were performed under a  $\text{N}_2$

atmosphere. As shown in Fig. 1b, the flat TGA curve of MoS<sub>2</sub> HNSs exhibits apparent thermodynamic stability. As for O-MoS<sub>2</sub> HNSs, a 1.6% weight loss is observed in the heating process, and an obvious endothermic peak emerges at 245 °C in the DSC curve. XRD was further carried out to investigate O-MoS<sub>2</sub> HNSs after the TGA test. As can be seen in the inset of Fig. 1b, the right shift of the (002) peak verifies the structural conversion; thus the MoS<sub>2</sub> HNSs can be obtained by eliminating oxygen in a H<sub>2</sub>/Ar atmosphere. Additionally, another interesting observation is the appearance of a MoO<sub>2</sub> peak in the XRD pattern of heat-treated O-MoS<sub>2</sub> HNSs, which should originate from the incorporated Mo(OH)<sub>4</sub>. Moreover, the existence of hydroxyl groups in O-MoS<sub>2</sub> HNSs was confirmed by FT-IR tests in paraffin oil (Fig. S2†), further verifying Mo(OH)<sub>4</sub> incorporation. All the above results indicate that Mo(OH)<sub>4</sub> is a suitable species for incorporation into the interlayers of MoS<sub>2</sub>.

SEM and TEM were further performed to study the morphology of the as-prepared samples. The SEM images indicate that the MoG precursors are highly uniform spheres having a diameter of around 500 nm and a rather smooth surface (Fig. 2a). Mo, C and O elements are confirmed to be present on the spheres by EDS analysis (Fig. S3†). The SEM (Fig. 2b and S4a†) and TEM (Fig. 2c and S4b†) images show the hollow spherical morphology of O-MoS<sub>2</sub> HNSs with a uniform diameter of around 600 nm, and the hierarchical shells are constructed with nanosheet subunits. In addition, after shortening the sulfidation time, residual MoG cores are detected in

the hollow spheres (Fig. S5†), verifying the abovementioned formation mechanism of the anion exchange reaction. Interestingly, highly dispersed ultrathin pristine MoS<sub>2</sub> nanosheets instead of whole MoS<sub>2</sub> hollow spheres are obtained as the sulfidation temperature is increased to 220 °C under otherwise identical conditions (XRD pattern and SEM image in Fig. S6†). This phenomenon is also consistent with the abovementioned formation mechanism of O-MoS<sub>2</sub> synthesized at a low sulfidation temperature with residual Mo–O bonds inherited from the precursors.<sup>22</sup> The collapsed architectures are caused by the excessively intense reaction. The EDS maps in Fig. 2d show the homogeneous distribution of the Mo, S, and O elements on the nanosheets of O-MoS<sub>2</sub> HNSs, and the ratio of Mo/S/O in O-MoS<sub>2</sub> is about 1/1.96/0.24 (O<sub>0.24</sub>MoS<sub>1.96</sub>, O = 7.60, Mo = 31.19, and S = 61.21 atom%, Fig. S7†), implying successful oxygen incorporation into MoS<sub>2</sub>. In contrast, the O element is rarely found on the MoS<sub>2</sub> HNS nanosheets (Fig. S8†).

The HRTEM image (Fig. 2e) reveals that the O-MoS<sub>2</sub> HNSs have interlayer spacings ranging from 9.5 Å to 10.0 Å, which is in good agreement with the value calculated from the XRD result. The SAED result displaying a pattern of concentric rings (Fig. S9†) reveals the polycrystallinity of O-MoS<sub>2</sub> HNSs. As for MoS<sub>2</sub> HNSs, compared with O-MoS<sub>2</sub> HNSs, the same morphology with no apparent deformation (Fig. 2f and S10†), and similar surface area (60.3 m<sup>2</sup> g<sup>-1</sup> of MoS<sub>2</sub> HNS vs. 63.5 m<sup>2</sup> g<sup>-1</sup> of O-MoS<sub>2</sub> HNS) and pore structure (Fig. S11†) are found, except for the decreased interlayer spacing of ~6.2 Å (Fig. 2g).

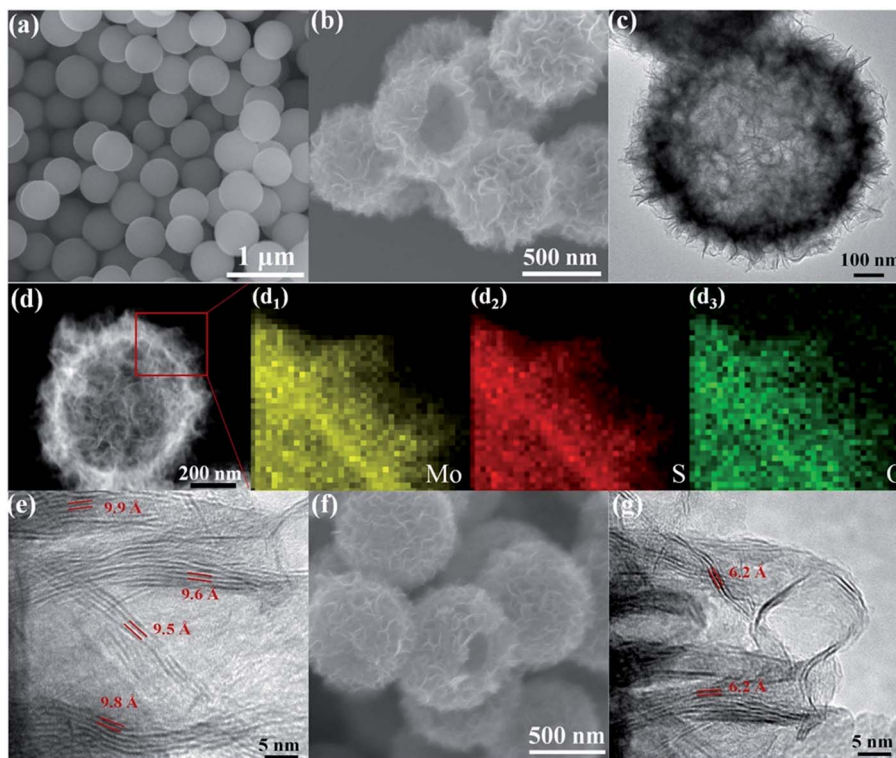


Fig. 2 (a) SEM image of the MoG spheres; (b) SEM and (c) TEM images of O-MoS<sub>2</sub> HNSs; (d<sub>1</sub>, d<sub>2</sub>, and d<sub>3</sub>) elemental mapping images of O-MoS<sub>2</sub> HNS nanosheets shown in (d): Mo (d<sub>1</sub>), S (d<sub>2</sub>) and O (d<sub>3</sub>) elements are homogeneously distributed; (e) HRTEM image of O-MoS<sub>2</sub> HNSs; (f) SEM and (g) HRTEM images of MoS<sub>2</sub> HNSs.



XPS was carried out to investigate the chemical composition of O-MoS<sub>2</sub> HNSs and MoS<sub>2</sub> HNSs. The atom% of the O element is 8.10% in O-MoS<sub>2</sub> HNSs and the ratio of Mo/S/O is about 1/1.95/0.26 (Fig. S12<sup>†</sup>), consistent with the EDS results. The deconvolution of the Mo 3d spectrum reveals that the binding energies of the Mo 3d<sub>3/2</sub> and Mo 3d<sub>5/2</sub> peaks for O-MoS<sub>2</sub> HNSs (228.48 and 231.73 eV, Fig. 3a) are lower than those for MoS<sub>2</sub> HNSs (229.43 and 232.53 eV, Fig. 3c). The peaks at 235.8 and 233.0 eV are attributed to Mo(VI).<sup>27,38</sup> Similar downshifts are also observed for the S 2p peaks of O-MoS<sub>2</sub> HNSs (161.43 eV and 162.68 eV, Fig. 3b) compared with those of MoS<sub>2</sub> HNSs (162.23 eV and 163.53 eV, Fig. 3d). This phenomenon indicates that O-MoS<sub>2</sub> HNSs exhibit a dominant 1T phase,<sup>39,40</sup> and MoS<sub>2</sub> HNSs exhibit a 2H phase. The existence of Mo(IV)-O bonds is proved by the deconvolution of the O 1s spectrum (Fig. S13<sup>†</sup>), which further verifies Mo(OH)<sub>4</sub> incorporation. The electronic structure of MoS<sub>2</sub> may be influenced by the incorporated species; thus the O-MoS<sub>2</sub> HNSs exhibit properties of the 1T phase.<sup>41,42</sup> The Raman spectroscopy results further verify the formation of the 1T phase and oxygen incorporation in O-MoS<sub>2</sub> HNSs (Fig. S14<sup>†</sup>). Four additional peaks between 140 and 350 cm<sup>-1</sup> are detected, which can be assigned to the 1T phase of MoS<sub>2</sub>.<sup>43,44</sup> In addition, the vibrational modes for Mo-O bonds are observed at 285 and 334 cm<sup>-1</sup>, further proving the successful oxygen incorporation in the product.

To understand the effect of larger interlayer spacing on electrochemical behavior, CV was performed to examine the Li-ion storage mechanism. As illustrated in Fig. S15,<sup>†</sup> in the initial cycles, MoS<sub>2</sub> HNSs undergo an obvious phase transition from 2H to 1T in the cathodic sweeps, while O-MoS<sub>2</sub> HNSs exhibit unobvious variation with a stable phase. In addition, compared with that of MoS<sub>2</sub> HNSs, the less well-defined peaks in the CV curve of O-MoS<sub>2</sub> HNSs indicate the mitigatory interlayer interactions of O-MoS<sub>2</sub> during the Li-ion intercalation/deintercalation process because of the larger interlayer

spacing.<sup>16</sup> Galvanostatic study was carried out to evaluate the electrochemical performances of O-MoS<sub>2</sub> HNSs and MoS<sub>2</sub> HNSs in LIBs. Fig. 4a shows the discharge capacities of both materials in a wide range from 1C to 100C (1C = 0.167 A g<sup>-1</sup>). MoS<sub>2</sub> HNSs deliver a specific capacity of 158 mA h g<sup>-1</sup> at 1C rate, close to the theoretical specific capacity (167 mA h g<sup>-1</sup>). Remarkably, O-MoS<sub>2</sub> HNSs deliver a higher specific capacity of 220 mA h g<sup>-1</sup> at 1C rate, nearly 32% higher than the theoretical value for MoS<sub>2</sub>. In addition, the O-MoS<sub>2</sub> HNSs exhibit a markedly better rate performance compared with MoS<sub>2</sub> HNSs as the C-rate increases. For example, O-MoS<sub>2</sub> HNSs maintain a capacity of 111 mA h g<sup>-1</sup> at a high rate of 50C (50% of the original 1C capacity); at 100C, the O-MoS<sub>2</sub> HNSs still deliver a specific capacity of 72 mA h g<sup>-1</sup>, nearly three times that of MoS<sub>2</sub> HNSs (25 mA h g<sup>-1</sup>). To eliminate the interference of the phase transition from 2H to 1T of MoS<sub>2</sub> HNSs during the initial cycles (Fig. S16<sup>†</sup>), the charge/discharge curves corresponding to the 10th cycle of each rate in Fig. 4a are shown in Fig. 4b and c. The consecutive decrease of voltage in the charge/discharge curves is observed in both materials, suggesting a pseudocapacitive behavior instead of a phase transition process.<sup>45,46</sup> Moreover, O-MoS<sub>2</sub> HNSs also exhibit a more stable cycling performance compared with MoS<sub>2</sub> HNSs (Fig. 4d). After 5000 cycles at 20C, the specific capacity of O-MoS<sub>2</sub> HNSs is 122 mA h g<sup>-1</sup> (over 83% capacity retention), while MoS<sub>2</sub> HNSs retain a specific capacity of 64 mA h g<sup>-1</sup> (only 63.4% capacity retention). This means that O-MoS<sub>2</sub> HNSs possess more suitable lattice spacings for fast Li-ion transport. The coulombic efficiency of O-MoS<sub>2</sub> HNSs is higher than 99.9%, demonstrating the good reversibility of Li-ion intercalation/deintercalation in O-MoS<sub>2</sub> HNSs.

To provide insight into the intrinsic capacity of O-MoS<sub>2</sub> HNSs, the kinetics of both O-MoS<sub>2</sub> HNSs and MoS<sub>2</sub> HNSs (after phase transition) was analyzed to investigate the charge storage mechanism based on the CV measurements (see method details in "Kinetics analysis", ESI<sup>†</sup>). First, the *b*-values were calculated to analyse the charge storage process. As shown in Fig. 5a and b, the various *b*-values at the peak currents in the anodic and cathodic processes for both materials are all in the range from 0.96 to 1.00, indicating that both materials exhibit dominant capacitive-controlled behavior instead of the traditional diffusion dominated charge storage.<sup>47,48</sup> Furthermore, the capacitive contributions were determined quantitatively over the entire voltage range. The fractions of capacitive contributions at the scan rate of 1 mV s<sup>-1</sup> for both materials are shown in Fig. 5c and d. It can be found that 92.4% of the total capacity is capacitive for O-MoS<sub>2</sub> HNSs, and the total integrated capacitive contribution of MoS<sub>2</sub> HNSs is 90.9%. Accordingly, the main charge storage in both materials is capacitive, and the capacitive currents occupy the main area of the peak regions of the CV curves, in good agreement with the calculated *b*-values.

The high capacitive contribution in MoS<sub>2</sub> can be divided into intercalation pseudocapacitance and surface double-layer capacitance (*C*<sub>dl</sub>), originating from the ultra-fast Li-ion intercalation in the MoS<sub>2</sub> layers and the charge adsorbed on the MoS<sub>2</sub> surface, respectively, according to Dunn's work.<sup>7,8,47,49</sup> Both of the capacitive contributions can help the electrochemical kinetics as they tend to be free from the semi-infinite

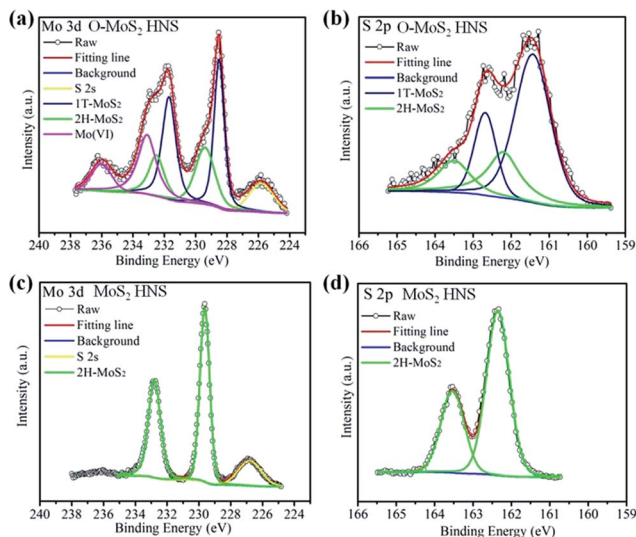


Fig. 3 (a) Mo 3d and (b) S 2p spectra of O-MoS<sub>2</sub> HNSs; (c) Mo 3d and (d) S 2p spectra of MoS<sub>2</sub> HNSs.

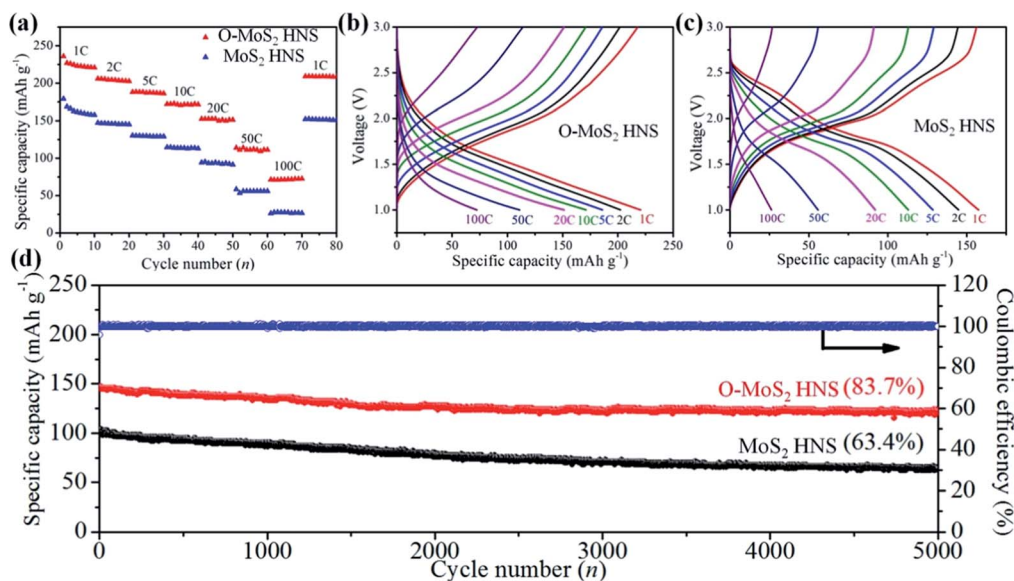


Fig. 4 (a) Comparison of the rate performances of O-MoS<sub>2</sub> HNSs and MoS<sub>2</sub> HNSs at various current rates. The galvanostatic charge/discharge curves of (b) O-MoS<sub>2</sub> HNSs and (c) MoS<sub>2</sub> HNSs; the curves are based on the 10th cycle of the various current rates in Fig. 4a. (d) The cycling performances of O-MoS<sub>2</sub> HNSs and of MoS<sub>2</sub> HNSs at 20C rate. The blue trace shows the coulombic efficiency of O-MoS<sub>2</sub> HNSs. Both materials were pre-cycled 30 times at 1C before the cycling stability measurement.

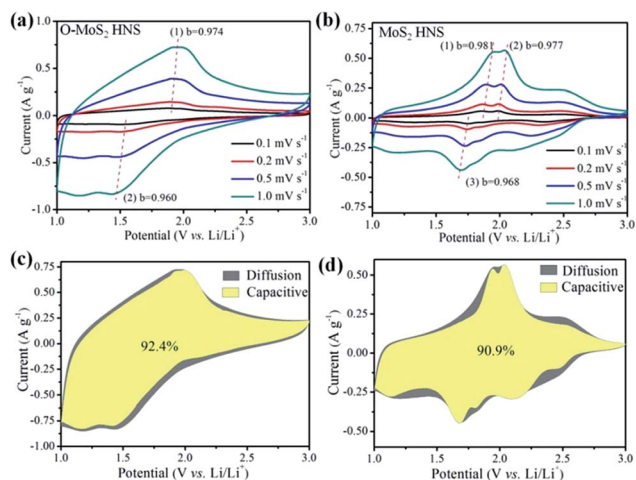


Fig. 5 CV curves of (a) O-MoS<sub>2</sub> HNSs and (b) MoS<sub>2</sub> HNSs at different scan rates; *b*-values are determined by using the relationship between peak current and scan rate. The capacitive and diffusion controlled contributions of (c) O-MoS<sub>2</sub> HNSs and (d) MoS<sub>2</sub> HNSs at 1 mV s<sup>-1</sup>.

diffusion control. Therefore, the contributions of the two kinds of capacitance should be distinguished to confirm the Li-ion intercalation capacities of the materials.

Here, the values of  $C_{dl}$  in the two materials were measured. CV tests were performed at high scan rates (75, 100, 125, 150, 175, and 200 mV s<sup>-1</sup>) in a selected potential range of 2.80–2.90 V (vs. Li/Li<sup>+</sup>), in which, faradaic currents on both O-MoS<sub>2</sub> HNSs and MoS<sub>2</sub> HNSs are negligible (as shown in the CV curves between 1 and 3 V vs. Li/Li<sup>+</sup> in Fig. 5a and b). The CV curves of both materials (Fig. S17<sup>†</sup>) are nearly rectangular in shape, indicating good charge propagation within the electrodes.<sup>50</sup> The

$C_{dl}$  is estimated by plotting the current gap  $\Delta J/(J_{anodic} - J_{cathodic})$  at 2.85 V (vs. Li/Li<sup>+</sup>) against the scan rate (Fig. 6), where the slope is  $2C_{dl}$ . The results show that both O-MoS<sub>2</sub> HNSs and MoS<sub>2</sub> HNSs exhibit very low  $C_{dl}$  values of 0.55 mF g<sup>-1</sup> and 0.47 mF g<sup>-1</sup>, respectively.

Based on the above results, we can conclude that the stored charge in both O-MoS<sub>2</sub> HNSs and MoS<sub>2</sub> HNSs mainly originates from the intercalation pseudocapacitance instead of  $C_{dl}$ . Considering that O-MoS<sub>2</sub> HNSs and MoS<sub>2</sub> HNSs have the same morphology and similar surface area, the increased capacity of O-MoS<sub>2</sub> HNSs should result from the increased Li-ion storage amount in the expanded interlayer spacing.

Moreover, the Li-ion transport properties in both samples at 1C (after phase transition) were further studied by EIS (see

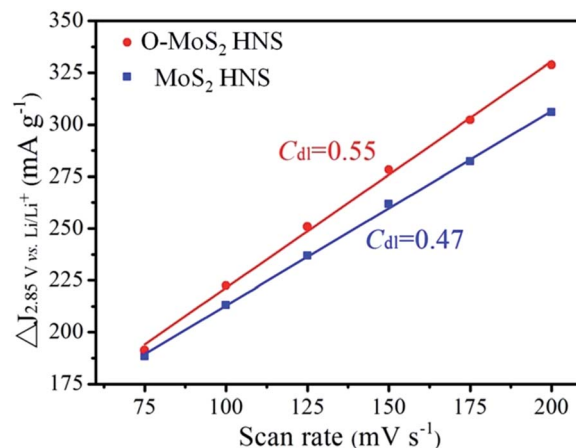


Fig. 6 The relationship between  $\Delta J(J_{anodic} - J_{cathodic})$  and the scan rate of both O-MoS<sub>2</sub> HNSs and MoS<sub>2</sub> HNSs at 2.85 V vs. Li/Li<sup>+</sup>.

method details in “Impedance Spectroscopy Analysis”, ESI†). As shown in Fig. S18,† O-MoS<sub>2</sub> HNSs show an obviously lower internal resistance than MoS<sub>2</sub> HNSs, since the oxygen incorporation in MoS<sub>2</sub> ultrathin nanosheets can lead to more charge carriers and higher intrinsic conductivity.<sup>22</sup> The Warburg coefficient ( $\sigma$ ) value of O-MoS<sub>2</sub> HNSs ( $\sigma = 68.7$ ) is smaller than that of MoS<sub>2</sub> HNSs ( $\sigma = 86.0$ ), indicating that the Li-ion transport kinetics of O-MoS<sub>2</sub> HNSs is 1.5 times higher than that of MoS<sub>2</sub> HNSs. Therefore, the expanded interlayer spacing leads to easier and faster Li-ion intercalation/deintercalation kinetics, leading to the better rate capability of O-MoS<sub>2</sub> HNSs.

DFT calculations were performed to verify the role of the larger interlayer spacing of MoS<sub>2</sub> in increasing the Li-ion intercalation amount. Considering the many difficulties in achieving global minima when taking the intercalating species into account and considering the limited amount of incorporated Mo(OH)<sub>4</sub>, only the interlayer spacing variation was considered for Li-ion intercalation in the calculations. A sulfur atom in MoS<sub>2</sub> is substituted by an oxygen atom in one unit of MoS<sub>2</sub> to build the O-MoS<sub>2</sub> model. The formation energies of lithium intercalation into the interlayer spacing were calculated within a  $3 \times 3$  supercell of MoS<sub>2</sub>. As shown in Fig. 7a and b, for pristine MoS<sub>2</sub> ( $d = 6.2$  Å),  $n = 1, 2, 3, 6, 9,$  and  $10$  Li atoms were accommodated which results in Li<sub>*x*</sub>MoS<sub>2</sub> with  $x = 0.11, 0.22,$

$0.33, 0.67, 1,$  and  $1.11$ . As for O-MoS<sub>2</sub> ( $d = 9.8$  Å), the intercalation number of Li atoms was  $n = 1, 2, 6, 12, 18,$  and  $19$ , resulting in  $x = 0.11, 0.22, 0.67, 1.33, 2,$  and  $2.11$ . Fig. 7c shows that the formation energies of Li in O-MoS<sub>2</sub> are always more negative than those in MoS<sub>2</sub>, which indicates a more favourable exothermic reaction between the MoS<sub>2</sub> layers and Li.<sup>51</sup> In addition, the open-circuit voltage (OCV) profiles were investigated for evaluation of the specific capacities, as the maximum Li content can be obtained when the OCV begins to change from positive to negative.<sup>52</sup> It is clear that the OCV of pristine MoS<sub>2</sub> switches to negative from  $x = 1$  to  $x = 1.11$ , while O-MoS<sub>2</sub> has a positive OCV up to  $x = 2.11$  (Fig. 7d). The corresponding calculated specific capacity is  $167 \text{ mA h g}^{-1}$  ( $x = 1$ ) for MoS<sub>2</sub> and more than  $334 \text{ mA h g}^{-1}$  ( $x = 2$ ) for O-MoS<sub>2</sub>. Based on the simulation results, it is confirmed that the larger interlayer spacing of MoS<sub>2</sub> is able to accommodate more Li-ions, leading to higher specific capacity.

Furthermore, we synthesized O-MoS<sub>2</sub> microsized particles (MPS) to inspect the universality of enlarged MoS<sub>2</sub> accommodating higher Li-ion intercalation amounts. The preparation method is taken from Xie's work.<sup>22</sup> In spite of the similar morphology of the two samples, O-MoS<sub>2</sub> MPS have an expanded interlayer spacing of around  $10.0$  Å, in contrast to the spacing value ( $\sim 6.2$  Å) of pristine MoS<sub>2</sub> MPS (XRD pattern is shown in

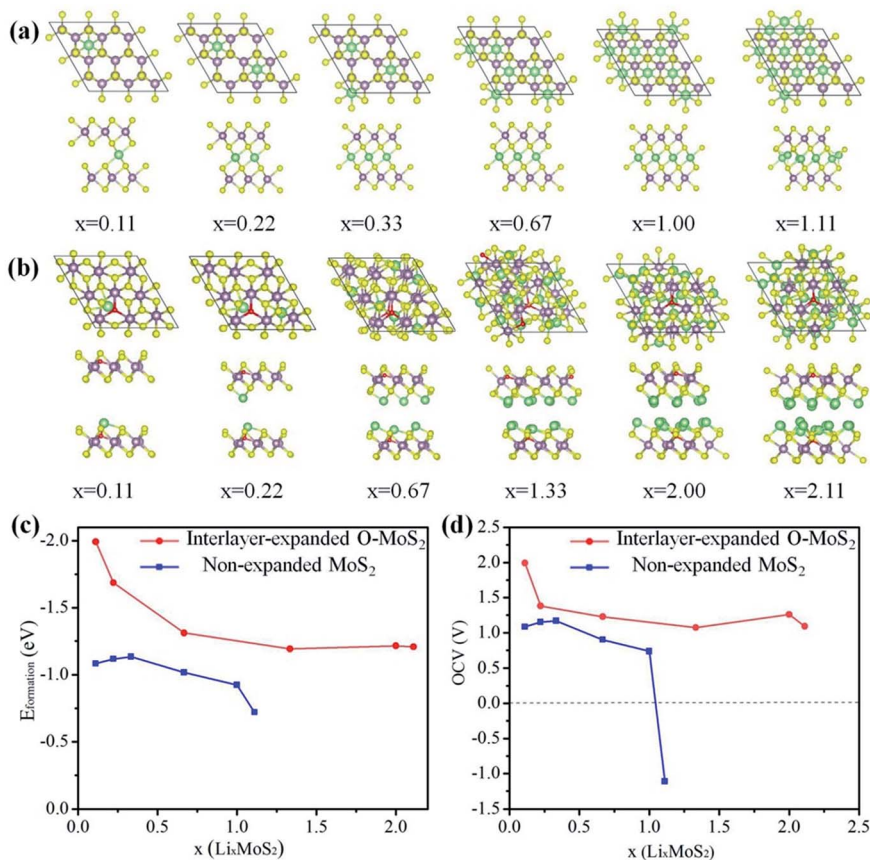


Fig. 7 The atomic structures of Li intercalation in (a) non-expanded MoS<sub>2</sub> and (b) interlayer-expanded O-MoS<sub>2</sub>; the top and side views are shown, respectively. (c) The formation energies of  $x$  Li atoms in non-expanded MoS<sub>2</sub> and interlayer-expanded O-MoS<sub>2</sub>. (d) The OCV profiles with respect to the Li content ( $x$ ) for non-expanded MoS<sub>2</sub> and interlayer-expanded O-MoS<sub>2</sub>.

Fig. S19; † SEM and HRTEM images are shown in Fig. S20†). Fig. S21a† shows the rate performances of O-MoS<sub>2</sub> MPS and MoS<sub>2</sub> MPS at various current rates. O-MoS<sub>2</sub> MPS exhibit a specific capacity of nearly 200 mA h g<sup>-1</sup> at 1C, which is apparently larger than the theoretical capacity of pristine MoS<sub>2</sub>; MoS<sub>2</sub> electrodes deliver a specific capacity of 152 mA h g<sup>-1</sup> at the same rate. This result indicates the universality of the higher capacity originating from interlayer engineering on MoS<sub>2</sub>. Moreover, a specific capacity of 68 mA h g<sup>-1</sup> is retained for O-MoS<sub>2</sub> MPS at a high rate of 50C (35% of the original 1C capacity), while MoS<sub>2</sub> MPS only retain 21% of the original 1C capacity at 50C. The better rate performance of O-MoS<sub>2</sub> MPS also verifies the viewpoint that larger interlayer spacing leads to faster Li-ion intercalation kinetics. In addition, compared with those of O-MoS<sub>2</sub> HNSs, the limited capacity and rate capability of O-MoS<sub>2</sub> MPS are caused by the lower electrode/electrolyte contact area and longer distance for Li-ion diffusion. The corresponding galvanostatic charge/discharge curves of O-MoS<sub>2</sub> and MoS<sub>2</sub> MPS also show marked pseudocapacitive behaviors (Fig. S21b and c†).

## Conclusions

In summary, O-MoS<sub>2</sub> HNSs (with an expanded interlayer spacing around 9.8 Å) and MoS<sub>2</sub> HNSs (interlayer spacing of 6.2 Å, possessing the same morphology as O-MoS<sub>2</sub> HNSs) have been synthesized. They serve as model compounds to unambiguously demonstrate that Li-ion storage amounts are closely linked with their interlayer spacings. The results show that the capacities of MoS<sub>2</sub> materials increase with their interlayer spacings. The O-MoS<sub>2</sub> HNSs exhibit a specific capacity of 220 mA h g<sup>-1</sup> at 1C rate, nearly 32% higher than the theoretical Li-ion intercalation capacity of MoS<sub>2</sub>. Electrochemical measurements show that the stored charge mainly originates from the intercalation pseudocapacitance and the C<sub>dl</sub> contributes little to the increase in capacity. Therefore, expanding its interlayer spacing is an effective way to conquer the drawback of MoS<sub>2</sub> in intrinsic capacity limitation. Meanwhile, O-MoS<sub>2</sub> HNSs also show improved rate performance and cycling stability in comparison to MoS<sub>2</sub> HNSs, owing to the more suitable lattice spacing of O-MoS<sub>2</sub> HNSs for fast Li-ion transport. In addition, DFT calculations reveal the effect of larger layer spacing on the Li-ion intercalation amount. Moreover, bulk MoS<sub>2</sub> was synthesized and used for inspecting the universality of the enlarged interlayer accommodating more Li-ions. On the basis of the advantages (good safety, stability, rate capability, and long life) of pristine MoS<sub>2</sub>, such an interlayer-expanded MoS<sub>2</sub> with enhanced capacity is a more promising material as high-rate anode for LIBs. This strategy can also be extended to other intercalation host materials and can pave the way for exploring high-rate and high-safety electrodes for LIBs and other alkali metal-ion batteries.

## Conflicts of interest

There are no conflicts to declare.

## Acknowledgements

This work was supported by the National Natural Science Foundation of China (No. 21776052), the Natural Science Foundation of Heilongjiang Province (No. QC2016010) and the Fundamental Research Funds for the Central Universities (No. HIT. IBRSEM. A. 201407).

## Notes and references

- Z. Xing, S. Wang, A. Yu and Z. Chen, *Nano Energy*, 2018, **50**, 229–244.
- J. Mao, T. Zhou, Y. Zheng, H. Gao, H. K. Liu and Z. Guo, *J. Mater. Chem. A*, 2018, **6**, 3284–3333.
- Y. He, A. Muhetaer, J. Li, F. Wang, C. Liu, Q. Li and D. Xu, *Adv. Energy Mater.*, 2017, **7**, 1700950.
- V. Augustyn, J. Come, M. A. Lowe, J. W. Kim, P. Taberna, S. H. Tolbert, H. D. Abruña, P. Simon and B. Dunn, *Nat. Mater.*, 2013, **12**, 518–522.
- T. Stephenson, Z. Li, B. Olsen and D. Mitlin, *Energy Environ. Sci.*, 2014, **7**, 209–231.
- J. Cabana, L. Monconduit, D. Larcher and M. R. Palacín, *Adv. Mater.*, 2010, **22**, E170–E192.
- J. B. Cook, H. Kim, T. C. Lin, C. Lai, B. Dunn and S. H. Tolbert, *Adv. Energy Mater.*, 2017, **7**, 1601283.
- J. B. Cook, H. Kim, Y. Yan, J. S. Ko, S. Robbennolt, B. Dunn and S. H. Tolbert, *Adv. Energy Mater.*, 2016, **6**, 1501937.
- Y. Xue, Q. Zhang, W. Wang, H. Cao, Q. Yang and L. Fu, *Adv. Energy Mater.*, 2017, **7**, 1602684.
- Y. Wen, K. He, Y. Zhu, F. Han, Y. Xu, I. Matsuda, Y. Ishii, J. Cumings and C. Wang, *Nat. Commun.*, 2014, **5**, 4033.
- J. Yang, X. Zhou, D. Wu, X. Zhao and Z. Zhou, *Adv. Mater.*, 2017, **29**, 1604108.
- Y. Kang, S. C. Jung, J. W. Choi and Y. Han, *Chem. Mater.*, 2015, **27**, 5402–5406.
- P. Lian, Y. Dong, Z. Wu, S. Zheng, X. Wang, S. Wang, C. Sun, J. Qin, X. Shi and X. Bao, *Nano Energy*, 2017, **40**, 1–8.
- M. Clites and E. Pomerantseva, *Energy Storage Materials*, 2018, **11**, 30–37.
- M. Clites, B. W. Byles and E. Pomerantseva, *J. Mater. Chem. A*, 2016, **4**, 7754–7761.
- Y. Li, Y. Liang, F. C. Robles Hernandez, H. Deog Yoo, Q. An and Y. Yao, *Nano Energy*, 2015, **15**, 453–461.
- Z. Hu, L. Wang, K. Zhang, J. Wang, F. Cheng, Z. Tao and J. Chen, *Angew. Chem.*, 2014, **126**, 13008–13012.
- J. Guo, H. Zhu, Y. Sun, L. Tang and X. Zhang, *J. Mater. Chem. A*, 2016, **4**, 4783–4789.
- K. D. Rasamani, F. Alimohammadi and Y. Sun, *Mater. Today*, 2017, **20**, 83–91.
- J. Xu, J. Zhang, W. Zhang and C. Lee, *Adv. Energy Mater.*, 2017, **7**, 1700571.
- M. Acerce, D. Voiry and M. Chhowalla, *Nat. Nanotechnol.*, 2015, **10**, 313–318.
- J. Xie, J. Zhang, S. Li, F. Grote, X. Zhang, H. Zhang, R. Wang, Y. Lei, B. Pan and Y. Xie, *J. Am. Chem. Soc.*, 2013, **135**, 17881–17888.

- 23 A. Liu, L. Zhao, J. Zhang, L. Lin and H. Wu, *ACS Appl. Mater. Interfaces*, 2016, **8**, 25210–25218.
- 24 D. Wu, Y. Wang, F. Wang, H. Wang, Y. An, Z. Gao, F. Xu and K. Jiang, *Carbon*, 2017, **123**, 756–766.
- 25 J. Zhou, G. Fang, A. Pan and S. Liang, *ACS Appl. Mater. Interfaces*, 2016, **8**, 33681–33689.
- 26 Q. Liu, X. Li, Q. He, A. Khalil, D. Liu, T. Xiang, X. Wu and L. Song, *Small*, 2015, **11**, 5556–5564.
- 27 Y. Tang, Y. Wang, X. Wang, S. Li, W. Huang, L. Dong, C. Liu, Y. Li and Y. Lan, *Adv. Energy Mater.*, 2016, **6**, 1600116.
- 28 H. Jiang, D. Ren, H. Wang, Y. Hu, S. Guo, H. Yuan, P. Hu, L. Zhang and C. Li, *Adv. Mater.*, 2015, **27**, 3687–3695.
- 29 P. Xiong, R. Ma, N. Sakai, L. Nurdiwijayanto and T. Sasaki, *ACS Energy Lett.*, 2018, **3**, 997–1005.
- 30 S. Gong, G. Zhao, P. Lyu and K. Sun, *Small*, 2018, 1803344.
- 31 J. P. Perdew, K. Burke and M. Ernzerhof, *Phys. Rev. Lett.*, 1996, **77**, 3865–3868.
- 32 P. E. Blöchl, *Phys. Rev. B: Condens. Matter Mater. Phys.*, 1994, **50**, 17953–17979.
- 33 G. Kresse and J. Furthmüller, *Comput. Mater. Sci.*, 1996, **6**, 15–50.
- 34 G. Kresse and D. Joubert, *Phys. Rev. B: Condens. Matter Mater. Phys.*, 1999, **59**, 1758–1775.
- 35 H. J. Monkhorst and J. Pack, *Phys. Rev. B: Solid State*, 1976, **12**, 5188.
- 36 F. Ma, H. Hu, H. B. Wu, C. Xu, Z. Xu, L. Zhen and X. W. Lou, *Adv. Mater.*, 2015, **27**, 4097–4101.
- 37 Y. Wang, L. Yu and X. W. Lou, *Angew. Chem., Int. Ed.*, 2016, **55**, 7423–7426.
- 38 H. Tang, J. Wang, H. Yin, H. Zhao, D. Wang and Z. Tang, *Adv. Mater.*, 2015, **27**, 1117–1123.
- 39 H. Wang, Z. Lu, S. Xu, D. Kong, J. J. Cha, G. Zheng, P. C. Hsu, K. Yan, D. Bradshaw, F. B. Prinz and Y. Cui, *Proc. Natl. Acad. Sci. U. S. A.*, 2013, **110**, 19701–19706.
- 40 Y. Yin, J. Han, Y. Zhang, X. Zhang, P. Xu, Q. Yuan, L. Samad, X. Wang, Y. Wang, Z. Zhang, P. Zhang, X. Cao, B. Song and S. Jin, *J. Am. Chem. Soc.*, 2016, **138**, 7965–7972.
- 41 M. A. Py and R. R. Haering, *Can. J. Phys.*, 1983, **61**, 76–84.
- 42 M. A. Lukowski, A. S. Daniel, F. Meng, A. Forticaux, L. Li and S. Jin, *J. Am. Chem. Soc.*, 2013, **135**, 10274–10277.
- 43 Y. Yin, P. Miao, Y. Zhang, J. Han, X. Zhang, Y. Gong, L. Gu, C. Xu, T. Yao, P. Xu, Y. Wang, B. Song and S. Jin, *Adv. Funct. Mater.*, 2017, **27**, 1606694.
- 44 L. Huang, Q. Wei, X. Xu, C. Shi, X. Liu, L. Zhou and L. Mai, *Phys. Chem. Chem. Phys.*, 2017, **19**, 13696–13702.
- 45 J. Zhou, L. Wang, M. Yang, J. Wu, F. Chen, W. Huang, N. Han, H. Ye, F. Zhao, Y. Li and Y. Li, *Adv. Mater.*, 2017, **29**, 1702061.
- 46 H. Sun, L. Mei, J. Liang, Z. Zhao, C. Lee, H. Fei, M. Ding, J. Lau, M. Li, C. Wang, X. Xu, G. Hao, B. Papandrea, I. Shakir, B. Dunn, Y. Huang and X. Duan, *Science*, 2017, **356**, 599–604.
- 47 G. A. Muller, J. B. Cook, H. Kim, S. H. Tolbert and B. Dunn, *Nano Lett.*, 2015, **15**, 1911–1917.
- 48 B. K. Lesel, J. S. Ko, B. Dunn and S. H. Tolbert, *ACS Nano*, 2016, **10**, 7572–7581.
- 49 T. Brezesinski, J. Wang, S. H. Tolbert and B. Dunn, *Nat. Mater.*, 2010, **9**, 146–151.
- 50 M. D. Stoller, S. Park, Y. Zhu, J. An and R. S. Ruoff, *Nano Lett.*, 2008, **8**, 3498–3502.
- 51 Y. Yu, *J. Phys. Chem. C*, 2016, **120**, 5288–5296.
- 52 D. Er, J. Li, M. Naguib, Y. Gogotsi and V. B. Shenoy, *ACS Appl. Mater. Interfaces*, 2014, **6**, 11173–11179.

# **Attachment No. 8**



Cite this: *RSC Adv.*, 2017, 7, 19630

# Theoretical investigation of CO catalytic oxidation by a Fe–PtSe<sub>2</sub> monolayer

Pengbo Lyu,  Junjie He  and Petr Nachtigall \*

CO oxidation under mild conditions is investigated computationally for the catalysts based on a single transition metal (Sc–Zn) embedded at the Se vacancy of a PtSe<sub>2</sub> monolayer. The iron-embedded Fe–PtSe<sub>2</sub> monolayer is identified as the most suitable catalyst among the investigated systems. Both, Langmuir–Hinshelwood (LH) and Eley–Rideal (ER) reaction paths were considered for the CO oxidation by adsorbed O<sub>2</sub> molecules and by adsorbed O atoms. The CO oxidation by O atoms bound to Fe–PtSe<sub>2</sub> proceeds *via* the ER mechanism in a single reaction step with a small activation barrier (21 kJ mol<sup>-1</sup>). Both LH and ER reaction mechanisms can take place for CO oxidation by adsorbed O<sub>2</sub> molecules. Whereas the barrier for the rate-determining step of the LH reaction path (72 kJ mol<sup>-1</sup>) is higher than that for the ER path (53 kJ mol<sup>-1</sup>), the kinetics analysis shows that both processes have comparable rate constants at 300 K. Langmuir–Hinshelwood mechanism becomes dominant at a lower temperature. Results reported here indicate that the Fe–PtSe<sub>2</sub> catalyst can efficiently catalyze CO oxidation under mild conditions.

Received 29th November 2016

Accepted 27th March 2017

DOI: 10.1039/c6ra27528a

[rsc.li/rsc-advances](http://rsc.li/rsc-advances)

## 1. Introduction

An efficient CO oxidation is considered as the most practical process for CO removal, in particular in fuel cells where CO is the catalytic poison.<sup>1,2</sup> The practical importance of the CO oxidation has triggered the search for suitable catalysts with high activity. A high catalytic activity of gold nanoparticles (NP) on an oxide support in CO oxidation by molecular oxygen has been reported already in 1987 by Haruta *et al.*<sup>3,4</sup> and this catalyst still serves as a benchmark catalyst for other catalysts tested for CO oxidation. It is generally accepted that CO binds on Au NPs while O<sub>2</sub> adsorbs on Au NPs only at temperatures below 170 K and several models were proposed for the O<sub>2</sub> activation at higher temperatures.<sup>5</sup> A number of other catalysts were tested for the CO oxidation reaction, including Pt-group metals, however, they are an order of magnitude less active than Au NPs.<sup>6</sup> This lower activity is assigned to strong interaction of CO with metals that prevents O<sub>2</sub> from being adsorbed and activated. A promising way to improve the catalytic activity of Pt-group metals is the reduction of NP size to sub-nano or even to single atoms. It is apparent that in addition to low reaction barriers an efficient CO oxidation catalyst should have sufficiently strong interaction not only with CO but also with O<sub>2</sub>. Better catalytic performance has been shown for particles with reduced size; a particle size reduction leads to increased number of available surface sites and other advantages such as

exposed unsaturated metal centers,<sup>7</sup> quantum size effects<sup>8</sup> and metal–support interactions.<sup>9,10</sup> Sub-nanometer metal clusters have been reported to further improve the catalytic performance.<sup>11,12</sup> The single-atom catalysts (SAC),<sup>13–15</sup> where the single metal atom anchored on metal surface, metal oxide,<sup>16,17</sup> graphene<sup>18,19</sup> or ion-exchanged metals in porous materials, represents the catalytically active site, were also considered for CO oxidation under mild conditions. Nanoparticles have lower energy barriers than single crystal metal surfaces; *e.g.*, supported Au nanoparticles exhibit lower energy barriers (35–39 kJ mol<sup>-1</sup>)<sup>20</sup> than stepped Au surfaces.<sup>21</sup> A single Au atom on FeO<sub>x</sub> (ref. 22) also exhibits high activity, similar to that reported for small Au (2–3 nm) nanoparticles while there is a very small Au loading (0.03 wt%) in Au<sub>1</sub>/FeO<sub>x</sub> catalyst. These experimental findings agree well with the theoretical investigation that reports barrier of only 0.31 eV (30 kJ mol<sup>-1</sup>) for single Au atoms supported on graphene.<sup>23</sup> Therefore, SACs are considered as suitable catalysts for CO oxidation.

Among SACs, catalysts based on the single metal atom embedded in two-dimensional atomically thin materials have drawn significant attention.<sup>24</sup> Graphene was considered as a potential support for metal atoms; several graphene-supported transition-metal (TM) atoms were theoretically predicted to show a high catalytic activity, including Au,<sup>23</sup> Fe,<sup>25</sup> Cu,<sup>26</sup> Pt,<sup>27</sup> Zn<sup>28</sup> and Mo<sup>29</sup> atoms with energy barriers ranging from 30 to 58 kJ mol<sup>-1</sup>. Note that stable structures of single Pt, Co, or In atoms,<sup>30</sup> as well as Fe dimers,<sup>31</sup> on graphene have been experimentally observed. Other 2D materials, such as the single-layer transition-metal dichalcogenides (TMDs) (MX<sub>2</sub>, M is group 4–10 transition metal and X = S, Se, Te) were also considered as

Department of Physical and Macromolecular Chemistry, Faculty of Science, Charles University in Prague, 128 43 Prague 2, Czech Republic. E-mail: petr.nachtigall@natur.cuni.cz



possible matrixes for single atom metal catalysts. The MoS<sub>2</sub> monolayer consists of three atomic layers with S atoms terminating both upper and lower surfaces; consequently, there are no dangling bonds on Mo atoms and material is catalytically inactive.<sup>32–34</sup> However, S vacancies on MoS<sub>2</sub> surfaces can accommodate various transition metal atoms, thus, the material becomes catalytically active.<sup>35,36</sup> The activity of these materials for the CO oxidation catalysis was already investigated theoretically: Fe atoms at the S vacancy on MoS<sub>2</sub> (denoted Fe–MoS<sub>2</sub>) showed activation barrier of 49 kJ mol<sup>−1</sup><sup>35</sup> and Cu<sub>4</sub> clusters at the S vacancy were predicted to be even more active (energy barrier of 36 kJ mol<sup>−1</sup>).<sup>36</sup> It is clear that the transition metal (TM) embedded in vacancies of otherwise inactive TMD layered materials are legitimate candidates for efficient catalysis of CO oxidation. A single-crystal monolayer platinum diselenide (PtSe<sub>2</sub>), a new type of single-layer TMDs, has been recently prepared experimentally using the direct selenization of Pt(111) surface.<sup>37</sup> Potential applications in optoelectronics, photocatalysis and for valley-tronic devices were proposed. Monolayer PtSe<sub>2</sub> consists of three atomic Se–Pt–Se layers similar to MoS<sub>2</sub> and it could be also a promising substrate for the single metal atom catalysts. As for the metal embedded MoS<sub>2</sub>, the S vacancy could be formed by the low energy argon sputtering<sup>38</sup> or electron irradiation,<sup>39</sup> subsequent metal vapor deposition leads to the metal atom embedding on MoS<sub>2</sub> surfaces. The same procedure can be also proposed for the preparation of TM–PtSe<sub>2</sub> catalysts. The structure and properties of transition metals-embedded PtSe<sub>2</sub> systems are reported herein based on the density functional theory (DFT) investigation. A potential of these materials as a catalyst for CO oxidation is the main target of our investigation. First, the TM embedded PtSe<sub>2</sub> (TM = Sc–Zn) materials were computationally screened to select the most promising catalyst for CO oxidation. Second, CO oxidation reactions over the Fe embedded PtSe<sub>2</sub> surface were explored, considering both Eley–Rideal (ER) and Langmuir–Hinshelwood (LH) mechanisms.

## 2. Computational methods

Calculations were performed at the density functional theory (DFT) level with the projected augmented wave (PAW) approximation as implemented in Vienna ab initio simulation package (VASP 5.3.3).<sup>40–42</sup> The generalized gradient approximation (GGA)

using the Perdew–Burke–Ernzerhof (PBE) exchange–correlation functional and a 500 eV cutoff for the plane-wave basis set were adopted. The Brillouin zone was sampled with the Monkhorst–Pack<sup>43</sup> special *k*-point mesh on 3 × 3 × 1 grid. Geometry optimizations were performed with a convergence threshold of 10<sup>−5</sup> eV for a total energy and 0.01 eV Å<sup>−1</sup> for the force. All atoms were allowed to relax during the geometry optimizations while the optimized lattice constant was kept fixed. Transition states on the reaction path were located with the climbing image nudged elastic band method (CI-NEB)<sup>44</sup> and the dimer algorithm<sup>45</sup> as implemented in Transition State Tools for VASP (VTST).<sup>46</sup> Vibrational frequencies were calculated for stationary points along the reaction path to identify the character of individual stationary points. Activation barriers of elementary reaction steps were recalculated with the hybrid PBE0 exchange correlation functional.<sup>47,48</sup>

The PtSe<sub>2</sub> layer was represented by the 4 × 4 supercell (Fig. 1a) and the interlayer distance of 15 Å was adopted to avoid the artificial interlayer interactions within the periodic model. The structure of the PtSe<sub>2</sub> and localized densities of states (LDOS) projected on Pt(5d), Pt(6s) and Se(4p) orbitals are shown in Fig. 1; a position of the Se atom to be replaced by the TM atom is also shown. The calculated lattice constant of PtSe<sub>2</sub> monolayer (3.75 Å) is in good agreement with the experimentally observed value (3.7 Å).<sup>37</sup>

The binding energy of TM atom in the Se vacancy is defined as:

$$E_b(\text{TM}) = E_{\text{tot}}(\text{TM–PtSe}_2) - E(\text{V}_{\text{Se}}/\text{PtSe}_2) - E(\text{TM}), \quad (1)$$

where  $E_{\text{tot}}(\text{TM–PtSe}_2)$ ,  $E(\text{V}_{\text{Se}}/\text{PtSe}_2)$  and  $E(\text{TM})$  stand for the total energy of the TM embedded PtSe<sub>2</sub>, the monolayer PtSe<sub>2</sub> with a Se vacancy and the cohesive energy of bulk metal, respectively. Adsorption energies of CO, O<sub>2</sub> and CO<sub>2</sub> were calculated as:

$$E_{\text{ads}}(\text{molecule}) = E(\text{molecule/TM–PtSe}_2) - E(\text{TM–PtSe}_2) - E(\text{molecule}), \quad (2)$$

where  $E(\text{molecule/TM–PtSe}_2)$ ,  $E(\text{TM–PtSe}_2)$ , and  $E(\text{molecule})$  stand for the total energy of the adsorption complex, bare TM–PtSe<sub>2</sub> surface, and the molecule in the gas phase, respectively. The DFT-D3 method of Grimme was employed to evaluate the dispersion contribution for the adsorption.<sup>49</sup>

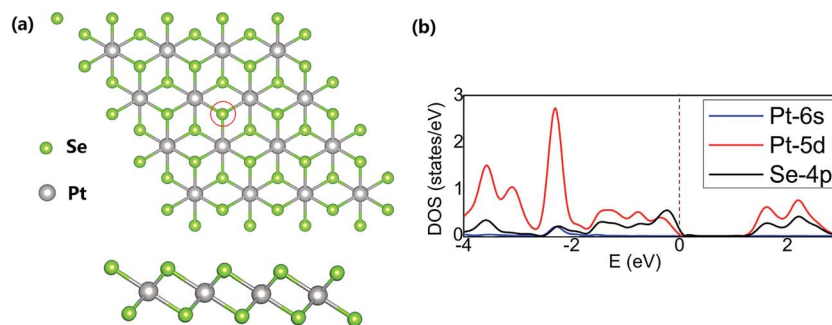


Fig. 1 (a) Top and side views of a 4 × 4 UC of PtSe<sub>2</sub>. The position of Se atom to be replaced with the TM (TM = Sc–Zn) atom is denoted with a red circle. (b) The LDOS projected on the Pt(5d), Pt(6s) and Se(4p) orbitals. The brown dash line indicates the Fermi level (eV).





Rate constants to be used in kinetic analysis were calculated using the following formula:

$$k = \frac{k_B T}{h} \frac{q^\ddagger}{q} \exp\left(\frac{-E_a}{k_B T}\right) \quad (3)$$

$E_a$  is the activation energy of an elementary step, and  $q$  and  $q^\ddagger$  are partition functions of relevant stationary points on the potential energy surface; the effect of vibrational degrees of freedom is included for molecules bound on the surface while translational, rotational, and vibrational degrees of freedom are included for molecules in the gas phase. Only those degrees of freedom related to Fe atom and surface species are considered in frequency calculations.

### 3. Results and discussions

#### 3.1. Screening the catalytic potential of TM-PtSe<sub>2</sub> (TM = Sc–Zn)

The suitability of TM embedded in PtSe<sub>2</sub> monolayer (TM–PtSe<sub>2</sub>) for the catalytic oxidation of CO under mild conditions was first screened with respect to the criteria stated for the suitable catalytic system previously:<sup>50</sup> (i) the total activation energy of CO oxidation should not be higher than about 1 eV (96 kJ mol<sup>-1</sup>). (ii) A preferential O<sub>2</sub> adsorption on the catalyst. (iii) The CO<sub>2</sub> adsorption energy should not exceed –50 kJ mol<sup>-1</sup>. Interaction energies of 3d transition metals with the Se vacancy in PtSe<sub>2</sub> and corresponding geometrical parameters are reported in Table 1. The strong interaction (binding energies between –523 and –258 kJ mol<sup>-1</sup>) was found for TM from Sc to Fe while weaker interaction was found for late TM (Co through Zn). Adsorption energies of CO, O<sub>2</sub>, and CO<sub>2</sub> on the TM–PtSe<sub>2</sub> surface (Fig. 2) can be used for an assessment of the catalytic suitability for the CO oxidation under mild conditions. The TM–PtSe<sub>2</sub> catalysts based on the late transition metals is not suitable since the CO interaction with the catalyst is stronger than the O<sub>2</sub> interaction (criteria (ii) is not met). A strong interaction of CO<sub>2</sub> with the catalyst has been found for early transition metals Sc–Cr, thus, corresponding catalysts do not meet criteria (iii). Therefore, two suitable candidates for the CO oxidation under mild conditions are Mn–PtSe<sub>2</sub> and Fe–PtSe<sub>2</sub>. The absolute value of CO adsorption energy on Mn–PtSe<sub>2</sub> is rather low compared to a typical energy barrier for CO oxidation (50–67 kJ mol<sup>-1</sup>),<sup>25,51</sup> therefore, CO may desorb before the oxidation takes place. It follows that the Fe–PtSe<sub>2</sub> material appears to be the most promising candidate for the catalysis of CO oxidation and it is investigated in detail below.

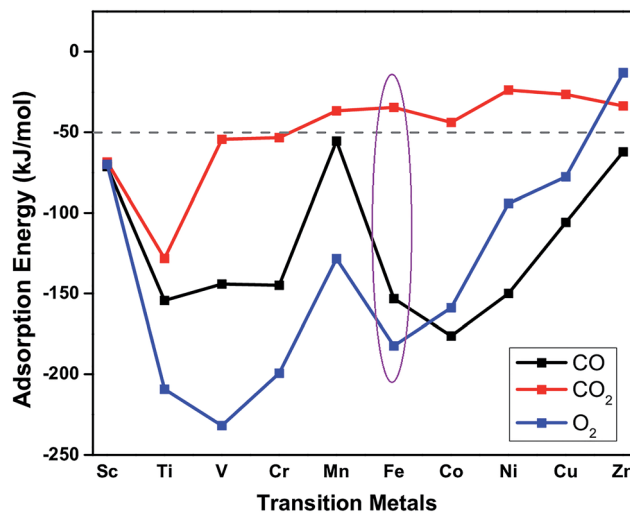


Fig. 2 Adsorption energies of CO (black), O<sub>2</sub> (blue) and CO<sub>2</sub> (red) on TM–PtSe<sub>2</sub> (TM = Sc–Zn).

#### 3.2. Geometry, electronic structure and stability of Fe–PtSe<sub>2</sub>

The Fe atom located at the Se vacancy is bonded to 3 Pt atoms with the Fe–Pt bond length of 2.43 Å (Table 1), which is shorter than the Pt–Se bond 2.53 Å. Consequently, Fe is slightly below the Se plane. The Bader charge analysis<sup>52</sup> shows electron density of +0.76 |e| on the embedded Fe atom; the charge on Pt atom adjacent to the Se vacancy is 0.16, 0.10, and –0.06 |e| for pristine PtSe<sub>2</sub> monolayer, a monolayer with single Se atom vacancy and for PtSe<sub>2</sub> monolayer with vacancy occupied by Fe, respectively. The charge density difference between PtSe<sub>2</sub> with Se vacancy and Fe–PtSe<sub>2</sub> is depicted in Fig. 3a. Spin densities also shown in Fig. 3 are mainly located on the Fe atom (2.889 μ<sub>B</sub>) and the three next-nearest neighbor Se atoms (–0.091 μ<sub>B</sub> for each). The spin-polarized DOS of PtSe<sub>2</sub> and Fe–PtSe<sub>2</sub> shown in Fig. 3c indicate that conduction and valence bands differ significantly around the Fermi level. The band structure around the Fermi level is mainly attributed to Fe(3d) and Pt(5d) orbitals.

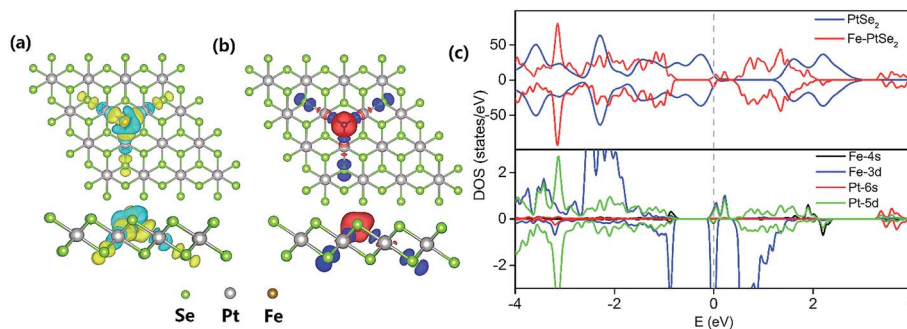
The stability of the Fe atom bound at the Se vacancy with respect to Fe adsorbed on the Se surface has been also investigated. The adsorption of Fe atom on the Se surface in the vicinity of the Se vacancy can take place either on the center of the Se–Pt–Se hexagonal ring (Fig. 4, FS1) or on the top of Pt (Fig. 4, FS2). Corresponding adsorption energies (–140 and –91 kJ mol<sup>-1</sup>, respectively) are both significantly smaller compared to adsorption at the Se vacancy (–258 kJ mol<sup>-1</sup>). Energy barriers

Table 1 Calculated interaction energies and geometrical parameters for TM atoms at the vacancy of PtSe<sub>2</sub> monolayer<sup>a</sup>

TM	Sc	Ti	V	Cr	Mn	Fe	Co	Ni	Cu	Zn
$E_b$	–390	–337	–310	–461	–523	–258	–107	–46	9	–25
$r(\text{TM–Pt})$	2.49	2.40	2.37	2.51	2.46	2.43	2.43	2.43	2.50	2.50
$D$	–0.19	–0.34	–0.41	–0.11	–0.17	–0.24	–0.21	–0.16	–0.08	–0.16

<sup>a</sup> Energies in kJ mol<sup>-1</sup>. Distance between Pt and TM atoms  $r(\text{TM–Pt})$  and distance of TM atom from the Se layer ( $D$ , negative sign means TM atom is below Se) reported in Å.





**Fig. 3** Top and side views of the optimized structure of Fe embedded in PtSe<sub>2</sub> monolayer showing also the charge density difference (a) and spin densities (b). The yellow and cyan regions in (a) represent the electron accumulation and loss, respectively, and the red and blue regions in (b) represent the spin-up and spin-down electron densities, respectively (isosurfaces plotted for a value of 0.003 e bohr<sup>-3</sup>). (c) The upper panel shows the TDOS of the PtSe<sub>2</sub> and Fe–PtSe<sub>2</sub> monolayer, and the lower panel shows the Fe–PtSe<sub>2</sub> spin-polarized LDOS projected on Fe(3d), Fe(4s), Pt(5d) and Pt(6s) orbitals. The grey dash line indicates the Fermi level.

for the Fe atom migration from the Se vacancy to Se–Pt–Se hexagonal and to Pt top sites are 230 and 224 kJ mol<sup>-1</sup>, respectively. All these results indicate that Fe atoms are preferentially located at the Se vacancies and both thermodynamic and kinetic characteristics are not in favor of a Fe atom migration on the surface and formation of Fe clusters.

### 3.3. Adsorption of O<sub>2</sub> and CO on Fe–PtSe<sub>2</sub>

The most energetically favored adsorption complex of O<sub>2</sub> on Fe–PtSe<sub>2</sub> is a side-on configuration with the adsorption energy –156 kJ mol<sup>-1</sup> at the PBE level of theory (Fig. 5a). The dispersion contribution accounts for additional –26 kJ mol<sup>-1</sup>. The projection of oxygen bond in the basal plane almost coincides with one of the three Fe–Pt bonds, and the distances between Fe–O1 and Fe–O2 are 1.80 Å and 1.86 Å, respectively. The bond length of O1–O2 is elongated from 1.21 Å (gas phase value) to 1.39 Å. The Bader charge analysis shows 0.77 |e| transfer from

Fe–PtSe<sub>2</sub> to O<sub>2</sub>. This electron density shift comes mainly from the adsorbent HOMO, localized Fe(3d) orbitals, to LUMO O(2π\*) orbitals, explaining the significant elongation of the O–O bond. The charge density differences are shown in Fig. 5b. The adsorption of O<sub>2</sub> also partially reduces the magnetic moment of embedded Fe from –2.889 to –2.263 μ<sub>B</sub>. All these results show that O<sub>2</sub> can be effectively activated when adsorbed on Fe–PtSe<sub>2</sub>.

As for the adsorption of CO on Fe–PtSe<sub>2</sub>, the most stable configuration is a C end-on configuration as shown in Fig. 5c. The Fe–C distance is 1.71 Å and the C–O bond length changes from 1.14 Å (the gas phase value) to 1.17 Å, showing just a moderate activation of CO. The charge transfer from the substrate to CO is calculated to be 0.40 |e| and the charge density difference depicted in Fig. 5d shows the charge accumulation on the Fe–C bond. Furthermore, the Bader charge analysis shows only 0.08 |e| transfer to O, while 0.32 |e| transfers to C. The adsorption of CO reduces the magnetic moment of Fe–PtSe<sub>2</sub> to 0. The calculated CO adsorption energy is –125 kJ mol<sup>-1</sup>, and the dispersion corrected value is –153 kJ mol<sup>-1</sup>. The changes in geometry of the Fe/PtSe<sub>2</sub> due to the adsorption of CO and O<sub>2</sub> and during the course of the reaction are also shown in Table 4 where Pt–Fe and Se–Fe distances are also reported. Note that adsorption of O<sub>2</sub> as well as the structure of some reaction intermediates results in the symmetry lowering; therefore two values for individual Pt–Fe and Se–Fe distances are reported in those cases.

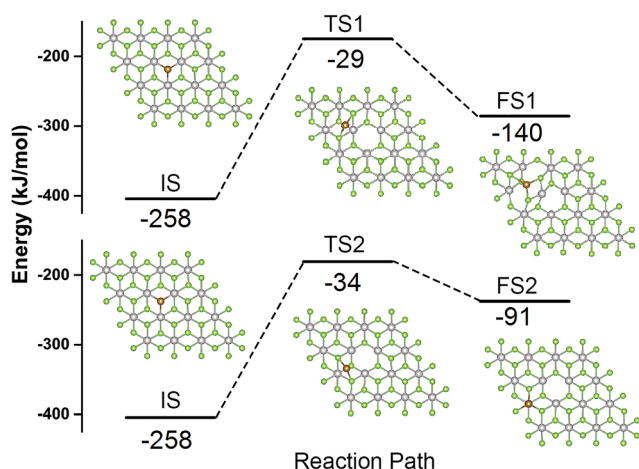


**Fig. 4** Geometries of the IS, TS and FS and corresponding energy profiles along the MEP for Fe migration from the Se vacancy to the center position of neighboring hexagonal ring (upper part) and on top of the Pt atom (lower part). Se, Pt, and Fe atoms depicted in green, grey, and brown color, respectively.

### 3.4. CO oxidation catalyzed by Fe–PtSe<sub>2</sub>

Two well-known mechanisms for CO oxidation, Eley-Rideal (ER) and Langmuir–Hinshelwood (LH) mechanisms<sup>25,27</sup> are both investigated. If the adsorbed O<sub>2</sub> is attacked by the CO molecule from the gas phase directly (CO does not equilibrate on the surface), the reaction proceeds *via* ER mechanism. Otherwise, the reaction starts by the co-adsorption of CO and O<sub>2</sub> molecules and it is followed by the formation of a peroxo-type intermediate state and completed by desorption of CO<sub>2</sub> (LH mechanism). The activation energy barriers were calculated at the PBE0 level



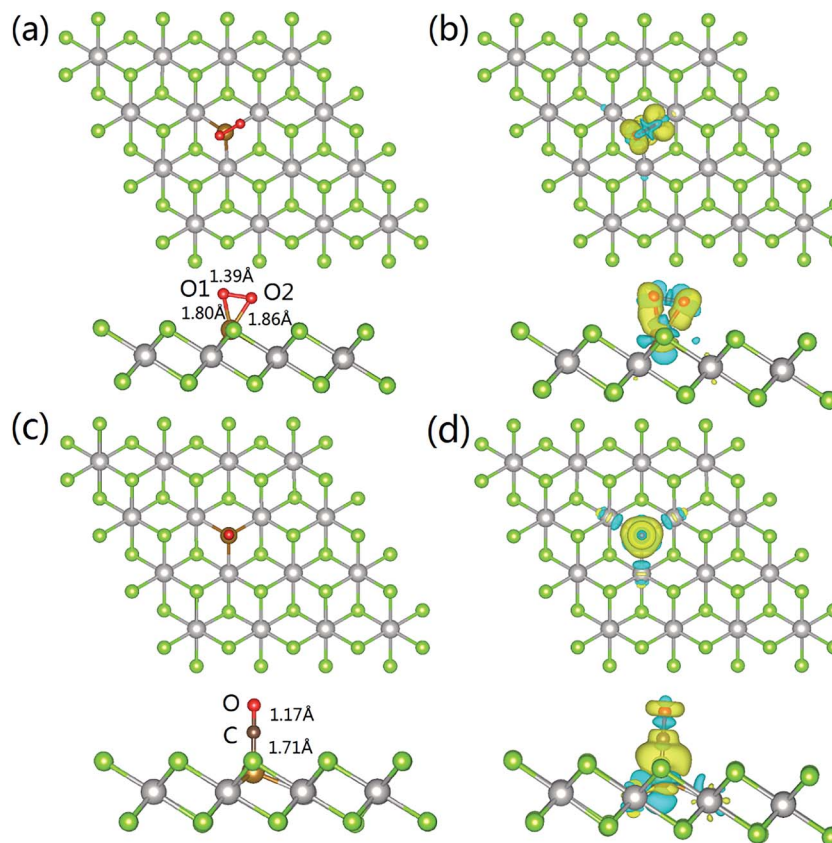


Fig. 5 Structures of  $O_2$  and CO adsorption complexes on Fe-PtSe<sub>2</sub> (parts (a) and (c), respectively) and charge density differences upon  $O_2$  and CO adsorption (parts (b) and (d), respectively). The yellow and cyan denote the charge accumulation and loss, respectively; the isosurface value set to  $0.003 e \text{ bohr}^{-3}$ .

(single point energy calculations at structures optimized at the PBE level).

As shown above the Fe site of Fe-PtSe<sub>2</sub> is preferentially occupied by  $O_2$ . The weakly interacting adsorption complex of CO on  $O_2$ /Fe-PtSe<sub>2</sub> is taken as the initial structure for both reaction pathways (denoted IS in Fig. 6) and its energy is taken as a reference. The ER mechanism proceeds in a single reaction step (red path in Fig. 6); it starts directly with the formation of

TS structure (barrier of  $53 \text{ kJ mol}^{-1}$ ) that leads to the  $CO_2$  molecule weakly adsorbed on O/Fe-PtSe<sub>2</sub> (structure denoted MS). The reaction is completed by desorption of adsorbed  $CO_2$  molecule to the gas phase which is a  $6 \text{ kJ mol}^{-1}$  endothermic step (not accounting for dispersion).

The LH mechanism (blue path in Fig. 6) starts with the formation of adsorption complex where both  $O_2$  and CO molecules are bound to a single Fe atom (MS1 complex).<sup>53</sup> This

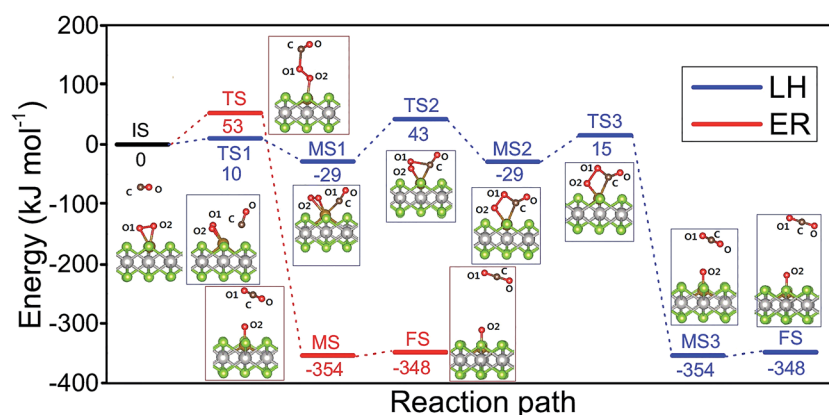


Fig. 6 Configurations of IS, TS, MS and FS along the MEP of CO oxidation catalyzed by Fe-PtSe<sub>2</sub> via the LH (blue) and ER (red) mechanisms, with the corresponding energy profiles. The end points (FS) of LH and ER mechanisms are the same (physisorbed  $CO_2$ ).



process proceeds *via* the transition state TS1 with the energy barrier of 10 kJ mol<sup>-1</sup> and it is 29 kJ mol<sup>-1</sup> exothermic, indicating that co-adsorption of O<sub>2</sub> and CO on single Fe atom can take place. The reaction further proceeds in two elementary steps: a peroxy-type intermediate MS2 (isoenergetic with MS1) is formed *via* a transition state TS2 with an activation barrier of 72 kJ mol<sup>-1</sup>; this is a rate-determining step in LH mechanism. The peroxy-type intermediate then decomposes to CO<sub>2</sub> weakly bound to the surface and O adatom with the energy barrier of 40 kJ mol<sup>-1</sup>. Thus formed MS3 structure of CO<sub>2</sub> interacting with the O/Fe–PtSe<sub>2</sub> site is identical with MS structure found for ER mechanism.

The catalytic cycle is completed by the reaction of O adatom (O/Fe–PtSe<sub>2</sub>) with another CO molecule (Fig. 7). The energy of weakly interaction CO adsorption complex (IS in Fig. 7) is again taken as reference energy. CO<sub>2</sub> is formed in a single exothermic (–237 kJ mol<sup>-1</sup>) reaction step with the activation barrier of 21 kJ mol<sup>-1</sup>. Adsorbed CO<sub>2</sub> thus formed can readily desorb from the surface. Thus the reaction of CO with O adatom (O/Fe–PtSe<sub>2</sub>) proceeds *via* ER mechanism and it has significantly smaller activation barrier than the reaction of CO with adsorbed O<sub>2</sub> (O<sub>2</sub>/Fe–PtSe<sub>2</sub>). Relevant geometrical parameters are listed in Table 2.

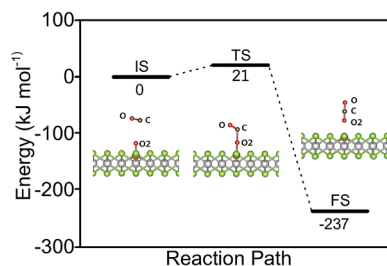
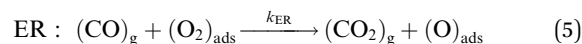
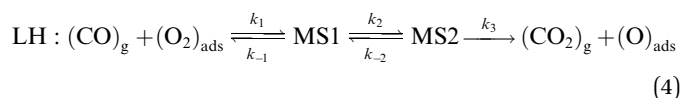


Fig. 7 Configurations of IS, TS and FS and energy profile along the MEP for CO reacting with O/Fe–PtSe<sub>2</sub>.

Our calculations show that CO oxidation catalyzed by Fe–PtSe<sub>2</sub> proceeds *via* a peroxy-type intermediate (Fig. 6). The CO oxidation over single Fe atom on the graphene has been proposed to go through a carbonate-like intermediate with an energy barrier of 0.57 eV.<sup>25</sup> Rather similar observation has been reported for CO oxidation by single Pt atom,<sup>19</sup> for a Pt atom on the pristine graphene and for the Pt atom embedded in graphene single-atom vacancy reaction paths *via* carbonate-like and peroxy-type intermediates were found.<sup>27</sup> It is apparent that the CO oxidation mechanism depends on the electronic structure of transition metal atoms that, in turn, depends on the type of metal–support interactions.

Overall reaction rate is thus determined by the reaction of CO with adsorbed O<sub>2</sub> molecule described above. While the ER mechanism consists of single reaction step ( $\Delta E^\ddagger = 53$  kJ mol<sup>-1</sup>), the LH mechanism requires three reaction steps characterized with barriers  $\Delta E^\ddagger = 10, 72,$  and  $44$  kJ mol<sup>-1</sup> for TS1, TS2, and TS3, respectively. To understand which of the mechanisms prevails, the reaction rates were calculated for both ER and LH paths using eqn (3) for rate constants. CO in the gas phase and O<sub>2</sub> adsorbed on the Fe sites were taken as reactants for both process.



(O<sub>2</sub>)<sub>ads</sub> and (O)<sub>ads</sub> denote O<sub>2</sub> and O bound to Fe atom; notation from Fig. 6 is used for reaction intermediates. The concentration of CO<sub>2</sub> formed *via* ER mechanism, [CO<sub>2</sub>]<sup>ER</sup>, is then

$$[\text{CO}_2]^{\text{ER}} = k_{\text{ER}} \cdot p_{\text{CO}} [(\text{O}_2)_{\text{ads}}], \quad (6)$$

where  $p_{\text{CO}}$  and  $[(\text{O}_2)_{\text{ads}}]$  stand for CO partial pressure and concentration of O<sub>2</sub> molecules adsorbed on Fe sites, respectively.

Table 2 Structural parameters of Fe–PtSe<sub>2</sub> and reaction intermediates on both ER and LH reaction paths<sup>a</sup>

Distance		$d_{(\text{O1}-\text{O2})}$	$d_{(\text{C}-\text{O1})}$	$d_{(\text{C}-\text{O2})}$	$d_{(\text{C}-\text{Fe})}$	$d_{(\text{Pt}-\text{Fe})}$	$d_{(\text{Se}-\text{Fe})}$
Fe–PtSe <sub>2</sub>		—	—	—	—	2.43	3.21
O <sub>2</sub> ads		1.39	—	—	—	2.47, 2.63	3.30, 3.43
CO ads		—	—	—	1.71	2.37	3.06
ER	IS	1.39	3.50	3.54	5.14	2.46, 2.63	3.30, 3.43
	TS	1.40	1.74	2.65	4.29	2.47	3.29
	MS	3.13	1.18	2.88	4.43	2.41	3.16
	FS	5.10	1.18	4.96	6.50	2.42	3.17
LH	IS	1.39	3.50	3.54	5.14	2.46, 2.63	3.30, 3.43
	TS1	1.38	2.63	2.58	2.32	2.54, 2.75	3.40, 3.58
	MS1	1.34	2.67	2.68	1.92	2.62	3.47
	TS2	1.43	1.82	2.43	1.98	2.50, 2.57	3.26, 3.36
	MS2	1.51	1.35	2.17	2.05	2.48	3.28
	TS3	1.67	1.32	2.19	2.07	2.49, 2.57	3.25, 3.37
	MS3	3.13	1.18	2.88	4.43	2.41	3.16
	FS	5.10	1.18	4.96	6.50	2.42	3.17
ER O/Fe–PtSe <sub>2</sub>	IS	—	—	3.08	4.66	2.42	3.17
	TS	—	—	1.71	3.39	2.44	3.23
	FS	—	—	1.18	3.41	2.47	3.27

<sup>a</sup> All distances reported in Å.



The concentration of CO<sub>2</sub> formed *via* LH mechanism, [CO<sub>2</sub>]<sup>LH</sup>, can be obtained from eqn (5), considering the constant concentration of MS2 intermediate during the reaction:

$$[\text{CO}_2]^{\text{LH}} = \frac{k_1}{k_{-1}} \frac{k_2 k_3}{k_{-2} + k_3} p_{\text{CO}} [(\text{O}_2)_{\text{ads}}] = k_{\text{LH}} p_{\text{CO}} [(\text{O}_2)_{\text{ads}}]. \quad (7)$$

Rate constants calculated using eqn (3) for  $T = 300$  K (Table 3) give ratio  $k_{\text{ER}}/k_{\text{LH}} = 1.1$ , leading to the conclusion that both reaction paths are possible for this catalyst. Rate constants ratios calculated for 250 K and 350 K are 0.5 and 1.9, respectively, indicating that LH mechanism will be more favored at lower temperatures.

Results reported above show that the catalytic oxidation of CO proceeds readily on Fe–PtSe<sub>2</sub> under mild conditions.<sup>54</sup> Activation barriers are comparable to those reported in the literature for other SAC systems based on 2D layered materials (Table 4). Results reported in Table 4 are based on DFT calculations employing either local or semi-local exchange–correlation functionals. However, our results show that there is a qualitative difference between the results obtained with semi-local and hybrid functionals: changing the level of theory from PBE to PBE0 results in an increase of the activation barrier for rate determining step along LH path from 45 to 72 kJ mol<sup>−1</sup> and in a decrease of activation barrier for ER path from 63 to 53 kJ

mol<sup>−1</sup>. In addition, the analysis of the preferable reaction path based only on activation barriers can be misleading; even if the ER barrier is 20 kJ mol<sup>−1</sup> lower than activation barrier on LH path, calculated rate constants are comparable for both reaction paths. The rate constants were reported for some catalysts, *e.g.*, supported Au nanoparticles,<sup>55,56</sup> they were not reported for SAC-type catalysts summarized in Table 4. It is therefore difficult to discuss the catalytic activity of particular catalysts reported in Table 4 without knowledge of rate constants. The lowest activation barrier reported so far for mild CO oxidation by SAC 2D systems are 30 and 45 kJ mol<sup>−1</sup> found at the PBE level for Au-graphene<sup>23</sup> and Au–BN,<sup>57</sup> respectively; this is similar as found herein (at the same level of theory) for Fe–PtSe<sub>2</sub>. Note that activation barriers reported here for the Fe–PtSe<sub>2</sub> catalyst are lower than those reported previously for Pt(111).<sup>58</sup> The effect of dispersion on the stability of individual reaction intermediates was also investigated (using the D3 dispersion correction scheme). Calculated dispersion corrections are relatively constant for all stationary states on both reaction paths investigated herein, thus, the relative energies of individual intermediates are not affected by dispersion. Relative energies of TS1 and TS3 become about 15 kJ mol<sup>−1</sup> with respect to other TS's and reaction intermediates.

A good catalytic performance of the Fe–PtSe<sub>2</sub> catalyst for the CO oxidation can be attributed to highly localized Fe(3d) states around Fermi level<sup>60</sup> resulting from the Fe–support interaction (Fig. 3c). A relatively strong interaction of O<sub>2</sub> with these Fe(3d) orbitals leads to weakening of the O–O bond and consequently it results in a low activation barrier found for CO oxidation (Fig. 6). It has been shown both experimentally and theoretically that iron oxide clusters can catalyze CO oxidation.<sup>61</sup> A good performance of quasicubic  $\alpha$ -Fe<sub>2</sub>O<sub>3</sub> nanoparticles in CO oxidation has been reported as well.<sup>62</sup> Our results show that the coordinatively unsaturated single Fe atom can efficiently catalyze CO oxidation, similarly as shown previously for other systems.<sup>63</sup> The rate limiting step in CO oxidation is the O<sub>2</sub> adsorption and activation for various catalysts, *e.g.*, Pt-group metals. Tang *et al.* have reported that Pt atom located on pristine graphene favors the CO adsorption, however, for the Pt atom embedded in the graphene single vacancy, the adsorption of O<sub>2</sub> is favored.<sup>27</sup> It has been attributed to the electron density transfer from platinum to graphene and corresponding build-up of positive charge on Pt. Similarly in the case of Fe–PtSe<sub>2</sub> catalyst, Fe atom becomes +0.76 |e| positively charged when embedded in Se vacancy. Consequently, the adsorption of O<sub>2</sub> is favored over the adsorption of CO.

## 4. Summary

Transition metal-embedded PtSe<sub>2</sub> 2D materials were computationally screened to select the most promising catalyst for CO oxidation, considering all 3d transition metals (Sc–Zn). Considering the criteria stated for the suitable catalytic system previously,<sup>50</sup> Fe–PtSe<sub>2</sub> emerged as the most suitable candidate for CO oxidation. The electronic structure, structural stability and reaction mechanisms were investigated in detail for this catalyst. The Fe atom embedded in the Se vacancy of PtSe<sub>2</sub> was

Table 3 Rate constants for ER and LH mechanisms calculated at various temperatures

Rate constants (s <sup>−1</sup> )	$T = 250$ K	$T = 300$ K	$T = 350$ K
$k_{\text{ER}}$	$1.9 \times 10^1$	$4.3 \times 10^2$	$4.1 \times 10^3$
$k_{-\text{ER}}$	$3.1 \times 10^{-71}$	$1.8 \times 10^{-57}$	$1.2 \times 10^{-47}$
$k_1$	$1.6 \times 10^9$	$1.4 \times 10^9$	$1.3 \times 10^9$
$k_{-1}$	$5.8 \times 10^5$	$1.5 \times 10^7$	$1.4 \times 10^8$
$k_2$	$1.4 \times 10^{-2}$	$4.2 \times 10^0$	$2.5 \times 10^2$
$k_{-2}$	$3.9 \times 10^{-2}$	$9.4 \times 10^0$	$4.9 \times 10^2$
$k_3$	$4.6 \times 10^3$	$2.3 \times 10^5$	$3.8 \times 10^6$
$k_{-3}$	$7.4 \times 10^{-66}$	$4.1 \times 10^{-53}$	$5.2 \times 10^{-44}$
$k_{\text{LH}}$	$4.0 \times 10^1$	$3.9 \times 10^2$	$2.3 \times 10^3$

Table 4 Energy barriers ( $\Delta E^\ddagger$ )<sup>a</sup> of CO oxidation for different metal-embedded 2D systems

System	Mechanism	$\Delta E^\ddagger$	Methods	Reference
Au–graphene	LH	30	PBE + DND	23
Fe–graphene	ER	56	PW91 + DND	25
Cu–graphene	LH	52	PWC + DNP	26
Fe–MoS <sub>2</sub>	LH	49	PBE + PAW, 450 eV	35
CoPc	LH	63	PWC + DNP	50
Au–BN	ER	45	PBE + PAW, 400 eV	57
Co–BN	ER	50	PBE + PAW, 400 eV	59
Fe–PtSe <sub>2</sub>	LH	45	PBE + PAW, 500 eV	Present work
	LH	72	PBE0 + PAW, 500 eV	Present work
	ER	63	PBE + PAW, 500 eV	Present work
	ER	53	PBE0 + PAW, 500 eV	Present work

<sup>a</sup> Energies in kJ mol<sup>−1</sup>.



found to be sufficiently stable to avoid a metal-cluster formation. The catalytic performance of Fe–PtSe<sub>2</sub> was investigated using the PBE functional for structure optimizations and a hybrid PBE0 exchange–correlation functional for single point energy calculations. The reaction paths of CO oxidation by O<sub>2</sub> adsorbed on Fe–PtSe<sub>2</sub> were investigated for both LH and ER mechanisms. The barrier for rate-determining step of LH reaction path is higher than that for ER path (71 and 53 kJ mol<sup>-1</sup>, respectively). Nevertheless, the kinetics analysis shows that both processes have comparable rate constants at 300 K. Langmuir–Hinshelwood mechanism becomes dominant at a lower temperature. The CO oxidation by the O atom adsorbed on Fe–PtSe<sub>2</sub> proceeds *via* ER mechanism in a single reaction step with only small activation energy of 21 kJ mol<sup>-1</sup>. Results reported here indicate that the Fe–PtSe<sub>2</sub> catalyst can efficiently catalyze CO oxidation under mild conditions. Therefore, the iron-embedded Fe–PtSe<sub>2</sub> system is a potential catalyst for CO oxidation.

## Acknowledgements

This work was funded by the Czech Science Foundation Grant No. P106/12/G015 (Centre of Excellence) and by OP VVV “Excellent Research Teams”, project No. CZ.02.1.01/0.0/0.0/15\_003/0000417 – CUCAM.

## References

- 1 A. Hornes, A. B. Hungria, P. Bera, A. L. Camara, M. Fernandez-Garcia, A. Martinez-Arias, L. Barrio, M. Estrella, G. Zhou, J. J. Fonseca, J. C. Hanson and J. A. Rodriguez, *J. Am. Chem. Soc.*, 2010, **132**, 34–35.
- 2 S. Royer and D. Duprez, *ChemCatChem*, 2011, **3**, 24–65.
- 3 M. Haruta, T. Kobayashi, H. Sano and N. Yamada, *Chem. Lett.*, 1987, 405–408.
- 4 M. Haruta, N. Yamada, T. Kobayashi and S. Iijima, *J. Catal.*, 1989, **115**, 301–309.
- 5 D. Widmann and R. J. Behm, *Acc. Chem. Res.*, 2014, **47**, 740–749.
- 6 J. Lin, X. Wang and T. Zhang, *Chin. J. Catal.*, 2016, **37**, 1805–1813.
- 7 N. Lopez, T. V. W. Janssens, B. S. Clausen, Y. Xu, M. Mavrikakis, T. Bligaard and J. K. Nørskov, *J. Catal.*, 2004, **223**, 232–235.
- 8 J. Li, X. Li, H.-J. Zhai and L.-S. Wang, *Science*, 2003, **299**, 864–867.
- 9 C. T. Campbell, *Nat. Chem.*, 2012, **4**, 597–598.
- 10 H. Tang, J. Wei, F. Liu, B. Qiao, X. Pan, L. Li, J. Liu, J. Wang and T. Zhang, *J. Am. Chem. Soc.*, 2016, **138**, 56–59.
- 11 A. A. Herzing, C. J. Kiely, A. F. Carley, P. Landon and G. J. Hutchings, *Science*, 2008, **321**, 1331–1335.
- 12 F. Li, H. Shu, C. Hu, Z. Shi, X. Liu, P. Liang and X. Chen, *ACS Appl. Mater. Interfaces*, 2015, **7**, 27405–27413.
- 13 B. Qiao, A. Wang, X. Yang, L. F. Allard, Z. Jiang, Y. Cui, J. Liu, J. Li and T. Zhang, *Nat. Chem.*, 2011, **3**, 634–641.
- 14 X.-F. Yang, A. Wang, B. Qiao, J. Li, J. Liu and T. Zhang, *Acc. Chem. Res.*, 2013, **46**, 1740–1748.
- 15 J. Liu, *ACS Catal.*, 2017, **7**, 34–59.
- 16 J.-X. Liang, X.-F. Yang, A. Wang, T. Zhang and J. Li, *Catal. Sci. Technol.*, 2016, **6**, 6886–6892.
- 17 B. Qiao, J. Liu, Y.-G. Wang, Q. Lin, X. Liu, A. Wang, J. Li, T. Zhang and J. Liu, *ACS Catal.*, 2015, **5**, 6249–6254.
- 18 X. Liu, Y. Yang, M. Chu, T. Duan, C. Meng and Y. Han, *Catal. Sci. Technol.*, 2016, **6**, 1632.
- 19 X. Liu, Y. Sui, T. Duan, C. Meng and Y. Han, *Catal. Sci. Technol.*, 2015, **5**, 1658–1667.
- 20 N. Remediakis, N. Lopez and J. K. Nørskov, *Angew. Chem., Int. Ed.*, 2005, **44**, 1824–1826.
- 21 Z. P. Liu, P. Hu and A. Alavi, *J. Am. Chem. Soc.*, 2002, **124**, 14770–14779.
- 22 B. Qiao, J.-X. Liang, A. Wang, C.-Q. Xu, J. Li, T. Zhang and J. Liu, *Nano Res.*, 2015, **8**, 2913–2924.
- 23 Y.-H. Lu, M. Zhou, C. Zhang and Y.-P. Feng, *J. Phys. Chem. C*, 2009, **113**, 20156–20160.
- 24 Z. Lu, P. Lv, Y. Liang, D. Ma, Y. Zhang, W. Zhang, X. Yang and Z. Yang, *Phys. Chem. Chem. Phys.*, 2016, **18**, 21865–21870.
- 25 Y. Li, Z. Zhou, G. Yu, W. Chen and Z. Chen, *J. Phys. Chem. C*, 2010, **114**, 6250–6254.
- 26 E. H. Song, Z. Wen and Q. Jiang, *J. Phys. Chem. C*, 2011, **115**, 3678–3683.
- 27 Y. Tang, Z. Yang and X. Dai, *Phys. Chem. Chem. Phys.*, 2012, **14**, 16566–16572.
- 28 Y. Tang, X. Dai, Z. Yang, Z. Liu, L. Pan, D. Ma and Z. Lu, *Carbon*, 2014, **71**, 139–149.
- 29 Y. Tang, L. Pan, W. Chen, C. Li, Z. Shen and X. Dai, *Appl. Phys. A*, 2015, **119**, 475–485.
- 30 H. Wang, Q. Wang, Y. Cheng, K. Li, Y. Yao, Q. Zhang, C. Dong, P. Wang, U. Schwingenschlöggl, W. Yang and X. X. Zhang, *Nano Lett.*, 2012, **12**, 141–144.
- 31 Z. He, K. He, A. W. Robertson, A. I. Kirkland, D. Kim, J. Ihm, E. Yoon, G.-D. Lee and J. H. Warner, *Nano Lett.*, 2014, **14**, 3766–3772.
- 32 T. Wang, D. Gao, J. Zhuo, Z. Zhu, P. Papanikolaou, Y. Li and M. Li, *Chem.–Eur. J.*, 2013, **19**, 11939–11948.
- 33 Z. Chen, J. He, P. Zhou, J. Na and L. Z. Sun, *Comput. Mater. Sci.*, 2015, **110**, 102–108.
- 34 Y. Zhou, Q. Su, Z. Wang, H. Deng and X. Zu, *Phys. Chem. Chem. Phys.*, 2013, **15**, 18464–18470.
- 35 D. Ma, Y. Tang, G. Yang, J. Zeng, C. He and Z. Lu, *Appl. Surf. Sci.*, 2015, **328**, 71–77.
- 36 Z. W. Chen, J. M. Yan, W. T. Zheng and Q. Jiang, *Sci. Rep.*, 2015, **5**, 11230.
- 37 Y. Wang, L. Li, W. Yao, S. Song, J. T. Sun, J. Pan, X. Ren, C. Li, E. Okunishi, Y.-Q. Wang, E. Wang, Y. Shao, Y. Y. Zhang, H. Yang, E. F. Schwier, H. Iwasawa, K. Shimada, M. Taniguchi, Z. Cheng, S. Zhou, S. Du, S. J. Pennycook, S. T. Pantelides and H.-J. Gao, *Nano Lett.*, 2015, **15**, 4013–4018.
- 38 Q. Ma, P. M. Odenthal, J. Mann, D. Le, C. S. Wang, Y. Zhu, T. Chen, D. Sun, K. Yamaguchi, T. Tran, M. Wurch, J. L. McKinley, J. Wyrick, K. M. Magnone, T. F. Heinz, T. S. Rahman, R. Kawakami and L. Bartels, *J. Phys.: Condens. Matter*, 2013, **25**, 252201.



- 39 H.-P. Komsa, J. Kotakoski, S. Kurasch, O. Lehtinen, U. Kaiser and A. V. Krashennikov, *Phys. Rev. Lett.*, 2012, **109**, 035503.
- 40 P. E. Blöchl, *Phys. Rev. B: Condens. Matter Mater. Phys.*, 1994, **50**, 17953–17979.
- 41 G. Kresse and J. Furthmüller, *Comput. Mater. Sci.*, 1996, **6**, 15–50.
- 42 G. Kresse and D. Joubert, *Phys. Rev. B: Condens. Matter Mater. Phys.*, 1999, **59**, 1758–1775.
- 43 H. J. Monkhorst and J. D. Pack, *Phys. Rev. B: Solid State*, 1976, **13**, 5188–5192.
- 44 G. Henkelman, B. P. Uberuaga and H. Jónsson, *J. Chem. Phys.*, 2000, **113**, 9901–9904.
- 45 J. Kästner and P. Sherwood, *J. Chem. Phys.*, 2008, **128**, 014106.
- 46 G. Henkelman, “*Vasp TST tools*”, can be found in <http://theory.cm.utexas.edu/vtsttools/>.
- 47 J. Perdew, M. Ernzerhof and K. Burke, *J. Chem. Phys.*, 1996, **105**, 9982.
- 48 C. Adamo and V. Barone, *J. Chem. Phys.*, 1999, **110**, 6158.
- 49 S. Grimme, J. Antony, S. Ehrlich and H. Krieg, *J. Chem. Phys.*, 2010, **132**, 154104.
- 50 Q. Deng, L. Zhao, X. Gao, M. Zhang, Y. Luo and Y. Zhao, *Small*, 2013, **9**, 3506–3513.
- 51 F. Li, J. Zhao and Z. Chen, *J. Phys. Chem. C*, 2012, **116**, 2507.
- 52 G. Henkelman, A. Arnaldsson and H. Jónsson, *Comput. Mater. Sci.*, 2006, **36**, 354–360.
- 53 C. Schiwiek, J. Meiners, M. Förster, C. Würtele, M. Diefenbach, M. C. Holthausen and S. Schneider, *Angew. Chem.*, 2015, **127**, 15486–15490.
- 54 K. H. Warnick, B. Wang, D. E. Cliffl, D. W. Wright, R. F. Haglund and S. T. Pantelides, *Nano Lett.*, 2013, **13**, 798–802.
- 55 Y. Kim, H. M. Lee and G. Henkelman, *J. Am. Chem. Soc.*, 2012, **134**, 1560–1570.
- 56 S. Kwon, K. Shin, K. Bang, H. Y. Kim and H. M. Lee, *Phys. Chem. Chem. Phys.*, 2016, **18**, 13232–13238.
- 57 P. Zhao, Y. Su, Y. Zhang, S. J. Li and G. Chen, *Chem. Phys. Lett.*, 2011, **515**, 159–162.
- 58 C. Dupont, Y. Jugnet and D. Loffreda, *J. Am. Chem. Soc.*, 2006, **128**, 9129–9136.
- 59 S. Lin, X. Ye, R. S. Johnson and H. Guo, *J. Phys. Chem. C*, 2013, **117**, 17319–17326.
- 60 B. Hammer and J. K. Norskov, in *Advances in Catalysis*, Academic Press Inc, San Diego, 2000, pp. 71–129.
- 61 W. Xue, Z. C. Wang, S. G. He, Y. Xie and E. R. Bernstein, *J. Am. Chem. Soc.*, 2008, **130**, 15879.
- 62 Y. Zheng, T. Cheng, Y. Wang, F. Bao, L. Zhou, X. Wei, Y. Zhang and Q. Zheng, *J. Phys. Chem. B*, 2006, **110**, 3093–3097.
- 63 D. Deng, X. Chen, L. Yu, X. Wu, Q. Liu, Y. Liu, X. Bao, *et al.*, *Sci. Adv.*, 2015, **1**, e1500462.



# **Attachment No. 9**



Cite this: *J. Mater. Chem. C*, 2016,  
4, 6500

# High temperature spin-polarized semiconductivity with zero magnetization in two-dimensional Janus MXenes†

Junjie He,<sup>a</sup> Pengbo Lyu,<sup>a</sup> L. Z. Sun,<sup>\*b</sup> Ángel Morales García<sup>a</sup> and Petr Nachtigall<sup>\*a</sup>

Searching for two-dimensional (2D) materials with room-temperature magnetic order and high spin-polarization is essential for the development of next-generation nanospintronic devices. A new class of 2D magnetic materials with high Néel temperature, fully compensated antiferromagnetic order (zero magnetization) and completely spin-polarized semiconductivity is proposed for the first time. Based on the density functional theory calculations, we predict these properties for asymmetrically functionalized MXenes (Janus Cr<sub>2</sub>C) – Cr<sub>2</sub>CXX' (X, X' = H, F, Cl, Br, OH). The valence and conduction bands in these materials are made up of opposite spin channels and they can behave as bipolar magnetic semiconductors with zero magnetization. A Néel temperature as high as 400 K has been found for Cr<sub>2</sub>CFCl, Cr<sub>2</sub>CClBr, Cr<sub>2</sub>CHCl, Cr<sub>2</sub>CHF, and Cr<sub>2</sub>CFOH materials. Remarkably, the spin carrier orientation and induced transition from bipolar magnetic semiconductors to half-metal antiferromagnets can be easily controlled by electron or hole doping. The band gap of Janus MXenes can be effectively tuned by the selection of a pair of chemical elements/functional groups terminating the upper and the lower surfaces. The spin-polarized semiconductivity with zero magnetism is preserved when MXenes are put on the SiC(0001) support. The results presented herein open a new road towards the construction of 2D high-temperature spin-polarized materials with antiferromagnetism potentially suitable for spintronic applications.

Received 29th March 2016,  
Accepted 9th June 2016

DOI: 10.1039/c6tc01287f

www.rsc.org/MaterialsC

## 1. Introduction

Two dimensional (2D) materials with room-temperature magnetic order and high spin-polarization are crucial for the next-generation of electronic devices.<sup>1</sup> A majority of 2D materials including graphene,<sup>2</sup> boron nitride,<sup>3</sup> graphyne,<sup>4</sup> and transition-metal (TM) chalcogenides<sup>5,6</sup> (MoS<sub>2</sub> and WS<sub>2</sub>) are intrinsically non-magnetic and spin non-polarized; consequently their applications in spintronics are limited. Modification of these 2D materials by the presence of defects,<sup>7</sup> transition-metal (TM) doping<sup>8–10</sup> or surface functionalization<sup>11,12</sup> can introduce both the spin-polarization and magnetic properties. Unfortunately, it is still a challenge to achieve an ordered spin structure and high spin-polarization at room temperature due to uncontrollable dopant or defect distributions, or due to the cluster effect of dopants and weak spin interactions. Only a few 2D systems are predicted to have both intrinsic ferromagnetism (FM) and

100% spin-polarization at the Fermi level or at the valence band maximum (VBM) and the conduction band minimum (CBM). Based on their electronic structure these materials can be divided into half-metals,<sup>13–15</sup> half-semiconductors,<sup>16–19</sup> and bipolar magnetic semiconductors.<sup>20</sup> Most of them exhibit a Curie temperature generally below room-temperature due to the weak FM superexchange interactions. For conventional antiferromagnetic (AF) materials the Néel temperature ( $T_N$ ) is usually high, whereas their net magnetization and spin polarization vanish due to the symmetrical distribution of d state electrons of magnetic ions.<sup>21–24</sup> Moreover, the FM materials unavoidably introduce magnetic domains and stray fields that, in turn, influence the generation and manipulation of the spin-polarized current.<sup>20,25</sup>

To overcome these problems, Van Leuken and de Groot<sup>26,27</sup> proposed that the half-metallic antiferromagnets (HMAFs) can be achieved as completely spin-polarized materials with compensated AF (zero magnetization). HMAFs have been theoretically predicted for Heusler alloys,<sup>28–30</sup> perovskite compounds,<sup>31,32</sup> transition metal (TM) oxides,<sup>33,34</sup> etc. Half-Heusler Mn<sub>2</sub>Ru<sub>x</sub>Ga and Mn<sub>2</sub>Pt<sub>x</sub>Ga alloys were recently prepared experimentally and novel physical properties such as the anomalous Hall effect were observed for such HMAFs.<sup>35–37</sup> Similarly, compensated AF semiconductors including half-semiconductor antiferromagnets

<sup>a</sup> Department of Physical and Macromolecular Chemistry, Faculty of Science, Charles University in Prague, 128 43 Prague 2, Czech Republic.

E-mail: petr.nachtigall@natur.cuni.cz

<sup>b</sup> Hunan Provincial Key Laboratory of Thin Film Materials and Devices, School of Material Sciences and Engineering, Xiangtan University, Xiangtan 411105, China. E-mail: lzsun@xtu.edu.cn

† Electronic supplementary information (ESI) available. See DOI: 10.1039/c6tc01287f

(HSCAFs) and bipolar magnetic semiconductors with antiferromagnetic coupling (BMSAF) have been theoretically predicted.<sup>21,38</sup> The advantages of these materials include both full spin-polarization and a compensated AF, and consequently no stray field, insensitivity to magnetic interfaces, lower energy consumption, and a higher magnetic order temperature.<sup>21,37</sup> Such properties were even found experimentally for complicated bulk Heusler alloys upon doping. However, the complicated crystal structure of such HMAF materials is accompanied by the lattice distortion and strong spin-orbital coupling effects,<sup>20</sup> thus, the bulk-compensated AF properties are destroyed. It remains a challenge to precisely control the doping concentration experimentally in the synthesis of HMAF materials.

Two fundamental questions remain to be answered: (i) Do the 2D materials with high-temperature spin-polarization and fully compensated AF order have desired magnetic properties? (ii) Are they experimentally accessible? MXenes, a family of 2D transition metal carbides (TMC) and nitrides (TMN), have been prepared experimentally by the chemical exfoliation technique.<sup>39,40</sup> The synthesized MXenes are generally terminated with a surface element/group such as H, F, and OH.<sup>41</sup> The previous theoretical investigations have shown that Cr<sub>2</sub>CX<sub>2</sub> (X = OH, H, F and Cl), Ti<sub>2</sub>CO<sub>2</sub>, Zr<sub>2</sub>CO<sub>2</sub>, Hf<sub>2</sub>CO<sub>2</sub>, and Sc<sub>2</sub>X<sub>2</sub> (X = O, OH, F) are semiconductors or antiferromagnetic semiconductors, while V<sub>2</sub>CX<sub>2</sub> (X = F, OH), Cr<sub>2</sub>NX<sub>2</sub> (X = F, OH, O) and Ti<sub>2</sub>N are antiferromagnetic metals.<sup>14,42–45</sup> Asymmetrical functionalization results in a different chemical environment of TM ions on each side of the layer and, thus, it may lead to the Fermi level shift between spin-up and spin-down channels. If asymmetrically functionalized MXenes keep an AF order, these 2D systems should have the desired magnetic properties: fully compensated AF with high  $T_N$  and spin-polarization. The asymmetrically functionalized Ti<sub>2</sub>C MXenes with –OCH<sub>3</sub> and –OH groups have been studied at the DFT level reporting high stability for these Ti<sub>2</sub>C(OCH<sub>3</sub>)(OH) 2D materials.<sup>46</sup> Note that chemically modified graphene with asymmetrical upper and lower surfaces (Janus graphene) was obtained experimentally, *e.g.*, fluorographene (asymmetrically functionalized by fluorine and hydrogen).<sup>47,48</sup> By analogy with Janus graphene one can assume that Janus MXenes (asymmetrically functionalized) could also be obtained experimentally, while this is still a challenge for the experimental community. A comprehensive theoretical study of electronic and magnetic properties of Janus MXenes, including Cr<sub>2</sub>C (Cr<sub>2</sub>CXX', X, X' = H, F, Cl, Br, OH) and V<sub>2</sub>CFOH, based on first-principles calculations is reported herein. It is shown for the first time that the Janus Cr<sub>2</sub>C and V<sub>2</sub>C 2D materials behave as high temperature compensated BMSAF due to the mismatch of d states of TM atoms induced by asymmetric functionalization. Moreover, the carriers' spin orientation of Cr<sub>2</sub>CXX' and V<sub>2</sub>CXX' can be easily controlled and the transition from BMSAF to HMAF can be achieved.

## 2. Method and computational details

All calculations are performed using the Vienna *ab initio* simulation package (VASP),<sup>49,50</sup> within the generalized gradient

approximation employing the Perdew–Burke–Ernzerhof (PBE) exchange–correlation functional. Interactions between electrons and nuclei are described by the projector-augmented wave (PAW) method.<sup>51</sup> The criteria of energy and atom force convergence are set to 10<sup>−5</sup> eV per unit cell and 0.01 eV Å<sup>−1</sup>, respectively. The Brillouin zone (BZ) is sampled using 15 × 15 × 1 and 21 × 21 × 1 gamma-centered Monkhorst–Pack grids for the calculations of relaxation and electronic structures, respectively. To account for the energy of localized 3d orbitals of TM atoms properly, the Hubbard “*U*” correction is employed within the rotationally invariant DFT + *U* approach proposed by Dudarev *et al.*<sup>52</sup> A correction of *U* = 3 eV is employed based on the relevant previous reports.<sup>14,15</sup> Using linear-response theory proposed by Cococcioni *et al.*,<sup>53</sup> the *U* parameters were also evaluated for Cr<sub>2</sub>CFCl and Cr<sub>2</sub>CHBr systems. The calculated *U* parameters are 2.54/2.68 eV and 2.73/2.91 eV for Cr<sub>2</sub>CFCl and Cr<sub>2</sub>CHBr, respectively, in good agreement with the *U* parameters calculated previously for monolayer chromium trihalides due to the same valence configuration.<sup>16</sup> These results suggest that the selected *U* = 3 eV is a reasonable value. Moreover, the test calculation of the effective *U* value for Cr<sub>2</sub>CFCl (*U* = 2, 4, 5 eV) yielded similar results as obtained with *U* = 3 eV (see Fig. S1 in ESI†).

The vacuum space of 15 Å along the Cr<sub>2</sub>C normal is adopted. A plane-wave kinetic energy cutoff of 500 eV is employed. Test calculations including the spin-orbital coupling (SOC) effects and non-collinear magnetization for Cr<sub>2</sub>CFCl in electronic and magnetic properties are also performed; the SOC effect was found to be very small, not large enough to affect the zero magnetization and spin-polarization properties.

## 3. Results and discussion

### 3.1. Structure, and magnetic and electronic properties of Janus Cr<sub>2</sub>CXX'

The lattice constant of 2D Cr<sub>2</sub>C calculated at the PBE – *U* level of theory, 3.191 Å, is in agreement with the previous results obtained using the hybrid functional.<sup>14</sup> 2D Cr<sub>2</sub>C is a ferromagnetic half-metal, however, the symmetrically functionalized structures Cr<sub>2</sub>CX<sub>2</sub>, such as Cr<sub>2</sub>C(OH)<sub>2</sub>, Cr<sub>2</sub>CH<sub>2</sub>, and Cr<sub>2</sub>CCl<sub>2</sub> systems, are intrinsic antiferromagnetic semiconductors without spin polarization as shown in Table S1 (ESI†). The calculated geometry and magnetic parameters of Cr<sub>2</sub>CX<sub>2</sub> are also presented in this table. Considering the asymmetric surface functionalization of Janus MXenes (denoted as Cr<sub>2</sub>CXX', where X and X' stand for different chemical groups, such as H, OH, F, Cl or Br), it is possible to design spin-polarized semiconductors with fully-compensated antiferromagnetism due to the fact that Cr atoms in the upper and the lower layers have chemically different environments, which result in a mismatch of their d states.

To explore this idea further, geometries of Janus Cr<sub>2</sub>CXX' materials (X, X' = H, OH, F, Cl, Br) together with their electronic and magnetic properties were investigated and they are reported in Table 1. The FM states of all Cr<sub>2</sub>CXX' MXenes have a total magnetic moment of 6μ<sub>B</sub> (per unit cell), which is mainly contributed by Cr atoms. The calculated local magnetic moments

**Table 1** Calculated structural and magnetic characteristics of ten different Janus Cr<sub>2</sub>CXX' MXenes. *L* is the lattice constant,  $\Delta E_{\text{ex1}}$  and  $\Delta E_{\text{ex2}}$  define the difference between  $E_{\text{Néel}}$  and  $E_{\text{FM}}$ , and  $E_{\text{Néel}}$  and  $E_{\text{zigzag}}$ , respectively.  $J_1$  and  $J_2$  represent the nearest neighbor and next nearest neighbor coupling constants according to the Heisenberg model, respectively

Structure	<i>L</i> (Å)	$\Delta E_{\text{ex1}}$ (eV)	$\Delta E_{\text{ex2}}$ (eV)	$J_1$ (meV)	$J_2$ (meV)	$T_N$ (K)
Cr <sub>2</sub> CFCl	3.195	0.608	1.095	-22.534	19.155	395
Cr <sub>2</sub> CHBr	3.206	0.442	0.855	-16.352	15.569	320
Cr <sub>2</sub> CClBr	3.332	0.573	1.141	-21.211	21.088	385
Cr <sub>2</sub> CFBr	3.252	0.530	0.677	-19.631	8.980	310
Cr <sub>2</sub> CBrOH	3.259	0.524	0.659	-19.419	8.581	300
Cr <sub>2</sub> CHCl	3.150	0.494	1.283	-18.292	26.487	430
Cr <sub>2</sub> CHF	3.054	0.509	1.093	-18.846	20.974	380
Cr <sub>2</sub> CClOH	3.203	0.594	1.049	-22.002	18.135	375
Cr <sub>2</sub> CFOH	3.111	0.664	1.036	-24.580	16.496	390
Cr <sub>2</sub> CHOH	3.066	0.460	0.481	-17.019	4.842	270

show that Cr atoms are in the high spin (HS) state with  $d^{3\uparrow}$  spin configurations; each Cr atom carries a 3+ charge. To determine the preferred magnetic ground state structures of Cr<sub>2</sub>CXX' systems, the collinear FM, Néel, and zigzag states are considered as shown in Fig. 1a. The relative stabilities of FM states ( $E_{\text{FM}}$ ), Néel states ( $E_{\text{Néel}}$ ) and zigzag states ( $E_{\text{zigzag}}$ ) are defined as:  $\Delta E_{\text{ex1}} = E_{\text{FM}} - E_{\text{Néel}}$  and  $\Delta E_{\text{ex2}} = E_{\text{zigzag}} - E_{\text{Néel}}$ , respectively. The relative stability of the Néel state increases with increasing  $\Delta E_{\text{ex1}}$  and  $\Delta E_{\text{ex2}}$  values. It is found that the Néel states are stable in all Cr<sub>2</sub>CXX' systems, similarly to previously reported results for symmetrically functionalized Cr<sub>2</sub>CX<sub>2</sub>.<sup>14</sup> The nearest- and next-nearest-neighbor exchange coupling parameters  $J_1$  and  $J_2$ , respectively, were calculated by mapping the total energies of the systems with different magnetic structures to a classical Heisenberg model:

$$H_{\text{spin}} = - \sum_{i,j} J_1 S_i \cdot S_j - \sum_{k,l} J_2 S_k \cdot S_l \quad (1)$$

where  $S_i$  is the net spin at the Cr site  $i$  and  $(i,j)$  and  $(k,l)$  stand for the nearest and next-nearest Cr atoms, respectively. We only consider the nearest- and next-nearest-neighbor exchange interactions, since the third neighbor exchange parameters are small.

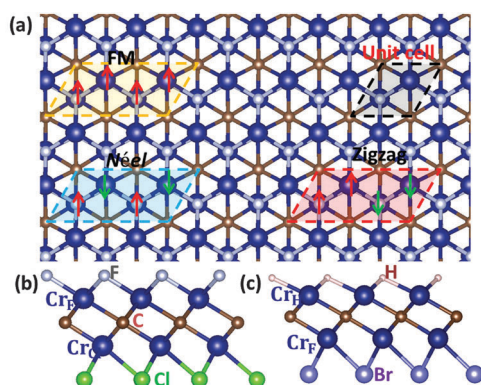


**Fig. 1** The top and side views of Cr<sub>2</sub>CXX' (parts a and b, respectively) and a side view of the Cr<sub>2</sub>CX<sub>2</sub> monolayer (c); the color scheme for Cr, C, X and X' atoms is described in the figure. The rhombic unit cell is marked by a black dotted line, while FM, Néel, and zigzag states are marked by yellow, cyan and red dotted lines, respectively.

By mapping the DFT energies to the Heisenberg spin Hamiltonian,  $J_1$  and  $J_2$  can be calculated in the following way:

$$E_{\text{FM}} - E_{\text{Néel}} = 12J_1S^2, \quad (2)$$

$$E_{\text{zigzag}} - E_{\text{Néel}} = (4J_1 + 16J_2)S^2, \quad (3)$$

where  $S = 3/2$  corresponds to the Cr<sup>3+</sup> configuration. The calculated exchange coupling parameters of Cr<sub>2</sub>CXX' are summarized in Table 1. These results clearly demonstrate that the Néel state configurations for all Cr<sub>2</sub>CXX' are magnetic ground states with high magnetic stability.

The Néel temperatures  $T_N$  for Janus Cr<sub>2</sub>CXX' are estimated based on the classical Heisenberg Hamiltonian using the DFT derived spin exchange parameters and Monte-Carlo (MC) simulations on a  $50 \times 50$  2D honeycomb lattice and  $10^5$  steps for each temperature (test calculations show that a larger lattice ( $80 \times 80$ ) and a larger number of MC steps ( $10^8$ ) give very similar  $T_N$  values).  $T_N$  was found as a maximum on the temperature dependent specific heat  $C_V(T)$  curve (Fig. 2b). Specific heat values were calculated as  $C_V = (\langle E^2 \rangle - \langle E \rangle^2)/T^2$ . From the simulated  $C_V(T)$  curve, the  $T_N$  value is found to be 395 K for Cr<sub>2</sub>CFCl. All Janus Cr<sub>2</sub>CXX' are predicted to have a high Néel temperature (as shown in Table 1), suggesting potential applications for room-temperature electronic devices.

### 3.2. Manipulation of spin-polarization orientation for Janus Cr<sub>2</sub>CXX'

The Néel states are the most stable magnetic configurations for all Janus Cr<sub>2</sub>CXX' considered herein. The electronic properties of Cr<sub>2</sub>CFCl are discussed below while the results of other Cr<sub>2</sub>CXX' structures are reported in the ESI† (Fig. S2). The calculated band structure and the density of states (DOS) for Cr<sub>2</sub>CFCl show 100% spin polarization in the VBM and the CBM with opposite spin channels (Fig. 2). The Cr<sub>2</sub>CFCl system is a bipolar magnetic semiconductor with AF coupling (BMSAF). The BMS's have been proposed as a new class of materials for spintronics, where the spin-polarization direction can be controlled simply by applying a gate voltage.<sup>22,54–56</sup> According to the definition of BMS,<sup>22,54</sup> a typical BMS can be described by three energy gaps ( $\Delta_1$ ,  $\Delta_2$  and  $\Delta_3$ ) reported in Fig. 2a. The  $\Delta_1$  gap is defined as a spin-flip gap with opposite spin polarization between the VBM and the CBM. In addition, one can manipulate the spin polarization of carriers in the BMS simply by shifting the Fermi level. Following the notation of ref. 22 and 54,  $(\Delta_1 + \Delta_2)$  and  $(\Delta_1 + \Delta_3)$  are defined as spin-conserved gaps and the Fermi level will shift up and down to be located in the  $\Delta_1$  and  $\Delta_3$  gaps in the positive and negative gate voltages, respectively. The calculated  $\Delta_1$ ,  $\Delta_2$ , and  $\Delta_3$  gaps are 1.02, 0.31, and 0.41 eV, respectively, for Cr<sub>2</sub>CFCl, (see Fig. 3a for  $\Delta$  values of other MXenes).

Cr<sub>2</sub>CXX' behaves as a BMSAF in which the VBM and CBM states are 100% spin polarized with opposite spin channels. It can be controlled easily by applying a gate voltage in practical applications. The doping electron and hole will shift the Fermi level to different spin-polarized VBM and CBM regions, resulting in a tunable carrier spin orientation and the transition from

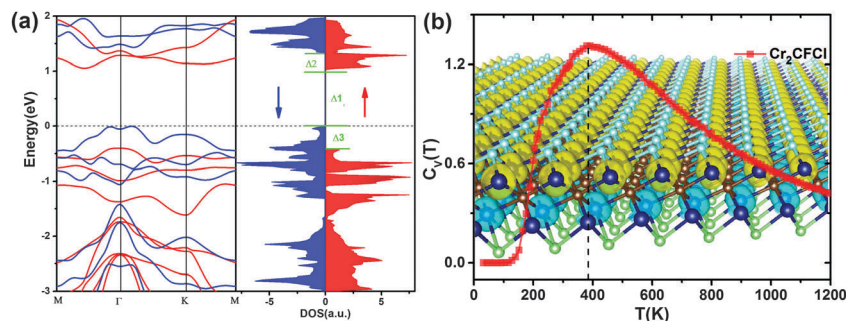


Fig. 2 (a) Band structure and total DOS for  $\text{Cr}_2\text{CFCl}$ . The spin-up and spin-down channels are depicted in red and blue, respectively. (b) Simulated specific heat  $C_V$  as a function of temperature ( $T$ ) for  $\text{Cr}_2\text{CFCl}$ . The inserted background figure shows spin polarized charge densities of  $\text{Cr}_2\text{CFCl}$ , where spin-up and spin-down densities are shown in yellow and cyan, respectively.

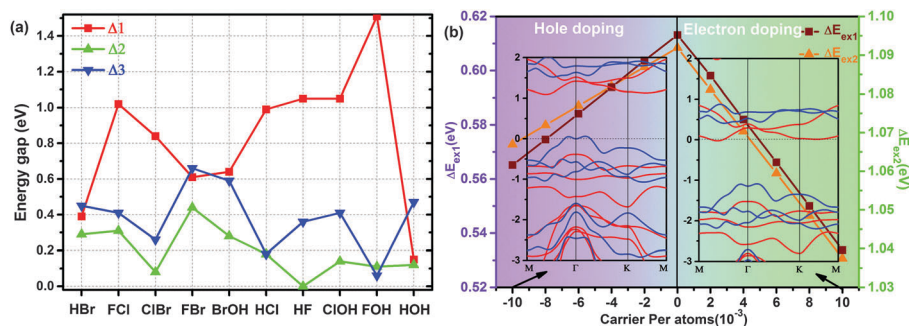


Fig. 3 Spin-flip gaps and spin-conserved gaps ( $\Delta_1$ ,  $\Delta_2$  and  $\Delta_3$ ) for  $\text{Cr}_2\text{CXX}'$  Janus MXenes are reported in part (a).  $\Delta E_{\text{ex}1}$  and  $\Delta E_{\text{ex}2}$  as a function of carrier concentration calculated for  $\text{Cr}_2\text{CFCl}$  (b). The positive and negative values are for the electron and for the hole doping, respectively. The calculated band structures for electron doping and hole doping for various carrier concentrations are presented as well; red and blue lines represent spin-up and spin-down directions, respectively.

BMSAF to HFAF as shown in Fig. 3b for  $\text{Cr}_2\text{CFCl}$ . For small electron doping,  $\text{Cr}_2\text{CFCl}$  changes from the BMSAF to HMAF states with spin-down polarization, while a spin-up polarized HMAF state is obtained in the case of hole doping. Thus, completely spin-polarized currents with tunable spin orientation of carriers and HMAF properties can be realized easily by electron or hole doping. Moreover, the HMAF properties are primarily determined by a compensated AF order. It has been reported previously for 2D  $\text{MnPSe}_3$  materials where both the electron doping and the hole doping can induce transition from Néel to FM states.<sup>55</sup> Although the low concentration of the carrier dopant can decrease the energy of the magnetic exchange coupling, the  $\text{Cr}_2\text{CFCl}$  system still shows high stability for Néel states. The electron or hole doping was also considered for  $\text{Cr}_2\text{CHBr}$  (reported in Fig. S3 of the ESI<sup>†</sup>) and the results are very similar to those reported in Fig. 3b for  $\text{Cr}_2\text{CFCl}$ . The tunable spin-polarization direction provides a potential strategy to manipulate the carrier spin-polarization in 2D Janus MXenes simply by applying a gate voltage.

### 3.3. The origin of electronic structure of Janus $\text{Cr}_2\text{CXX}'$

The chemically substituted  $\text{Cr}_2\text{CX}_2$  structures, such as  $\text{Cr}_2\text{C}(\text{OH})_2$ ,  $\text{Cr}_2\text{CH}_2$ , and  $\text{Cr}_2\text{CCl}_2$  systems, are intrinsic antiferromagnetic semiconductors that are non-magnetic and spin non-polarized. The partial densities of states (PDOS) are plotted in Fig. S4 (ESI<sup>†</sup>)

for d states of magnetic ions in  $\text{Cr}_2\text{CF}_2$  and  $\text{Cr}_2\text{CCl}_2$  MXenes. One can find that the total d states on  $\text{Cr}_A$  and  $\text{Cr}_B$  (Cr ions in the upper and lower layers, respectively) in  $\text{Cr}_2\text{CF}_2$  and  $\text{Cr}_2\text{CCl}_2$  have a perfectly symmetrical distribution of spin-up and spin-down states due to the equivalent chemical environment of all Cr atoms resulting in the same exchange splitting. Although the individual  $\text{Cr}_A$  and  $\text{Cr}_B$  atoms are spin-polarized (Fig. 4c), they do not contribute to the net spin-polarization of the  $\text{Cr}_2\text{CF}_2$  system due to the equivalent chemical environment and the antiferromagnetic coupling between them. It follows that all  $\text{Cr}_2\text{CX}_2$  MXenes are intrinsic spin non-polarized semiconductors. For Janus MXenes, the chemically different functionalization of the upper and the lower surfaces induces the mismatch of d states for  $\text{Cr}_A$  and  $\text{Cr}_B$  atoms that now have chemically different environments (Fig. 4d). As pointed out by Li *et al.*,<sup>22</sup> a bipolar magnetic semiconductor is obtained when the occupied spin-up state of one TM ion is located in the crystal field splitting gap of the other TM ion. It is apparent from this figure that the VBM states of  $\text{Cr}_F$  are located exactly in the crystal field splitting gap of  $\text{Cr}_{Cl}$ , thus resulting in a BMSAF feature.

To gain insight into the BMSAF properties of  $\text{Cr}_2\text{CXX}'$ , the partial electronic density of states (PDOS) and the magnetic coupling mechanism are discussed below. The PDOS of  $\text{Cr}_F$  and  $\text{Cr}_{Cl}$  atoms of  $\text{Cr}_2\text{CFCl}$  are shown in Fig. 4. According to the  $D_{3d}$  local symmetry of the crystal field on Cr magnetic ions, the 3d

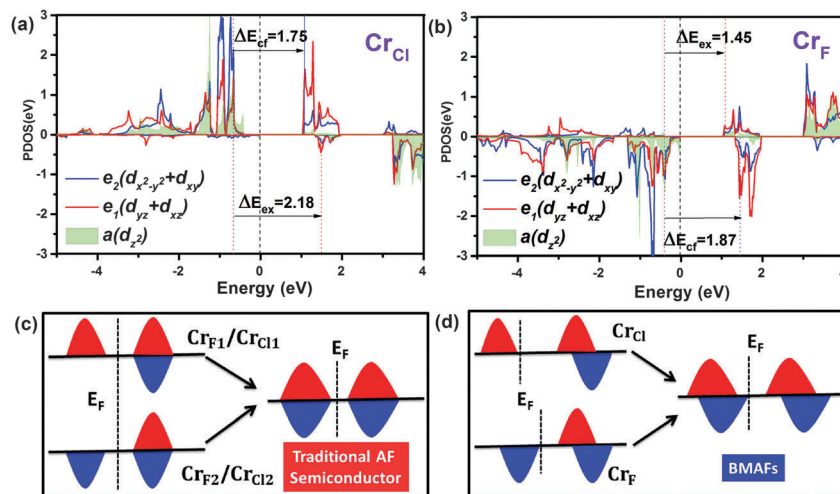


Fig. 4 PDOS of d states for Cr<sub>Cl</sub> (a) and Cr<sub>F</sub> (b) calculated for Cr<sub>2</sub>CFCl. The crystal field splittings ( $\Delta E_{cf}$ ) and the exchange splittings ( $\Delta E_{ex}$ ) are shown. The Fermi level is set to zero. Schematic diagrams of the Cr spin exchange splitting in symmetrically and asymmetrically functionalized surfaces are shown in parts (c) and (d), respectively.

orbitals split into a non-degenerate  $a(d_{z^2})$  orbital and two 2-fold degenerate  $e_1(d_{xz}/d_{yz})$  and  $e_2(d_{xy}/d_{x^2-y^2})$  orbitals (the  $z$  axis being along the surface normal). The VBM and CBM states of Cr<sub>2</sub>CFCl are mainly derived from Cr<sub>F</sub>- $a$  and mixed Cr<sub>Cl</sub>- $e_1$ /Cr<sub>Cl</sub>- $e_2$  states, respectively. The d states of Cr ions reflect the crystal field splitting ( $\Delta E_{cf}$ ) and the exchange splitting ( $\Delta E_{ex}$ ) due to the crystal field interactions and the on-site Coulomb interactions, respectively. For instance, the spin-up d states of the Cr<sub>Cl</sub> atom mainly lie within  $(-4, 0)$  eV and  $(1, 2)$  eV energy windows, whereas some spin-down d states mostly correspond to the unoccupied states above the Fermi level. The crystal field and exchange splittings of Cr<sub>Cl</sub>-d states are 1.75 and 2.18 eV, respectively, and for Cr<sub>F</sub>-d states they are 1.87 eV and 1.45 eV, respectively. The differences in crystal and exchange field splittings on Cr<sub>F</sub> and Cr<sub>Cl</sub> ions (due to the differences in the chemical environment of these ions) result in different values of splitting parameters. This give rise to the mismatch of d states, which further induces the spin-polarized effect in Cr<sub>2</sub>CFCl materials. The other Cr<sub>2</sub>CXX' materials can be understood by the same mechanism.

Another key point is to understand the origin of AF order for Cr<sub>F</sub> and Cr<sub>Cl</sub>. The spin-polarized charge densities (SCD), electron localization functions (ELF) and schemes of the exchange mechanism are plotted in Fig. 5 for Cr<sub>2</sub>C and Cr<sub>2</sub>CFCl. ELF maps show that Cr<sub>2</sub>C and Cr<sub>2</sub>CFCl have distinct characteristics of d orbitals:<sup>14</sup> itinerant d electrons for Cr<sub>2</sub>C and localized d electrons for Cr<sub>2</sub>CFCl. Itinerant d electrons can induce the spin-polarization of the neighboring C atoms (C shows the spin-polarization in the SCD figure) and Cr<sub>2</sub>C maintains the AF coupling between the Cr and the neighboring C atoms. They can form the spin arrangement like Cr<sub>1</sub>↑-C<sub>1</sub>-Cr<sub>2</sub>↑.<sup>57</sup> Therefore, the FM coupling of Cr ions in Cr<sub>2</sub>C is mediated by C-2p states *via* a double-exchange mechanism (Fig. 5a). However, for Cr<sub>2</sub>CFCl, the local Cr<sub>Cl</sub>-d orbitals can directly induce the antiparallel spin arrangement on neighboring Cr<sub>F</sub> (Cr<sub>Cl</sub>↑-Cr<sub>F</sub>↓ configuration) *via* the super-exchange mechanism as shown in Fig. 5b. Therefore, the AF states are more favorable in

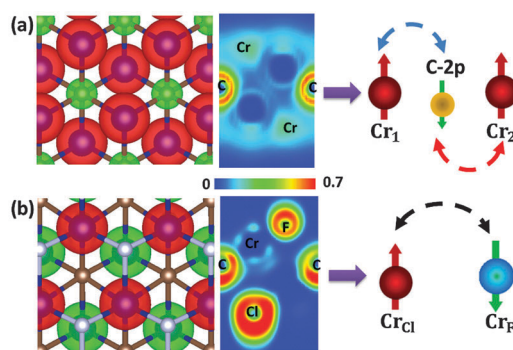


Fig. 5 The spin-polarized densities (SCD), electron localization functions (ELF) and schemes of the exchange mechanism for Cr<sub>2</sub>C (a) and Cr<sub>2</sub>CFCl (b) are presented. For the SCD figure, the spin-up and spin-down directions are depicted in yellow and cyan, respectively.

Cr<sub>2</sub>CFCl. The other Cr<sub>2</sub>CXX' can be understood in the same way. A similar magnetic coupling mechanism has been used to explain the origin of cation vacancies in GaN,<sup>58</sup> 2D transition metal dichalcogenides<sup>59,60</sup> and TM-doped 2D materials<sup>57</sup>

### 3.4. Stability of Janus Cr<sub>2</sub>CXX'

The surface termination of MXenes plays a critical role in their physical and chemical properties. Functionalized surfaces of Ti<sub>3</sub>C<sub>2</sub> MXenes were investigated both experimentally and computationally.<sup>61-63</sup> There are two types of hollow sites for MXenes depicted for Cr<sub>2</sub>C in the ESI† (Fig. S5): hollow site 1 (on the top of the Cr atom) and hollow site 2 (on the top of the C atom). The relative stabilities of X atoms in hollow sites 1 and 2 on the Cr<sub>2</sub>C surface (Table S2 in ESI†) show that site 1 is the most stable in all cases investigated herein.

It is important to investigate whether Janus MXenes are experimentally feasible. To evaluate the stability of functionalized Cr<sub>2</sub>C structures shown in Fig. 1, the formation energy,

$E_{\text{form}}$ , defined with respect to chemical potentials of functional groups/atoms<sup>64</sup> is calculated:

$$E_{\text{form}} = E_{\text{tot}}(\text{Cr}_2\text{CX}_n\text{X}'_m) - E_{\text{tot}}(\text{Cr}_2\text{C}) - (n/2)E_{\text{tot}}(\text{X}) - n\Delta\mu_{\text{X}} - (m/2)E_{\text{tot}}(\text{X}') - m\Delta\mu_{\text{X}'} \quad (4)$$

where  $E_{\text{tot}}(\text{Cr}_2\text{C})$  and  $E_{\text{tot}}(\text{Cr}_2\text{CXX}')$  stand for the total energies of pristine and functionalized MXenes, respectively. Energies of  $\text{O}_2$ ,  $\text{H}_2$ ,  $\text{F}_2$ ,  $\text{Cl}_2$ , and  $\text{Br}_2$  in the gas phase are taken for the energies of  $E_{\text{tot}}(\text{X})$  and  $E_{\text{tot}}(\text{X}')$ . And  $\Delta\mu_{\text{X}} = \mu - (1/2)E_{\text{tot}}(\text{X})$ , where  $\mu$  is the chemical potential of the functional group which can vary as a function of pressure and temperature.  $n$  and  $m$  stand for the number of functional groups in the  $2 \times 2$  supercell ( $\text{Cr}_8\text{C}_4\text{F}_n\text{Cl}_m$ ). The results of formation energy calculations at  $\Delta\mu = 0.0$  eV are shown in Fig. 6a. It can be seen that formation energies of these structures are all negative and much lower than that of a pristine  $\text{Cr}_2\text{C}$  monolayer (pristine  $\text{Cr}_2\text{C}$  has been shown to be stable<sup>14</sup>). Formation energies of asymmetrically functionalized  $\text{Cr}_2\text{CXX}'$  are just in between formation energies of the corresponding symmetrically functionalized  $\text{Cr}_2\text{CX}'_2$  MXenes. These results indicate the formation of strong chemical bonds between the transition metals and the functional groups and they are consistent with the fact that chemically functionalized MXenes were synthesized experimentally.<sup>38,39</sup>

Using the formation energy defined above the stability of  $\text{Cr}_2\text{CXX}'$  with respect to pristine  $\text{Cr}_2\text{C}$  can be compared for a range of X and X' chemical potentials  $\Delta\mu$  (from  $-2.0$  to  $0.0$  eV). The results of  $\text{Cr}_2\text{CFCl}$  obtained using the  $2 \times 2$  supercell ( $\text{Cr}_8\text{C}_4\text{F}_n\text{Cl}_m$ ) are shown in Fig. 6b. Temperatures from  $0$  to  $800$  K correspond to chemical potential ranges ( $0$ ,  $-0.93$ ) eV and ( $0$ ,  $-0.84$ ) eV for F and Cl, respectively. Within the range of chemical potentials investigated the  $\text{Cr}_2\text{CFCl}$  Janus MXene ( $m, n = 4$ ) is always thermodynamically favorable not only with respect to  $\text{Cr}_2\text{C}$  but also with respect to any surface with just a fractional occupation ( $n, m < 4$ ).

To confirm the dynamic stability of the  $\text{Cr}_2\text{CFCl}$  material, its phonon dispersion curves were calculated (Fig. 6d) within the density-functional perturbation theory<sup>65</sup> as implemented in the QUANTUM-ESPRESSO code.<sup>66</sup> The absence of imaginary frequencies proves that the  $\text{Cr}_2\text{CFCl}$  monolayer is dynamically stable. Furthermore, to evaluate the thermal stability of the  $\text{Cr}_2\text{CFCl}$  material, the *ab initio* molecular dynamics simulations were also performed at  $300$  K in a canonical ensemble using the Nosé heat bath approach. The results reported in Fig. 6c indicate that the atomic structure of  $\text{Cr}_2\text{CFCl}$  remains intact at  $300$  K for the duration of the simulation (more than  $8$  ps with a time step of  $2$  fs). Only a small variation of the total potential energy along the simulation time suggests that  $\text{Cr}_2\text{CFCl}$  is thermally stable at room temperature.

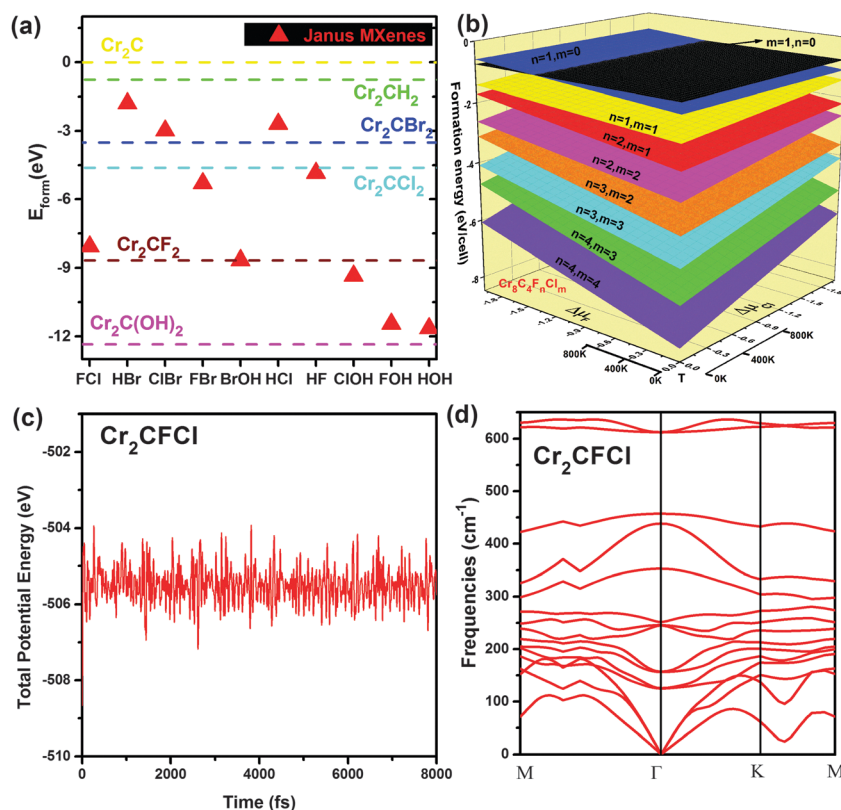


**Fig. 6** (a) Formation energies,  $E_{\text{form}}$ , defined in eqn (5), are reported for various Janus MXenes with respect to those calculated for symmetrically functionalized MXenes and unfunctionalized  $\text{Cr}_2\text{C}$ . (b) Formation energies of  $\text{Cr}_8\text{C}_4\text{F}_n\text{Cl}_m$  ( $n, m = 0, 1, \dots, 4$ ) represented by the  $2 \times 2$  supercell as a function of F/Cl chemical potentials. (c) Variations of the total potential energy of Janus  $\text{Cr}_2\text{CFCl}$  during *ab initio* molecular dynamics simulations at  $300$  K. (d) Phonon dispersion curves for Janus  $\text{Cr}_2\text{CFCl}$ .

### 3.5. Partially asymmetrical $\text{Cr}_2\text{CF}_x\text{Cl}_y$ with uneven distribution of F and Cl

The Janus  $\text{Cr}_2\text{CXX}'$  with the perfectly asymmetrical functionalization of upper and lower surfaces is an ideal system. The most relevant system synthesized until today is a Ti-based MXene obtained by exfoliation in hydrogen fluoride solution where both surfaces are partially functionalized by H and F atoms.<sup>67,68</sup> It is therefore important to investigate the electronic properties of variously substituted surfaces that are far from the ideal situation described above. Three model situations were investigated and the results are reported in Fig. 7. First, starting from the symmetrically substituted  $\text{Cr}_2\text{CF}_2$  MXene, a single F atom on the upper surface was replaced by a Cl atom; such an isolated Cl surface atom was considered (varying the supercell size) for Cl coverages 11 and 25% (Fig. 7a). Second, starting from the symmetrically substituted  $\text{Cr}_2\text{CF}_2$  MXenes, several adjacent F atoms on the upper surface were replaced by Cl atoms (forming a Cl island) considering 33, 56, and 67% coverages of Cl on the upper surface (Fig. 7b). Third, starting from perfectly asymmetrically substituted  $\text{Cr}_2\text{CFCl}$ , one, two, and three (randomly selected) F atoms from the upper surface were switched with the corresponding number of Cl atoms from the lower surface (Fig. 7c). All considered model situations show completely compensated AF ground states and spin-polarized semiconductor behavior. The increasing concentration of Cl atoms in the first and second model situations leads to increased spin splittings. It leads to an important conclusion that even

imperfect asymmetrical functionalization of  $\text{Cr}_2\text{C}$  is sufficient to effect the chemical environment of Cr atoms in the upper and lower surfaces enough to observe BMSAF characteristics. In addition, the varying concentration of X/X' on one of the surfaces provides an effective way to control the AF spin-splitting.

### 3.6. $\text{Cr}_2\text{CXX}'$ and $\text{Cr}_2\text{CX}_2$ on the SiC(0001) substrate

The results reported above were obtained for the models representing free-standing MXenes. The effect of the MXene interaction with the substrate (unavoidable in potential applications) on the electronic structure and compensated AF couplings is discussed below. Moreover, the placement of symmetrically functionalized  $\text{Cr}_2\text{CX}_2$  MXenes on the support is important for partial or full asymmetrical functionalization. The large area epitaxial growth of graphene layers on a SiC(0001) surface shows huge application potentials.<sup>69</sup> In particular, the hydrogen saturated SiC(0001) surface can effectively decrease the coupling between graphene and the substrate.<sup>70</sup> Therefore, the  $\text{Cr}_2\text{CF}_2$  and  $\text{Cr}_2\text{CFCl}$  MXenes on SiC(0001) were also investigated herein. The lattice constant for the SiC(0001) slab model is 3.080 Å, which matches well with the lattice constants of  $\text{Cr}_2\text{CF}_2$  (3.100 Å) and  $\text{Cr}_2\text{CFCl}$  (3.195 Å). The SiC(0001) substrate was represented by the bulk consisting of Si layers and H-terminated surfaces; the 14 Å vacuum between the upper MXene and the lower SiC surface was used. The calculations were performed at the PBE + D2 level.<sup>71</sup>

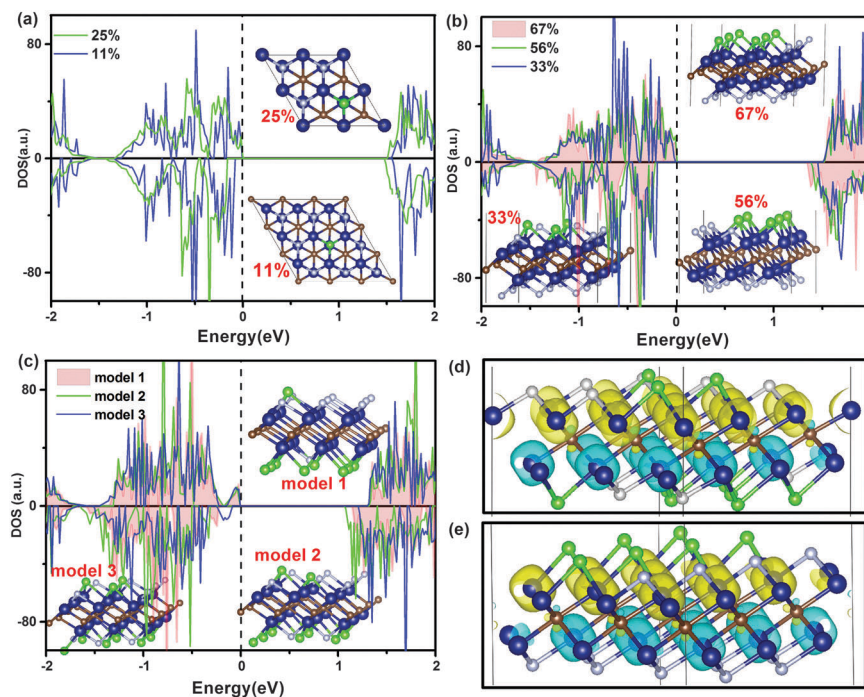


Fig. 7 DOS for various  $\text{Cr}_2\text{CF}_x\text{Cl}_y$  systems; spin-up and spin-down channels shown in the upper and the lower parts of individual panels, respectively. (a) A single Cl atom on the upper surface of  $\text{Cr}_2\text{CF}_2$  (11 and 25% of Cl on the upper surface). (b) Cl islands on the upper surface of  $\text{Cr}_2\text{CF}_2$  (33, 56, and 67% of Cl on the upper surface). (c)  $\text{Cr}_2\text{CFCl}$  with randomly switched F/Cl atom(s) (one, two and three F/Cl atom pairs switched). (d) The spin-polarized charge density (SCD) for three randomly switched F/Cl pairs (model 3 in part c of the figure); blue and yellow colors represent the spin-up and spin-down spin-polarized charge densities, respectively.

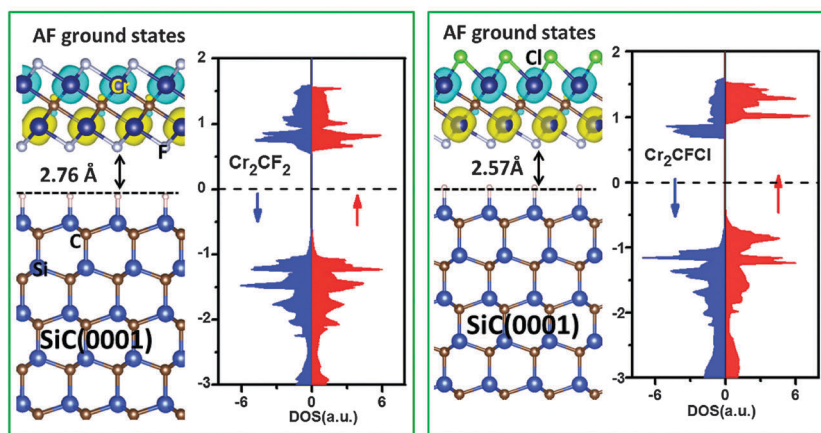


Fig. 8 DOS of  $\text{Cr}_2\text{CF}_2$  (a) and  $\text{Cr}_2\text{CFCl}$  (b) supported on the  $\text{SiC}(0001)$  substrate. Cyan and yellow represent the spin-polarized charge densities for spin-up and spin-down channels, respectively.

The distance between MXene and the substrate is 2.76 and 2.57 Å for  $\text{Cr}_2\text{CF}_2$  and  $\text{Cr}_2\text{CFCl}$ , respectively, indicating just a weak van-der-Waals bonding.  $\text{Cr}_2\text{CF}_2$  and  $\text{Cr}_2\text{CFCl}$  on  $\text{SiC}(0001)$  retain the compensated antiferromagnetic coupling as shown in Fig. 8. The DOS of  $\text{Cr}_2\text{CF}_2$  with symmetrical distribution indicates no spin polarization, while  $\text{Cr}_2\text{CFCl}$  maintains the BMSAF features. These results show that the asymmetrically functionalized Janus  $\text{Cr}_2\text{CXX}'$  MXenes retain the BMSAF features even if they interact with the substrate, the conclusion being important for potential applications in nanoelectronic devices.

### 3.7. BMSAF features in other MXenes

The spin-polarized AF semiconductor feature discussed above in detail for  $\text{Cr}_2\text{CFCl}$  systems is also found for other asymmetrically functionalized  $\text{Cr}_2\text{C}$  materials. The calculated band structures for  $\text{Cr}_2\text{ClBr}$ ,  $\text{Cr}_2\text{FBr}$ ,  $\text{Cr}_2\text{BrOH}$ ,  $\text{Cr}_2\text{HCl}$ ,  $\text{Cr}_2\text{HF}$ ,  $\text{Cr}_2\text{ClOH}$ ,  $\text{Cr}_2\text{FOH}$ , and  $\text{Cr}_2\text{HOH}$  are shown in Fig. S2 (ESI<sup>†</sup>), and the magnetic coupling parameters, spin-flip gaps and spin-conserved gaps are presented in Table 1 and Fig. 3a. The surface functional groups can effectively modulate the magnetic and electronic properties that change the metallic  $\text{Cr}_2\text{C}$  into a BMSAF material. With an appropriate choice of surface functional groups, one can tailor the band gap to different regions (from 0.15 to 1.51 eV in the case of materials investigated herein).

Besides the  $\text{Cr}_2\text{CX}_2$  systems, other MXenes, *e.g.*,  $\text{V}_2\text{CF}_2$ ,  $\text{V}_2\text{C}(\text{OH})_2$ ,  $\text{Cr}_2\text{N}(\text{OH})_2$ , and  $\text{Cr}_2\text{NF}_2$ , show antiferromagnetism. In particular,  $\text{V}_2\text{CF}_2$  and  $\text{V}_2\text{C}(\text{OH})_2$  have been reported as small-gap AF semiconductors.<sup>45</sup> Is it possible to achieve BMSAF analogues of these systems? It should be possible as long as the AF magnetic ground states are maintained after the asymmetric functionalization. To verify this hypothesis, electronic and magnetic properties of Janus  $\text{V}_2\text{CFOH}$  MXenes were investigated.  $\text{V}_2\text{CFOH}$  shows a  $4\mu_{\text{B}}$  magnetic moment per unit cell with a compensated AF coupling, suggesting that vanadium is a  $\text{V}^{3+}$  magnetic ion with  $d^{2\uparrow}$  spin configurations. The AF coupling of the V ions is 75 meV more favorable than the FM coupling. Moreover,  $\text{V}_2\text{CFOH}$  shows zero magnetization BMS characteristics with a small band gap (0.17 eV) as shown in Fig. 9. These results indicate that the zero magnetization spin-polarized nature is a general feature of Janus MXenes, an observation that can lead to promising applications of Janus MXenes in spintronics.

## 4. Summary

A new class of 2D magnetic materials – asymmetrically functionalized MXenes with high Néel temperature, fully compensated antiferromagnetic order, and completely spin-polarized

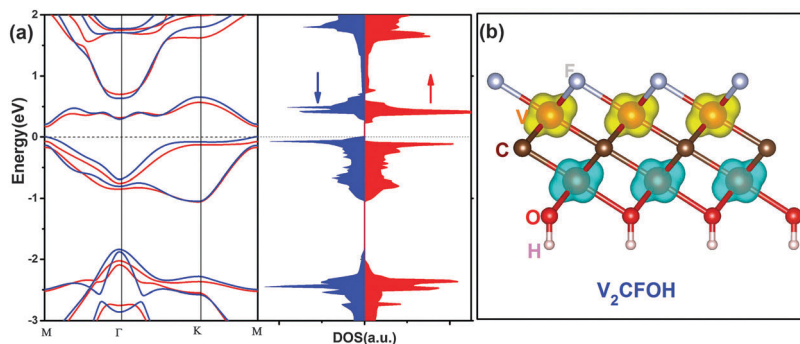


Fig. 9 The calculated band structure and DOS for  $\text{V}_2\text{CFOH}$  (a) and spin-polarized densities of  $\text{V}_2\text{CFOH}$  (b); spin-up and spin-down densities are depicted in yellow and cyan, respectively.



semiconductivity – is proposed for the first time. The properties of asymmetrically functionalized MXenes (Janus MXenes), such as  $\text{Cr}_2\text{CXX}'$  ( $X, X' = \text{H}, \text{F}, \text{Cl}, \text{Br}, \text{OH}$ ), were calculated at the DFT level of theory. The valence and conduction bands in these materials are made up of opposite spin channels and these materials show BMSAF characteristics. These BMSAF characteristics result from: (i) the asymmetrical functionalization of the upper and the lower  $\text{Cr}_2\text{C}$  surfaces inducing the mismatch of d states on the Cr sublattice and (ii) Cr atoms maintain a perfect AF super-exchange interaction.

A Néel temperatures as high as 400 K has been found for  $\text{Cr}_2\text{CFCl}$ ,  $\text{Cr}_2\text{CClBr}$ ,  $\text{Cr}_2\text{CHCl}$ ,  $\text{Cr}_2\text{CHF}$ , and  $\text{Cr}_2\text{CFOH}$  materials. The band gap of Janus MXenes can be effectively tuned to different regions by a selection of a suitable pair of chemical elements (groups) terminating the upper and the lower surfaces. It is also shown that BMSAF characteristics are present even in  $\text{Cr}_2\text{CF}_x\text{Cl}$ , systems with only partially asymmetrical substitution of the upper and the lower surfaces. Moreover, the  $x/y$  ratio can be used for the band gap tuning. In addition to  $\text{Cr}_2\text{CXX}'$ , BMSAF was also found for the  $\text{V}_2\text{CFOH}$  MXene.

Electron or hole doping leads to easy control of the spin carrier orientation, leading to the transition from BMSAF to HMAFs, which could be realized experimentally through the gate voltage. Janus MXenes described herein can find applications in spintronic devices. Our results provide a general strategy to identify the 2D high-temperature antiferromagnetic spin-polarized materials from transition-metal based layered materials.

## Acknowledgements

This work was funded by the Czech Science Foundation Grant No. P106/12/G015 (Centre of Excellence). The calculations were partially performed at MetaCentrum and CERIT-SC computational facilities (MSM/LM2010005 and OP VaVpI CZ. 1.05/3.2.00/08.0144). Support by the National Natural Science Foundation of China through Grant No. 11574260 is also acknowledged. J. H. acknowledges support from the STARS Research Scholarship of Charles University in Prague.

## References

- S. A. Wolf, D. D. Awschalom, R. A. Buhrman, J. M. Daughton, S. Von Molnar, M. L. Roukes, A. Y. Chtchelkanova and D. M. Treger, *Science*, 2001, **294**, 1488–1495.
- K. S. Novoselov, A. K. Geim, S. Morozov, D. Jiang, Y. Zhang, S. Dubonos, I. Grigorieva and A. Firsov, *Science*, 2004, **306**, 666–669.
- D. Pacile, J. Meyer, C. O. Girit and A. Zettl, *Appl. Phys. Lett.*, 2008, **92**, 133107.
- R. Baughman, H. Eckhardt and M. Kertesz, *J. Chem. Phys.*, 1987, **87**, 6687.
- P. Joensen, R. Frindt and S. R. Morrison, *Mater. Res. Bull.*, 1986, **21**, 457–461.
- B. K. Miremadi and S. R. Morrison, *J. Appl. Phys.*, 1988, **63**, 4970–4974.
- F. Banhart, J. Kotakoski and A. V. Krasheninnikov, *ACS Nano*, 2010, **5**, 26–41.
- A. V. Krasheninnikov, P. O. Lehtinen, A. S. Foster, P. Pyykkö and R. M. Nieminen, *Phys. Rev. Lett.*, 2009, **102**, 126807.
- J. He, S. Y. Ma, P. Zhou, C. X. Zhang, C. He and L. Z. Sun, *J. Phys. Chem. C*, 2012, **116**, 26313–26321.
- J. He, N. Jiao, C. Zhang, H. Xiao, X. Chen and L. Sun, *J. Phys. Chem. C*, 2014, **118**, 8899–8906.
- J. Zhou, Q. Wang, Q. Sun, X. S. Chen, Y. Kawazoe and P. Jena, *Nano Lett.*, 2009, **9**, 3867–3870.
- J. Zhou, Q. Wang, Q. Sun and P. Jena, *Phys. Rev. B: Condens. Matter Mater. Phys.*, 2010, **81**, 085442.
- E. Torun, H. Sahin, S. K. Singh and F. M. Peeters, *Appl. Phys. Lett.*, 2015, **106**, 192404.
- C. Si, J. Zhou and Z. Sun, *ACS Appl. Mater. Interfaces*, 2015, **7**, 17510–17515.
- J. He, S. Ma, P. Lyu and P. Nachtigall, *J. Mater. Chem. C*, 2016, **4**(13), 2518–2526.
- W. B. Zhang, Q. Qu, P. Zhu and C. H. Lam, *J. Mater. Chem. C*, 2015, **3**, 12457–12468.
- J. Liu, Q. Sun, Y. Kawazoe and P. Jena, *Phys. Chem. Chem. Phys.*, 2016, **18**, 8777–8784.
- M. Kan, S. Adhikari and Q. Sun, *Phys. Chem. Chem. Phys.*, 2014, **16**, 4990–4994.
- H. L. Zhuang, Y. Xie, P. R. C. Kent and P. Ganesh, *Phys. Rev. B: Condens. Matter Mater. Phys.*, 2015, **92**, 035407.
- X. Li, X. Wu, Z. Li, J. Yang and J. G. Hou, *Nanoscale*, 2012, **4**, 5680–5685.
- X. Hu, *Adv. Mater.*, 2012, **24**, 294–298.
- X. Li, X. Wu, Z. Li and J. Yang, *Phys. Rev. B: Condens. Matter Mater. Phys.*, 2015, **92**, 125202.
- N. S. Rogado, J. Li, A. W. Sleight and M. A. Subramanian, *Adv. Mater.*, 2005, **17**, 2225–2227.
- Y. Singh, M. A. Green, Q. Huang, A. Kreyssig, R. J. McQueeney, D. C. Johnston and A. I. Goldman, *Phys. Rev. B: Condens. Matter Mater. Phys.*, 2009, **80**, 100403.
- Y. M. Nie and X. Hu, *Phys. Rev. Lett.*, 2008, **100**, 117203.
- H. Van Leuken and R. A. De Groot, *Phys. Rev. Lett.*, 1995, **74**, 1171.
- R. A. de Groot, *Phys. B: Condens. Matter*, 1991, **172**, 45–50.
- I. Galanakis and P. Mavropoulos, *J. Phys.: Condens. Matter*, 2007, **19**, 315213.
- E. Şaşıoğlu, *Phys. Rev. B: Condens. Matter Mater. Phys.*, 2009, **79**, 100406.
- I. Galanakis, P. H. Dederichs and N. Papanikolaou, *Phys. Rev. B: Condens. Matter Mater. Phys.*, 2002, **66**, 174429.
- W. E. Pickett, *Phys. Rev. Lett.*, 1996, **77**, 3185.
- W. E. Pickett, *Phys. Rev. B: Condens. Matter Mater. Phys.*, 1998, **57**, 10613.
- D. Ködderitzsch, W. Hergert, Z. Szotek and W. M. Temmerman, *Phys. Rev. B: Condens. Matter Mater. Phys.*, 2003, **68**, 125114.
- M. Nakao, *Phys. Rev. B: Condens. Matter Mater. Phys.*, 2008, **77**, 134414.
- H. Kurt, K. Rode, P. Stamenov, M. Venkatesan, Y. C. Lau, E. Fonda and J. M. D. Coey, *Phys. Rev. Lett.*, 2014, **112**, 027201.

- 36 A. K. Nayak, M. Nicklas, S. Chadov, P. Khuntia, C. Shekhar, A. Kalache and U. Zeitler, *Nat. Mater.*, 2015, **14**, 679–684.
- 37 N. Thiyagarajah, Y. C. Lau, D. Betto, K. Borisov, J. M. D. Coey, P. Stamenov and K. Rode, *Appl. Phys. Lett.*, 2015, **106**, 122402.
- 38 J. He, P. Zhou, N. Jiao, X. Chen, W. Lu and L. Z. Sun, *RSC Adv.*, 2015, **5**, 46640–46647.
- 39 M. Naguib, M. Kurtoglu, V. Presser, J. Lu, J. Niu, M. Heon and M. W. Barsoum, *Adv. Mater.*, 2011, **23**, 4248–4253.
- 40 M. Naguib, O. Mashtalir, J. Carle, V. Presser, J. Lu, L. Hultman and M. W. Barsoum, *ACS Nano*, 2012, **6**, 1322–1331.
- 41 M. Naguib, V. N. Mochalin, M. W. Barsoum and Y. Gogotsi, *Adv. Mater.*, 2014, **26**, 992–1005.
- 42 M. Khazaei, M. Arai, T. Sasaki, C. Y. Chung, N. S. Venkataramanan, M. Estili and Y. Kawazoe, *Adv. Funct. Mater.*, 2013, **23**, 2185–2192.
- 43 Y. Xie and P. R. C. Kent, *Phys. Rev. B: Condens. Matter Mater. Phys.*, 2013, **87**, 235441.
- 44 Y. Lee, S. B. Cho and Y. C. Chung, *ACS Appl. Mater. Interfaces*, 2014, **6**, 14724–14728.
- 45 J. Hu, B. Xu, C. Ouyang, S. A. Yang and Y. Yao, *J. Phys. Chem. C*, 2014, **118**, 24274–24281.
- 46 A. N. Enyashin and A. L. Ivanovskii, *J. Phys. Chem. C*, 2013, **117**, 13637–13643.
- 47 F. Karlicky, K. Kumara Ramanatha Datta, M. Otyepka and R. Zboril, *ACS Nano*, 2013, **7**, 6434–6464.
- 48 L. Zhang, J. Yu, M. Yang, Q. Xie, H. Peng and Z. Liu, *Nat. Commun.*, 2013, **4**, 1443.
- 49 G. Kresse and J. Hafner, *Phys. Rev. B: Condens. Matter Mater. Phys.*, 1993, **47**, 558.
- 50 G. Kresse and D. Joubert, *Phys. Rev. B: Condens. Matter Mater. Phys.*, 1999, **59**, 1758.
- 51 J. P. Perdew, K. Burke and M. Ernzerhof, *Phys. Rev. Lett.*, 1996, **77**, 3865.
- 52 S. L. Dudarev, G. A. Botton, S. Y. Savrasov, C. J. Humphreys and A. P. Sutton, *Phys. Rev. B: Condens. Matter Mater. Phys.*, 1998, **57**, 1505.
- 53 M. Cococcioni and S. De Gironcoli, *Phys. Rev. B: Condens. Matter Mater. Phys.*, 2005, **71**, 035105.
- 54 X. Li and J. Yang, *Phys. Chem. Chem. Phys.*, 2013, **15**, 15793–15801.
- 55 X. Li, X. Wu and J. Yang, *J. Am. Chem. Soc.*, 2014, **136**, 11065–11069.
- 56 X. Li and J. Yang, *J. Mater. Chem. C*, 2014, **2**, 7071–7076.
- 57 J. He, P. Zhou, N. Jiao, S. Y. Ma, K. W. Zhang, R. Z. Wang and L. Z. Sun, *Sci. Rep.*, 2014, **4**, 4014.
- 58 H. Jin, Y. Dai, B. Huang and M. H. Whangbo, *Appl. Phys. Lett.*, 2009, **94**, 162505.
- 59 Y. Ma, Y. Dai, M. Guo, C. Niu, Y. Zhu and B. Huang, *ACS Nano*, 2012, **6**, 1695–1701.
- 60 Y. Zhou, Z. Wang, P. Yang, X. Zu, L. Yang, X. Sun and F. Gao, *ACS Nano*, 2012, **6**(11), 9727–9736.
- 61 C. Shi, M. Beidaghi and M. Naguib, *et al.*, *Phys. Rev. Lett.*, 2014, **112**(12), 125501.
- 62 M. Ghidui, M. Naguib and C. Shi, *et al.*, *Chem. Commun.*, 2014, **50**(67), 9517–9520.
- 63 Q. Tang, Z. Zhou and P. Shen, *J. Am. Chem. Soc.*, 2012, **134**(40), 16909–16916.
- 64 K. Reuter and M. Scheffler, *Phys. Rev. B: Condens. Matter Mater. Phys.*, 2001, **65**, 035406.
- 65 S. Baroni, S. de Gironcoli, A. D. Corso and P. Gianozzi, *Rev. Mod. Phys.*, 2001, **73**, 515–562.
- 66 P. Giannozzi, *et al.*, *J. Phys.: Condens. Matter*, 2009, **21**, 395502.
- 67 X. Wang, X. Shen, Y. Gao, Z. Wang, R. Yu and L. Chen, *J. Am. Chem. Soc.*, 2015, **137**(7), 2715–2721.
- 68 M. A. Hope, A. C. Forse, K. J. Griffith, M. R. Lukatskaya, M. Ghidui, Y. Gogotsi and C. P. Grey, *Phys. Chem. Chem. Phys.*, 2016, **18**, 5099.
- 69 F. Varchon, R. Feng, J. Hass, X. Li, B. N. Nguyen, C. Naud and L. Magaud, *Phys. Rev. Lett.*, 2007, **99**, 126805.
- 70 R. Balog, B. Jørgensen, J. Wells, E. Lægsgaard, P. Hofmann, F. Besenbacher and L. Hornekær, *J. Am. Chem. Soc.*, 2009, **131**, 8744–8745.
- 71 S. Grimme, *J. Comput. Chem.*, 2006, **27**, 1787.

# **Attachment No. 10**



Cite this: *J. Mater. Chem. C*, 2016, 4, 11143

## New two-dimensional Mn-based MXenes with room-temperature ferromagnetism and half-metallicity†

Junjie He, Pengbo Lyu and Petr Nachtigall\*

Magnetic properties of  $Mn_2CT_2$  ( $T = F, Cl, OH, O,$  and  $H$ ) MXenes are reported based on a computational investigation. While other two dimensional  $Mn_2CT_2$  MXenes become non-magnetic upon symmetrical functionalization of their surfaces, the  $Mn_2C$  MXene functionalized with a functional group bearing formal charge  $-1$  ( $F, Cl,$  and  $OH$ ) retains the ferromagnetic ground state upon functionalization. Based on density functional theory calculations and Monte Carlo simulations the  $Mn_2CF_2$  MXene is predicted to be an intrinsic half-metal with high Curie temperature (520 K), wide half-metallic gap (0.9 eV) and a sizable magnetic anisotropy (24  $\mu$ eV). These magnetic properties make the  $Mn_2CF_2$  MXene an optimal material for applications in spintronics. Different surface functional groups lead to either quantitative ( $Cl$  and  $OH$ ) or qualitative ( $O$  and  $H$ ) changes in  $Mn_2CT_2$  magnetic properties. It is proposed that  $Mn_2CT_2$  MXenes can be prepared experimentally from the already existing parent  $Mn_2GaC$  MAX phase by exfoliation techniques.

Received 8th September 2016,  
Accepted 31st October 2016

DOI: 10.1039/c6tc03917k

[www.rsc.org/MaterialsC](http://www.rsc.org/MaterialsC)

### 1. Introduction

Two dimensional (2D) materials, such as graphene, have great potential for applications in a next generation of electronic and spintronic devices.<sup>1–4</sup> However, a majority of 2D materials are intrinsically non-magnetic, consequently their applications in spintronics are limited.<sup>2</sup> For practical applications in spintronics it is crucial to find 2D materials with room-temperature ferromagnetism and 100% spin polarization. Half-metallic magnets, with a metallic nature and complete (100%) spin polarization in one spin channel and an insulating/semiconducting property in the other spin channel, are considered to be the most promising materials for spintronics. They have a theoretically infinite magnetoresistance and can be potentially used as spin filters or detectors and sensors.<sup>5</sup> Defects, dopants or external electric field can induce a high spin-polarization, half-metallic character and magnetic effects in various 2D materials,<sup>6–12</sup> however, it remains a challenge for experiment to prepare materials with an ordered spin structure and high spin-polarization at room temperature using dopants or by defect generation. Dopant or defect distributions cannot be easily controlled and the dopant or defect clustering effects represent additional complications.<sup>13,14</sup> The nanoribbons of 2D materials (graphene in particular) can be turned into a half-metal

by external electric field, strain or by an asymmetrical chemical modification of edges.<sup>15–17</sup> Unfortunately, these materials show in general rather weak spin–spin interactions due to the magnetism contributed dominantly by p electrons and, thus, rather a strong external electric field is required. Only a few 2D materials have so far been predicted to be intrinsic half-metals.<sup>13,14,18,19</sup> Therefore, finding 2D half-metallic materials with a room temperature spin-polarization is highly important for developing the next generation devices.

Rather desirable magnetic properties have been recently predicted computationally for materials based on 2D layered transition metal carbides or nitrides, the so called MXenes.<sup>20–22</sup> Various MXenes were already prepared experimentally from parent MAX phase materials.<sup>21,22</sup> The MAX phase has a general formula  $M_{n+1}AX_n$  and they consists of  $M_{n+1}X_n$  blocks separated by A-layers ( $M$  is transition metal,  $A$  is an A-group element and  $X$  is either carbon or nitrogen). MXenes were prepared experimentally from the corresponding MAX phase by exfoliation in hydrofluoric acid.<sup>21,22</sup> The MXenes attract great attention due to their potential applications in sensors, catalysis, energy storage and nanoelectronics.<sup>21</sup> Previous investigations have demonstrated that  $Ti, Ta$  and  $Cr$  based MXenes have magnetic properties.<sup>14,23–26</sup> However, the magnetism of MXenes generally disappears when their surfaces are functionalized due to the completely compensated antiferromagnetic (AFM) ground states. For example, theoretical investigations have confirmed that  $Cr_2CT_2$  ( $T = OH, H, F$  and  $Cl$ ),  $Ti_2CO_2$ , and  $V_2CT_2$  ( $T = F, OH$ ) are AFM semiconductors or metals.<sup>14,27–29</sup> Although the bare  $Cr_2C$  is predicted to be ferromagnetic (FM) half-metal,

Department of Physical and Macromolecular Chemistry, Faculty of Science, Charles University in Prague, 128 43 Prague 2, Czech Republic.

E-mail: [petr.nachtigall@natur.cuni.cz](mailto:petr.nachtigall@natur.cuni.cz)

† Electronic supplementary information (ESI) available: Structural stability of  $Mn_2C$  and  $Mn_2CF_2$  MXenes and the band structure of  $Mn_2CF_2$  calculated with the hybrid HSE06 functional. See DOI: 10.1039/c6tc03917k

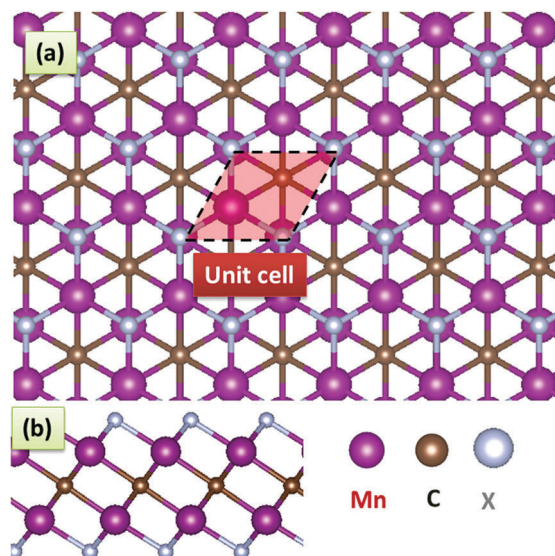


Fig. 1 Top (a) and side (b) views of the  $\text{Mn}_2\text{CT}_2$  MXene monolayer. The color scheme for Mn, C and X atoms is described in the figure.

experimentally prepared MXenes have surfaces terminated with F, OH or other atoms.<sup>14</sup> The functionalized MXenes are thermodynamically more favorable than the unfunctionalized ones.

A new magnetic  $\text{Mn}_2\text{GaC}$  MAX phase was recently predicted theoretically and subsequently synthesized as a thin film with ferromagnetic order.<sup>30–33</sup> It remains to be seen whether the  $\text{Mn}_2\text{GaC}$  MAX phase can be experimentally converted to 2D  $\text{Mn}_2\text{CT}_2$  MXene in analogy with several MAX phases that have been transformed into  $\text{Ti}_2\text{CT}_2$  and  $\text{V}_2\text{CT}_2$  MXenes. And it remains to be seen whether such  $\text{Mn}_2\text{CT}_2$  MXenes have magnetic properties suitable for potential applications. For that reason, a theoretical study of electronic and magnetic properties of  $\text{Mn}_2\text{CT}_2$  MXenes based on first-principles calculations is reported herein. It is shown that  $\text{Mn}_2\text{CF}_2$  is a half-metal with a wide half-metallic gap and room-temperature ferromagnetism, which could be of interest as a suitable material for spintronics. Electronic and magnetic properties of  $\text{Mn}_2\text{CT}_2$  MXenes depend on the characteristics of surface functional groups (H, OH, O, Cl, or F) (Fig. 1) and, therefore, these properties can be “chemically” tuned for particular applications.

## 2. Results and discussions

The initial structure of the 2D MXene was obtained simply by removing the Ga layer from the bulk  $\text{Mn}_2\text{GaC}$  MAX phase. The 2D  $\text{Mn}_2\text{C}$  forms a hexagonal layer with  $C_{3v}$  symmetry known as the T structure; C atoms are sandwiched between two layers of Mn atoms. This T structure has lower energy (by 0.38 eV per UC) than the H structure with  $D_{3h}$  symmetry (Fig. S1, ESI<sup>†</sup>). After exfoliation of the bulk MAX phase by HF acid solutions, it is expected that the surfaces of  $\text{Mn}_2\text{C}$  are terminated with chemical elements/groups, e.g., F in the case of HF solution, which has been found experimentally for  $\text{Ti}_2\text{CF}_2$  and  $\text{V}_2\text{CF}_2$  MXenes.<sup>21,22</sup> There are two types of hollow sites on the  $\text{Mn}_2\text{C}$

surface (see Fig. S2, ESI<sup>†</sup>): (i) type I sites where the surface atoms are located above the hollow sites formed by three neighboring C atoms (above Mn from a more distant surface); (ii) type II sites where surface atoms are above the C atom. Type I is energetically more stable for all  $\text{Mn}_2\text{CT}_2$  systems investigated herein.

The results obtained for an F functionalized  $\text{Mn}_2\text{C}$  monolayer,  $\text{Mn}_2\text{CF}_2$ , are reported and discussed first and the results obtained for other  $\text{Mn}_2\text{CT}_2$  systems ( $X = \text{Cl}, \text{H}, \text{O}, \text{OH}$ ) are discussed later. The geometry optimization of 2D  $\text{Mn}_2\text{CF}_2$  gives lattice parameters 3.10 Å. The calculated  $\text{Mn}_2\text{CF}_2$  formation energy (−8.63 eV) is relatively large (comparable to  $\text{Cr}_2\text{CF}_2$  reported in ref. 12) indicating the formation of strong chemical bonds between Mn and F atoms and thermodynamic feasibility. Moreover, AIMD calculations show that the  $\text{Mn}_2\text{CF}_2$  monolayer is thermally stable at 500 K (Fig. S3a, ESI<sup>†</sup>). The phonon spectra shown in Fig. S3b (ESI<sup>†</sup>) show no negative frequency phonons at the whole Brillouin zone. All these results indicate that the  $\text{Mn}_2\text{CF}_2$  MXene monolayers are dynamically stable and they could exist as free-standing 2D monolayers.

The FM states of  $\text{Mn}_2\text{CF}_2$  MXenes have a total magnetic moment of 8  $\mu_B$  (per unit cell), which is mainly contributed by Mn atoms. Each Mn atom has a magnetic moment of 4.15  $\mu_B$ , that can be expected for a formally  $\text{Mn}^{3+}$  electronic configuration, and there is −0.43  $\mu_B$  on C atoms. Calculated local magnetic moments show that Mn atoms are in the high spin (HS) state with four unpaired d electrons and  $d^{41}$  spin configurations. To study the magnetic ground state structures of the  $\text{Mn}_2\text{CF}_2$  monolayer, the collinear ferromagnetic state and AFM states (AFM-a, AFM-b and AFM-c define Fig. 2) were considered. The lowest energy has been found for the FM state and this has been set as a reference energy. The  $E_{\text{AFM-a}}$ ,  $E_{\text{AFM-b}}$  and  $E_{\text{AFM-c}}$  states have energies 0.42, 1.84 and 2.30 eV higher, respectively, than the FM state, considering a  $2 \times 1$  supercell. These results clearly demonstrate that the FM state configuration of the  $\text{Mn}_2\text{CF}_2$  monolayer is the magnetic ground state with high magnetic stability.

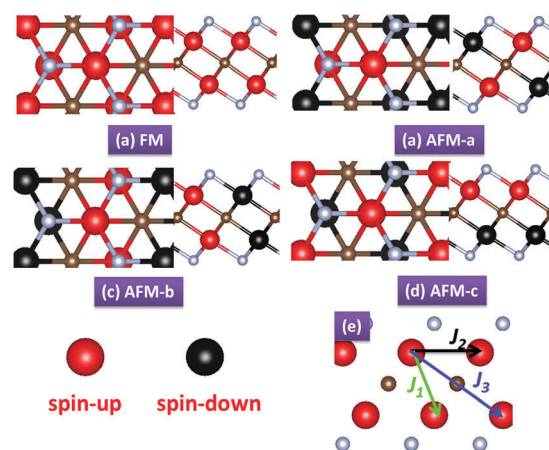


Fig. 2 Possible magnetic configurations with top and side views of  $\text{Mn}_2\text{CT}_2$  MXene layers: FM (a), AFM-a (b), AFM-b (c), and AFM-c (d). Red and black balls represent Mn atoms with spin up and spin down electron configurations. The spin exchange path (e) for  $J_1$ ,  $J_2$  and  $J_3$  are also marked.

To determine the magnetic structure, the nearest-, next-nearest- and next-next-nearest-neighbors exchange-coupling parameters ( $J_1$ ,  $J_2$ , and  $J_3$ , respectively) were calculated by mapping the total energies of the systems with different magnetic structures to the Ising model:

$$H_{\text{spin}} = - \sum_{i,j} J_1 M_i \cdot M_j - \sum_{k,l} J_2 M_k \cdot M_l - \sum_{m,n} J_3 M_m \cdot M_n, \quad (1)$$

where  $M$  is the net magnetic moment ( $4 \mu_B$ ) at the Mn site  $i$  and  $(i, j)$ ,  $(k, l)$  and  $(m, n)$  run over the nearest, next-nearest and next-next-nearest Mn atoms, respectively. By mapping the DFT energies to the Ising Hamiltonian,  $J_1, J_2$  and  $J_3$  can be expressed from the following equations:<sup>34</sup>

$$E_{\text{FM/AFM-c}} = E_0 - (\pm 3J_1 + 6J_2 \pm 3J_3)M^2 \quad (2)$$

and

$$E_{\text{AFM-b/AFM-a}} = E_0 - (\pm J_1 - 2J_2 \mp 3J_3)M^2. \quad (3)$$

The  $J_1, J_2$  and  $J_3$  parameters can be calculated by the following matrix expression:

$$\begin{pmatrix} J_1 \\ J_2 \\ J_3 \\ E_0 \end{pmatrix} = \begin{pmatrix} E_0 & -3M^2 & -6M^2 & -3M^2 \\ E_0 & 3M^2 & -6M^2 & 3M^2 \\ E_0 & -M^2 & 2M^2 & 3M^2 \\ E_0 & M^2 & 2M^2 & -3M^2 \end{pmatrix}^{-1} \begin{pmatrix} E_{\text{FM}} \\ E_{\text{AFM-c}} \\ E_{\text{AFM-b}} \\ E_{\text{AFM-a}} \end{pmatrix} \quad (4)$$

The calculated  $J_1, J_2$  and  $J_3$  parameters are 6.8 meV,  $-0.1$  meV and 17.1 meV, respectively. The first and the third neighbor exchange parameters for  $\text{Mn}_2\text{CF}_2$  are FM, while the second exchange parameter ( $J_2$ ) is weakly AFM. The Curie temperature calculated with these exchange-coupling parameters (Fig. 3) is rather high;  $T_C = 520$  K found for  $\text{Mn}_2\text{CF}_2$  is higher than for a majority of previously studied 2D magnetic materials.<sup>12,13,34,35</sup>

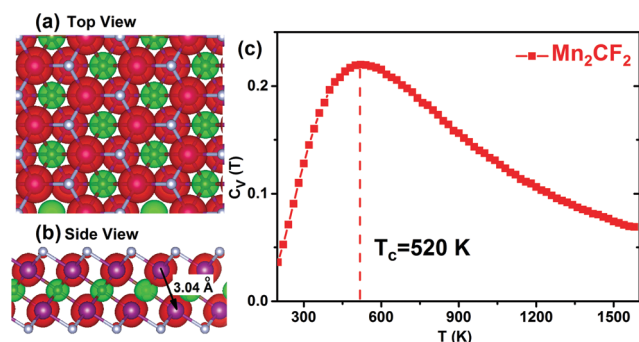


Fig. 3 The simulated specific heat  $C_V$  as a function of temperature ( $T$ ) for  $\text{Mn}_2\text{CF}_2$ . The inserted background figure shows spin polarized charge densities on  $\text{Mn}_2\text{CF}_2$ , where spin up and spin down densities are shown in red and green color, respectively.

This value is similar to previously calculated  $T_C = 660$  K for the corresponding  $\text{Mn}_2\text{GaC}$  MAX phase.<sup>31</sup>

The band structure of  $\text{Mn}_2\text{CF}_2$  obtained at the PBE+ $U$  level is shown in Fig. 4. The calculated band structure clearly shows half-metallic character (energy gap for minority-spin electrons and metallic character of majority-spin electrons) leading to 100% spin-polarized electrons at the Fermi level. The half-metallic gap is defined as the spin-flip transition energy from a majority- to a minority-spin channel ( $\delta$  in Fig. 3). A large half-metallic gap can efficiently prevent the spin flip transitions and can guarantee the half-metallic character. The half-metallic gap calculated for  $\text{Mn}_2\text{CF}_2$  (0.94 eV at PBE+ $U$  level) is larger or comparable to those reported for double perovskites, chalcogenides and similar materials.<sup>36,37</sup> To validate the half-metallic character of  $\text{Mn}_2\text{CF}_2$  calculations carried out with the hybrid HSE06 functional are shown in Fig. S4 (ESI<sup>†</sup>). While band structures obtained at HSE06 and PBE+ $U$  levels are qualitatively similar the half-metallic gap calculated at the HSE06 level (2.52 eV) is significantly larger than the one obtained at the PBE+ $U$  level; note that the calculated gap is comparable to the gap obtained at the same level of theory for the  $\text{Cr}_2\text{C}$  monolayer.<sup>14</sup>

The magnetic anisotropy energy of materials, which determines the orientation of the magnetization at low-temperature, is an important property for their applications in high density storage or quantum spin processing. It is obvious that reduced dimensionality and symmetry, as in the case of 2D MXenes, should lead to increased MAE compared to the corresponding 3D bulk structures. The noncollinear magnetic calculations were performed for magnetization along  $X[100]$ ,  $Y[010]$  and  $Z[001]$  directions, where  $Z$  is the surface normal. The energy difference between  $X(Y)$  and  $Z$  directions is denoted  $E_{XZ}$  ( $E_{YZ}$ ). The easy magnetization axis is  $Z[001]$ . The calculated MAE  $E_{XZ} = E_{YZ} = 24 \mu\text{eV}$  per (Mn atom) is similar to those reported for 2D materials previously.<sup>38</sup> And it is significantly larger than that found for commonly used ferromagnetic materials such as bulk Fe ( $1.4 \mu\text{eV}$  per atom) and bulk Ni ( $2.7 \mu\text{eV}$  per atom).<sup>39</sup>

Rather unusual magnetic properties of the  $\text{Mn}_2\text{CF}_2$  MXene reported above triggered our interest in electronic and magnetic properties of other 2D MXenes that can be derived from  $\text{Mn}_2\text{C}$  by a chemical modification of the surface. Therefore, structural, thermodynamic, electronic and magnetic properties of  $\text{Mn}_2\text{CT}_2$  MXenes ( $X = \text{Cl}, \text{OH}, \text{O}, \text{H}$ ) were investigated computationally following exactly the same approach as reported above for  $\text{Mn}_2\text{CF}_2$ ; results are reported in Fig. 5 and Table 1. Magnetic properties depend primarily on the formal oxidation state of surface functional species. For  $\text{Mn}_2\text{C}$  surfaces functionalized by functional groups bearing  $(-1)$  formal charge (F, Cl, and OH), the net magnetization per unit cell is  $8 \mu_B$  and they all are ferromagnetic half metals with similar (but different) magnetic characteristics (Table 1). Calculated Curie temperatures (520, 460 and 380 K for  $\text{Mn}_2\text{CF}_2$ ,  $\text{Mn}_2\text{C}(\text{OH})_2$  and  $\text{Mn}_2\text{CCl}_2$ , respectively) are all well above the room temperature. For the  $\text{Mn}_2\text{C}$  surface functionalized by O atoms (formal charge  $-2$ ) and by H atoms (formal charge  $+1$ ), the net magnetization drops to  $6 \mu_B$  and the resulting 2D materials are no longer half metals. The  $\text{Mn}_2\text{CO}_2$  MXene shows an indirect AFM semiconductor

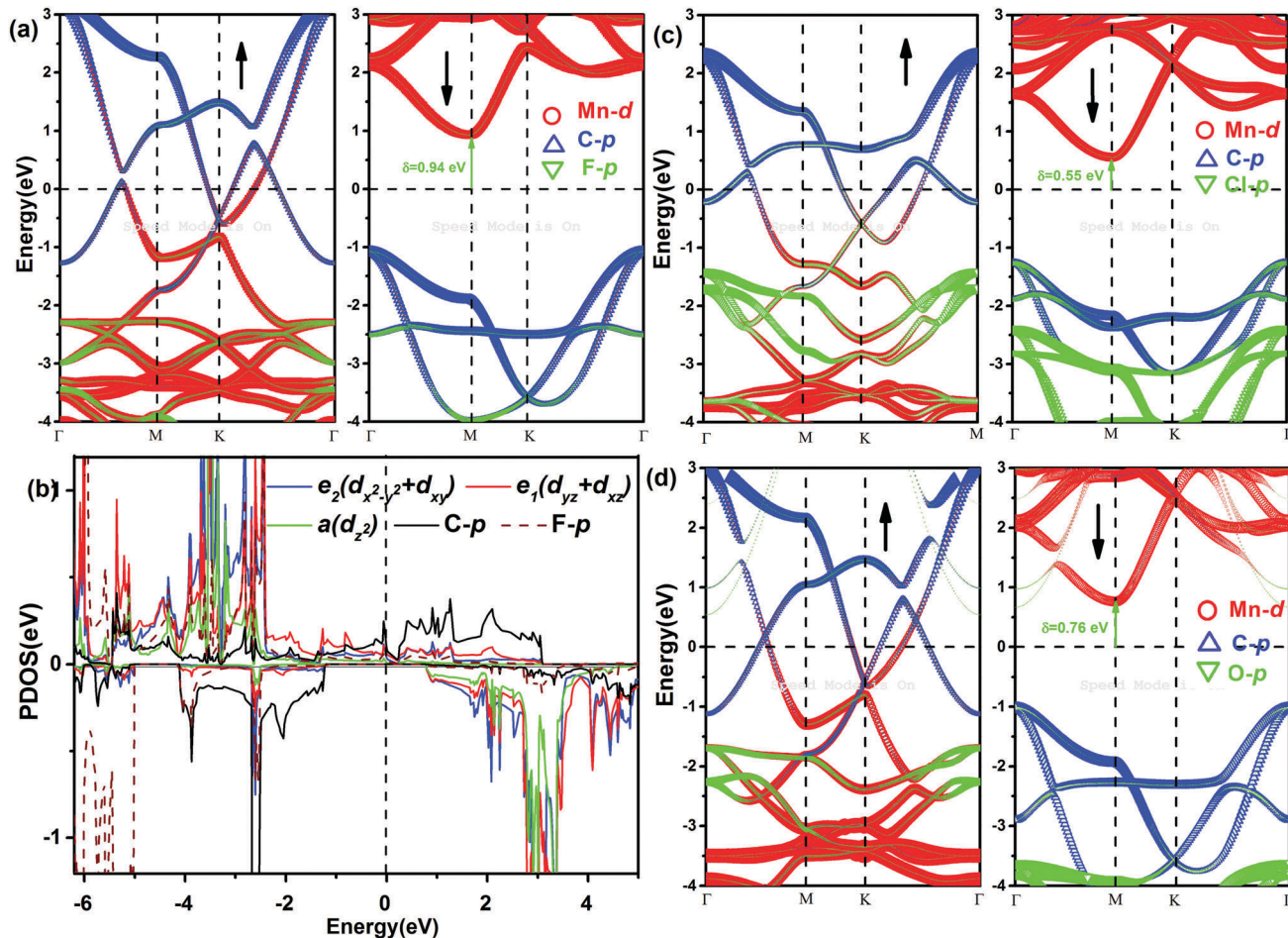


Fig. 4 (a) Band structure of  $\text{Mn}_2\text{CF}_2$  MXene. Red, blue and green marks represent the weights of the Mn-d, C-p, and F-p orbitals, respectively. (b) PDOS of Mn d states (blue, red, and green) and C and F p states (black and brown, respectively). Band structures with the orbital weights for  $\text{Mn}_2\text{CCL}_2$  (c) and  $\text{Mn}_2\text{C}(\text{OH})_2$  (d). The Fermi level is set to zero.

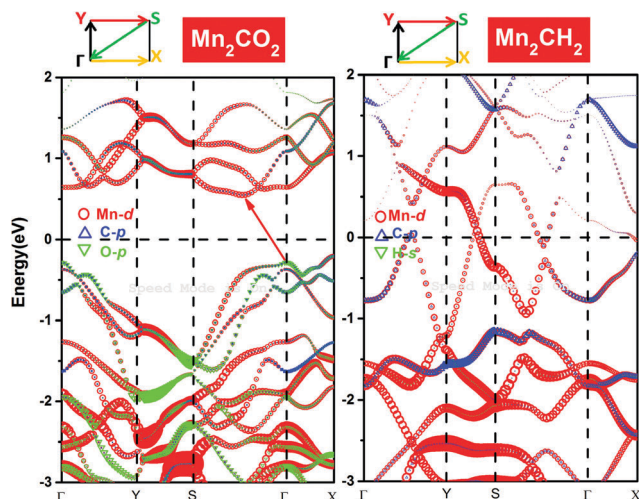


Fig. 5 The band structure of  $\text{Mn}_2\text{CO}_2$  and  $\text{Mn}_2\text{CH}_2$  MXenes. The paths for high-symmetrical points are shown as well.

characteristic with a 0.83 eV gap at the PBE+ $U$  level. Previous theoretical studies also reported that  $\text{Ti}_2\text{CO}_2$ ,  $\text{Zr}_2\text{CO}_2$ ,  $\text{Hf}_2\text{CO}_2$ ,

and Sc- and Cr-based MXenes are semiconductors.<sup>14,25</sup> In contrast, the  $\text{Mn}_2\text{CH}_2$  MXene is an AFM metal with 120 K Neel temperature. The changes in magnetic ground states in  $\text{Mn}_2\text{CT}_2$  MXenes result from the changes in electron acceptor/donor characteristics of the surface functional group. Moreover, all  $\text{Mn}_2\text{CT}_2$  materials investigated herein have an easy magnetization axis along  $Z[001]$  with considerable MAE as shown in Table 1.

The partial electronic density of states (PDOS) of  $\text{Mn}_2\text{CF}_2$  is shown in Fig. 4b for understanding the magnetic properties of Mn-based MXenes. The atomic and orbital resolved band structures show that both Mn(d) states and C(p) states contribute to half-metallic states near the Fermi level. According to the local symmetry of the crystal field on Mn magnetic ions, the 3d orbitals split into a non-degenerate  $a(d_{z^2})$  orbital and two 2-fold degenerate  $e_1(d_{xz}/d_{yz})$  and  $e_2(d_{xy}/d_{x^2-y^2})$  orbitals (the  $z$  axis being along the surface normal). The states of Mn atoms can be divided into two parts: first, localized states with energies below  $-2$  eV; second, delocalized d states with energies ranging from  $-2$  eV to 2.5 eV. One can see that the metal states in the spin up channel near the Fermi level are derived mainly from delocalized Mn(d) and C(p) states. A majority of Mn(d) states is below the Fermi level and only minority of Mn(d) states is just above the Fermi level. Such an

Table 1 Calculated structural and magnetic characteristics of five different Mn<sub>2</sub>CT<sub>2</sub> MXenes

Structure	$L^a$	$E_{\text{form}}^b$	$M^c$	$E_{\text{FM}}^d$	$E_{\text{AFM-a}}$	$E_{\text{AFM-b}}$	$E_{\text{AFM-c}}$	$T_{\text{C/N}}^e$	$E_{\text{YZ}}^f$	$E_{\text{XZ}}^f$
Mn <sub>2</sub> CF <sub>2</sub>	3.11	-8.63	8	0	0.415	1.842	2.295	520	24	24
Mn <sub>2</sub> CO <sub>2</sub>	2.95	-12.22	6	0.056	0.338	0	0.161	110	90	91
Mn <sub>2</sub> C(OH) <sub>2</sub>	3.17	-14.22	8	0	0.407	1.810	2.021	460	19	26
Mn <sub>2</sub> CCl <sub>2</sub>	3.35	-4.74	8	0	0.347	1.971	2.137	380	37	38
Mn <sub>2</sub> CH <sub>2</sub>	2.89	-0.90	6.06	0.059	0	0.325	0.763	120	233	233

<sup>a</sup>  $L$  is the lattice constant (in Å). <sup>b</sup>  $E_{\text{form}}$  is the formation energy defined in eqn (5) (in eV). <sup>c</sup>  $M$  is the magnetization per UC (in  $\mu_{\text{B}}$ ). <sup>d</sup> Relative energies for FM ( $E_{\text{FM}}$ ) and AFM ( $E_{\text{AFM-a}}$ ,  $E_{\text{AFM-b}}$  and  $E_{\text{AFM-c}}$ ) states are in eV. <sup>e</sup>  $T_{\text{C/N}}$  stands for the Curie and Neel temperatures, respectively (in K). <sup>f</sup> The magnetic anisotropy between  $Y$  and  $Z$  ( $E_{\text{YZ}}$ ) and  $X$  and  $Z$  ( $E_{\text{XZ}}$ ) directions is in  $\mu\text{eV}$ .

electronic structure corresponds to Mn<sup>3+</sup> ions with the Mn( $d^{4\uparrow 4\downarrow 0}$ ) spin configuration which is also consistent with a total 8  $\mu_{\text{B}}$  spin magnetic moment per unit cell. Similarly, Mn atoms in the Mn<sub>2</sub>C and Mn<sub>2</sub>CO<sub>2</sub> MXenes can be formally considered as Mn<sup>2+</sup> and Mn<sup>4+</sup> ions, respectively.

The microscopic origin of various magnetic couplings in Mn-based MXenes can be understood as follows: the pristine T structure Mn<sub>2</sub>C MXene is predicted to be an antiferromagnet, similarly to the previously reported H structure of Mn<sub>2</sub>C. The magnetic coupling ground states can be understood in terms of two competing interactions, *i.e.*, the direct exchange through space (M–M direct) and superexchange through bond (M–C–M indirect), which are determined by the overlap integral and overlap density components, respectively.<sup>40,41</sup> The small distance (2.86 Å) of the first Mn–Mn neighbor pair (2.86 Å, see Fig. S5a, ESI†) in Mn<sub>2</sub>C results in a larger direct exchange between Mn atoms, giving rise to an antiferromagnetic coupling between Mn atoms and spin arrangement [Mn<sub>1</sub>↑–Mn<sub>2</sub>↓]. Upon functionalization with F atoms, the Mn–Mn distance significantly increases (3.04 Å, see Fig. 3b), leading to a weaker direct exchange between Mn atoms. Moreover, the Mn( $d$ ) orbitals are delocalized at the Fermi level, inducing the spin-polarization of neighboring C atoms. The spin-polarization of C atoms can be characterized by spin-polarized charge densities shown in Fig. 3. Therefore, the Mn atoms in Mn<sub>2</sub>CF<sub>2</sub> maintain the AFM coupling with the neighboring C atoms with the Mn<sub>1</sub>↑–C↓–Mn<sub>2</sub>↑ arrangement of spins. It follows that the FM coupling of Mn ions in Mn<sub>2</sub>CF<sub>2</sub> is mediated by C( $p$ ) states *via* a superexchange mechanism. As for Mn<sub>2</sub>CO<sub>2</sub> MXenes, the first and second exchange parameters  $J_1$  and  $J_2$  show FM and AFM couplings, respectively. The  $J_2$  AFM coupling can be attributed to the competition between direct exchange through Mn1–Mn2 and superexchange through Mn1–O–Mn2 (along the spin polarized  $O$  direction); the AFM direct exchange dominates the FM superexchange resulting in an AFM state in the Mn<sub>2</sub>CO<sub>2</sub> MXene. The spin non-polarized C atoms and spin polarized O atoms can be found in PDOS (Fig. S6, ESI†). The magnetic coupling mechanism discussed above for Mn-based MXenes has also been used to explain the characteristics of Cr<sub>2</sub>C MXenes,<sup>42</sup> transition-metal trihalides,<sup>18</sup> 2D transition metal dichalcogenides<sup>43</sup> and TM doped 2D materials.<sup>44</sup>

### 3. Summary

While 2D Mn<sub>2</sub>CT<sub>2</sub> have not been prepared experimentally yet, their parent MAX phase Mn<sub>2</sub>CGa material has been reported

recently<sup>31</sup> and it is reasonable to expect that exfoliation to MXenes is feasible as has been shown for similar materials, *e.g.*, Cr<sub>2</sub>CT<sub>2</sub> or V<sub>2</sub>CT<sub>2</sub> MXenes.<sup>14,27</sup> A new type of 2D Mn<sub>2</sub>CT<sub>2</sub> MXene investigated herein computationally shows unique electronic and magnetic features, very advantageous for potential applications in spintronics. The most important features of Mn<sub>2</sub>CT<sub>2</sub> MXenes include:

(i) The Mn<sub>2</sub>CT<sub>2</sub> MXenes retain the FM ground state even upon the symmetrical functionalization of surfaces with groups bearing  $-1$  formal charge (F, Cl or OH). These are the first and only functionalized MXenes with FM ground states reported so far. Note that some unfunctionalized M<sub>2</sub>C (M = V, Cr) MXenes have FM ground states, however, upon symmetrical functionalization of upper and lower MXene surfaces these materials become nonmagnetic or compensated AFM materials.

(ii) All Mn<sub>2</sub>CT<sub>2</sub> MXenes investigated herein except X = H have relatively large formation energy suggesting that these materials are feasible and can be obtained experimentally. The thermal and dynamic stabilities have been confirmed by the *ab initio* molecular dynamic calculations and phonon spectra calculations.

(iii) Magnetic properties of Mn<sub>2</sub>CT<sub>2</sub> MXenes can be modulated by the surface functional group. Depending on the electronegativity of functional groups these MXenes can be either FM half metals, AFM metals, or AFM semiconductors.

The 2D Mn<sub>2</sub>CF<sub>2</sub> MXene is predicted to be an intrinsic half-metal with above room-temperature ferromagnetism ( $T_{\text{C}} = 520$  K), wide half-metallic gap (0.9 and 2.5 eV at PBE+ $U$  and HSE06 levels, respectively) and a sizable magnetic anisotropy (24  $\mu\text{eV}$ ). Changing the surface functional group from F<sup>-</sup> to different functional groups bearing  $-1$  formal charge does not change magnetic properties qualitatively, however, it leads to a quantitative change in individual characteristics. However, functional groups with different formal charges (O<sup>2-</sup> and H<sup>+</sup>) change magnetic properties qualitatively (to AFM semiconductors and AFM metals, respectively). Our results indicate that new 2D Mn<sub>2</sub>CT<sub>2</sub> materials have magnetic features ideal for applications in spintronics: tunable magnetic order including half metallicity, high Curie temperature and magnetic anisotropy.

### 4. Methods and computational details

All calculations are performed using the Vienna *ab initio* simulation package (VASP)<sup>45,46</sup> within the generalized gradient



approximation employing the Perdew–Burke–Ernzerhof (PBE) exchange–correlation functional.<sup>47</sup> Interactions between electrons and nuclei are described by the projector-augmented wave (PAW) method.<sup>48</sup> The criteria of energy and atom force convergence are set to  $10^{-5}$  eV per unit cell and  $0.01 \text{ eV \AA}^{-1}$ , respectively. The Brillouin zone is sampled using  $15 \times 15 \times 1$  and  $21 \times 21 \times 1$  Gamma-centered Monkhorst–Pack grids for geometry optimizations and for the calculations of magnetic and electronic properties, respectively. To account for the energy of localized 3d orbitals of transition metal (TM) atoms properly, the Hubbard “ $U$ ” correction is employed within the rotationally invariant DFT+ $U$  approach proposed by Dudarev *et al.*<sup>49</sup> A correction of  $U = 3 \text{ eV}$  is employed based on the relevant previous reports.<sup>36</sup> Calculations with the hybrid HSE06 functional<sup>50</sup> were also carried out. The vacuum space of  $15 \text{ \AA}$  along the  $\text{Mn}_2\text{CT}_2$  normal is adopted. A plane-wave kinetic energy cutoff of  $500 \text{ eV}$  is employed. The magnetic anisotropy energy (MAE) calculations were performed using the non-collinear magnetic approach with the spin–orbit coupling and magnetization axis aligned along the most relevant directions. The total energies for MAE calculations were converged to a precision of  $10^{-7} \text{ eV}$ . *Ab initio* molecular dynamics (AIMD) were carried out for  $9 \text{ ps}$  (with a time step of  $3 \text{ fs}$ ) at the PBE– $U$  level at  $500 \text{ K}$  using a  $4 \times 4$  supercell.

Curie temperatures ( $T_C$ ) are calculated based on the Ising model and Monte-Carlo (MC) simulations. Using the DFT derived spin-exchange parameters, MC simulations are performed at the  $(50 \times 50)$  lattice with  $10^8$  steps for each temperature.  $T_C$  is defined as a maximum on the temperature dependent specific heat  $C_V(T)$  curve, where  $C_V = (\langle E^2 \rangle - \langle E \rangle^2)/T^2$ . To evaluate the stability of  $\text{Mn}_2\text{CT}_2$  MXene monolayers, the formation energy,  $E_{\text{form}}$ , defined with respect to the chemical potentials of functional groups/atoms is calculated.<sup>51</sup>

$$E_{\text{form}} = E_{\text{tot}}(\text{Mn}_2\text{CT}_n) - E_{\text{tot}}(\text{Mn}_2\text{C}) - (n/2)E_{\text{tot}}(\text{T}), \quad (5)$$

where  $E_{\text{tot}}(\text{Mn}_2\text{C})$  and  $E_{\text{tot}}(\text{Mn}_2\text{CT}_2)$  stand for the total energies of pristine and functionalized  $\text{Mn}_2\text{CT}_2$ , respectively. Energies of  $\text{O}_2$ ,  $\text{H}_2$ ,  $\text{F}_2$  and  $\text{Cl}_2$ , in the gas phase are taken for the energy of  $E_{\text{tot}}(\text{X})$ .

## Acknowledgements

This work was funded by the Czech Science Foundation Grant No. P106/12/G015 (Centre of Excellence). A support from OP VVV “Excellent Research Teams”, project CUCAM, is also acknowledged. J. H. and P. L. also acknowledges support from STARS Research Scholarship of Charles University in Prague.

## References

- 1 A. K. Geim and K. S. Novoselov, *Nat. Mater.*, 2007, **6**(3), 183–191.
- 2 A. C. Neto, F. Guinea, N. M. R. Peres, K. S. Novoselov and A. K. Geim, *Rev. Mod. Phys.*, 2009, **81**(1), 109.
- 3 K. S. Novoselov, A. Mishchenko, A. Carvalho and A. C. Neto, *Science*, 2016, **353**, 6298.
- 4 Y. Liu, N. O. Weiss, X. Duan, H. C. Cheng, Y. Huang and X. Duan, *Nat. Rev. Mater.*, 2016, **1**, 16042.
- 5 M. I. Katsnelson, V. Y. Irkhin, L. Chioncel, A. I. Lichtenstein and R. A. De Groot, *Rev. Mod. Phys.*, 2008, **80**(2), 315.
- 6 F. Banhart, J. Kotakoski and A. V. Krasheninnikov, *ACS Nano*, 2010, **5**, 26–41.
- 7 A. V. Krasheninnikov, P. O. Lehtinen, A. S. Foster, P. Pyykkö and R. M. Nieminen, *Phys. Rev. Lett.*, 2009, **102**, 126807.
- 8 J. He, S. Y. Ma, P. Zhou, C. X. Zhang, C. He and L. Z. Sun, *J. Phys. Chem. C*, 2012, **116**, 26313–26321.
- 9 Y. Zhou, P. Yang, H. Zu, F. Gao and X. Zu, *Phys. Chem. Chem. Phys.*, 2013, **15**(25), 10385–10394.
- 10 Y. W. Son, M. L. Cohen and S. G. Louie, *Nature*, 2006, **444**(7117), 347–349.
- 11 H. Wang, J. Zhang, X. Hang, X. Zhang, J. Xie, B. Pan and Y. Xie, *Angew. Chem.*, 2015, **127**(4), 1211–1215.
- 12 M. Kan, J. Zhou, Q. Sun, Y. Kawazoe and P. Jena, *J. Phys. Chem. Lett.*, 2013, **4**(20), 3382–3386.
- 13 E. Torun, H. Sahin, S. K. Singh and F. M. Peeters, *Appl. Phys. Lett.*, 2015, **106**(19), 192404.
- 14 C. Si, J. Zhou and Z. Sun, *ACS Appl. Mater. Interfaces*, 2015, **7**, 17510–17515.
- 15 E.-J. Kan, X. Wu, Z. Li, X. C. Zeng, J. Yang and J. G. Hou, *J. Chem. Phys.*, 2008, **129**(8), 084712.
- 16 M. Wu, X. Wu, Y. Gao and X. C. Zeng, *Appl. Phys. Lett.*, 2009, **94**(22), 223111.
- 17 M. Wu, X. Wu and X. C. Zeng, *J. Phys. Chem. C*, 2010, **114**(9), 3937–3944.
- 18 J. He, S. Ma, P. Lyu and P. Nachtigall, *J. Mater. Chem. C*, 2016, **4**(13), 2518–2526.
- 19 E. Kan, W. Hu, C. Xiao, R. Lu, K. Deng, J. Yang and H. Su, *J. Am. Chem. Soc.*, 2012, **134**(13), 5718–5721.
- 20 M. Naguib, M. Kurtoglu, V. Presser, J. Lu, J. Niu, M. Heon and M. W. Barsoum, *Adv. Mater.*, 2011, **23**, 4248–4253.
- 21 M. Naguib, O. Mashtalir, J. Carle, V. Presser, J. Lu, L. Hultman and M. W. Barsoum, *ACS Nano*, 2012, **6**, 1322–1331.
- 22 M. Naguib, V. N. Mochalin, M. W. Barsoum and Y. Gogotsi, *Adv. Mater.*, 2014, **26**, 992–1005.
- 23 N. J. Lane, M. W. Barsoum and J. M. Rondinelli, *EPL*, 2013, **101**(5), 57004.
- 24 I. R. Shein and A. L. Ivanovskii, *Comput. Mater. Sci.*, 2012, **65**, 104–114.
- 25 M. Khazaei, M. Arai, T. Sasaki, C. Y. Chung, N. S. Venkataramanan, M. Estili and Y. Kawazoe, *Adv. Funct. Mater.*, 2013, **23**(17), 2185–2192.
- 26 G. Gao, G. Ding, J. Li, K. Yao, M. Wu and M. Qian, *Nanoscale*, 2016, **8**(16), 8986–8994.
- 27 J. Hu, B. Xu, C. Ouyang, S. A. Yang and Y. Yao, *J. Phys. Chem. C*, 2014, **118**(42), 24274–24281.
- 28 Y. Xie and P. R. C. Kent, *Phys. Rev. B: Condens. Matter Mater. Phys.*, 2013, **87**, 235441.
- 29 Y. Lee, S. B. Cho and Y. C. Chung, *ACS Appl. Mater. Interfaces*, 2014, **6**, 14724–14728.
- 30 A. S. Ingason, A. Petruhins, M. Dahlqvist, F. Magnus, A. Mockute, B. Alling and J. Rosen, *Mater. Res. Lett.*, 2014, **2**(2), 89–93.

- 31 A. Thore, M. Dahlgqvist, B. Alling and J. Rosén, *Phys. Rev. B*, 2016, **93**(5), 054432.
- 32 A. Thore, M. Dahlgqvist, B. Alling and J. Rosén, *J. Appl. Phys.*, 2014, **116**(10), 103511.
- 33 M. Dahlgqvist, A. S. Ingason, B. Alling, F. Magnus, A. Thore, A. Petruhins and I. A. Abrikosov, *Phys. Rev. B*, 2016, **93**(1), 014410.
- 34 W. B. Zhang, Q. Qu, P. Zhu and C. H. Lam, *J. Mater. Chem. C*, 2015, **3**(48), 12457–12468.
- 35 X. Li and J. Yang, *J. Mater. Chem. C*, 2014, **2**(34), 7071–7076.
- 36 K. I. Kobayashi, T. Kimura and H. Sawada, *et al.*, *Nature*, 1998, **395**(6703), 677–680.
- 37 W. H. Xie, Y. Q. Xu and B. G. Liu, *et al.*, *Phys. Rev. Lett.*, 2003, **91**(3), 037204.
- 38 L. Hu, X. Wu and J. Yang, *Nanoscale*, 2016, **8**, 12939–12945.
- 39 G. H. O. Daalderop, P. J. Kelly and M. F. H. Schuurmans, *Phys. Rev. B: Condens. Matter Mater. Phys.*, 1990, **41**(17), 11919.
- 40 P. J. Hay, J. C. Thibeault and R. Hoffmann, *J. Am. Chem. Soc.*, 1975, **97**(17), 4884–4899.
- 41 H. Xiang, C. Lee, H. J. Koo, X. Gong and M. H. Whangbo, *Dalton Trans.*, 2013, **42**(4), 823–853.
- 42 J. He, P. Lyu, L. Sun, A. Morales-Garcia and P. Nachtigall, *J. Mater. Chem. C*, 2016, **4**, 6500–6509.
- 43 Y. Zhou, Z. Wang, P. Yang, X. Zu, L. Yang, X. Sun and F. Gao, *ACS Nano*, 2012, **6**(11), 9727–9736.
- 44 J. He, P. Zhou, N. Jiao, S. Y. Ma, K. W. Zhang, R. Z. Wang and L. Z. Sun, *Sci. Rep.*, 2014, **4**, 4014.
- 45 G. Kresse and H. Jürgen, *Phys. Rev. B: Condens. Matter Mater. Phys.*, 1993, **47**(1), 558.
- 46 G. Kresse and D. Joubert, *Phys. Rev. B: Condens. Matter Mater. Phys.*, 1999, **59**, 1758.
- 47 J. P. Perdew, K. Burke and M. Ernzerhof, *Phys. Rev. Lett.*, 1996, **77**, 3865.
- 48 P. E. Blöchl, *Phys. Rev. B: Condens. Matter Mater. Phys.*, 1994, **50**(24), 17953.
- 49 S. L. Dudarev, G. A. Botton, S. Y. Savrasov, C. J. Humphreys and A. P. Sutton, *Phys. Rev. B: Condens. Matter Mater. Phys.*, 1998, **57**, 1505.
- 50 J. Heyd, G. E. Scuseria and M. Ernzerhof, *J. Chem. Phys.*, 2003, **118**, 8207.
- 51 K. Reuter and M. Scheffler, *Phys. Rev. B: Condens. Matter Mater. Phys.*, 2001, **65**(3), 035406.

# **Attachment No. 11**

CrossMark  
click for updatesCite this: *J. Mater. Chem. C*, 2016,  
4, 2518

# Unusual Dirac half-metallicity with intrinsic ferromagnetism in vanadium trihalide monolayers

Junjie He,<sup>a</sup> Shuangying Ma,<sup>b</sup> Pengbo Lyu<sup>a</sup> and Petr Nachtigall<sup>\*a</sup>

The Dirac half-metallicity (H. Ishizuka *et al.*, *Phys. Rev. Lett.* 2012, **109**, 237207, Li *et al.* *Phys. Rev. B: Condens. Matter Mater. Phys.*, 2015, **92**, 201403(R)) with a gap in one spin channel but a Dirac cone in the other has been proposed and attracted considerable attention. We report these exciting properties for VCl<sub>3</sub> and VI<sub>3</sub> layered materials based on density functional theory combined with the self-consistently determined Hubbard *U* approach (DFT+*U*<sub>scf</sub>). Using DFT+*U*<sub>scf</sub>, the stability and electronic and magnetic structures of VCl<sub>3</sub> and VI<sub>3</sub> monolayers are systematically investigated. The DFT+*U*<sub>scf</sub> shows that VCl<sub>3</sub> and VI<sub>3</sub> monolayers have intrinsic ferromagnetism and half-metallicity. Remarkably, the VCl<sub>3</sub> and VI<sub>3</sub> monolayers possess a rather rare half-metallic Dirac point around the Fermi level with just one spin channel. In contrast to the Dirac point in graphene, the Dirac points in VCl<sub>3</sub> and VI<sub>3</sub> monolayers are mainly due to the V-d electrons and consequently they show a large spin-orbital coupling induced gaps of about 29 meV and 12 meV for VCl<sub>3</sub> and VI<sub>3</sub> monolayers, respectively. The Monte Carlo simulations based on the Ising model demonstrate that the Curie temperatures of VCl<sub>3</sub> and VI<sub>3</sub> sheets are only 80 K and 98 K, respectively. However, the Curie temperature can be increased up to room temperature by carrier doping. The feasibility of an exfoliation from VCl<sub>3</sub> and VI<sub>3</sub> layered bulk phases is confirmed due to the small cleavage energies. Our results greatly broaden the family of potential 2D Dirac materials. The calculated properties of VCl<sub>3</sub> and VI<sub>3</sub> monolayers show that these materials have great application potential, opening the way towards the development of high-performance electronic devices.

Received 27th January 2016,  
Accepted 6th March 2016

DOI: 10.1039/c6tc00409a

www.rsc.org/MaterialsC

## 1. Introduction

Two dimensional (2D) materials, such as graphene,<sup>1</sup> have great potential applications for high performance electronic and spintronic devices.<sup>2</sup> In particular, 2D Dirac materials exhibit novel physical properties such as linear band dispersion, ballistic charge transport, enormously high carrier mobility, and topological phases.<sup>3–5</sup> The great effort being devoted towards the development of such 2D Dirac materials is thus understandable. Dirac states have been discovered and investigated in materials, such as janugraphene and chlorographene,<sup>6</sup> silicene,<sup>7</sup> germanene,<sup>7</sup> graphyne,<sup>8</sup> graphene/intercalated transition metal/SiC,<sup>9,10</sup> TiB<sub>2</sub>,<sup>11</sup> metal-organic frameworks, *etc.*<sup>12</sup> The key point for practical applications in spintronic devices is to develop 2D materials with ordered spin structure and 100% spin polarization. Half-metals with one conducting spin channel and one insulating/semiconducting spin channel have been considered as the ideal materials for spintronic applications. A modification of graphene by the presence of defects, atom doping or surface functionalization

and nanoribbons can introduce half-metallicity.<sup>13–15</sup> For example, half-metallicity has been predicted in a zigzag graphene nanoribbon in the presence of an electric field.<sup>16</sup> However, the half-metallicity due to graphene functionalization would inevitably destroy its Dirac states. By combining the two fascinating properties of massless Dirac fermions and 100% spin polarization, Dirac half-metallicity (DHM) has been recently proposed based on model calculations for a triangle lattice.<sup>17</sup> Subsequently, Li *et al.*<sup>18</sup> predicted that the Dirac half-metal can be obtained by Mn intercalation into epitaxial graphene on SiC(0001), indicating that the DHM states show an intrinsic quantum anomalous Hall effect. The search for materials with intrinsic DHM states is of great importance for both fundamental interest and device applications.

The layered transition-metal (TM) compounds, such as TM trichalcogenides, TM trihalides and TM dinitrides, have recently attracted a great deal of attention due to their intrinsic 2D ferromagnetism and potential applications in nanoelectronic devices.<sup>19–24</sup> For instance, 2D chromium tellurosilicate (CrSiTe<sub>3</sub>) has been exfoliated experimentally from its bulk phase and it was shown that it exhibits intrinsic ferromagnetism at 80 K Curie temperature.<sup>25</sup> Moreover, Du *et al.* obtained the 2D metal phosphorus trichalcogenides *via* the exfoliation process with unusual ferroelectric, optical and magnetic properties.<sup>26</sup> Transition metal trihalides (TMHs) encompass a family of materials with

<sup>a</sup> Department of Physical and Macromolecular Chemistry, Faculty of Science, Charles University in Prague, 128 43 Prague 2, Czech Republic.

E-mail: petr.nachtigall@natur.cuni.cz

<sup>b</sup> Department of Physics, Xiangtan University, Xiangtan 411105, China

the general formula (TMX<sub>3</sub>), (TM = Ti, V, Cr, Mn, Fe, Mo, Ru and X = Cl, Br, I).<sup>27–29</sup> Such van der Waals materials stacked on top of each other can be exfoliated into 2D materials from the bulk phase, as has been shown experimentally, *e.g.*, for TM chalcogenides.<sup>30</sup> It has been recently reported that the transition metal trihalide monolayer can be easily exfoliated from the bulk crystal and that the exfoliated layers are intrinsic 2D ferromagnetic semiconductors.<sup>22,23,31</sup> The TMX<sub>3</sub> materials have TM centers in an octahedral environment with a TM honeycomb arrangement in the plane. The existence of Dirac states in a TM honeycomb spin lattice like graphene structure has been reported recently in the transition-metal monolayer,<sup>32</sup> honeycomb BaFe<sub>2</sub>(PO<sub>4</sub>)<sub>2</sub>,<sup>33</sup> metal–organic frameworks (Ni<sub>2</sub>C<sub>18</sub>H<sub>12</sub> and Co<sub>2</sub>C<sub>18</sub>H<sub>12</sub>),<sup>12</sup> TM doped zinc blende boron nitride,<sup>34</sup> *etc.* These results suggest that the Dirac states in TMX<sub>3</sub> can exist due to the honeycomb spin lattice of TMX<sub>3</sub> materials. In this work, using first-principles calculations and the self-consistent Hubbard *U* approach (DFT+*U*<sub>scf</sub>) together with the Monte Carlo simulations, we investigate the geometry, stability, electronic and magnetic properties of VCl<sub>3</sub> and VI<sub>3</sub> monolayers.

## 2. Methods and computational details

Bulk and monolayer VCl<sub>3</sub> and VI<sub>3</sub> structures are shown in Fig. 1. All calculations were performed using the Vienna *ab initio* simulation package (VASP)<sup>35,36</sup> within the generalized gradient approximation, using the Perdew–Burke–Ernzerhof (PBE) exchange–correlation functional.<sup>37</sup> Interactions between electrons and nuclei were described using the projector-augmented wave (PAW) method. The criteria of energy and atom force convergence were set to 10<sup>−5</sup> eV and 0.01 eV Å<sup>−1</sup>, respectively. A plane-wave kinetic energy cutoff of 500 eV was employed. The vacuum space of 15 Å along the VCl<sub>3</sub> and VI<sub>3</sub> normal was adopted for calculations on monolayers. The Brillouin zone (BZ) was sampled using 15 × 15 × 1 Gamma-centered Monkhorst–Pack grids for the calculation of relaxation and electronic structures. To account for the energy of

localized 3d orbitals of TM atoms accurately, the Hubbard “*U*” correction was employed within the rotationally invariant DFT+*U* approach proposed by Dudarev *et al.*,<sup>38</sup> where only the *U*<sub>eff</sub> = *U* − *J* value is meaningful instead of individual *U* and *J* values. The linear response theory (LRT) introduced by Cococcioni *et al.*<sup>39</sup> was applied to evaluate the *U* parameter. The Hubbard *U* can be calculated directly by the response function as follows:

$$\chi_{IJ} = \frac{\partial E}{\partial n_I \partial n_J} = -\frac{\partial n_I}{\partial \alpha_J} \quad (1)$$

In the LRT approach,  $\chi_{IJ}$  is obtained from the response of *d* state occupations (*n*) to a small localized perturbation potential shift  $\alpha$ . An occupation-dependent energy functional is required for the self-consistent solution of the Kohn–Sham equations. The effective interaction parameter *U* of site *I* can then be calculated as follows:

$$U = \frac{\partial n_{I,0}}{\partial (n_I)} - \frac{\partial n_I}{\partial (n_I)} = [\chi_0^{-1} - \chi^{-1}]_I, \quad (2)$$

where  $\chi_0^{-1}$  and  $\chi^{-1}$  represent the Kohn–Sham and the non-interacting inverse density response functions of the system with respect to the localized potential shift, respectively. The self-consistent determination of *U* was performed with the Quantum Espresso code<sup>40</sup> using the GGA (PBE) exchange–correlation functional and PAW pseudopotentials. A similar approach has been used previously for monolayer chromium trihalides.<sup>23</sup> The calculated *U*<sub>scf</sub> parameters based on a linear response theory are 3.35 and 3.68 eV for VCl<sub>3</sub> and VI<sub>3</sub>, respectively (Fig. 2). These values are very close to each other due to the similar valence configurations of V atoms in VCl<sub>3</sub> and VI<sub>3</sub>. The phonon frequencies were calculated by using a supercell approach as implemented in the PHONOPY code.<sup>41,42</sup> To evaluate the feasibility of exfoliation from its bulk structure, the cleavage energy was calculated by the following procedure: introducing a fracture in the bulk and then gradually increasing the interlayer distance *d* (Fig. 1) and calculating the variation of the total

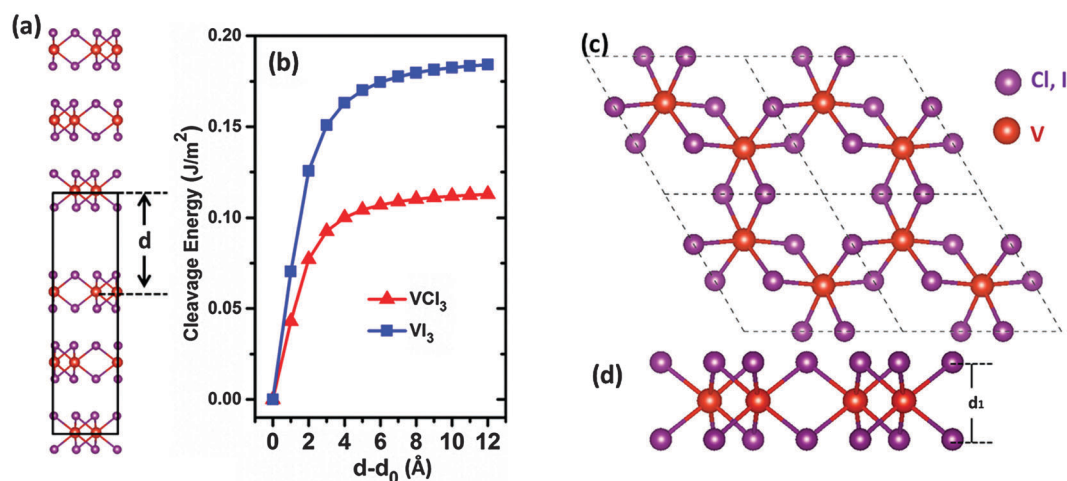


Fig. 1 Bulk model (a) of VX<sub>3</sub> (X = Cl, I) used to simulate the exfoliation procedure and the cleavage energy (b) calculated as a function of the separation between two fractured parts. The top (c) and side (d) views of the VX<sub>3</sub> monolayer are shown as well. *d*<sub>0</sub> represents the equilibrium interlayer distance of chromium trihalides.

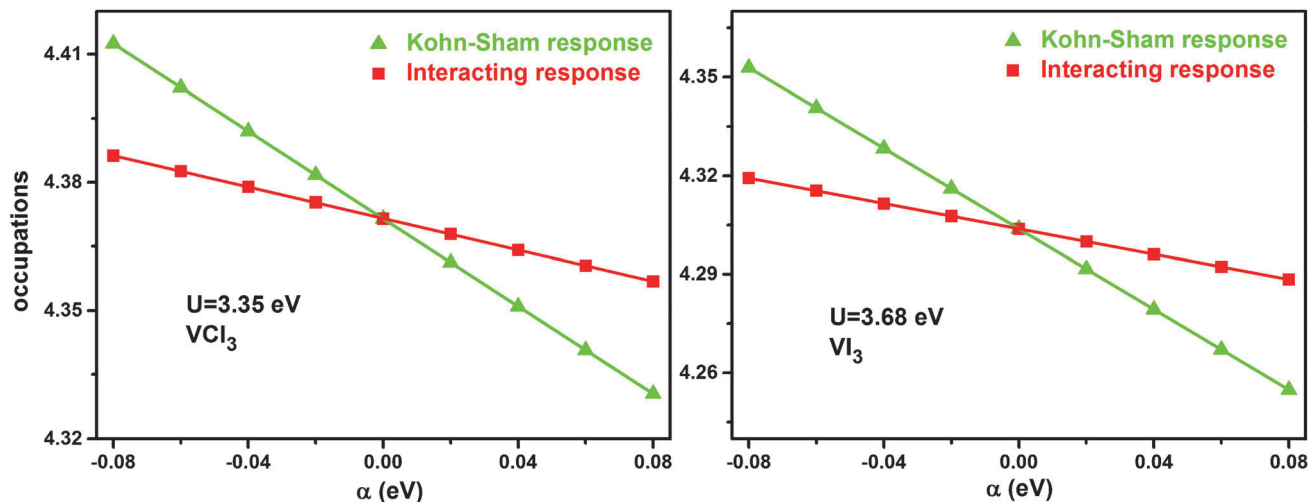


Fig. 2 The interacting and Kohn–Sham response functions of  $\text{VCl}_3$  and  $\text{VI}_3$  monolayers.

energy. Furthermore, to study the thermal stability of the  $\text{VCl}_3$  and  $\text{VI}_3$  layers the *ab initio* molecular dynamics (AIMD) simulations at 300 K in a canonical ensemble are performed using the Nosé heat bath approach. The total energy increases as the separation increases and slowly converges to the exfoliation energy. For calculations of cleavage energies it is necessary to account for van der Waals interactions (vdW), therefore vdW corrections were considered within the Grimme's approach (DFT-D2).<sup>43</sup>

### 3. Results and discussion

#### 3.1 Cleavage energy and structure stability

The bulk  $\text{VCl}_3$  and  $\text{VI}_3$  structures have a rhombohedral  $\text{BiI}_3$  crystal structure type with the  $R\bar{3}$  space group. V atoms (with  $d^2$  spin configurations) are arranged in a honeycomb lattice. To explore the possible exfoliation of a monolayer from the bulk structure of  $\text{VCl}_3$  and  $\text{VI}_3$ , cleavage energies were calculated as shown in Fig. 1(a). The calculated cleavage energies are 0.11 and 0.18  $\text{J m}^{-2}$  for  $\text{VCl}_3$  and  $\text{VI}_3$ , respectively. The results are comparable with those of the  $\text{CrX}_3$  ( $X = \text{Cl}, \text{Br}, \text{I}$ ) materials.<sup>23</sup> The cleavage energies are however smaller than those for other previously reported 2D layered materials, such as  $\text{CrSiTe}_3$  (0.35  $\text{J m}^{-2}$ ),  $\text{CrGeTe}_3$  (0.38  $\text{J m}^{-2}$ )<sup>25</sup> and  $\text{MnPSe}_3$  (0.24  $\text{J m}^{-2}$ ).<sup>19</sup> Consequently, these results suggest that  $\text{VCl}_3$  and  $\text{VI}_3$  monolayers can be possibly obtained by the exfoliation process from their layered bulk phases. To further confirm the stability of  $\text{VCl}_3$  and  $\text{VI}_3$  monolayers, their phonon spectra were measured (Fig. 3). There are no negative frequency phonons found at the whole Brillouin zone. The results indicate that the  $\text{VCl}_3$  and  $\text{VI}_3$  monolayers are dynamically stable (at least at sufficiently low temperatures) and they can exist as free-standing 2D crystals, and we will focus on various properties of these monolayers. Moreover, AIMD calculations carried out for 9 ps (with a time step of 3 fs) show that both  $\text{VCl}_3$  and  $\text{VI}_3$  layers are stable. The total potential energies with respect to the simulation time (Fig. 3(c) and (d)) are almost invariant during the simulation, suggesting that the  $\text{VCl}_3$  and  $\text{VI}_3$  monolayers are thermally stable

at room temperature. The geometries of the 2D  $\text{VCl}_3$  and  $\text{VI}_3$  lattice structures are shown in Fig. 1. The lattice constants of 2D  $\text{VCl}_3$  and  $\text{VI}_3$  are calculated to be 6.28 and 7.14 Å, respectively, at the  $\text{PBE}+U_{\text{scf}}$  level of theory. The lattice constants of  $\text{VCl}_3$  monolayers are consistent with those reported previously for the bulk crystal, indicating that the linear response Hubbard  $U$  method is reliable.<sup>44</sup> The lattice constant, the V-halide bond length, and the vertical distance between two halide planes ( $d_1$ ) are significantly larger for  $\text{VI}_3$  than for  $\text{VCl}_3$  (Table 1).

#### 3.2 Magnetic ground states and electronic structures

The FM states of  $\text{VCl}_3$  and  $\text{VI}_3$  have total magnetic moments of 4  $\mu_{\text{B}}$  (per unit cell). The spin configuration of V atoms is completely determined by the occupation of the transition-metal atomic orbitals based on Bader charge analysis. It shows that the V atoms have  $d^{2\uparrow}$  spin configurations; they behave as a  $\text{V}^{3+}$  ion in both  $\text{VCl}_3$  and  $\text{VI}_3$  systems. V atoms predominantly contribute to the total magnetic moments while the neighboring X atoms have only a small contribution. To determine the preferred magnetic ground state structures of  $\text{VCl}_3$  and  $\text{VI}_3$  systems, the collinear FM, Néel, zigzag and stripy states are considered as shown in Fig. 4. The FM states are the most stable magnetic configurations. The nearest-, next-nearest- and the next-next-nearest-neighbor exchange-coupling parameters  $J_1$ ,  $J_2$ , and  $J_3$  can be extracted by mapping the total energies of the systems with different magnetic structures from a classical Heisenberg model:

$$H_{\text{spin}} = - \sum_{i,j} J_1 M_i \cdot M_j - \sum_{k,l} J_2 M_k \cdot M_l - \sum_{m,n} J_3 M_m \cdot M_n, \quad (3)$$

where  $M$  is the net magnetic moment at the V site  $i$ , ( $i, j$ ), ( $k, l$ ) and ( $m, n$ ) stand for the nearest, next-nearest and the next-next-nearest V atoms, respectively. By mapping the DFT energies to the Heisenberg spin Hamiltonian,  $J_1$ ,  $J_2$  and  $J_3$  can be calculated from following equations:<sup>45</sup>

$$E_{\text{FM/Néel}} = E_0 - (\pm 3J_1 + 6J_2 \pm 3J_3)M^2 \quad (4)$$

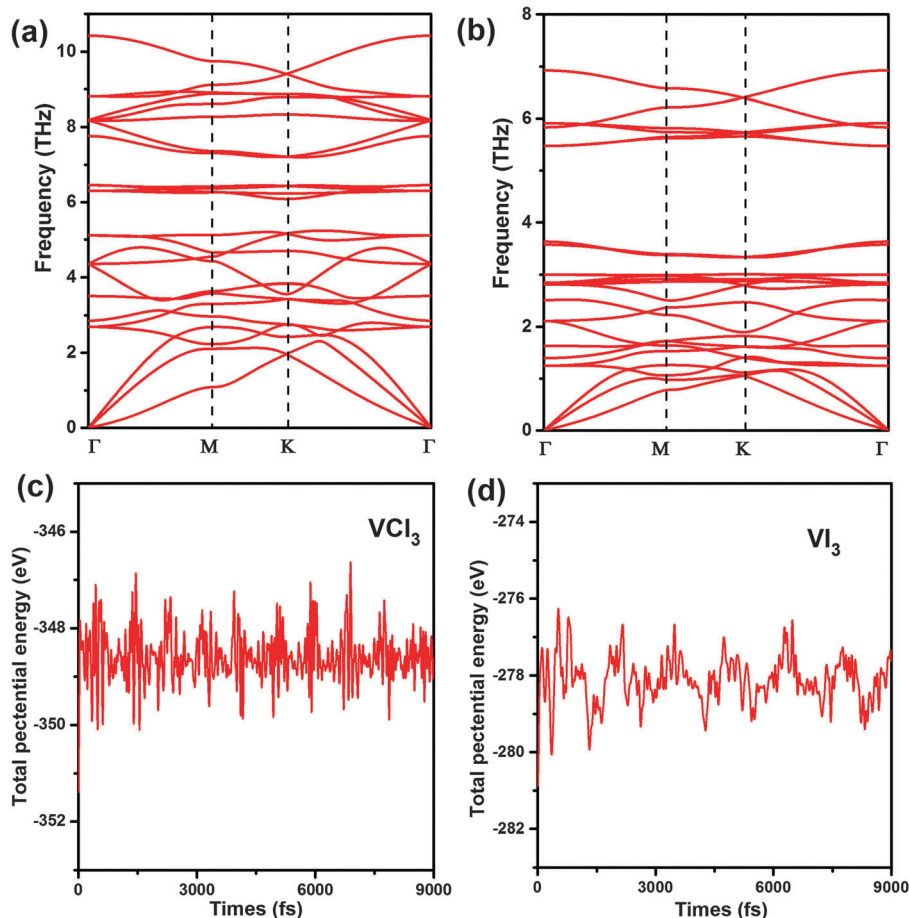


Fig. 3 Phonon band structures of (a)  $\text{VCl}_3$  and (b)  $\text{VI}_3$ , respectively. Variations of the total potential energy of  $\text{VCl}_3$  (c) and  $\text{VI}_3$  (d) along AIMD simulations.

**Table 1** Calculated characteristics of  $\text{VCl}_3$  and  $\text{VI}_3$  monolayers.  $L$  is the lattice constant,  $d_1$  is the vertical distance between two halide planes,  $d_{\text{V-X}}$  and  $d_{\text{V-V}}$  represent the bond length of V-X and V-V, respectively. ' $U$ ' is the calculated  $U$  parameter using the linear response method.  $J_1$ ,  $J_2$  and  $J_3$  represent the nearest neighbor, next-nearest neighbor and the third neighbor coupling constants according to the Heisenberg model, respectively, and  $T_C$  is the Curie temperature

Structure	$L$ (Å)	$d_1$ (Å)	$d_{\text{V-X}}$ (Å)	$d_{\text{V-V}}$ (Å)	$U$ (eV)	$J_1$ (meV)	$J_2$ (meV)	$J_3$ (meV)	$T_C$ (K)
$\text{VCl}_3$	6.28	2.76	2.42	3.66	3.35	2.227	0.144	0.02	80
$\text{VI}_3$	7.18	3.30	2.81	4.14	3.68	2.754	-0.019	0.110	98

and

$$E_{\text{zigzag/stripy}} = E_0 - (\pm J_1 - 2J_2 \mp 3J_3)M^2. \quad (5)$$

The calculated exchange coupling parameters of  $\text{VCl}_3$  and  $\text{VI}_3$  are summarized in Table 1. The magnetic interaction for the  $\text{VI}_3$  monolayer is larger than that for the  $\text{VCl}_3$  one. The first neighboring and the third neighboring exchange parameters for both  $\text{VCl}_3$  and  $\text{VI}_3$  are ferromagnetic. The second exchange parameter ( $J_2$ ) for the next-nearest neighbors is ferromagnetic for  $\text{VCl}_3$ , while it is weakly antiferromagnetic for the  $\text{VI}_3$  monolayer. However, it should be noted that  $J_1$  is one order of magnitude larger than  $J_2$  and  $J_3$ . Using the DFT derived spin

exchange parameters, the Curie temperatures  $T_C$  for  $\text{VCl}_3$  and  $\text{VI}_3$  are estimated by Monte Carlo (MC) simulations based on the Ising model (MC simulations on a  $50 \times 50$  2D honeycomb lattice and  $10^6$  steps for each temperature). Test calculations also show that a larger lattice ( $80 \times 80$ ) and larger number of MC steps ( $10^8$ ) give very similar  $T_C$  values. The  $T_C$  value is found to be 80 K and 98 K for  $\text{VCl}_3$  and  $\text{VI}_3$  monolayers, respectively (Fig. 5). It is comparable for other 2D ferromagnetic materials, like  $\text{CrSiTe}_3$  (80 K).<sup>25</sup>

The FM states are the most stable magnetic configurations for  $\text{VCl}_3$  and  $\text{VI}_3$  monolayers considered herein. The  $\text{VCl}_3$  and  $\text{VI}_3$  structures are considered below in a more detailed investigation of their electronic properties. The electronic band structures and density of states (DOS) of  $\text{VCl}_3$  and  $\text{VI}_3$  are depicted in Fig. 6. For both  $\text{VCl}_3$  and  $\text{VI}_3$ , the spin-down channels possess a very large band gap, whereas the spin-up ones do not show any gap. Therefore, the electronic structure has an intrinsic half-metallicity without any artificial modification. Although a number of systems showing half-metallicity has been proposed, it is still of interest to find the 2D half-metallicity with intrinsic ferromagnetism. Both 2D materials reported herein show half-metallic character and they can be used as ideal spin-filter devices; moreover, they both show rather unusual Dirac half-metallicity. A linear dispersion relation near the Fermi level indicates that the spin-polarized

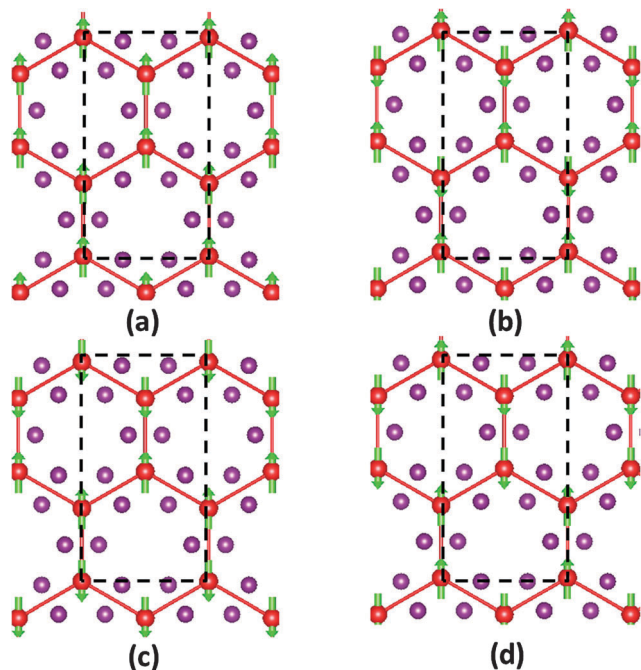


Fig. 4 The possible magnetic configurations of a single  $VX_3$  ( $X = \text{Cl}, \text{I}$ ) layer: FM (a), AF-Neel (b), AF-zigzag (c), and AF-stripy (d) orderings were considered. Green arrows represent the spin direction of electrons on V atoms. The crystal cells used in these calculations are also shown (dashed lines).

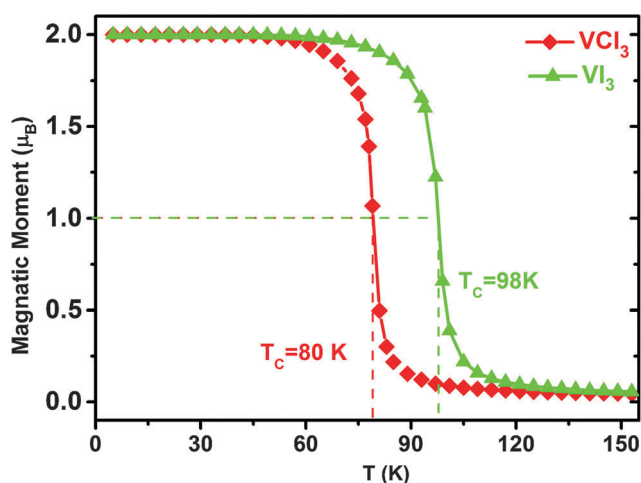


Fig. 5 Variations of the average magnetic moment per unit cell with respect to the temperature calculated for  $VCl_3$  and  $VI_3$ .

massless Dirac fermions are found in the spin-up channels of  $VCl_3$  and  $VI_3$  at the high-symmetry  $K$  point of the Brillouin zone. The Dirac points located at  $K$  for  $VCl_3$  and  $VI_3$  are just 20 and 106 meV above the Fermi level, respectively. Due to the similar symmetries the positioning of Dirac points in the Brillouin zone is the same as found for graphene (Fig. 6). Examination of Dirac states near the Fermi level (Fig. 6(a) and (b) insets) reveals that the linear dispersion relation of band energies essentially remains unchanged when approaching the cross points. For further insight into the distribution of the linear dispersion

relation in the Brillouin zone, the corresponding bands around the Fermi level in three dimensions are presented in Fig. 6(c). The calculated Fermi velocities ( $\nu_F$ ) of Dirac fermions using  $\nu_F = \partial E(k)/\partial(\hbar k)$  are about  $0.16 \times 10^6 \text{ m s}^{-1}$  and  $0.1 \times 10^6 \text{ m s}^{-1}$  for  $VCl_3$  and  $VI_3$  monolayers, respectively, values high enough for the applications as high-speed devices and circuits. These Fermi velocities are comparable to those of silicene, germanene,<sup>46</sup> stanine<sup>47</sup> and  $\text{Gi/Mn/SiC}$  materials.<sup>10</sup> It can thus be concluded that both, the Dirac half-metallicity and intrinsic ferromagnetism, were found in  $VCl_3$  as well as in  $VI_3$  monolayers. The electron mobility in the spin channel is always relatively low for conventional half-metallic materials because of the lack of the linear band dispersion. However, for  $VCl_3$  and  $VI_3$  materials, due to the existence of Dirac states, high electron mobility in one spin channel and a relatively large band gap in another spin channel constitute a great potential for applications in nanoelectronics and spintronics.

The partial electronic density of states (PDOS) is calculated for the  $VX_3$  monolayer to gain insight into the origin of Dirac states (Fig. 7). With respect to the octahedral crystal field of V magnetic ions in  $VCl_3$  and  $VI_3$  monolayers, the 3d orbitals split into 2-fold  $e_g$  ( $d_{z^2}$  and  $d_{x^2-y^2}$ ) orbitals and 3-fold degenerate  $t_{2g}$  ( $d_{xz}$ ,  $d_{yz}$  and  $d_{xy}$ ) orbitals. These  $e_g$  and  $t_{2g}$  orbitals of the V atom together with the p ( $p_x$ ,  $p_y$ ,  $p_z$ ) orbitals of Cl and I atoms are shown in Fig. 7. It clearly shows that most of Cl and I atomic states are located in the lower energy range of the valence band and in the higher energy range of the conduction band, while only a small amount of weight of the Cl and I states contributes to the states near the Fermi level. In contrast, the V states have high weights near the Dirac states. The Dirac states of  $VCl_3$  and  $VI_3$  are mainly derived from the V-d states, where the X- $p_z$  ( $X = \text{Cl}, \text{I}$ ) does not contribute significantly. Most theoretically predicted and experimentally confirmed Dirac materials, such as graphene and topological insulators, are composed of p-orbital electrons. However, the d-orbital Dirac materials have in general a stronger spin exchange interaction and a larger spin-orbit coupling (SOC), which may show interesting physical properties, such as an anomalous quantum Hall effect.

Following the above analysis, the Dirac cones of  $VCl_3$  and  $VI_3$  result from a stronger spin-orbital coupling between d-electrons than is typically observed for p-electrons. The SOC-induced gaps obtained by relativistic DFT calculations are shown in Fig. 8 for  $VCl_3$  and  $VI_3$  layers. Remarkably, gaps of 29 meV and 12 meV open at the spin-up Dirac points of  $VCl_3$  and  $VI_3$  structures, respectively. The SOC-induced gap is comparable to that of d-electronic Dirac materials such as  $\text{G/i-Mn/SiC}$  (30 meV)<sup>10</sup> and is much larger than those in pure graphene and silicene,<sup>44</sup> implying that a possible quantum anomalous Hall effect or a quantum spin Hall effect can be found in these 2D materials.

To understand the origin of exchange interactions in  $VCl_3$  and  $VI_3$ , the spin-polarized charge density (SCD) and schematics of the exchange mechanisms are plotted in Fig. 9. The d electrons on vanadium can induce the spin-polarization on neighboring Cl and I atoms (Cl and I atoms show the spin-down polarization in the SCD figure). This is also apparent from the spin splittings on Cl and I atoms in PDOS shown in Fig. 7. The V and the nearest



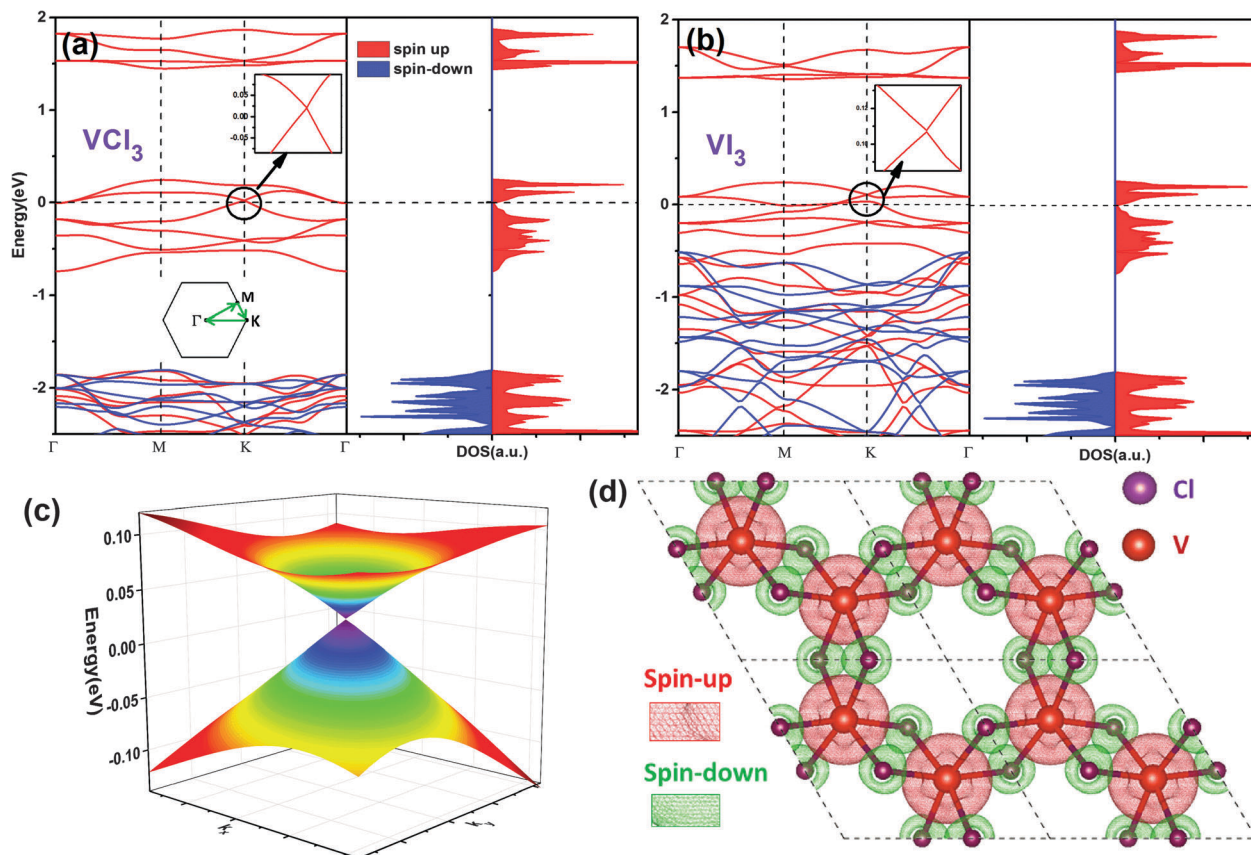


Fig. 6 Band structure and total DOS for  $\text{VCl}_3$  (a) and  $\text{VI}_3$  (b). The red and blue lines/areas in the band/DOS structures represent the spin-up and spin-down channels, respectively. Details of Dirac states near the Fermi level are shown in insets. The three-dimensional Dirac band structure for  $\text{VCl}_3$  (c) and spin-polarized charge densities of  $\text{VCl}_3$  (d) are shown as well.

neighboring Cl/I atoms can maintain the antiferromagnetic coupling mediated by the p orbitals of Cl and I atoms and the spin arrangement like  $\text{V}_1\uparrow-\text{X}_1-\text{V}_2\uparrow$  can be established.<sup>48</sup> Therefore, the FM couplings of V ions in  $\text{VCl}_3$  and  $\text{VI}_3$  are mediated by X-2p states through a double-exchange mechanism (Fig. 9) and the FM states become the most favorable. A similar magnetic coupling mechanism was used to explain the origin of cation vacancies in GaN,<sup>49</sup> 2D transition metal dichalcogenides<sup>50</sup> and TM doped 2D materials.<sup>46,51</sup>

### 3.3 Tuning the Curie temperature and Dirac states by carrier doping

The Dirac states for  $\text{VCl}_3$  and  $\text{VI}_3$  are not located exactly at the Fermi level. They are just 20 and 106 meV above the Fermi level for  $\text{VCl}_3$  and  $\text{VI}_3$  monolayers, respectively. A suitable doping can move the Fermi level downwards to shift the Dirac states of  $\text{VCl}_3$  and  $\text{VI}_3$  materials exactly at the Fermi level. Since there are some bands in between the Fermi level and Dirac points, the electron doping can shift their relative positions, and this can be achieved experimentally, *e.g.*, via gate voltage. Moreover, the Curie temperatures of  $\text{VCl}_3$  and  $\text{VI}_3$  monolayers are far below room temperature; it is thus important to examine if the carrier doping can lead to a Curie temperature increase. Previous investigations have revealed that the carrier doping is

an effective approach to increase the Curie temperature in some materials.<sup>19,23</sup> Following the recent report dealing with the  $\text{CrX}_3$  (X = Cl, Br and I) materials,<sup>23</sup> the low doping concentration (up to 0.75 hole per electron per unit cell) is considered herein for  $\text{VCl}_3$  and  $\text{VI}_3$  monolayers. The variation of exchange energies with the carrier doping concentration is shown in Fig. 10. Both, hole and electron doping, can enhance FM coupling in the  $\text{VCl}_3$  and  $\text{VI}_3$  monolayers. The increase of the exchange energy by the hole doping is larger than that by electron doping in the case of  $\text{VCl}_3$  and the exactly opposite observation is made for  $\text{VI}_3$ . Therefore, the electron and hole doping are effective ways to improve the ferromagnetism of  $\text{VCl}_3$  and  $\text{VI}_3$  monolayers. At the maximal considered carrier doping concentration (0.75 hole for  $\text{VCl}_3$  and 0.75 electron for  $\text{VI}_3$ ), the calculated spin exchange parameters  $J_1$ ,  $J_2$  and  $J_3$  are 9.84,  $-1.23$ , and 4.51 meV, respectively, for  $\text{VCl}_3$  and they are 5.802, 1.20, 3.248 meV, respectively, in the case of  $\text{VI}_3$ . The estimated  $T_C$  values obtained from MC simulations are 353 K and 246 K for the doped  $\text{VCl}_3$  and  $\text{VI}_3$ , respectively. Thus, the carrier doping can effectively increase the Curie temperatures of  $\text{VCl}_3$  and  $\text{VI}_3$  monolayers up to room temperature. At the same time, the electron doping can move the Fermi level downwards. For electron doping levels of 0.1 and 0.7 per unit cell for  $\text{VCl}_3$  and  $\text{VI}_3$  monolayers, respectively, the Dirac states

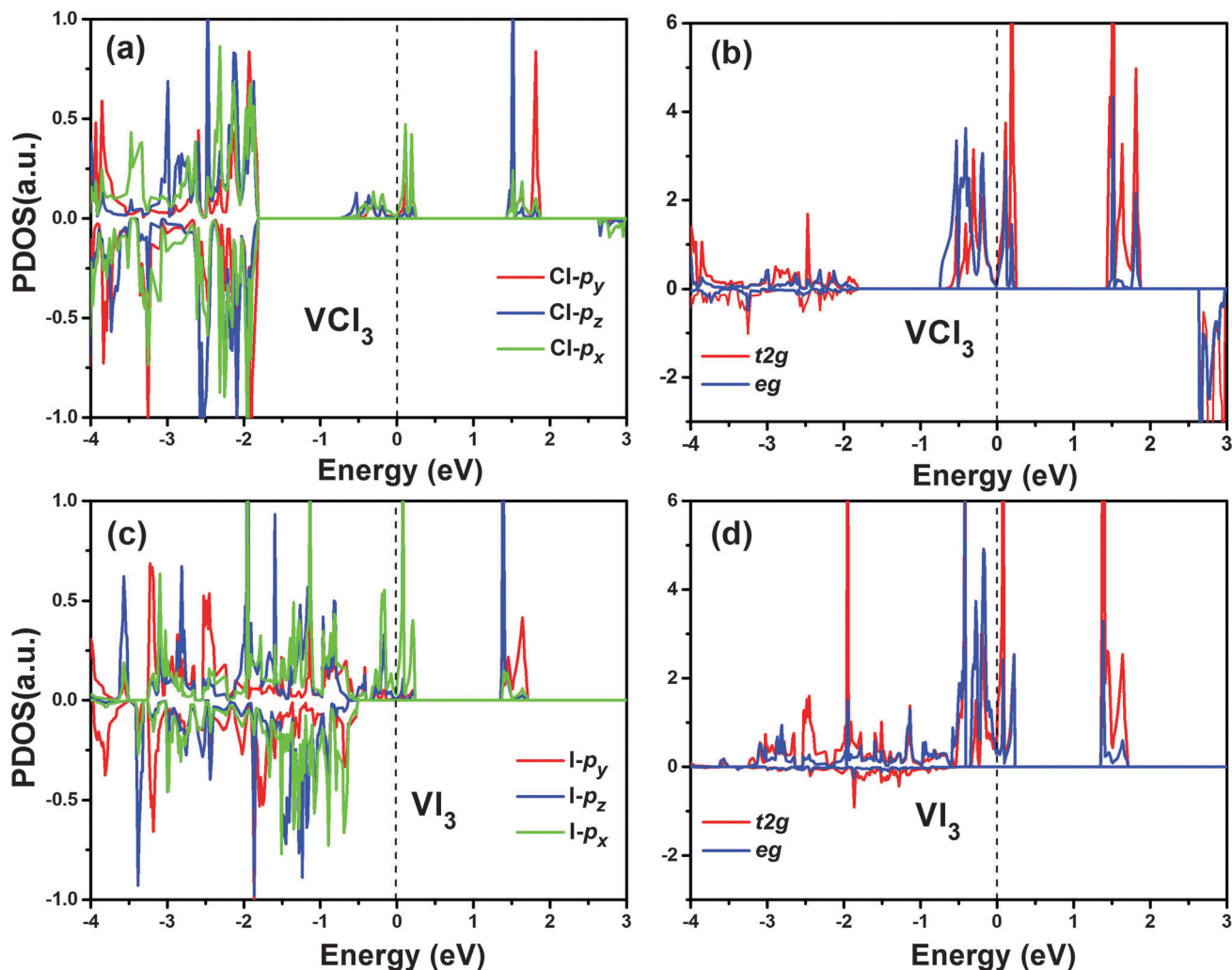


Fig. 7 PDOS of Cl (a) and V (b) atoms of  $\text{VCl}_3$  monolayer and PDOS of I (c) and V (d) atoms of  $\text{VI}_3$  monolayers are shown. The Fermi level is set to zero.

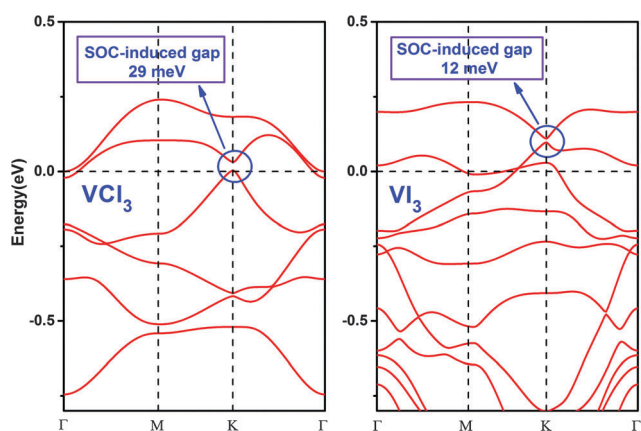


Fig. 8 Electronic band structures of  $\text{VCl}_3$  and  $\text{VI}_3$  monolayers with spin-orbit couplings. The horizontal dashed lines indicate the Fermi level.

are exactly located at the Fermi level. The increasing exchange coupling can be understood by the p-d exchange mechanism, which has been found in the  $\text{CrX}_3$  monolayers.<sup>23</sup> The carrier

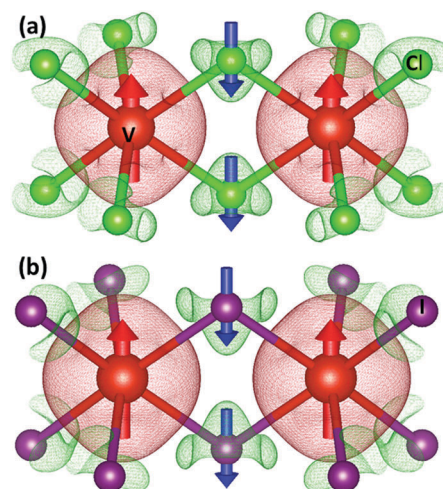


Fig. 9 Spin-polarized charge densities (SCD) with spin directions for  $\text{VCl}_3$  (a) and  $\text{VI}_3$  (b) are shown (red and green dotted areas show spin-up and spin-down SCD, respectively). Up and down arrows indicate the up- and down-spins, respectively.

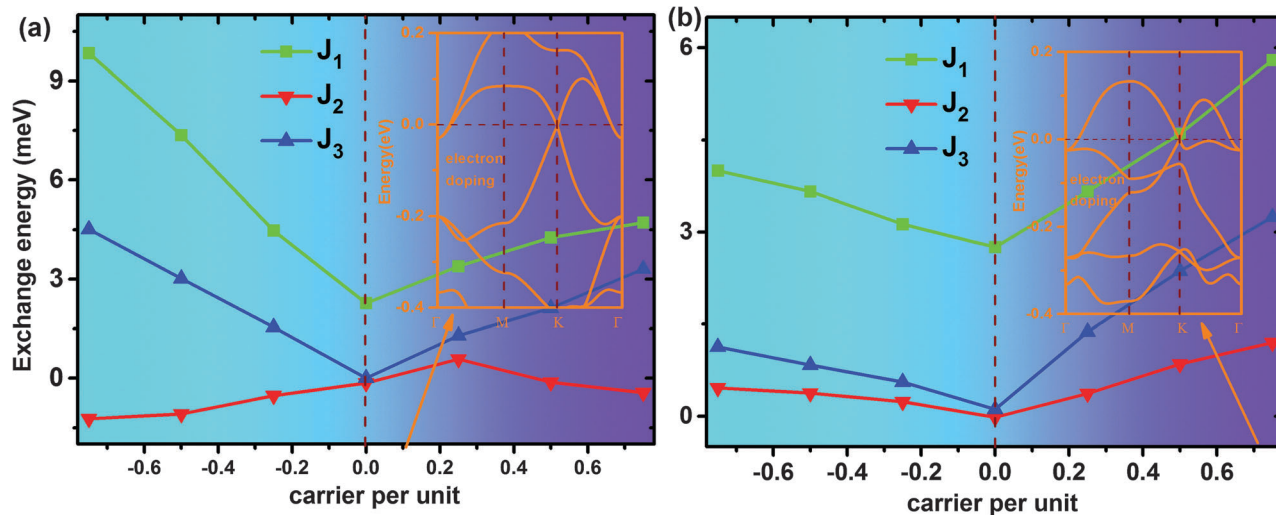


Fig. 10 The spin exchange parameters as a function of carrier concentration calculated for  $\text{VCl}_3$  (a) and  $\text{VI}_3$  (b). The positive and negative values are for electron and hole doping, respectively. The calculated band structures for electron doping of 0.1 and 0.7 are presented in the insets for  $\text{VCl}_3$  and  $\text{VI}_3$ , respectively.

doping can enhance the p-d exchange interaction and give rise to a stronger indirect ferromagnetic interactions between the nearest neighboring V ions *via* Cl and I bridges. The carrier doping is usually implemented experimentally *via* a gate voltage. Therefore, it will be possible to apply a gate voltage to control the ferromagnetism and Dirac states.

## 4. Conclusions

The DFT+ $U_{\text{scf}}$  approach was used in systematic investigation of the stability and electronic and magnetic structures of  $\text{VCl}_3$  and  $\text{VI}_3$  monolayers. The feasibility of exfoliation from their layered bulk phases is predicted computationally based on small cleavage energies. The phonon calculations suggest that single layers of  $\text{VCl}_3$  and  $\text{VI}_3$  are dynamically stable and that they can exist as freestanding 2D crystals. DFT+ $U_{\text{scf}}$  indicates that  $\text{VCl}_3$  and  $\text{VI}_3$  monolayers show an intrinsic ferromagnetism and the half-metallicity. Remarkably, the  $\text{VCl}_3$  and  $\text{VI}_3$  monolayers possess exciting half-metallic Dirac points around the Fermi level with just one spin channel. Contrary to the p-state character of the Dirac point in graphene, the Dirac points in  $\text{VCl}_3$  and  $\text{VI}_3$  monolayers are mainly due to the V-d states and consequently they show stronger spin-couplings than those found in graphene. The Monte Carlo simulations based on the Ising model demonstrate that the Curie temperature of  $\text{VCl}_3$  and  $\text{VI}_3$  layers are 80 K and 98 K, respectively. The carrier doping can not only effectively control the ferromagnetism and increase further the Curie temperature up to the room temperature, but also shift the Dirac states with respect to the Fermi level. Our results greatly broaden the family of 2D Dirac materials and opens up possibilities for developing high-performance electronic or spintronic devices.

## Acknowledgements

This work was funded by the Czech Science Foundation Grant No. P106/12/G015 (Centre of Excellence). The calculations were

partially performed at MetaCentrum and CERIT-SC computational facilities (MSM/LM 2010005 and OP VaVpI CZ. 1.05/3.2.00/08.0144). J. H. and P. L. acknowledge support from STARS Scholarship of Faculty of Science, Charles University in Prague.

## References

- 1 A. K. Geim and K. S. Novoselov, *Nat. Mater.*, 2007, **6**(3), 183–191.
- 2 A. C. Neto, F. Guinea, N. M. R. Peres, K. S. Novoselov and A. K. Geim, *Rev. Mod. Phys.*, 2009, **81**(1), 109.
- 3 Z. F. Wang, Z. Liu and F. Liu, *Nat. Commun.*, 2013, **4**, 1471.
- 4 M. Zhou, W. Ming, Z. Liu, Z. Wang, P. Li and F. Liu, *Proc. Natl. Acad. Sci. U. S. A.*, 2014, **111**(40), 14378–14381.
- 5 M. Zhou, Z. Liu, W. Ming, Z. Wang and F. Liu, *Phys. Rev. Lett.*, 2014, **113**(23), 236802.
- 6 Y. Ma, Y. Dai and B. Huang, *J. Phys. Chem. Lett.*, 2013, **4**(15), 2471–2476.
- 7 S. Cahangirov, M. Topsakal, E. Aktürk, H. Şahin and S. Ciraci, *Phys. Rev. Lett.*, 2009, **102**(23), 236804.
- 8 D. Malko, C. Neiss, F. Viñes and A. Görling, *Phys. Rev. Lett.*, 2012, **108**(8), 086804.
- 9 Y. Li, P. Tang, P. Chen, J. Wu, B. L. Gu, Y. Fang and W. Duan, *Phys. Rev. B: Condens. Matter Mater. Phys.*, 2013, **87**(24), 245127.
- 10 Y. Li, P. Chen, G. Zhou, J. Li, J. Wu, B. L. Gu and W. Duan, *Phys. Rev. Lett.*, 2012, **109**(20), 206802.
- 11 L. Z. Zhang, Z. F. Wang, S. X. Du, H. J. Gao and F. Liu, *Phys. Rev. B: Condens. Matter Mater. Phys.*, 2014, **90**(16), 161402.
- 12 Y. Ma, Y. Dai, X. Li, Q. Sun and B. Huang, *Carbon*, 2014, **73**, 382–388.
- 13 S. Dutta and S. K. Pati, *J. Phys. Chem. B*, 2008, **112**(5), 1333–1335.
- 14 S. Dutta, A. K. Manna and S. K. Pati, *Phys. Rev. Lett.*, 2009, **102**(9), 096601.
- 15 R. Y. Oeiras, F. M. Araújo-Moreira and E. Z. Da Silva, *Phys. Rev. B: Condens. Matter Mater. Phys.*, 2009, **80**(7), 073405.
- 16 Y. W. Son, M. L. Cohen and S. G. Louie, *Nature*, 2006, **444**, 347–349.

- 17 H. Ishizuka and Y. Motome, *Phys. Rev. Lett.*, 2012, **109**(23), 237207.
- 18 Y. Li, D. West, H. Huang, J. Li, S. B. Zhang and W. Duan, *Phys. Rev. B: Condens. Matter Mater. Phys.*, 2015, **92**(20), 201403.
- 19 X. Li, X. Wu and J. Yang, *J. Am. Chem. Soc.*, 2014, **136**(31), 11065–11069.
- 20 X. Li and J. Yang, *J. Mater. Chem. C*, 2014, **2**(34), 7071–7076.
- 21 H. L. Zhuang, Y. Xie, P. R. C. Kent and P. Ganesh, *Phys. Rev. B: Condens. Matter Mater. Phys.*, 2015, **92**(3), 035407.
- 22 W. B. Zhang, Q. Qu, P. Zhu and C. H. Lam, *J. Mater. Chem. C*, 2015, **3**(48), 12457–12468.
- 23 J. Liu, Q. Sun, Y. Kawazoe and P. Jena, *Phys. Chem. Chem. Phys.*, 2016, DOI: 10.1039/C5CP04835D.
- 24 F. Wu, C. Huang, H. Wu, C. Lee, K. Deng, E. Kan and P. Jena, *Nano Lett.*, 2015, **15**(12), 8277–8281.
- 25 M. W. Lin, H. L. Zhuang, J. Yan, T. Z. Ward, A. A. Puzosky, C. M. Rouleau and P. Ganesh, *J. Mater. Chem. C*, 2016, **4**(2), 315–322.
- 26 K. Du, X. Wang, Y. Liu, P. Hu, M. I. B. Utama, C. K. Gan and C. Kloc, *ACS Nano*, 2016, **10**(2), 1738–1743.
- 27 M. A. McGuire, H. Dixit, V. R. Cooper and B. C. Sales, *Chem. Mater.*, 2015, **27**(2), 612–620.
- 28 H. Hillebrecht, P. J. Schmidt, H. W. Rotter, G. Thiele, P. Zönnchen, H. Bengel and M. H. Whangbo, *J. Alloys Compd.*, 1997, **246**(1), 70–79.
- 29 F. Hulliger, *Structural chemistry of layer-type phases*, Springer Science & Business Media., 2012.
- 30 P. Miró, M. Audiffred and T. Heine, *Chem. Soc. Rev.*, 2014, **43**(18), 6537–6554.
- 31 Y. Zhou, H. Lu, X. Zu and F. Gao, *Sci. Rep.*, 2016, **6**, 19407.
- 32 L. Li, Y. Wang, S. Xie, X. B. Li, Y. Q. Wang, R. Wu and H. J. Gao, *Nano Lett.*, 2013, **13**(10), 4671–4674.
- 33 Y. J. Song, K. W. Lee and W. E. Pickett, *Phys. Rev. B: Condens. Matter Mater. Phys.*, 2015, **92**(12), 125109.
- 34 M. Feng, B. Shao, X. Cao and X. Zuo, *J. Appl. Phys.*, 2015, **117**(17), 17C118.
- 35 G. Kresse and H. Jürgen, *Phys. Rev. B*, 1993, **47**, 558.
- 36 G. Kresse and D. Joubert, *Phys. Rev. B: Condens. Matter Mater. Phys.*, 1999, **59**, 1758.
- 37 J. P. Perdew, K. Burke and M. Ernzerhof, *Phys. Rev. Lett.*, 1996, **77**, 3865.
- 38 S. L. Dudarev, G. A. Botton, S. Y. Savrasov, C. J. Humphreys and A. P. Sutton, *Phys. Rev. B: Condens. Matter Mater. Phys.*, 1998, **57**, 1505.
- 39 M. Cococcioni and S. De Gironcoli, *Phys. Rev. B: Condens. Matter Mater. Phys.*, 2005, **71**, 035105.
- 40 <http://www.quantum-espresso.org/>.
- 41 K. Parlinski, Z. Q. Li and Y. Kawazoe, *Phys. Rev. Lett.*, 1997, **78**, 4063.
- 42 A. Togo, F. Oba and I. Tanaka, *Phys. Rev. B: Condens. Matter Mater. Phys.*, 2008, **78**(13), 134106.
- 43 S. Grimme, *J. Comput. Chem.*, 2006, **27**, 1787.
- 44 R. E. McCarley, J. W. Roddy and K. O. Berry, *Inorg. Chem.*, 1964, **3**, 50–54.
- 45 N. Sivadas, M. W. Daniels, R. H. Swendsen, S. Oakamoto and D. Xiao, *Phys. Rev. B: Condens. Matter Mater. Phys.*, 2015, **91**, 235425.
- 46 C. C. Liu, W. Feng and Y. Yao, *Phys. Rev. Lett.*, 2011, **107**(7), 076802.
- 47 Y. Xu, B. Yan, H. J. Zhang, J. Wang, G. Xu, P. Tang and S. C. Zhang, *Phys. Rev. Lett.*, 2013, **111**(13), 136804.
- 48 J. He, P. Zhou, N. Jiao, S. Y. Ma, K. W. Zhang, R. Z. Wang and L. Z. Sun, *Sci. Rep.*, 2014, **4**, 4014.
- 49 H. Jin, Y. Dai, B. Huang and M. H. Whangbo, *Appl. Phys. Lett.*, 2009, **94**, 162505.
- 50 Y. Ma, Y. Dai, M. Guo, C. Niu, Y. Zhu and B. Huang, *ACS Nano*, 2012, **6**, 1695–1701.
- 51 H. Shu, P. Luo, P. Liang, D. Cao and X. Chen, *ACS Appl. Mater. Interfaces*, 2015, **7**, 7534–7541.

# **Attachment No. 12**



Cite this: *Nanoscale*, 2017, 9, 2246

## Near-room-temperature Chern insulator and Dirac spin-gapless semiconductor: nickel chloride monolayer

Junjie He,<sup>a</sup> Xiao Li,<sup>\*b</sup> Pengbo Lyu<sup>a</sup> and Petr Nachtigall<sup>\*a</sup>

A great obstacle for practical applications of the quantum anomalous Hall (QAH) effect is the lack of suitable QAH materials (Chern insulators) with a large non-trivial band gap, room-temperature magnetic order and high carrier mobility. Based on first-principles calculations it is shown here that a nickel chloride (NiCl<sub>2</sub>) monolayer has all these characteristics. Thus, the NiCl<sub>2</sub> monolayer represents a new class of Dirac materials with Dirac spin-gapless semiconducting properties and high-temperature ferromagnetism (~400 K). Taking into account the spin-orbit coupling, the NiCl<sub>2</sub> monolayer becomes an intrinsic Chern insulator with a large non-trivial band gap of ~24 meV, corresponding to an operating temperature as high as ~280 K at which the quantum anomalous Hall effect could be observed. The calculated large non-trivial gap, high Curie temperature and single-spin Dirac states reported herein for the NiCl<sub>2</sub> monolayer led us to propose that this material gives a great promise for potential realization of a near-room temperature QAH effect and potential applications in spintronics. Last but not least the calculated Fermi velocities of Dirac fermions of about  $4 \times 10^5$  m s<sup>-1</sup> indicate very high mobility in NiCl<sub>2</sub> monolayers.

Received 31st October 2016,  
Accepted 7th January 2017

DOI: 10.1039/c6nr08522a

rsc.li/nanoscale

### 1. Introduction

A Chern insulator or quantum anomalous Hall insulator is a novel topological phase of matter characterized by a finite Chern number and helical edge electron states within the bulk band gap.<sup>1</sup> Without an external magnetic field, the internal magnetic exchange interaction (ferromagnetic or antiferromagnetic order) can break time-reversal symmetry (TRS) while opening a non-trivial spin-orbital coupling induced gap, giving rise to a quantized anomalous Hall conductivity.<sup>2</sup> The helical edge states are robust against defects and impurities and, thus, such materials are attractive for applications in low power consumption electronic and spintronic devices.<sup>2</sup> Introducing magnetic order to break the TRS in topological insulators (TIs), such as chromium-doped Bi<sub>2</sub>Te<sub>3</sub>,<sup>3</sup> manganese doped HgTe quantum wells (QWs)<sup>4</sup> etc., is expected to be a promising route for realizing the quantum anomalous Hall (QAH) effect. Very recently, the QAH effect has been observed experimentally in the topological insulator Cr doped (Bi,Sb)<sub>2</sub>Te<sub>3</sub> film<sup>5</sup> at an extremely low temperature (below 30 mK) due to only a weak magnetic coupling and a corres-

ponding small band gap. For practical applications it is crucial to search for QAH materials with a sizeable band gap, high Curie temperature ( $T_c$ ), as well as a high carrier mobility.<sup>6</sup> Recently, a variety of QAH materials have been predicted based on impurities,<sup>3,4,7</sup> adatoms,<sup>8,9</sup> or chemical decorations<sup>10</sup> of graphene-like and Bi-based materials, and also in metal-organic-frameworks,<sup>11,12</sup> interface structures<sup>13,14</sup> and heterostructure materials (*i.e.* CrO<sub>2</sub>/TiO<sub>2</sub>, (Bi,Sb)<sub>2</sub>Te<sub>3</sub>/GdI<sub>2</sub>, and double perovskites).<sup>15–17</sup> Most of these theoretically proposed materials show the QAH effect below the room-temperature  $T_c$  due to a weak magnetic order or a small spin-orbit coupling (SOC) gap.

Spin-gapless semiconductors (SGSs), exhibiting a band gap in one of the spin channels and a zero band gap in the other, have received considerable attention lately due to their unique electronic properties and potential applications in novel spintronic devices.<sup>18</sup> The Dirac spin-gapless semiconductors with half semi-Dirac states are based on a combination of single-spin massless Dirac fermions and half-semimetal with broken TRS. Such materials are particularly suitable for utilization of their electronic spin degrees in electronic devices.<sup>19–22</sup> Accounting for SOC, the gap opening may trigger QAH insulator transition in one spin channel only, which has been predicted for a few systems, such as transition-metal intercalated epitaxial graphene on SiC(0001),<sup>17</sup> and CrO<sub>2</sub>/TiO<sub>2</sub> heterostructures.<sup>14</sup> The search for a new member of the Dirac SGS family with the QAH effect is of great importance for both fundamental interest and practical applications.

<sup>a</sup>Department of Physical and Macromolecular Chemistry, Faculty of Science, Charles University in Prague, 128 43 Prague 2, Czech Republic.  
E-mail: lixiao150@gmail.com, petr.nachtigall@natur.cuni.cz

<sup>b</sup>Department of Physics, University of Texas at Austin, Austin, TX, USA



Transition metal trichlorides (TMCl<sub>3</sub>), a family of layered materials with the general formula TMCl<sub>3</sub> have unique electronic and magnetic properties.<sup>23–28</sup> Among them, relatively weakly interacting layers of a 3D RuCl<sub>3</sub> (dominated by van der Waals interactions) have been exfoliated into 2D materials from the bulk phase recently<sup>29</sup> and the first-principles calculations demonstrate that the RuCl<sub>3</sub> monolayer is metallic. Zhou *et al.*<sup>30</sup> have recently indicated that the mixed metal chlorides (NiRuCl<sub>6</sub>) are intrinsic half-metal antiferromagnets, which can lead towards the QAH effect with an antiferromagnetic order. Based on the first principles calculations we found that the 2D NiCl<sub>3</sub> monolayer, as another member of the TMH family, is an intrinsic Dirac spin-gapless semiconductor with a high temperature ferromagnetism. When SOC is taken into account, a large gap opening is found (24 meV at the HSE06 level), giving rise to the quantum anomalous Hall states. We further confirm that the NiCl<sub>3</sub> monolayer has non-trivial topological Dirac-gap states characterized by a Chern number of  $C = -1$  and chiral edge states. The physical origin of this QAH effect is due to both the intrinsic SOC and ferromagnetism of the NiCl<sub>3</sub> monolayer.

## 2. Results and discussion

The structure of the NiCl<sub>3</sub> monolayer is shown in Fig. 1a. Ni atoms form a 2D honeycomb lattice and each Ni atom is bonded to six Cl atoms in an octahedral environment. Geometry optimization carried out at the PBE level gives a lattice constant of 5.966 Å (Fig. 1b) and the d<sub>Ni–Cl</sub> bond length is 2.60 Å. The vertical distance between the two halide planes is calculated to be 2.93 Å. The 2D Young's modulus for the NiCl<sub>3</sub> monolayer is calculated as:

$$Y_{2D} = A_0 \left( \frac{\partial^2 E}{\partial A^2} \right)_{A_0} = \frac{1}{2\sqrt{3}} \left( \frac{\partial^2 E}{\partial a^2} \right)_{a_0}, \quad (1)$$

where  $E$  is the total energy of the NiCl<sub>3</sub> unit cell,  $a$  and  $A$  stand for the lattice constant and surface area, respectively. Thus the

calculated 2D Young's modulus 25 N m<sup>-1</sup> for the NiCl<sub>3</sub> monolayer is very close to values obtained previously for V- and Cr-based chlorides<sup>26–28</sup> and it is about 7% of the in-plane stiffness of graphene (340 N m<sup>-1</sup>).<sup>31</sup> The stability of the NiCl<sub>3</sub> monolayer is confirmed by phonon spectra calculations and *ab initio* molecular dynamics (AIMD) simulations (Fig. 2). We note that the phonon band has quite small imaginary frequencies (~0.02 THz) in the vicinity of the gamma point ( $k \rightarrow 0$ ), which can be caused by the numerical inaccuracy due to the limited supercell size. Such modes are of acoustic nature and they are derived from a collective vibration mode with a long wavelength approaching infinity,<sup>32,33</sup> which will not significantly affect the overall structural stability of the NiCl<sub>3</sub> monolayer. Moreover, AIMD calculations carried out for 9 ps (with a time step of 3 fs) at 500 K show clearly that the structure and energy of the NiCl<sub>3</sub> monolayer are nearly unchanged (Fig. 2b) suggesting that the NiCl<sub>3</sub> monolayers are thermally stable at room temperature. Most importantly, the system remains magnetic throughout the simulation with an average supercell magnetic moment of about 18μ<sub>B</sub> (2μ<sub>B</sub> per unit cell), demonstrating that the magnetic state of NiCl<sub>3</sub> is robust at room temperature.

The spin-polarized FM ground state with a total magnetic moment of 2μ<sub>B</sub> per unit cell was found for NiCl<sub>3</sub> at 0 K. It corresponds to the d<sup>4131</sup> spin configuration of Ni<sup>3+</sup>, which can be verified by the Bader charge analysis.<sup>34</sup> To determine the preferred magnetic ground state structures of NiCl<sub>3</sub> systems at  $T > 0$ , the collinear FM and AFM states were considered. The nearest-neighbor exchange-coupling parameter  $J$  (the second and the third neighbor exchange-coupling are found to be a magnitude smaller than the nearest-neighbor) can be extracted by mapping the total energies of the systems with different magnetic structures to the Ising model:

$$H_{\text{spin}} = - \sum_{ij} J S_i \cdot S_j, \quad (2)$$

where  $S$  is the net magnetic moment at the Ni site,  $i$  and  $j$  stand for the nearest Ni atoms. By mapping the DFT energies

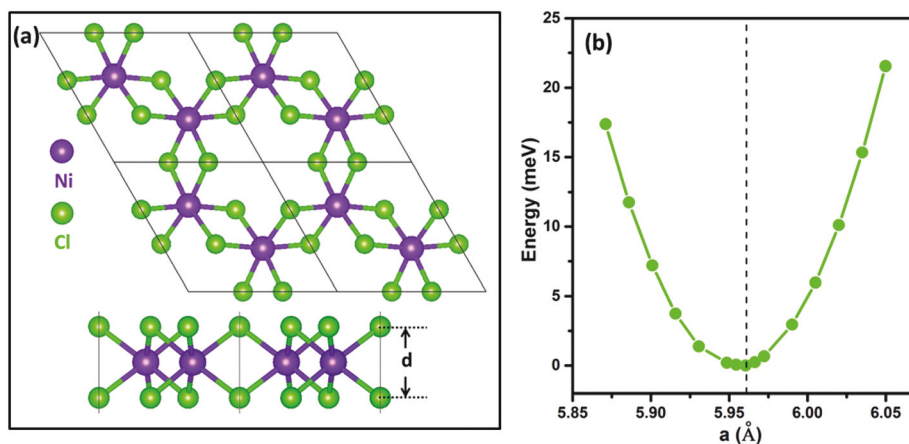
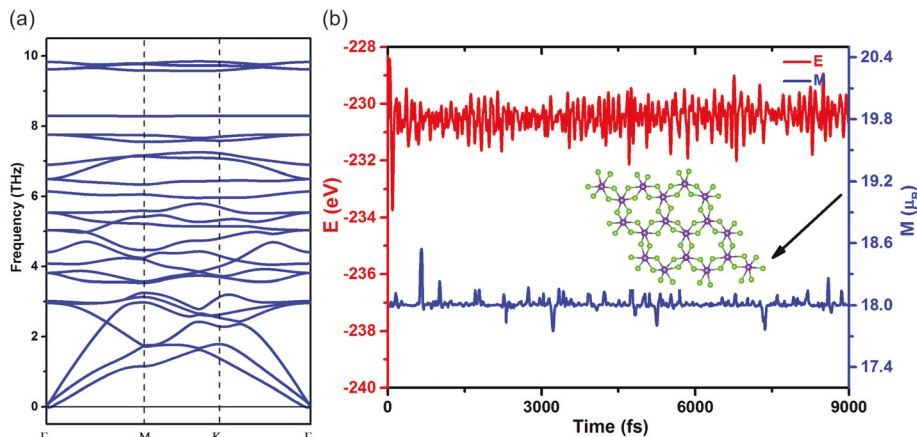


Fig. 1 (a) The top and the side views of the optimized NiCl<sub>3</sub> monolayer. (b) Variation of total energy with the lattice constant.





**Fig. 2** (a) Phonon band structure; (b) potential energy ( $E$ ) and total magnetic moment ( $M$ ) fluctuations of  $\text{NiCl}_3$  as a function of simulation time (depicted in red and blue, respectively). The inset shows the corresponding structure at 500 K after the simulation for 9 ps.

to the Heisenberg model,  $J$  can be calculated as  $J = \Delta E/6S^2$ , where  $\Delta E$  is the energy difference between the ferromagnetic and antiferromagnetic order, leading to the exchange coupling parameter of 89.6 meV.

The Curie temperature  $T_C$  is a key parameter for realization of the high temperature QAH effect and for spintronic applications. Based on the Weiss molecular-field theory (MFT),  $T_C$  can be simply estimated as:

$$T_C = \frac{2zJS(S+1)}{3k_B}, \quad (3)$$

where  $z = 3$  is the number of the nearest-neighbor Ni atoms in the  $\text{NiCl}_3$  monolayer, and  $k_B$  is the Boltzmann constant. Thus the calculated  $T_C = 520$  K is possibly overestimated, therefore, MC simulations based on the Ising model were also carried out. The MC simulations were performed on an  $80 \times 80$  2D honeycomb lattice using  $10^8$  steps for each temperature. The temperature dependence of specific heat capacity and magnetic moments (Fig. 3) shows that the magnetic moment decreases to  $0.8\mu_B$  at about 390 K and becomes  $0\mu_B$  at 400 K. Therefore, the  $T_C$  value for  $\text{NiCl}_3$  monolayers is estimated to be about 400 K, orders of magnitude higher than temperature for the experimentally observed QAH effect. We propose that the  $\text{NiCl}_3$  monolayers can be a potential candidate for the high temperature QAH effect in spintronic applications.

The band structure of the  $\text{NiCl}_3$  FM ground state is shown in Fig. 4. The spin-down channels of  $\text{NiCl}_3$  possess a 1.22 eV and 4.09 eV band gap at PBE and HSE06 levels, respectively, whereas the spin-up channel shows a gapless semiconductor feature with a linear dispersion relation around the Fermi level. The spin-polarized massless Dirac fermions are found in the spin up channels of  $\text{NiCl}_3$  at the high-symmetry  $K$  point of the Brillouin zone. The electronic structure of  $\text{NiCl}_3$  shows rather rare Dirac spin-gapless semiconductor characteristics that are essential for potential high-speed spin filter devices. To further investigate the distribution of the linear dispersion relation in the Brillouin zone, the corresponding three dimensional band structures are also presented (Fig. 4c).

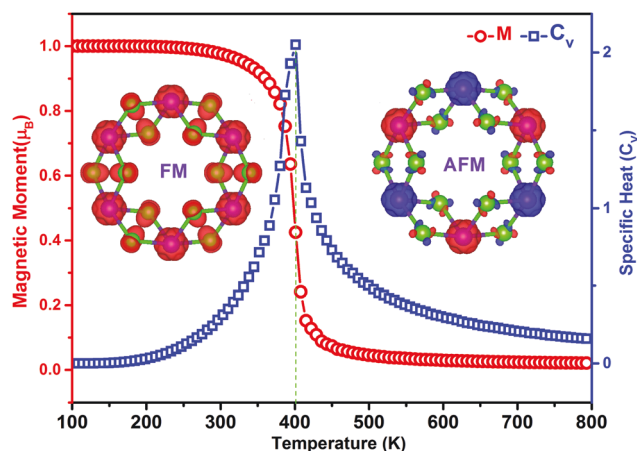


**Fig. 3** Variations of the average magnetic moment (red) and specific heat (blue) calculated for a  $\text{NiCl}_3$  monolayer with respect to the temperature. Spin-polarized charge densities with spin directions for  $\text{NiCl}_3$  are shown in insets (blue dotted areas depicts the spin up); iso-surface value of  $\pm 0.005 \text{ e} \text{ \AA}^{-3}$  is shown.

The calculated Fermi velocities ( $v_F$ ) of Dirac fermions are about  $4 \times 10^5 \text{ m s}^{-1}$  for  $\text{NiCl}_3$  monolayers at the HSE06 level, a value that is approximately half of that found for graphene ( $8 \times 10^5 \text{ m s}^{-1}$ ).<sup>36</sup>

Dirac materials, such as graphene, silicene, germanene, *etc.* are characterized by Dirac states composed of p-orbitals with weak spin-orbital couplings. Thus, SOC opens just a small gap, making these materials the Z2 topological insulators with TRS protected edged states. However, the Dirac states of  $\text{NiCl}_3$  are mainly derived from the Ni-d orbitals. The larger SOC gap of Ni-d orbitals with the broken TRS may lead to the Chern insulator and QAH effect. The SOC gap was calculated by relativistic PBE + SOC calculations to be 7 meV (Fig. 4). However, SOC gaps calculated at the HSE06 level are considered more reliable and they are often comparable with experimental values. The HSE06 + SOC calculations show the 24 meV gap which is sufficiently large for the QAH effect to be operative at





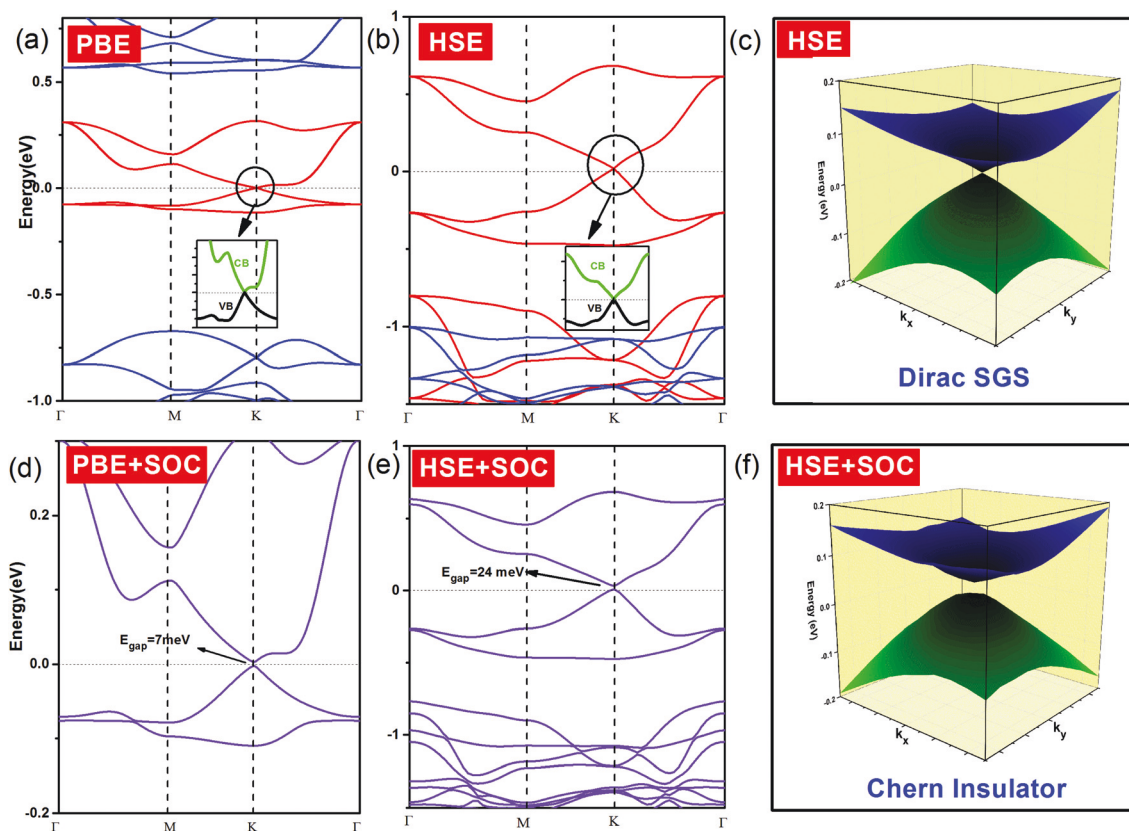


**Fig. 4** Band structures of 2D NiCl<sub>3</sub> with and without SOC calculated at the PBE and HSE levels. Details of Dirac states near the Fermi level are shown in the insets of parts a and b where VB and CB are marked by green and black, respectively. The horizontal dotted lines indicate the Fermi level. The red and blue lines represent the spin up and spin down channels, respectively. The 3D band structures around the Fermi level in the 2D *k* space obtained without (c) and with (f) SOC are also presented.

the temperature as high as 280 K. The Chern insulator states of the NiCl<sub>3</sub> monolayer can be confirmed by the non-zero Chern numbers (*C*) calculated from the *k*-space integral of the Berry curvature ( $\Omega(\vec{k})$ ) of all the states below the Fermi level using the formula of Kubo:<sup>35–37</sup>

$$C = \frac{1}{2\pi} \int_{\text{BZ}} \Omega(\vec{k}) d^2k \quad (4)$$

$$\Omega(k) = \sum_{n < E_f} \sum_{m \neq n} 2\text{Im} \frac{\langle \psi_{nk}^- | \nu_x | \psi_{nk}^- \rangle \langle \psi_{nk}^- | \nu_y | \psi_{nk}^- \rangle}{(\epsilon_{mk}^- - \epsilon_{nk}^-)^2} \quad (5)$$

$\psi_{nk}$  is the spinor Bloch wave function of band *n* with the corresponding eigenenergy  $\epsilon_{nk}$ .  $\nu_x$  and  $\nu_y$  are the *i*-th Cartesian components of the velocity operator.

The Berry curvature  $\Omega(\vec{k})$  along the high-symmetry direction (*M*'–*K*'– $\Gamma$ –*K*–*M*) has two sharp spikes of the same sign located at the *K* and *K*' points as shown in Fig. 5a. By integrating the Berry curvature in the entire Brillouin zone, the calculated Chern number *C* is  $-1$  with a non-trivial topological state. As expected from the non-zero Chern number, the anomalous Hall conductivity shows a quantized charge Hall plateau of  $\sigma_{xy} = Ce^2/h$  when the Fermi level is located in the insulating gap of the spin-up Dirac cone.

The existence of topologically protected chiral edge states is one of the most important consequences of the QAH state. To further reveal the nontrivial topological nature of the NiCl<sub>3</sub> monolayer, we calculate the edge states of the NiCl<sub>3</sub> monolayer with zigzag and armchair insulators using Green's functions based on Wannier functions obtained from PBE calculations, which reduces the cost of calculations while it does not change the topology of the electronic structure, besides a smaller band of 7 meV. As shown in Fig. 5, the nontrivial edge states (dark line) connecting the valence and conduction bands cross the insulating gap of the Dirac cone. The appearance of only one chiral edge state is consistent with the calculated Chern number  $C = -1$ , confirming the nontrivial topological nature of the NiCl<sub>3</sub> monolayer. The calculated gap of 24 meV corresponds roughly to 280 K, leading us to conclude that the QAH effect in NiCl<sub>3</sub> is expected to be robust up to 280 K. This is three orders of magnitude higher than the experimental temperature (<100 mK) at which QAH was observed for a Cr doped Bi<sub>2</sub>Se<sub>3</sub> film.<sup>5</sup> Furthermore, the FM ordering temperature as high as 400 K for NiCl<sub>3</sub> is large enough to retain the QAH phase in the above-mentioned temperature range. The single spin Dirac fermion mediated topological properties of the NiCl<sub>3</sub> monolayer show a great potential to generate the QAH effect. Moreover, manipulation of valley



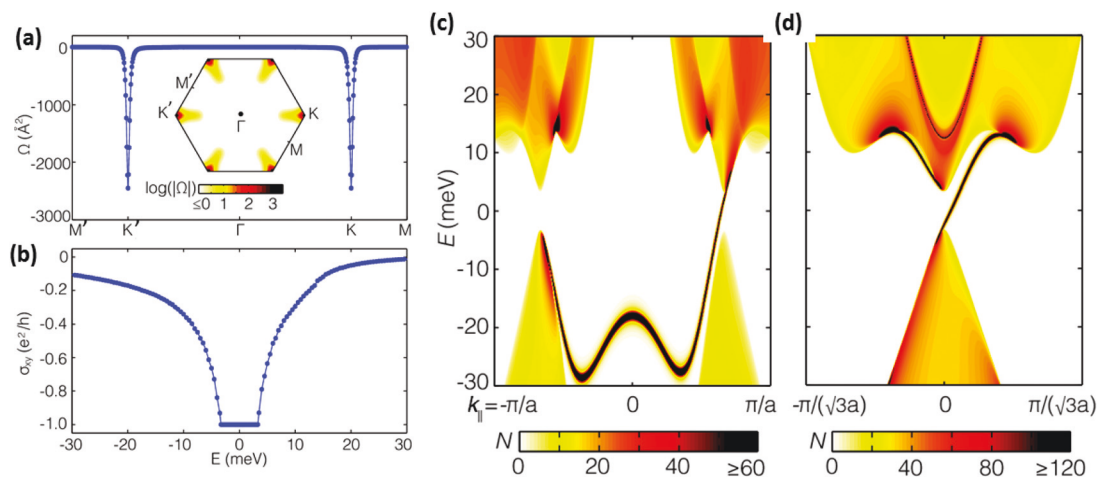


**Fig. 5** (a) The distribution of the Berry curvature in momentum space for NiCl<sub>3</sub>. (b) Anomalous Hall conductivity when the Fermi level is shifted from its original Fermi level. Calculated local density of states of edge states for (c) zigzag and (d) armchair insulators. The edge states are calculated on the edge of a semi-infinite plane. The warmer colors (darker) represent higher local density of states at the edge.

degrees of freedom for electrons may result in potential applications in nanoelectronic devices. The valley polarized edge states can be used as a valley filter analogous to a “spin filter”.<sup>38,39</sup> The 2D mirror symmetry breaking in TMCl<sub>3</sub> materials leads to Rashba SOC, which may lead to the valley-polarized edge state.<sup>40</sup> However, Fig. 5a shows that Berry phases of two valleys are nearly identical with  $\pi$  contribution in each valley. The edge states in Fig. 5c connect the VB of the left valley and the CB of the right valley. Therefore, there is no observable valley-polarized edge state in NiCl<sub>3</sub>. The valley-polarized edge states based on considerable Rashba SOC may be found in other TMCl<sub>3</sub> layered materials.

Finally, the PDOS and orbital-projected band structures around the Fermi level were calculated for the NiCl<sub>3</sub> monolayer to gain insight into the origin of electronic, magnetic and topological properties (Fig. 6). Under the distorted octahedral crystal field of Cl atoms, the d orbital of Ni would be split into

$e_1$  ( $d_{xz}$ ,  $d_{yz}$ ),  $e_2$  ( $d_{xy}$ ,  $d_{x^2-y^2}$ ) and  $a_1$  ( $d_{z^2}$ ) states. Based on Griffith's crystal field theory, the spin states of TM ions can be determined by the relative strength between crystal field splitting ( $\Delta E_{cf}$ ) and Hund exchange splitting ( $\Delta E_{ex}$ ) of d orbitals. The exchange splitting (0.4 eV) is smaller than the crystal field splitting (0.7 eV) for the NiCl<sub>3</sub> monolayer resulting in a low spin ( $1\mu_B$ ) state which is in agreement with the Ni( $d^{14}$ ) spin configuration. The states near the Fermi level have main contributions from the  $e_1$  and  $e_2$  states in  $[-0.2, 0.44$  eV] windows, while the  $a_1$  state does not contribute significantly. The partially occupied  $e_1$  and  $e_2$  orbitals around the Fermi level form a Dirac point in the NiCl<sub>3</sub> monolayer. PDOS for  $e_1$  and  $e_2$  orbitals are shown in Fig. 6 together with orbital-projected band structures. The states near the Fermi level are dominated by  $e_2$  orbitals with only a small contribution from  $e_1$  orbitals. Without SOC, both VB and CB show an equivalent weight for  $e_1$  and  $e_2$  states. Calculations with SOC show significantly increased

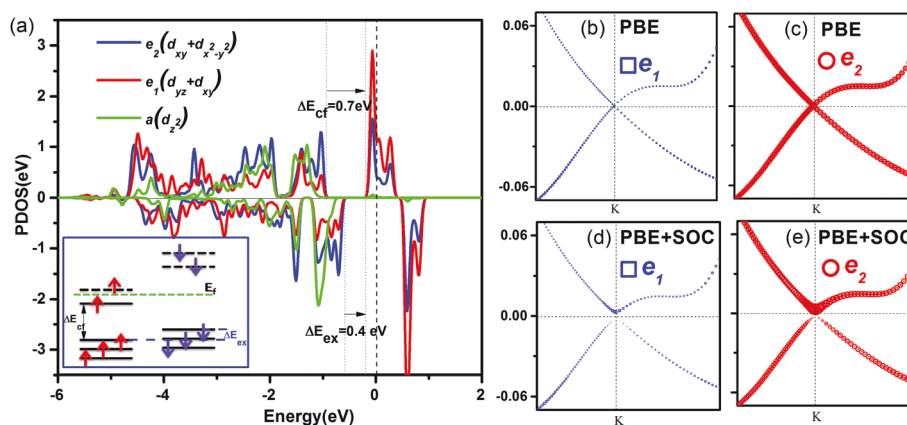


**Fig. 6** (a) The PDOS of d states for Ni atoms is shown. The schematic figure (inset in part a) is the crystal field splitting and exchange splitting for Ni ions. (b) The evolution of orbital-resolved band structures ( $e_1$  and  $e_2$  states) of a NiCl<sub>3</sub> monolayer without and with SOC. The Fermi level is set to zero.



contributions of both  $e_1$  and  $e_2$  in CB while the  $e_1$  and  $e_2$  contributions to VB decrease. As a result, the degeneracy of  $e_1$  levels (and similarly the degeneracy of  $e_2$  levels) around the Dirac point is lifted, opening thus a global energy gap between CB and VB bands (Fig. 6b). The SOC results in the significant changes of  $e_1$  and  $e_2$  orbital energies and their contributions to CB and VB and consequently it plays a crucial role in the topological properties of the NiCl<sub>3</sub> monolayer.

### 3. Conclusions

DFT calculations were used in a systematic investigation of the stability, and electronic and magnetic structures of NiCl<sub>3</sub> monolayers. The thermal and dynamical stabilities have been confirmed by phonon calculations and *ab initio* molecular dynamics simulations. The NiCl<sub>3</sub> monolayers show the Dirac spin-gapless semiconducting characteristics and high-temperature ferromagnetism. The Monte Carlo simulations based on the Ising model demonstrate that the Curie temperature of the NiCl<sub>3</sub> monolayer is estimated to be as high as 400 K. In addition, a Fermi velocity ( $v_F$ ) in the NiCl<sub>3</sub> monolayer is calculated to be  $4 \times 10^5$  m s<sup>-1</sup>, which is comparable to graphene ( $8 \times 10^5$  m s<sup>-1</sup>). Taking the spin-orbit coupling into account, the NiCl<sub>3</sub> monolayer becomes an intrinsic Chern insulator with a large non-trivial band gap of about 24 meV, corresponding to an operating temperature of 280 K. The large non-trivial gap, high Curie temperature and single-spin Dirac states for NiCl<sub>3</sub> monolayers give rise to great expectations for both the realization of near room temperature QAH effect and potential applications in spintronics.

### 4. Methods and computational details

All calculations were performed using the Vienna *ab initio* simulation package (VASP)<sup>41,42</sup> within the generalized gradient approximation, using the Perdew–Burke–Ernzerhof (PBE) exchange–correlation functional.<sup>43</sup> Electronic properties (SOC in particular) were also calculated with the hybrid HSE06 functional. Interactions between electrons and nuclei were described by the projector-augmented wave (PAW) method. The criteria of energy and atom force convergence were set to  $10^{-6}$  eV and  $0.001$  eV Å<sup>-1</sup>, respectively. A plane-wave kinetic energy cutoff of 500 eV was employed. The vacuum space of 15 Å along the NiCl<sub>3</sub> normal was adopted for calculations on monolayers. The Brillouin zone (BZ) was sampled using  $15 \times 15 \times 1$  gamma-centered Monkhorst–Pack grids for the calculations of relaxation and electronic structures. Furthermore, to examine the thermal stability of NiCl<sub>3</sub>, the *ab initio* molecular dynamics (AIMD) simulations at 300 K were performed using the Nosé heat bath approach in a canonical ensemble. A  $3 \times 3 \times 1$  supercell of the NiCl<sub>3</sub> monolayer was used in MD simulations. The phonon frequencies were calculated using a finite displacement approach as implemented in the PHONOPY code, in which a  $2 \times 2 \times 1$  supercell and a displacement of 0.01 Å from the equilibrium atomic positions were

employed.<sup>44,45</sup> The electronic properties of the NiCl<sub>3</sub> monolayer obtained by VASP have been further reproduced by the QUANTUM ESPRESSO package,<sup>46</sup> with the norm-conserving pseudopotentials from the PS library<sup>47</sup> and a 120 Ry plane wave cutoff. Based on the Wannier functions obtained from the first-principles calculations in QUANTUM ESPRESSO,<sup>48–50</sup> we construct the edge Green's function of the semi-infinite NiCl<sub>3</sub> monolayer. The edge spectral density of states, computed by the edge Green's function, shows the energy dispersion of edge states.<sup>51</sup> The Berry curvature and the anomalous Hall conductivity are also calculated by the Wannier interpolation.<sup>49</sup>

### Acknowledgements

This work was funded by the Czech Science Foundation Grant No. P106/12/G015 and by OP VVV “Excellent Research Teams”, project No. CZ.02.1.01/0.0/0.0/15\_003/0000417 – CUCAM. Support by the 973 Program (Projects 2013CB921900), DOE (DE-FG03-02ER45958, Division of Materials Science and Engineering) and Welch Foundation (F-1255) is also acknowledged (XL).

### References

- 1 F. D. M. Haldane, *Phys. Rev. Lett.*, 1988, **61**, 2015.
- 2 B. I. Halperin, *Phys. Rev. B: Condens. Matter*, 1982, **25**, 2185.
- 3 R. Yu, W. Zhang, H. J. Zhang, S. C. Zhang, X. Dai and Z. Fang, *Science*, 2010, **329**, 61–64.
- 4 C. X. Liu, X. L. Qi, X. Dai, Z. Fang and S. C. Zhang, *Phys. Rev. Lett.*, 2008, **101**, 146802.
- 5 C. Z. Chang, J. Zhang, X. Feng, J. Shen, Z. Zhang, M. Guo and Z. Q. Ji, *Science*, 2013, **340**, 167–170.
- 6 H. Weng, R. Yu, X. Hu, X. Dai and Z. Fang, *Adv. Phys.*, 2015, **64**, 227–282.
- 7 H. Jiang, Z. Qiao, H. Liu and Q. Niu, *Phys. Rev. B: Condens. Matter*, 2012, **85**, 045445.
- 8 H. Zhang, C. Lazo, S. Blügel, S. Heinze and Y. Mokrousov, *Phys. Rev. Lett.*, 2012, **108**, 056802.
- 9 J. Liu, S. Y. Park, K. F. Garrity and D. Vanderbilt, *Phys. Rev. Lett.*, 2016, **117**, 257201.
- 10 S. C. Wu, G. Shan and B. Yan, *Phys. Rev. Lett.*, 2014, **113**, 256401.
- 11 L. Dong, Y. Kim, D. Er, A. M. Rappe and V. B. Shenoy, *Phys. Rev. Lett.*, 2016, **116**, 096601.
- 12 Z. F. Wang, Z. Liu and F. Liu, *Phys. Rev. Lett.*, 2013, **110**, 196801.
- 13 H. Fu, Z. Liu, C. Lian, J. Zhang, H. Li, J. T. Sun and S. Meng, *Phys. Rev. B: Condens. Matter*, 2016, **94**, 035427.
- 14 K. F. Garrity and D. Vanderbilt, *Phys. Rev. B: Condens. Matter*, 2014, **90**, 121103.
- 15 A. M. Cook and A. Paramekanti, *Phys. Rev. Lett.*, 2014, **113**, 077203.
- 16 T. Cai, X. Li, F. Wang, S. Ju, J. Feng and C. D. Gong, *Nano Lett.*, 2015, **15**, 6434–6439.



- 17 G. Xu, J. Wang, C. Felser, X. L. Qi and S. C. Zhang, *Nano Lett.*, 2015, **15**, 2019–2023.
- 18 X. L. Wang, *Phys. Rev. Lett.*, 2008, **100**, 156404.
- 19 V. Pardo and W. E. Pickett, *Phys. Rev. Lett.*, 2009, **102**, 166803.
- 20 H. Ishizuka and Y. Motome, *Phys. Rev. Lett.*, 2012, **109**, 237207.
- 21 Y. Li, D. West, H. Huang, J. Li, S. B. Zhang and W. Duan, *Phys. Rev. B: Condens. Matter*, 2015, **92**, 201403.
- 22 X. L. Wang, 2016, *arXiv:1607.06057*.
- 23 M. A. McGuire, H. Dixit, V. R. Cooper and B. C. Sales, *Chem. Mater.*, 2015, **27**, 612–620.
- 24 H. Hillebrecht, P. J. Schmidt, H. W. Rotter, G. Thiele, P. Zönnchen, H. Bengel and M. H. Whangbo, *J. Alloys Compd.*, 1997, **246**, 70–79.
- 25 F. Hulliger, *Structural chemistry of layer-type phases*, Springer Science & Business Media, 2012.
- 26 J. He, S. Ma, P. Lyu and P. Nachtigall, *J. Mater. Chem. C*, 2016, **4**, 2518–2526.
- 27 W. B. Zhang, Q. Qu, P. Zhu and C. H. Lam, *J. Mater. Chem. C*, 2015, **3**, 12457–12468.
- 28 J. Liu, Q. Sun, Y. Kawazoe and P. Jena, *Phys. Chem. Chem. Phys.*, 2016, **18**, 8777–8784.
- 29 P. Miró, M. Audiffred and T. Heine, *Chem. Soc. Rev.*, 2014, **43**, 6537–6554.
- 30 P. Zhou, C. Q. Sun and L. Z. Sun, *Nano Lett.*, 2016, **16**(10), 6325–6330.
- 31 C. Lee, X. Wei, J. W. Kysar and J. Hone, *Science*, 2008, **321**, 385–388.
- 32 S. Cahangirov, M. Topsakal, E. Aktürk, H. Şahin and S. Ciraci, *Phys. Rev. Lett.*, 2009, **102**(23), 236804.
- 33 H. Şahin, S. Cahangirov, M. Topsakal, E. Bekaroglu, E. Akturk, R. T. Senger and S. Ciraci, *Phys. Rev. B: Condens. Matter*, 2009, **80**(15), 155453.
- 34 G. Henkelman, A. Arnaldsson and H. Jónsson, *Comput. Mater. Sci.*, 2006, **36**, 354–360.
- 35 D. J. Thouless, M. Kohmoto, M. P. Nightingale and M. Den Nijs, *Phys. Rev. Lett.*, 1982, **49**, 405.
- 36 Y. Yao, L. Kleinman, A. H. MacDonald, J. Sinova, T. Jungwirth, D. S. Wang and Q. Niu, *Phys. Rev. Lett.*, 2004, **92**, 037204.
- 37 D. Xiao, M. C. Chang and Q. Niu, *Rev. Mod. Phys.*, 2010, **82**, 1959.
- 38 A. Rycerz, J. Tworzydło and C. W. J. Beenakker, *Nat. Phys.*, 2007, **3**, 172–175.
- 39 S. G. Cheng, J. Zhou, H. Jiang and Q. F. Sun, *New J. Phys.*, 2016, **18**(10), 103024.
- 40 T. Zhou, J. Zhang, Y. Xue, B. Zhao, H. Zhang, H. Jiang and Z. Yang, 2016, *arXiv preprint arXiv:1611.04715*.
- 41 G. Kresse and H. Jürgen, *Phys. Rev. B: Condens. Matter*, 1993, **47**, 558.
- 42 G. Kresse and D. Joubert, *Phys. Rev. B: Condens. Matter*, 1999, **59**, 1758.
- 43 J. P. Perdew, K. Burke and M. Ernzerhof, *Phys. Rev. Lett.*, 1996, **77**, 3865.
- 44 K. Parlinski, Z. Q. Li and Y. Kawazoe, *Phys. Rev. Lett.*, 1997, **78**, 4063.
- 45 A. Togo, F. Oba and I. Tanaka, *Phys. Rev. B: Condens. Matter*, 2008, **78**, 134106.
- 46 P. Giannozzi, *et al.*, *J. Phys.: Condens. Matter*, 2009, **21**, 395502 <http://www.quantum-espresso.org>.
- 47 Pseudopotentials are available at <http://qe-forge.org/gf/project/pslibrary>.
- 48 N. Marzari and D. Vanderbilt, *Phys. Rev. B: Condens. Matter*, 1997, **56**, 12847.
- 49 A. Mostofi, J. R. Yates, Y. S. Lee, I. Souza, D. Vanderbilt and N. Marzari, *Comput. Phys. Commun.*, 2008, **178**, 685.
- 50 A. A. Mostofi, J. R. Yates, G. Pizzi, Y. S. Lee, I. Souza, D. Vanderbilt and N. Marzari, *Comput. Phys. Commun.*, 2014, **185**, 2309–2310.
- 51 M. L. Sancho, J. L. Sancho and J. Rubio, *J. Phys. F: Met. Phys.*, 1984, **14**, 1205.

